MULTI-DIMENSIONAL FROST HEAVE MODELING WITH SP POROSITY GROWTH FUNCTION

By

Koui Kim

RECOMMENDED:

Advisory Committee Chair

Chair, Department of Civil and Environmental Engineering

APPROVED:

Dean, College of Engineering and Mines

Dean of Graduate School

Apr 4, 2011

Date

MULTI-DIMENSIONAL FROST HEAVE MODELING WITH SP POROSITY GROWTH FUNCTION

A

THESIS

Presented to Faculty

of the University of Alaska Fairbanks

in Partial Fulfillment of the Requirements

for the Degree of

DOCTOR OF PHILOSOPHY

By

Koui Kim, B.S., M.S.

Fairbanks, Alaska

May 2011

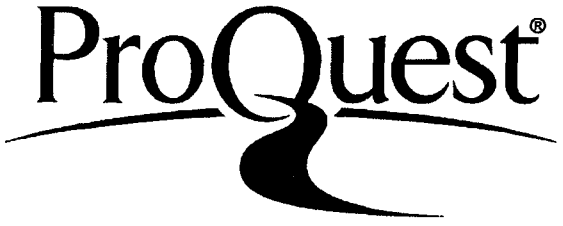

ProQuest LLC
789 East Eisenhower Parkway
P.O. Box 1346
Ann Arbor, MI 48106-1346

ABSTRACT

This dissertation presents a multi-dimensional frost-heave modeling with coupled heat transfer, moisture transfer, and mechanical analysis.

A series of laboratory frost-heave tests was conducted to determine segregation potential (SP) values using the effect of cooling rate and overburden pressure in two different freezing modes. Regardless of the freezing mode, consistent SP values were obtained at the formation of the final ice lens. Continuous heave and water-intake measurements made it possible to determine the time at the formation of the final ice lens.

The SP porosity growth function was developed using simulations of the growing ice lens and frozen fringe. The developed frost-heave model was verified by laboratory frost-heave tests in one dimension. The simulated temperature distribution and amount of heave were in good agreement with experimental values.

The SP porosity growth function was then expanded to two dimensions to simulate the soil-pipeline interaction of an experimental buried chilled pipeline constructed in Fairbanks, Alaska in the early 2000s. A two-dimensional frost-heave simulation was conducted at the free-field area, where the influence of pipeline resistance in frozen ground was negligible. This model, which considers the effect of frozen soil creep on stress distribution due to temperature variation, analyzed the influence of stress fields on soil frost-heave susceptibility and deformation. Simulations of pipe displacement were conducted for two cases, with and without the use of the long-term creep characteristics of frozen soils. Using the long-term creep characteristics, the simulated result agreed well with the observed value, differing by only a few percentage points. However, without using long-term creep characteristics, the simulated pipe heave was approximately 75% of the observed heave because of an unrealistic stress buildup.

Finally, the SP porosity growth function was expanded to predict soil-pipeline interaction around a frozen-unfrozen boundary. Temperature distribution was successfully predicted in both the pre-frozen soil and the unfrozen zones, as well as at the time when differential pipeline movement started. The developed three-dimensional frost-heave model could predict pipe movement and induced bending due to differential frost heave for a 20-year period.

TABLE OF CONTENTS

Page

LIST OF FIGURES

Page

LIST OF TABLES

Page

LIST OF APPENDICES

Page

ACKNOWLEDGMENTS

I am deeply grateful to my advisor, Dr. Scott Huang, for his interest, guidance, and encouragement throughout the development of this dissertation. I would also like to thank the other members of my advisory committee, Dr. Satoshi Akagawa, Dr. Douglas Goering, Dr. Paul Metz, Dr. Yuri Shur, and Dr. Wendy Zhou for their encouragement and assistance with my research.

I am indebted to Dr. Susumu Watanabe, Dr. Rorick Peterson, and Dr. Daniel Fortier for their valuable knowledge regarding frost heave and permafrost given from the perspective of their long-time experience.

I also thank Hokkaido University, Japan, and the University of Alaska Fairbanks' Civil and Environmental Department for allowing me to use laboratory test equipment and permitting me the space required to conduct this research. I would like to thank Dr. Margaret Darrow and Dr. Yuzuru Ito for useful suggestions on the setup of frost-heave tests.

I am grateful to Dr. Xiong Zhang and Dr. Shunji Kanie for their helpful discussions regarding numerical modeling. I am also indebted to the Arctic Region Supercomputing Center (ARSC) for their modeling support. I thank the Alaska Experimental Program to Stimulate Competitive Research (EPSCoR) for providing most of the funding support.

I would like to extend my sincere thanks to Dr. Matthew Bray who shared his valuable experience regarding a full-scale pipeline experiment, and offered useful creep test data and many helpful suggestions.

On the non-technical side, I am deeply grateful to Dr. Candace O'Connor who edited this dissertation and furthermore provided invaluable comments and encouragement.

Special thanks are extended to friends and colleagues who have offered encouragement and fruitful discussions during my stay in Fairbanks, Alaska.

Finally, I wish to acknowledge the support and understanding of my parents and brother throughout the project.

PREFACE

Portions of this research were previously published and presented in a journal and several conferences. The peer reviewed publications include:

Kim, K., Huang, S., Akagawa, S., and Kanie, S. (2005). "Field observation of pipe strain caused by soil pressure development in frost bulb." *Proceedings of the 40th U.S. Rock Mechanics Symposium*, Anchorage, Alaska, (CD-ROM).

Kim, K., Zhou, W., and Huang, S. (2008). "Frost heave predictions of buried chilled gas pipelines with the effect of permafrost." *Cold Regions Science and Technology*, 53(3), 382-396.

Kim, K., Zhou, W., and Huang, S. (2008). "A two-dimensional numerical heat transfer solution for frost heave prediction using the segregation potential concept." *Proceedings of the 9th International Conference on Permafrost*, Fairbanks, Alaska, 941-946.

CHAPTER 1: INTRODUCTION

1.1 Introduction

Since the 1960s, a pipeline system has been the most economical way to transport oil and gas from remote areas such as the Arctic (Williams 1986). Since 1977, the Trans-Alaska Pipeline System (TAPS) has been used to bring crude oil from Alaska's North Slope to market. Due to increases in the price of oil and concern about America's reliance on foreign energy sources, interest in oil and gas development in the energy fields of the North Slope, such as Prudhoe Bay, has increased recently, and there is much talk about building a new pipeline to carry natural gas to market. Three major problems exist for arctic pipeline designs - frost heave, thaw settlement, and thaw weakening (Nixon 2003).

According to the Permafrost Subcommittee (2005), "frost heave" is described thus "The upward or outward movement of the ground surface (or objects on, or in the ground) caused by the formation of ice in the soil". "Thaw settlement" is defined as follows: "Compression of the ground due to thaw consolidation, that time-dependent compression resulting from thawing of frozen ground and subsequent drainage of excess water". "Thaw weakening" is defined as the process by which "the reduction in shear strength due to the decrease in effective stresses resulting from the generation and slow dissipation of excess pore pressures when frozen soils containing ice are thawing".

Several oil and gas pipelines have been constructed in arctic regions. It is worth noting that cooling of oil in pipelines due to the cold climate, especially oil with a high paraffinic content, will result in the product congealing, causing a serious reduction in capacity or even a complete blockage. Also, special above-ground construction is necessary to protect the thaw-sensitive, ice-rich ground. One good example of such construction is the TAPS. Half of the TAPS was constructed on vertical support members (VSMs) equipped with heat pipe as heat exchanger for passive cooling to prevent thawing of ice-rich permafrost. The heat pipe removes heat from the ground when air temperatures are lower than the ground temperature. The requirement to protect the permafrost melting was one of the main reasons that the final construction cost rose to over US$7 billion, almost 7 times the original cost estimation (Williams 1986).

Like oil pipelines, gas pipelines face a series of obstacles if they are to function smoothly in the Arctic environment. Brouchkov and Griva (2004) reported that when gas temperature is above freezing and is not controlled, failures of underground pipeline sections in Norilsk, Russia are forty times more likely than failure of aboveground sections due to the thawing of ice-rich permafrost. In view of the reasons mentioned above, and for the sake of security, environmental considerations, and economy, a buried chilled gas pipeline is advocated by many oil and gas companies and pipeline

construction firms to transport the gas from arctic Alaska and Canada to the continental U.S. Although degradation and thaw settlement of permafrost can be minimized by buried chilled pipelines, differential frost-heave issues are anticipated near the interface between soils with different frost-heave susceptibilities or between frozen and unfrozen soils. Uniform heave movements are not of significant importance for pipeline design as long as their magnitudes are not larger than the stress tolerances of the pipeline. However, differential movements caused by frost heave can be a major source of induced pipeline load. Therefore, for the purposes of designing a buried chilled gas pipeline, it is essential to predict the differential ground movements due to frost heave in terms of soil parameters and thermal boundary conditions.

In the following sections, a brief review of the frost-heave mechanism is presented first. The capabilities and limitations of the existing numerical frost-heave models are discussed second. A review of full-scale pipeline experiments that have been described in the literature follows. Finally, the objectives of this research and the structure of this dissertation are presented.

1.2 Frost-heave mechanism

In the last three decades, extensive research efforts have been devoted to understanding the basic principles of the frost-heave process and their application in numerical frost-heave models. There have been reviews of the existing frost-heave models in papers (e.g. Loch 1980; O'Neill 1983; Black and Hardenberg 1991; Henry 2000), in textbook-style discussions (e.g. Miller 1980), and in books (e.g. Williams 1986). The details of thawing have also been reviewed (Ladanyi and Shen 1989).

1.2.1 Pore-water characteristics

Lunardini (1981) summarized the heat transfer characteristics of pore water in cold climates as follows. The pore water in porous media exists in a number of phases, potentials, and thermodynamic states. The pore water can be divided into two types: free water and adsorbed water. In general, the free water acts as normal water subject to the usual effect of solutes associated with the solid particles. If the free water is pure, it will solidify at a temperature very close to $0^{\circ}C$. This water can be bound due to surface force phenomena or chemical bonding. The adsorbed water can exist within the hygroscopic body or within the cavities in solid particles. Surface phenomena are associated with the adsorbed water, which can be bound either strongly or weakly. The surface of a clayey particle has a net negative charge. The energy of chemical and electrical bonds between the mineral surfaces and the surrounding medium binds a layer of liquid water to the soil particles. At

greater distances from the solid interfaces, the liquid water is less tightly bound and forms a layer that plays an important role in diffusion phenomena. The water in this diffusive layer is of variable potential, and is capable of releasing the heat of fusion and freezing at temperatures colder than 0°C. Water that is still liquid at temperatures colder than 0°C is commonly termed "unfrozen water". As the temperature cools down further, the unfrozen water will eventually solidify.

1.2.2 Forces acting on pore water

Lunardini (1981) also summarized the forces acting on pore water. The forces holding water within the continuous network of voids within a soil skeleton include: gravitational force, osmotic force, interfacial force, adsorption force, and vapor diffusion.

Gravitational force:

Compared to other forces, gravitational forces are quite weak and normally have an insignificant effect on pore water. They only become significant in granular materials at saturation, where the influence of osmotic, interfacial, and adsorption forces are reduced.

Osmotic force:

Osmotic forces arise due to the inevitable presence of ions in the pore water of soils such as clay. Solute ions attract the polar water molecules and reduce the natural random motion of the solvent molecules. Osmotic forces oppose removal of water through a semi-permeable membrane. Therefore, the osmotic potential of pore water is negative and increases with increasing solute concentration.

Interfacial force:

Interfacial forces arise because the inter-molecular attractive forces ordinarily present in any substance are unsatisfied at the phase boundary. The resulting force deforms the liquid water until the surface area and the free surface energy are minimized.

In narrow cylindrical capillaries, the contact angle is usually low and the interface shape becomes hemispherical. The reduced pressure on the convex water side causes water to rise up in the capillary tube until the weight of the water column balances the pressure difference. This is called "capillary rise". A soil matrix can be considered as a network of, albeit rather misshapen, capillary tubes. When the soil matrix is unsaturated, water will be withdrawn from the surrounding soil. As water is withdrawn, the air-water interfaces recede into progressively smaller-sized pores and the

pressure difference increases. A correspondingly greater amount of work must be done to extract the remaining pore water.

Adsorption force:

All solid surfaces tend to attract and retain liquids, gases, and dissolved substances. Adsorption is due to the attractive electromagnetic van der Waals forces acting between the solid and the molecules of the gas or liquid. These forces rapidly decrease in intensity with distance from the surface. Water will interact with the ionic crystal surfaces because of the polar nature of the water molecular structure. The relative magnitude of surface effects depends on the specific surface area of the material and on its chemical nature and level of charge. Clay particles have a large specific surface area due to their relatively small size and jagged shape. In addition, clay minerals generally have a high negative charge. The charge is balanced by adsorbed cations in the double layer of adsorbed water.

Vapor diffusion:

Many investigators (e.g. Jackson 1965; Evgin and Svec 1988) have reported that water and vapor diffusivity varies with the total water content in unsaturated soils. They observed that the overall diffusivity increases with the total water content, but this is mainly due to an increase in the water diffusivity. Observations presented by Nakano and his co-workers (Nakano and Tice 1983; Nakano et al. 1984) suggest that the vapor diffusion is several orders of magnitude lower than the water flow.

1.2.3 Historical works by Taber and Beskow

Taber (1929, 1930) and Beskow (1935) were the first to think clearly about the process of frost heave and to conduct appropriate experiments. They conducted frost-heave experiments in which frost-susceptible specimens were frozen uniaxially from the top, with free access of water from the bottom in an open-water system.

Taber (1929) first recognized that frost heave was due to water migration during freezing, which caused the formation of ice lenses in frost-susceptible materials. At that time, the popular belief was that frost heave was due to volume expansion of *in-situ* pore water upon freezing. Taber (1930) supported his hypothesis of soil expansion by replacing water with benzene and nitro-benzene, which freeze with a decrease in volume at 5.5°C and 5.85°C, respectively.

Beskow (1935) also contributed several important concepts to the understanding of frost heave. One of the most important contributions by Beskow is the understanding that increasing overburden pressure reduces the frost-heave rate. Beskow stated that the total compressive force acting on soil particles during freezing was the sum of the overburden pressure and the soil moisture tension due to capillary forces. Beskow also noticed that when capillary rise of water in the soil is less than the distance between the freezing front and the groundwater table, the soil does not heave.

The importance of their work still remains relevant today, as demonstrated by the re-publication of their original papers by the U.S. Army Cold Regions Research and Engineering Laboratory, CRREL (Black and Hardenberg 1991).

1.2.4 Capillary Theory (primary frost heave)

Capillary Theory is one of the earliest frost heave theories to describe frost-heave pressure and ice-lens formation in granular materials (e.g. Everett 1961; Chalmers and Jackson 1970). According to this theory, water migration to the freezing front is due to the pressure difference at the curved interface between the solid and liquid phases. It is written as:

$$[1.1] \qquad P_i - P_w = \frac{2\sigma_{i-w}}{r_{i-w}}$$

where P_i = ice pressure; P_w = pore-water pressure; σ_{i-w} = surface tension of ice-water interface; and r_{i-w} = radius of ice-water interface.

The ice pressure at a growing ice lens can be assumed to be equal to the overburden pressure in the system. When water migration stops ($P_w = 0$), the applied overburden pressure is determined to be the maximum frost-heave pressure. According to eq. [1.1], the calculated maximum frost-heave pressure does not depend on thermal conditions but only on the radius of curvature of the ice-water interface. The Capillary Theory was experimentally supported (e.g. Penner 1959, 1967). However, by the late 1960s, it was apparent that the Capillary Theory severely underestimates the maximum frost heave pressure (e.g. Hoekstra 1969; Radd and Oertle 1973).

It is known that not all of the pore water in a fine-grained soil freezes at a unique temperature, but rather freezes over a certain range. Experimental observations on frozen soil specimens under temperature gradients suggest that water migration still occurs beyond the freezing front in response to the temperature-induced unfrozen water content gradient and the pore-water pressure gradient. The migrating water freezes at the segregation temperature, which is slightly lower than the freezing temperature, and ice lenses continue to grow. Miller (1972) termed the partially-frozen zone between

the freezing front and the segregation freezing front as "frozen fringe". According to the Capillary Theory, however, an ice lens will only grow at the freezing front.

1.2.5 Thermodynamics equilibrium in static phase

The Capillary Theory was not suitable to predict the driving force of frost heave. In the late 1960s, the concept of thermodynamic equilibrium in the static phase advanced understanding of the driving force of frost heave.

The static phase is defined as a closed system which does not accompany water migration. Free energy is the measure of the energy level of a system, which represents the amount of work required to induce a change in the system. When pressure (P) and temperature (T) are selected as independent parameters, the total energy contained within the system is expressed using the Gibb's free energy (G) as:

[1.2] $$G(P,T) = u + P\overline{V} - sT$$

where u = internal energy; $\overline{V}$ = specific volume; and s = entropy.

A small change of the Gibb's free energy from the reference state to freezing is expressed as:

[1.3] $$\partial G(P,T) = \partial P\frac{\partial G}{\partial P} - \frac{\partial G}{\partial T}\partial T = \partial P\overline{V} - s\partial T$$

In static phase equilibrium, the difference between the free energies of water (G_w) and ice (G_i) can be described as:

[1.4] $$\partial\overline{G}_w - \partial\overline{G}_i = 0$$

Water-ice system:

In the water-ice system, pore-water pressure is equal to ice pressure ($P = P_w = P_i$). The free energies of water (G_w) and ice (G_i) can be described as:

[1.5] $$\begin{cases} \partial\overline{G}_w = \partial P\overline{V}_w - s_w\partial T \\ \partial\overline{G}_i = \partial P\overline{V}_i - s_i\partial T \end{cases}$$

where $\overline{V}_w$ = specific volume of water; $\overline{V}_i$ = specific volume of ice; s_w = entropy of water; and s_i = entropy of ice.

The relationship between the latent heat (L_w) and entropies of water and ice during freezing follows:

[1.6] $$s_w - s_i = \frac{L_w}{273.16 + T}$$

Substituting eqs. [1.5] and [1.6] into eq. [1.4] yields the following:

[1.7] $$\partial P\left(\overline{V}_w - \overline{V}_i\right) = L_w \frac{\partial T}{273.16 + T}$$

Integrating eq. [1.7] yields the following:

[1.8] $$P\left(\overline{V}_w - \overline{V}_i\right) = L_w \ln\left(\frac{273.16 + T}{273.16 + T_0}\right) \cong L_w \frac{T - T_0}{273.16 + T_0}$$

where $T_0 = 0°C$, the freezing temperature of pure water.

Eq. [1.8] is called Clausius-Clapeyron Equation. The approximation in eq. [1.8] is verified. Dividing eq. [1.8] by L_w, the equation is rendered dimensionless, as:

[1.9] $$\frac{P\left(\overline{V}_w - \overline{V}_i\right)}{L_w} = \ln\left(\frac{273.16 + T}{273.16 + T_0}\right) \cong \frac{T - T_0}{273.16 + T_0}$$

The dimensionless parameter $P(\overline{V}_w - \overline{V}_i)/L_w$ is then solely a function of temperature. Generally, an ice lens forms at a temperature as low as -1°C in frost heave. Within the range between -1 and 0°C, the effect of temperature on the dimensionless factor is negligible as shown in Figure 1.1. Therefore, it is reasonable to employ the eq. [1.8] approximation in frost-heave studies.

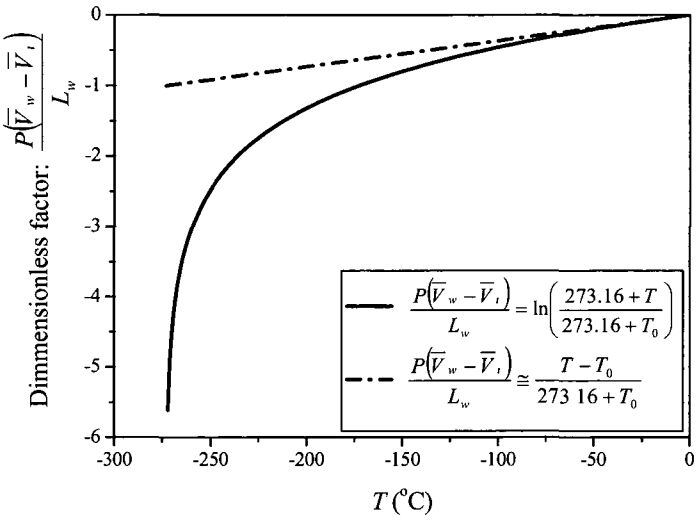

Figure 1.1 Effect of temperature on the dimensionless factor (modified from Akagawa, personal communication 2002)

Soil-water-ice system:

Edlefsen and Anderson (1943) clarified the physical meaning of the static state equation for the soil-water-ice system using the thermodynamics equilibrium. In the soil-water-ice system, the ice pressure at the onset of a growing ice lens is equal to the external force of the overburden pressure. Furthermore, the ice pressure is supported by the sum of the pore-water pressure and the effective soil pressure at the onset of a growing ice lens. Therefore, pore-water pressure is not equal to ice pressure ($P_w \neq P_i$).

The free energies of water (G_w) and ice (G_i) can be described as:

$$[1.10] \quad \begin{cases} \partial \overline{G}_w = \partial P \overline{V}_w - s_w \partial T \\ \partial \overline{G}_i = \partial P \overline{V}_i - s_i \partial T \end{cases}$$

Substituting eqs. [1.6] and [1.10] into eq. [1.4] yields the following:

$$[1.11] \quad \partial P_w \overline{V}_w - \partial P_i \overline{V}_i = L_w \frac{\partial T}{273.16+T}$$

Integrating eq. [1.11] yields the following:

$$[1.12] \quad P_w \overline{V}_w - P_i \overline{V}_i \cong L_w \frac{T-T_0}{273.16+T_0}$$

Eq. [1.12] is called the Generalized Clausius-Clapeyron Equation. The Generalized Clausius-Clapeyron Equation has been verified experimentally in both an open-water system and a closed-water system by many researchers. In an open-water system, the overburden pressure, which is equal to the ice pressure at the onset of a growing ice lens, was induced until water migration was "shut off". Investigators found that the Generalized Clausius-Clapeyron Equation was in good agreement at the overburden pressure required to stop water migration and the measured ice lens temperatures (e.g. Hoekstra 1969; Radd and Oertle 1973; Ishizaki and Kinoshita 1979).

In a closed-water system, investigators controlled ice and water pressure independently at the constant-temperature boundary condition, i.e. negative at the top and positive at the bottom. When the overburden pressure, which was equal to the ice pressure at the onset of a growing ice lens (P_i), was constant, the pore-water pressure gradually decreased as freezing progressed. After reaching the steady-state condition, pore-water pressure (P_w) attained a specific value. The Generalized Clausius-Clapeyron Equation is in good agreement at the obtained ice pressure and pore-water pressure, and the measured ice-lens temperature in the closed-water system as well as in the open-water system (e.g. Biermans et al. 1976, 1978; Takashi et al. 1981).

1.2.6 Miller Theory (secondary frost heave)

Koopmans and Miller (1966) showed that for non-colloidal soils, suction in the frozen fringe is much higher than the Capillary Theory can predict. Also, ice lenses tend to form in large masses that exclude soil particles. Based on this observation, they noted that there must be some other driving force or some other mode of water transport in freezing soil.

Miller (1978) developed the secondary frost-heave theory postulating that ice moves via a process of regelation around the soil particles during freezing. During the freezing process, pore ice is first nucleated. Once ice is nucleated, the primary ice crystals propagate into the pore space based on the Capillary Theory. The ice is considered to exist as continuous ice wedges, which extend within the frozen fringe. Miller defined this process as the "primary frost heave". The ice wedges are rigidly connected to the growing ice lens. The movement of ice through the pores is by a microscopic regelation process. The ice phase appears to move as a continuous rigid body at a velocity corresponding to the observed heave rate. This is why this model is also called the "Rigid Ice Model". Miller divided this process from the primary frost heave process and defined it as the "secondary frost heave".

The phenomena taking place in the frozen fringe, including the movement of the continuous ice wedge and the development of ice lenses, are explained in terms of the Generalized Clausius-

Clapeyron Equation and effective stress principles. Assuming that the soil is fully saturated with water, Miller (1978) divided the neutral stress, which constitutes the second factor in the Terzaghi's total stress as used in the geotechnical description of unfrozen soils, between the pore ice and pore water, using a suitable stress partition factor, as:

[1.13] $\sigma_{ov} = \sigma_e + \sigma_n = \sigma_e + \chi P_w + (1-\chi)P_i$

where σ_{ov} = overburden pressure; σ_e = effective stress; σ_n = neutral stress; and χ = stress partition factor.

The Miller Theory describes the formation of a new ice lens as a physical process as shown in Figure 1.2. There must be a temperature drop in order to enable the heaving process to begin. As the temperature drops, ice pressure and neutral stress rise. When the neutral stress reaches the overburden pressure, the effective stress becomes zero, fulfilling the condition for initiating a new ice lens. The new ice lens will form at the level where the ice pressure marginally exceeds the overburden pressure. The ice pressure declines and equals the overburden pressure at the base of the ice lens, since the ice lens sustains the overburden pressure. As the temperature continues to decrease, ice pressure increases beneath the new ice lens and the ice lens initiation cycle will repeat at a lower level.

The Miller Theory is one of the few theories that can describe discrete ice-lens formation; it has been widely applied to predict conditions such as those that exist beneath glaciers and ice sheets (e.g. Christoffersen and Tulaczyk 2003; Christoffersen et al. 2006).

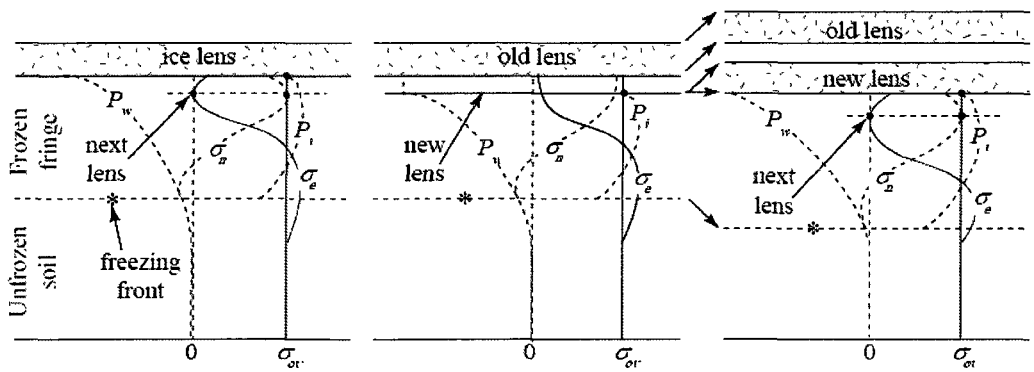

Figure 1.2 Stress profiles in a freezing soil. Left, situation before the initiation of a new lens; middle, situation just after a new lens has been established; and right, situation before initiation of another new lens (modified from Miller 1978).

1.2.7 Other approaches

The following sections present other frost-heave theories. Similarities and differences between those models are made apparent by highlighting the key physics.

Osmotic force:

Solute ions attract water molecules and reduce the natural random motion of the solvent molecules in the diffuse double layer. Mizoguchi (1993) included the effects of solutes in the formulation of Gibb's free energy, in which the pressure in the water phase is affected by an additional osmotic pressure term. The Generalized Clausius-Clapeyron Equation is presented as:

$$[1.14] \quad (P_w - \Pi)\overline{V}_w - P_i\overline{V}_i \cong L_w \frac{T - T_0}{273.16 + T_0}$$

where Π = osmotic pressure of water.

Eq. [1.14] predicts that heaving pressure decreases with increasing solute concentration. Horiguchi (1976, 1977) presented the experimental result indicating that powder materials with larger surface charges are more frost-susceptible than powders with smaller surface charges even though the surface area per unit volume is the same. Recently, Darrow et al. (2009) explained the effect of osmotic potential on frost-heave susceptibility using zeta potential.

The Miller Theory is modeled using non-colloidal soils; thus, the soil particles are connected and stress propagates through the connections in the frozen fringe. However, because the diffuse double layer exists around highly frost-susceptible soils, such as clay, the soil particles may not be in contact during the secondary frost heave. Assuming that the diffuse double layer of ions near the surface of soil particles follows the law of dilute aqueous solutions, Horiguchi (1987) presented a frost-heave theory for a normally consolidated soil, which has no solute in pore water.

Adsorption force:

Takagi (1980a, 1980b) proposed a model from the viewpoint of adsorbed water, called "Adsorption Force Theory". The Adsorption Force Theory considers that the adsorbed water has an equilibrium thickness, determined by the adsorption forces in the frozen fringe. Furthermore, the theory postulates that the adsorbed water along the freezing front generates the suction that draws adsorbed water to the frozen fringe in response to the loss of water thickness due to freezing. The role of the adsorption water layer as a driving force for frost heave was also emphasized by Beskow (1935). Beskow suggested that soil freezing is similar to soil drying. In both cases, water changes phase and the amount of liquid water in the soil decreases; thus, water flow from above the water table to the

zone where water is changing into ice is analogous to the flow of water to a zone where water is evaporating.

Although the adsorbed water is liquid, it can sustain the weight of the overburden, therefore, the anisotropic behavior of water is treated as solid-like. Vignes and Dijkena (1974) experimentally observed anisotropic water behavior in a nano-glass tube. The equilibrium thicknesses have been experimentally determined by Aguirre-Puente et al. (1973).

Kinetic force:

When the unfrozen water reaches equilibrium thickness at the onset of the growing ice lens, the chemical potential of water is equal to that of ice. As freezing propagates, the thickness of the adsorbed water will decrease. Kuroda (1985b, 1985a) proposed a model from the viewpoint of chemical potential, called "Kinetic Theory". The kinetic model assumes that the water migrating rate (v) is equal to the rate of change of the chemical potential between ice and water at the onset of the growing ice lens ($\Delta\Gamma_{i-w}$):

$$[1.15] \quad v = \frac{\Delta\Gamma_{i-w}}{R_1 + R_2}$$

where R_1 = resistance in the freezing process of the water film; and R_2 = resistance in the suction process.

Kuroda assumed that the pore-water pressure was equal to the ice pressure ($P_w = P_i$) at the onset of the growing ice lens. The chemical potential difference was determined using the Clausius-Clapeyron equation as:

$$[1.16] \quad \Delta\Gamma_{i-w} = -L_w \frac{T - T_0}{273.16 + T_0} - P_i\left(\overline{V}_i - \overline{V}_w\right)$$

However, since eq. [1.16] was not valid experimentally, Ozawa and Kinoshita (1989) modified eq. [1.16] by applying the Generalized Clausius-Clapeyron Equation ($P_w \neq P_i$) to yield:

$$[1.17] \quad \Delta\Gamma_{i-w} = -L_w \frac{T - T_0}{273.16 + T_0} - \left(P_i\overline{V}_i - P_w\overline{V}_w\right)$$

Premelting dynamics:

The Adsorption Force Theory and the Kinetic Theory postulate that water migration occurs to maintain the equilibrium thickness of the adsorbed water. Considerable recent progress has been made toward understanding the characteristics of adsorbed water by Dash and co-workers (e.g. Dash 1989;

Dash et al. 2006). They named adsorbed water "premelted water", so their approach is called "premelting dynamics".

According to premelting dynamics, the thickness of a premelted water film decreases as the temperature decreases; the thermomolecular pressure increases correspondingly. Thus, if the external pressure is held constant, the pressure in the liquid decreases and there is a tendency for premelted liquid to flow from warmer to colder regions.

An experiment to investigate premelting water by measuring such a flow was designed by Wilen and Dash (1995). In their experiment, water was sandwiched in a cylindrical layer between a lower glass slide and a flexible membrane; from the center to the outside of this apparatus a steady-state temperature gradient was imposed, as shown in Figure 1.3. The axis of the cylindrical layer was held at a temperature below the freezing temperature, causing a disk of ice to grow radially outward until its edge coincided with the freezing front. Without premelting, this would be the ultimate steady-state configuration of the system. However, the themomolecular pressure gradient in the premelted liquid film between the ice and the flexible membrane draws water radially inward, which results in a lateral deflection of the membrane. In order to maintain the equilibrium thickness of the premelted film, the additional water freezes onto the upper surface of the disk of ice as shown in Figure 1.4.

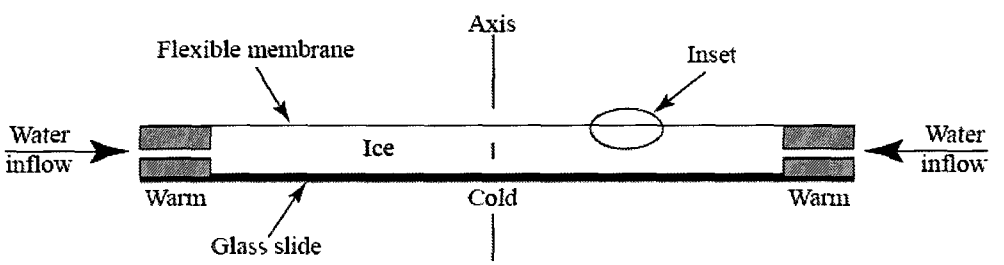

Figure 1.3 Schematic diagram of the premelted water experiment, showing an axial cross section through a cylindrical apparatus (modified from Wilen and Dash 1995).

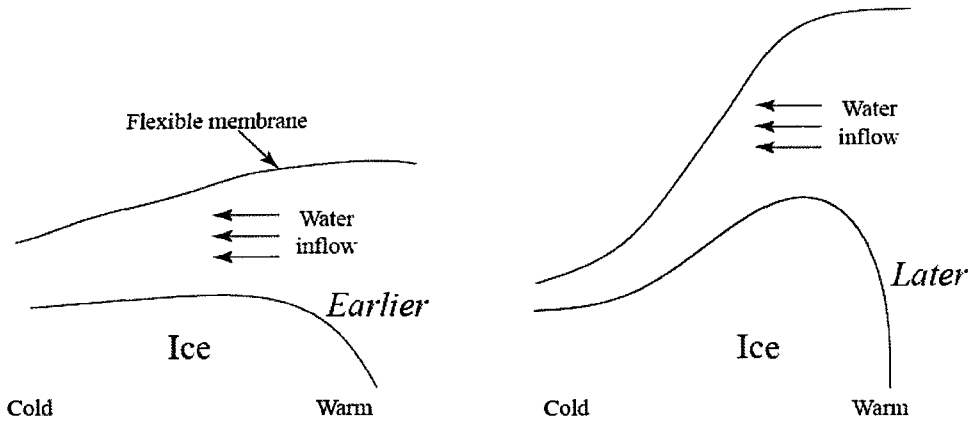

Figure 1.4 The local configuration within the inset of the apparatus shown in Figure 1.3. A disk of ice grows radially outward between a lower glass slide and an upper flexible membrane until its outer edge coincides with the freezing temperature. The pressure gradient in the premelted liquid between the ice and the membrane draws water radially inward (modified from Wettlaufer et al. 1996; vertical scale exaggerated).

Wettlaufer et al. (1996) simply modeled the process using lubrication theory to analyze the premelted water flow. More recently, Rempel et al. (2004) proposed a new microphysical explanation of frost heave based on premelting dynamics and associated intermolecular forces. This approach theoretically derived heat and moisture transfer from intermolecular forces and could explain various kinetic phenomena and discrete ice lensing formation. The details of ice-lens formation were described by Rempel (2007).

1.3 Numerical frost heave models

In the 1970s, numerous frost-heave models were developed as a result of frost-heave theories and advances in computer processing power. One of the first and simplest numerical approaches is Harlan's (1973) "hydrodynamic model". The model is governed in one-dimensional space as:

$$[1.18]\quad C\frac{\partial T}{\partial t}-L_w\rho_i\frac{\partial \theta_i}{\partial t}=\lambda\frac{\partial^2 T}{\partial x^2}-c_w\rho_w v\frac{\partial T}{\partial x}$$

where C = volumetric heat capacity of soil; L_w = specific latent heat of fusion for pure water; ρ_i = density of ice; ρ_w = density of water; θ_i = volumetric fraction of ice; λ = thermal conductivity of soil; c_w = specific heat capacity of water; and v = water intake rate.

Assuming Darcy's Law, the water transportation in the frozen fringe is derived as (Harlan 1973):

$$[1.19]\quad \frac{\partial v}{\partial x} = \frac{\partial}{\partial x}\left(\kappa_{ff} \frac{\partial\left(\frac{P_w}{\rho_w g}\right)}{\partial x} \right) = \frac{\partial \theta_w}{\partial t} + \frac{\overline{V}_w}{\overline{V}_i} \frac{\partial \theta_i}{\partial t}$$

where κ_{ff} = hydraulic conductivity of frozen fringe; and θ_w = volumetric fraction of water.

Harlan assumed that mass transportation across the frozen fringe is water flux only. The frozen fringe is taken care of by using the soil-water characteristic curve and the empirical relationship between hydraulic conductivity and pore-water pressure. The one-dimensional numerical model was implemented using the finite difference method.

The hydrodynamic model was followed by many variations. Guymon and his co-workers implemented Harlan's model using the finite element method (Guymon and Luthin 1974). Their model was expanded to two- and three-dimensional (Guymon and Hromadka 1977). Guymon et al. (1980) proposed a one-dimensional frost-heave model with the effect of a water table, and later extended it to two-dimensional (Guymon et al. 1984).

Kay et al. (1977) replaced the time derivative of the water content in order to solve the mass balance by using the standard technique of inversion of a tridiagonal matrix as:

$$[1.20]\quad \frac{\partial \theta_w}{\partial t} = \frac{\partial \theta_w}{\partial\left(\frac{P_w}{\rho_w g}\right)} \frac{\partial\left(\frac{P_w}{\rho_w g}\right)}{\partial t}$$

A simplified model was developed avoiding the convective heat transfer, which is the last term in eq. [1.18] (Taylor and Luthin 1978). They assumed that heave occurs when the ice content at any point exceeds 85% of porosity. The hydraulic conductivity was replaced by diffusivity (J). It is assumed that the water flow is driven by the gradient in water. Unfrozen water content is assumed to depend only on temperature, and the empirical relationship between diffusivity and water content is used. Their equation is:

$$[1.21]\quad v = \kappa_{ff}\frac{\partial\left(\frac{P_w}{\rho_w g}\right)}{\partial x} = \kappa_{ff}\frac{\partial\left(\frac{P_w}{\rho_w g}\right)}{\partial\theta_w}\frac{\partial\theta_w}{\partial x} = J\frac{\partial\theta_w}{\partial x}$$

Jame and Norum (1980) used the same simplified model to simulate the experimental results in a closed-water system. Their simulated results were in good agreement with the experimental results. Fukuda et al. (1980) conducted a frost-heave experiment with unsaturated soil. The water contents and temperature profiles in the freezing unsaturated soil were obtained by the gamma ray attenuation method. Fukuda (1983) simulated the frost-heave experiment using the simplified hydrodynamic model. The simulated results were in good agreement with the experimental results.

The hydrodynamic models discussed above use empirical relationships to determine frozen-fringe characteristics without the effect of overburden pressure. All of them use the Generalized Clausius-Clapeyron Equation but consider the ice pressure to be zero at any point within the frozen fringe in response to zero overburden pressure. The hydrodynamic approach will produce results in close agreement with a field problem such as the effect of freeze-thaw cycles in an active layer, which is under very small overburden pressure (Fukuda, personal communication December 2009). However, the case with the effect of overburden pressure is of greater importance to engineers. Hopke (1980), who was a researcher with an oil company, introduced the first numerical frost- heave model that includes the effect of overburden pressure. The adoption of the Generalized Clausius-Clapeyron Equation allowed the frozen fringe to be described with respect to temperature, pore-water pressure, and ice pressure. Comparing the laboratory frost-heave tests by Penner and Ueda (1977) with model results, the developed model over-predicts the heave at low overburden pressure and at a high temperature gradient. This may be because the hydraulic conductivity of frozen fringe was arbitrarily determined.

For the sake of engineering purposes, the hydrodynamic approach was modified by Hopke (1980) to yield useful simulations of temperature profile and water migration amount, but not to simulate discrete ice-lens formation. Gilpin (1980a) introduced the first numerical frost-heave model to simulate discrete ice-lens formation. Gilpin proposed a model that simplified the Miller Theory. Gilpin's model simulates mass transport quantified as equivalent to moisture transport even if mass transport does occur in frozen fringe by ice regelation, based on his earlier research on regelation (Gilpin 1979, 1980b). Gilpin also assumes that fringe ice bears stress, and an ice lens will initiate when the soil stress in the frozen fringe equals the sum of the overburden pressure and the separation pressure between soil grains. Comparing the simulated results with the experimental results of Penner

and Ueda (1977), the difference of heave amount was within one order of magnitude and the simulated ice lens resembled the observation However, Gilpin assumed the hydraulic conductivity values of the frozen fringe to be a function of temperature alone

Horiguchi and Miller (1980, 1981, 1983) conducted hydraulic conductivity experiments by placing impermeable ice layers at both ends of a sample They experimentally observed that not all the flow takes place either through the polycrystalline ice or at the edges They, therefore, concluded that the only possible flow mechanism is ice melting at the outflow side and supercooled water freezing at the inflow side, i e regelation From the magnitude of regelation, they obtained the apparent hydraulic conductivity in the temperature range between -0 3°C and 0°C O'Neill and Miller (1985) completed a numerical Rigid Ice Model using the apparent hydraulic conductivity and eq [1 13] for stress analysis Since the developed numerical Rigid Ice Model is very complex and input parameters are difficult to determine, simplified versions have been undertaken (e g Black and Miller 1985, Fowler and Krantz 1994, Black 1995, Peterson and Krantz 2003)

1.4 Empirical concepts

The hydraulic conductivity of the frozen fringe should be determined in order to solve the numerical frost-heave models discussed above Williams and his co-workers (Williams and Burt 1974, Burt and Williams 1976) measured the hydraulic conductivities over a range of temperatures within the frozen fringe Because of technical difficulty, a precise measurement of the hydraulic conductivity was not possible In addition, the measured hydraulic conductivity did not consider the stress dependency Furthermore, most numerical frost-heave models rely on the assumption that the Generalized Clausius-Clapeyron Equation, which relates ice and water pressure to temperature, holds anywhere in the frozen fringe regardless of the water flow and the dynamics of phase change in the frozen fringe It is noted that the Generalized Clausius-Clapeyron Equation is only valid in static phase (e g Miyata 1998) The Rigid Ice Model and premelting dynamics model are only two existing models, which theoretically explain the discrete ice-lens formations Although these two are essentially identical, there is still rigorous discussion regarding their reliance on the physics underlying the ice-lens formation criteria (Christoffersen et al 2007, Rempel et al 2007, Rempel 2008) Furthermore, there are still considerable unknowns regarding frozen-fringe characteristics For instance, no wired-regelation network was observed within the frozen fringe in frost-heave experiments using 9 7μm diameter micro-glass particles (Watanabe and Mizoguchi 2000) The observation is inconsistent with the Miller Theory

To overcome those unknowns, empirical concepts were developed in correct with laboratory frost-heave tests. Konrad and Morgenstern (1980, 1981) introduced the segregation potential (SP) concept, which provides a means to determine the frost-heave susceptibility of soils. They began with the theoretical assumptions that (a) the Generalized Clausius-Clapeyron Equation is valid at the base of an ice lens; (b) the frozen fringe is characterized by an overall hydraulic conductivity; (c) the temperature varies linearly in the frozen fringe; and (d) the external overburden pressure and the ice pressure in the frozen fringe are zero. From analyses based on these assumptions, they concluded that during the freezing of soil columns under the same warm-side temperatures but different cold-side temperatures, water flow rate (v) is proportional to the temperature gradient in the frozen fringe ($gradT_{ff}$) at the formation of the final ice lens. Accordingly:

$$[1.22] \quad \mathrm{SP} = \frac{v}{gradT_{ff}}$$

where SP = segregation potential.

They provided the variation of SP with the effect of cooling rate (Konrad and Morgenstern 1982b) and applied overburden pressure (Konrad and Morgenstern 1982a). Those modifications made it possible to predict water intake rate for a more general case of transient freezing with external overburden pressure.

One important aspect of frost heave is water transport beyond the warmest ice lens. Hoekstra and Chamberlain (1964) provided sufficient evidence that moisture moves through frozen soil by applying an electric gradient of 1V/cm to samples of frozen silt and clay. However, the moisture transport beyond the warmest ice-lens was negligible in frost-heave experiments (Mageau and Morgenstern 1980). Therefore, the SP concept assumes that frost heave is a problem of moisture transfer to a growing ice lens past the layered frozen fringe and the unfrozen soil. The SP concept clearly divides these two components, namely *in-situ* heave and segregation heave. The *in-situ* heave (h_{in}) accounts for primary frost heave. Konrad (1994) observed that *in-situ* freezing occurs in the frozen fringe without changing porosity; a given quantity of pore water is removed as ice forms and becomes the lens where it freezes. *In-situ* heave is calculated as the volume expansion of the "*in-situ*" water upon freezing. The segregation heave (h_{sp}) accounts for secondary frost heave. It is calculated as the summation of the water flow over the total time period. The total heave (h_t) is written as:

$$[1.23] \quad \Delta h_t = \Delta h_{in} + \Delta h_{sp} \approx 0.09\delta n \Delta X_0 + 1.09 v \Delta t$$

where δ = volumetric fraction taking into account the portion of unfrozen water in frozen soil; n = porosity of the soil; and ΔX_0 = thickness of the soil layer frozen in time interval (Δt).

The validity of the SP concept was interpreted using Gilpin's approach (Gilpin 1982; Nixon 1991). Their interpretation showed that the SP was a good alternative to detailed measurements of the more fundamental properties, i.e. hydraulic conductivity of the frozen fringe. The SP concept has been used over the last 20 years in engineering design, i.e. in designing road embankments (e.g. Konrad 1994). The SP concept has also predicted frost heave in full-scale pipeline experiments very well (e.g. Carlson and Butterwick 1983; Konrad and Morgenstern 1984; Konrad 1994; Konrad and Shen 1996; Kim et al. 2008). Because the SP concept allows design engineers an easy empirical measurement of the required input parameters, it has been an accepted test method in the U.S. and Canada. The SP numerical simulation has also shown a good agreement with observations during underground tunnel construction in Japan (Konrad 2002). Details of the SP concept will be presented, where appropriate, in subsequent chapters.

Takashi et al. (1974) presented the first empirical concept that relates frost-heave ratio (ξ) to the overburden pressure (σ_{ov}) and freezing penetration rate (U) from more than 140 frost-heave test results. Accordingly, the frost-heave ratio is as follows:

$$[1.24] \quad \xi = \xi_0 + \frac{\sigma_0}{\sigma_{ov}}\left(1+\sqrt{\frac{U_0}{U}}\right)$$

with

$$[1.25] \quad \xi = \frac{h_0 + h_t}{h_0}$$

where ξ_0, σ_0, and U_0 = soil constants; h_0 = initial height of the soil sample; and h_t = total heave.

The water intake rate (v) was determined using eq. [1.24] as:

$$[1.26] \quad v = \frac{U}{1.09}\frac{\sigma_0}{\sigma_{ov}}\left(1+\sqrt{\frac{U_0}{U}}\right) - \frac{0.09}{1.09}\delta n U$$

where δ = volumetric fraction taking into account the portion of unfrozen water in frozen soil; and n = porosity of the soil.

The ξ_0, σ_0, and U_0 are determined by a series of frost heave tests, which change overburden pressure and freezing-front penetration rate. Takashi's concept has been applied to over 400 thousand-cubic-meter engineering projects during the last 40 years in Japan, such as installing underground liquid natural gas (LNG) tanks, predicting ground freezing, and so on. Takashi's concept is currently used as the Japanese geotechnical standard test method to predict frost-heave susceptibility (Japan Geotechnical Society 2003). However, Ishizaki and co-workers (Ishizaki and Nishio 1988; Ishizaki

1993) reported that the water intake rate shows more dependency upon temperature gradients than freezing-front penetration rates.

1.5 Full-scale pipeline experiments

There have been several full-scale warm and chilled pipeline experiments conducted in the U.S. and Canada since early 1970.

Mackenzie Valley Pipeline Research Limited installed a test section of pipeline near Inuvik, Northwest Territories, Canada (N.W.T) to study the behavior of ice-rich permafrost surrounding a warm pipeline. The test section was comprised of a 27m long, 0.61m diameter pipe, through which 71°C air was circulated. The field experiment commenced on July 22, 1971. The instrumentation used at the site has been described by Slusarchuk et al. (1973) and the data collected during operation of the test facility were presented by Watson et al. (1973).

In early 1970s, Mackenzie Valley gas pipeline project proposals were recommended for approval within the coming 10 years in Canada (Williams 1986). Canadian oil and gas companies conducted field pipeline experiments as part of the project. The Gas Arctic Systems Study Group managed the program, which had four test facilities at Prudhoe Bay, Alaska; Norman Wells, N.W.T; Nordegg, Alberta; and Vanier Island, N.W.T (Gas Arctic Systems Study Group 1971). Separately, the Northwest Project Study Group conducted a field pipeline experiment at San Sault, N.W.T. (Northwest Project Study Group 1972). However, very little of the information from these experiments became public.

In the late 1970s, the Canadian Arctic Gas Study Group built and operated a full-scale chilled pipeline test facility on the University of Alberta campus in Calgary. The experiment is known as the Calgary frost-heave experiment, and has been widely reported in papers (e.g. Slusarchuk et al. 1978; Carlson and Ellwood 1982; Carlson and Nixon 1988), and reports (Northern Engineering Services Company Ltd 1975; LEC Engineering Ltd 1984). Six separate sections were constructed to measure frost heave for various candidate pipeline burial configurations. Steel pipes 12.2m long and 1.22m in diameter with 10mm wall thickness were buried in each section. The ground condition of each section was uniform over the short length of the pipe. Konrad and Morgenstern (1984) determined that there was no initial permafrost and the initial ground temperature was +6.5°C. Zero heat flux was assumed at a depth of 15.6m below the original center position of the buried pipes. The pipe temperature

fluctuated between -10 and -7°C due to seasonal ambient temperature variation. The groundwater table was observed to vary between 2.3m and 2.6m below the original ground surface. No observations were made of stresses that developed in pipe steel due to differential frost heave because at the Calgary frost-heave experiment the ground was uniformly susceptible to frost heave with a constant water table.

Since successful completion of the TAPS suggested that arctic pipeline construction was well within the abilities of modern technology in the late 1970s, the interest in gas development increased and the Alaska Highway Pipeline Project was proposed by Foothill Pipe Lines Ltd and the Northwest Alaska Pipeline Co. They constructed an experimental facility in Fairbanks as a portion of the Alaska Highway Pipeline Project in 1979. The data obtained from this facility are not available in the public domain, but very cursory data were reported (e.g. Foothill Pipe Lines Ltd 1981; Nixon 2003). Ten sections were constructed to look at the effects of mitigation techniques for controlling frost heave by soil replacement, pipe insulation, burial depth, chilled pipe temperature, and selected bedding material. In most of the test sections, the top of pipeline was buried to a depth of 0.76m. Steel pipe sections were 36m long and 1.2m in diameter, except for test section 9. Test section 9 was designed to investigate the bending of the pipe due to differential heave between permafrost and unfrozen soils with a 120m long and 1.2m diameter steel pipe. Approximately 39m was buried in permafrost, and the remaining 81m in unfrozen ground. During the next two or three years, seven more field experimental sites were established along the proposed pipeline route. Six chilled pipeline experiments were built in Alaska, from Wiseman, just south of the Brooks Range, to Sweetwater, just north of the Canadian border. Only a small amount of data was reported by Nixon (2003). The seventh field experiment program established a warm pipeline in permafrost. Carlson and Butterwick (1983) reported very little information regarding the Quill Creek experimental site. Foothills Pipe Lines Ltd constructed their facility in the Yukon Territory of Canada, approximately 165km southeast of the Alaska border. They observed that mitigattion designs such as insulation and embankments effectively minimized thaw settlement of the pipe.

France and Canada conducted modeling experiments in Caen, France in the 1980s and 1990s. Since the full-scale pipeline experiments which were described above were managed by private industries, very few data have been presented regarding those projects. In contract, a fourteen-volume set of books and a database regarding the Caen frost-heave experiment are available to the public for a fee (White 2006). A brief description of the experiment is presented below.

The Caen experimental facility consisted of a temperature-controlled hall, which was 18m long, 8m wide, and 5m high The test facility consisted of a container, which could be filled to a depth of 2m The base of the container isolated the thermal and hydraulic regime within it from the natural ground conditions The test container was filled with soil to a depth of 1 75m The objective of the experiment was to observe pipe bending due to a sharp contrast in soils with different frost susceptibilities To achieve this goal, two separate soils were used The Caen silt was used to model the soil with higher frost-heave susceptibility To model the soil with lower frost susceptibility, sand was used The Caen silt and the sand each occupied one-half of the container The pipeline consisted of a steel pipe 18m long and 0 273m diameter with a 5mm wall thickness The instrumented pipeline was buried in a trench at a depth of 0 33m to the top of the pipeline The entire 18m length of the pipeline was backfilled with the described soils In order to model a relatively long-distance pipeline, both ends of the pipe were kept free of any constraints

The Caen frost-heave experiment consisted of two major stages The objective of the first series of experiments was to examine the behavior of a chilled pipeline located at the intersection between two initially unfrozen soils with widely different frost-heave susceptibilities The second series of tests was designed to investigate the behavior of a chilled pipeline, which was located at the transition zone between pre-frozen and unfrozen frost-susceptible soil

In the first series of experiments, the initially unfrozen soils were subjected to four periods of freezing between 1982 and 1989 Four freeze/thaw cycles were imposed Pipe temperature ranged from -2 to -5°C Air temperature was -0 75°C during freezing and 4°C during thawing The groundwater table was maintained at a constant 0 3m below the base of the pipe

The second stage of the experiment was carried out in the same facility between 1990 and 1993 In this experiment, a pipeline was embedded at a transition region between pre-frozen and unfrozen soil The objective of the experiment was to examine the forces that would be generated on a pipeline, which was anchored by the pre-frozen soil In order to allow comparison between this and the previous experiments, the silt composition, pipe size, and burial depth were kept the same Two stress-relaxation cycles were imposed The groundwater table was maintained at a constant 1 0m and 1 2m below the base of the pipe, in the first and the second cycle, respectively

Prior to the start of the first stress-relaxation cycle as indicated by the commencement of pipeline cooling, the section with sand was pre-frozen for approximately 230 days After the pre-freezing period, the operation started on June 26, 1991 (day 0) The ambient air temperature in the facility was maintained at -0 75°C and the cooling temperature in the pipeline was maintained at -5°C This temperature specification was maintained from day 0 to day 214 From day 215 to day 256, the temperature in the pipe was lowered to approximately -8 5°C A relaxation phase followed from day

257 to day 269. During this period, the pipe temperature was raised to 5°C, while the ambient air temperature in the facility was maintained at -0.75°C. This change generated thawing of soil local to the pipe. Resulting soil weakening allowed the pipe to straighten, thus reducing its internal stress.

Prior to the start of the second stress-relaxation cycle, a transitional phase followed from day 270 to day 370 to re-establish the pre-frozen sand and unfrozen silt sections. During this period, the ambient air temperature was held at -5°C and 5°C in the sand section and the silt section, respectively. The second stress-relaxation cycle was initiated on July 1, 1992 (day 371). From day 371 to day 769, the pipe temperature was held at -6°C while the ambient air temperature was maintained at -4°C. A relaxation phase was inserted from day 659 to day 672. During this phase, the pipe temperature was raised to 5°C, while the ambient air temperature in the facility was maintained at -4°C.

The Caen frost-heave experiment was a controlled-environment experiment with high-quality scientific instruments. Such a controlled-environment experiment was designed to remove the complicating aspects of natural climate and soils vagaries from the experiments so the essential factors in the phenomenon being investigated could be clearly distinguished. However, a real large diameter pipe was not used for this experiment.

The University of Alaska Fairbanks (UAF) and Hokkaido University, Japan, conducted a full-scale field experiment to determine differential pipe heave near the frozen-unfrozen boundary from December 1999 to August 2003. The experimental site was the same site as that used by the Fairbanks frost-heave experiment. However, the UAF-Hokkaido University frost-heave experiment was conducted with a different pipeline, and the series of experiment that differed from the Fairbanks frost-heave experiment. A 0.914m diameter, 105m long chilled pipeline with X65 grade and 9mm wall thickness was used. The first 30m of the pipeline was in a shallower supra-permafrost-table area and the remaining 75m was in unfrozen ground in a deeper supra-permafrost-table area. The pipe was covered with approximately 0.9m of *in-situ* crushed soil. The UAF-Hokkaido University frost-heave experiment was the first full-scale experiment regarding pipe bending due to differential frost heave released to the public. Furthermore, it was conducted under natural conditions including such effects as air temperature and water table fluctuations. The details are described by Bray (2003) and Huang et al. (2004).

1.6 Research objectives and structure of dissertation

Most frost-heave theories and numerical models consider heave as a one-dimensional process both experimentally and numerically. However, many field problems are multi-dimensional, i.e. ground freezing, movement of a buried chilled gas pipeline, and so on. From an engineering viewpoint,

the prediction of multi-dimensional stress and deformation analysis during frost heave has to be coupled with hydrodynamic models.

Blanchard and Fremond (1985) were the first to propose a model for coupling the heat, moisture, and stress fields, but showed no results about the stress field.

Shen and Ladanyi (1991) developed a two-dimensional hydrodynamic model coupled with stress analysis. Selvadurai and co-workers (Selvadurai and Shinde 1993; Selvadurai et al. 1999a, 1999b) proposed three-dimensional models. Shar and Razapqur (1993) extended the Miller's Rigid Ice Model approach to two-dimensional. All of the above models showed good agreement with the Caen frost-heave experiment. However, these approaches require that the hydraulic conductivity of the frozen fringe be determined.

Michalowski and co-workers (Michalowski 1993; Michalowski and Zhu 2006) developed a multi-dimensional frost heave model that depends upon temperature gradient, cooling rate, and overburden pressure, and was very close to the SP concept. Their model was calibrated using one-dimensional frost-heave tests, and then two-dimensional simulations were conducted. They used a linear elastic constitutive law, though the results were not verified against field data.

Konrad and Shen (1996) successfully coupled a stress-strain-thermal finite element formulation using the SP concept in two dimensions. The developed two-dimensional SP frost-heave model successfully simulated the Calgary frost-heave experiment and suggested that a linear elastic constitutive law for frozen soil is unsuitable in a two-dimensional frost-heave simulation. At the present time, a three-dimensional SP frost-heave model has not been presented yet.

The objectives of this dissertation are as follows:

1) Improvement of frost-heave tests that can obtain consistent and reproducible values of segregation potential.
2) Mechanical analysis considering rate-dependent material properties.
3) Development of two- and three-dimensional consecutive frost-heave models by applying the SP concept.
4) Verification of the developed multi-dimensional frost heave models using full-scale frost-heave experiments.

The laboratory frost-heave test results are presented in Chapter 2. The explanation of the SP concept is also given in the same chapter, while analysis of the laboratory frost-heave tests based on the concept is discussed in Chapter 3. Chapter 4 explains the numerical implementation and solution procedures using the laboratory frost-heave test results. The numerical results of two-dimensional and three-dimensional examples that consider rate-dependent material properties are discussed in Chapter

5 and Chapter 6, respectively. Finally, the conclusion and recommendations for future work are given in Chapter 7.

CHAPTER 2: LABORATORY FROST HEAVE TESTS

2.1 Introduction

As stated in the previous chapter, the segregation potential (SP) concept has been widely accepted and used in many engineering designs (e.g. highway and buried chilled gas pipeline). Konrad (1987b) proposed a procedure to evaluate the SP value using frost heave tests. Ito et al. (1998) improved the test procedure to obtain more consistent and reproducible SP values by applying a more sophisticated frost-heave test.

The purpose of this chapter is to measure the SP value of Fairbanks silt from the University of Alaska Fairbanks (UAF)-Hokkaido University experimental gas pipeline site by frost-heave tests. Two different types of freezing mode were applied. The scope of the work includes:

1) A description of the test methods and test programs.
2) An interpretation of results to determine the SP values.

In the following sections, the SP concept is described in detail first. The two-types of frost-heave test equipment are described next. A description of the undisturbed soil sample and frost-heave tests follows. Finally, the results of the frost-heave tests and determination of the SP value are presented.

2.2 Segregation potential concept

2.2.1 Laboratory frost-heave tests

Laboratory frost-heave tests are necessary if the SP concept is to be used to determine the frost-heave susceptibility of a soil. Generally, there are three types of freezing tests: step-freezing test, ramp-freezing test, and the Japanese Geotechnical Standard Test (JGST)-freezing test.

In step-freezing, the cold and warm temperature boundary conditions are maintained at a constant level during the test. Figure 2.1a shows schematic ice-lens distribution in the step-freezing test. In the early stages of freezing, there is no visible ice lens; rather, water expulsion due to the rapid change of temperature across the sample is visible. "Freezing front" is defined as the location of the freezing temperature isotherm. The freezing temperature of soils is defined as $0^{\circ}C$ throughout this dissertation. As the freezing front penetration slows down, very thin and diffusive visible ice lenses appear.

The vertical spacing between ice lenses increases with a decreasing cooling rate of the frozen fringe during transient freezing. When the freezing front becomes stationary, the final ice lens starts to form.

Ramped-freezing (Figure 2.1b) consists of a linear reduction of the top and bottom temperature boundary conditions with time. The ramping boundary conditions can control the constant freezing-front penetration rate and temperature gradient.

The JGST-freezing test (Figure 2.1c) is the standard test method used to predict frost-heave susceptibility in Japan (Japan Geotechnical Society 2003). The cold-temperature boundary uniformly ramps down while the warm-temperature boundary is maintained at a constant temperature close to 0°C. JGST-freezing is controlled to produce a constant freezing-front penetration rate. However, the freezing front does not penetrate steadily due to the unsteady heat-transfer condition. The final ice lens could form if the warm-temperature boundary is slightly higher than 0°C.

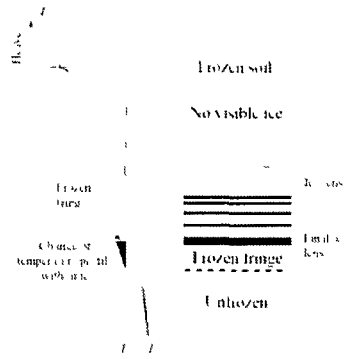

(a) Step-freezing (modified from Konrad and Morgenstern 1980)

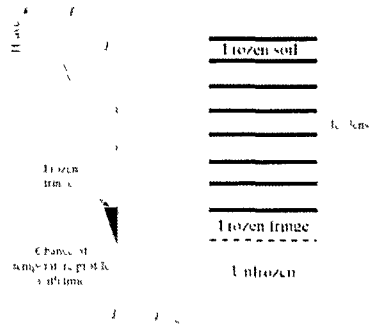

(b) Ramped-freezing (modified from Konrad 1994)

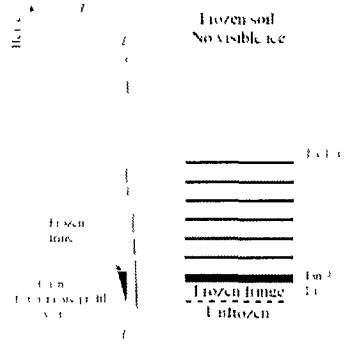

(c) JGST-freezing (modified from Japan Geotechnical Society 2003)

Figure 2.1 Schematic temperature distribution and ice lens formation in different freezing tests.

2.2.2 Theoretical background

Adsorbed unfrozen water exists around soil particles below the freezing temperature (T_0). Water migration occurs through the unfrozen water films. The ice lens grows at slightly colder than freezing temperature, which is called the segregation freezing temperature (T_s). The partially-frozen zone between T_0 and T_s is termed the "frozen fringe" (Miller 1972).

Frost heave can be described as moisture transfer to a growing ice lens past the layered frozen fringe and the unfrozen soil. This moisture-transfer process is termed the hydrodynamic model by several researchers (e.g. Harlan 1973). The hydraulic conductivity of the frozen fringe should be determined in order to solve the layered-moisture transfer problem. Williams and Burt (1974) measured the hydraulic conductivity over a range of temperatures simulating the frozen-fringe temperature. Because of technical difficulty, a precise measurement of the hydraulic conductivity was not possible. Successful verification of one-dimensional hydrodynamic models against laboratory frost heave test results has been reported (e.g. Selvadurai et al. 1999a). However, the hydraulic conductivity of the frozen fringe used in the simulations was not directly measured. Furthermore, a trail-and-error approach was used to adjust the hydraulic conductivities in order to obtain a match between laboratory test and model results. The hydrodynamic model relies on the assumption that the Generalized Clausius-Clapeyron Equation, which relates ice and water pressure to temperature, holds true anywhere in the frozen fringe. However, it has been noted by Miyata (1998) that the dynamics of phase change and water flow in the frozen fringe make it impossible for the Generalized Clausius-Clapeyron Equation to remain valid anywhere but at the ice lens where water flow is halted. Therefore, it appears that precise measurements of hydraulic conductivity, temperature distribution, and suction within the frozen fringe cannot produce exact results in a predictive frost-heave model. To overcome the difficulty, Konrad and Morgenstern (1980, 1981) developed the SP concept. The SP concept explains theoretical considerations as follows.

It has long been known that frost heave is caused not only by freezing of the *in-situ* pore water but also by water flow to the frozen fringe. The SP concept clearly divides these two components into *in-situ* heave and segregation heave, respectively. To determine the frost-heave susceptibility, Konrad and Morgenstern (1980) conducted step-freezing tests without overburden pressure. When the final ice lens initiates, the cooling rate of the frozen fringe will decrease to a value near zero. It is assumed that the static-phase equilibrium is reached at the onset of the final ice lens. The SP concept is empirically demonstrated from the results that the water-intake rate is related to the magnitude of the temperature gradient in the frozen fringe at the formation of the final ice lens in constant thermal boundary and no-overburden pressure conditions, as shown in Figure 2.2.

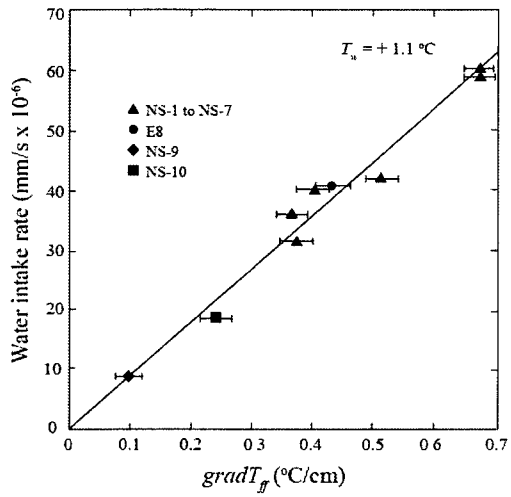

Figure 2.2 Relationship between water intake rate and temperature gradient in frozen fringe at the end of transient freezing (modified from Konrad and Morgenstern 1980).

Assuming that the variation of thermal conductivity within the frozen fringe is very little and very close to that of the unfrozen soil, the actual temperature profile could be fairly linear. Although the details of how hydraulic conductivity varies below the freezing point are still unknown, the hydraulic conductivity decreases in response to and at the same time as the temperature lowers and the unfrozen water content of the frozen soil decreases. The actual hydraulic conductivity profile, therefore, adopts a nonlinear trend. Also, the actual suction profile becomes qualitatively nonlinear in response to the actual nonlinear hydraulic conductivity as shown in Figure 2.3a.

The two fundamental assumptions made in the SP concept are that hydraulic conductivity of the frozen fringe (κ_{ff}) has an equivalent constant at the formation of the final ice lens and that κ_{ff} and T_s are intrinsic parameters of the soil. According to Darcy's Law, the suction profile adopts a linear trend corresponding to the equivalent constant hydraulic conductivity as shown in Figure 2.3b.

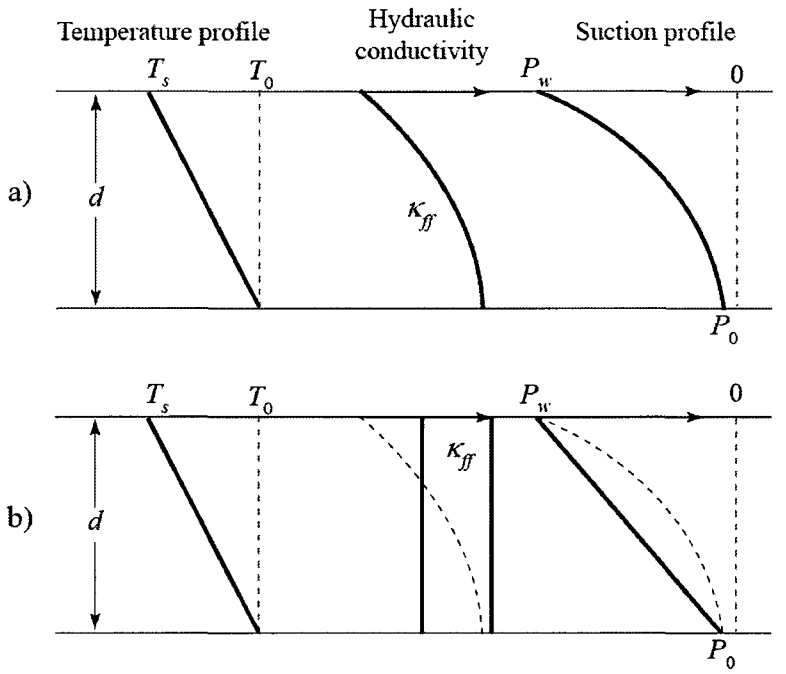

Figure 2.3 Characteristics of frozen fringe: a) actual; b) simplified shape (modified from Konrad and Morgenstern 1980).

These assumptions are evaluated against step-freezing tests with different sample heights under different thermal boundary conditions at the formation of the final ice lens as shown in Figure 2.4. The thermodynamic equilibrium between ice and water at the onset of the ice lens is ruled by the Generalized Clausius-Clapeyron Equation (e.g. Radd and Oertle 1973; Biermans et al. 1976) as:

$$[2.1] \qquad P_w = \frac{L_w}{\overline{V}_w}\frac{T_s - T_0}{273.16 + T_0} + \frac{\overline{V}_i}{\overline{V}_w}P_i$$

where P_w = pore-water pressure; P_i = ice pressure; $\overline{V}_w$ = specific volume of water; $\overline{V}_i$ = specific volume of ice; and L_w = specific latent heat of fusion for pure water.

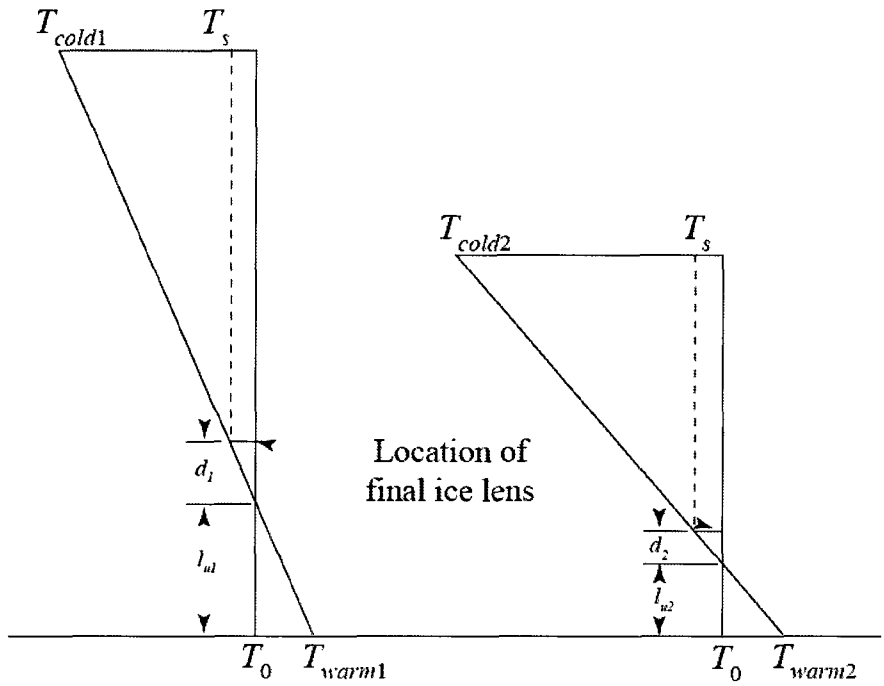

Figure 2.4 Conditions at the formation of the final ice lens for two different samples in step-freezing tests (modified from Konrad and Morgenstern 1980).

It is emphasized that eq. [2.1] is valid for phase equilibrium and for solute-free water at the onset of the ice lens where the water flow ceases. When no external pressure is applied and the weight of the soil above the ice lens is neglected, eq. [2.1] reduces to:

$$[2.2] \qquad P_w = \frac{L_w}{\overline{V}_w} \frac{T_s - T_0}{273.16 + T_0}$$

Atmospheric pressure is at the bottom of the soil sample. The total potential (H) at the onset of the final ice lens is defined as:

$$[2.3] \qquad H = \frac{P_w}{\rho_w g}$$

where ρ_w = density of liquid water; and g = gravitational acceleration.

Since T_s is assumed as intrinsic, T_s - T_0 is the same in the different sample heights as shown in Figure 2.4. Therefore, the suction potential developed at the onset of the final ice lens is the same:

[2.4] $$H_1 = H_2$$

Geometrical considerations provide the following relationships:

[2.5] $$\frac{d_1}{l_{u1}} = \frac{d_2}{l_{u2}} = \frac{T_s - T_0}{T_0 - T_{warm1}} = \frac{T_s - T_0}{T_0 - T_{warm2}} (= const)$$

where d = the thickness of the frozen fringe; l_u = the length of unfrozen soil; T_{warm} = the warm-end temperature; and T_{cold} = the cold-end temperature. Subscripts 1 and 2 denote the case numbers of the test.

Applying Darcy's Law, the water intake rates for the two samples can be calculated as below:

[2.6] $$v_1 = K_1 \frac{|0 - H_1|}{d_1 + l_{u1}} = \frac{d_1 + l_{u1}}{\frac{l_{u1}}{\kappa_{ff1}} + \frac{d_1}{\kappa_u}} \times \frac{H_1}{d_1 + l_{u1}} = \frac{H_1}{\frac{l_{u1}}{\kappa_{ff1}} + \frac{d_1}{\kappa_u}}$$

[2.7] $$v_2 = K_2 \frac{|0 - H_2|}{d_2 + l_{u2}} = \frac{d_2 + l_{u2}}{\frac{l_{u2}}{\kappa_{ff2}} + \frac{d_2}{\kappa_u}} \times \frac{H_2}{d_2 + l_{u2}} = \frac{H_2}{\frac{l_{u2}}{\kappa_{ff2}} + \frac{d_2}{\kappa_u}}$$

where v = water intake rate; and κ = the hydraulic conductivity. Subscripts ff and u denote frozen fringe and unfrozen soil, respectively.

From eqs. [2.3] through [2.7], the ratio between v_1 and v_2 is shown as:

[2.8] $$\frac{v_1}{v_2} = \frac{l_{u2}\kappa_{ff2} + \kappa_u d_2}{l_{u1}\kappa_{ff1} + \kappa_u d_1} = \frac{d_2}{d_1} \times \frac{\frac{l_{u1}}{d_1}\kappa_{ff2} + \kappa_u}{\frac{l_{u1}}{d_1}\kappa_{ff1} + \kappa_u}$$

Since the hydraulic conductivity of the frozen fringe is constant, eq. [2.8] becomes:

[2.9] $$\frac{v_1}{v_2} = \frac{d_2}{d_1} = \frac{\frac{T_0 - T_s}{d_1}}{\frac{T_0 - T_s}{d_2}} (= const)$$

Therefore, eq. [2.9] indicates that the water intake rate inversely depends on the thickness of frozen fringe, and especially the temperature gradient of the frozen fringe, because T_s is assumed as intrinsic.

The following relationships could be satisfied based on the above considerations, as shown in Figure 2.5:

$$[2.10] \quad v = \kappa_{ff} \frac{\left(\frac{P_w}{\rho_w g} - \frac{P_0}{\rho_w g}\right)}{d} = \left(\kappa_{ff} \frac{\left(\frac{P_w}{\rho_w g} - \frac{P_0}{\rho_w g}\right)}{T_s - T_0} \right) \times \frac{T_s - T_0}{d} = \mathrm{SP} \times gradT_{ff}$$

where P_0 = suction pressure at the freezing front; SP = segregation potential; and $gradT_{ff}$ = temperature gradient of the frozen fringe.

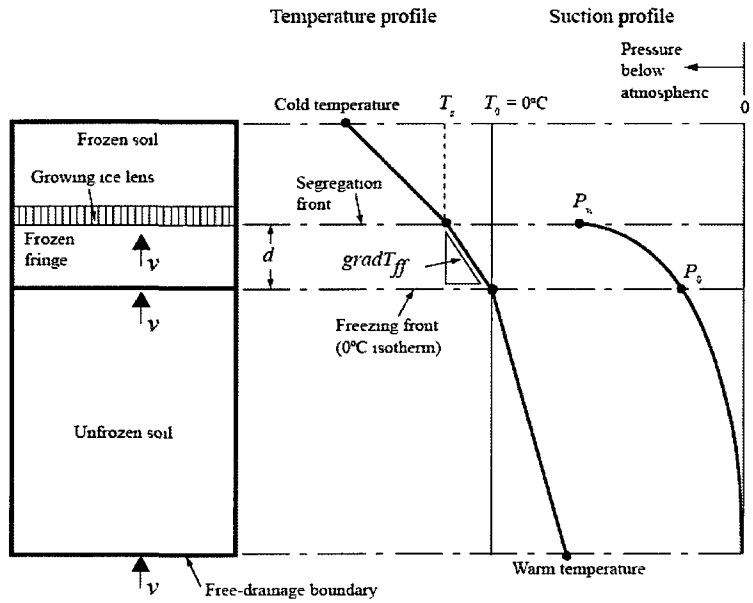

Figure 2.5 Schematic of conditions in a freezing soil (modified from Konrad 1999).

The applicability of $gradT_{ff}$ has been questioned because $gradT_{ff}$ produced in laboratory frost-heave tests had been much greater than that found in field conditions. Konrad and Nixon (1994) conducted the frost-heave experiment using a 68.5cm-long soil sample. The experimental results obtained from the long soil sample proved that the SP concept was valid for $gradT_{ff}$ as small as 4°C/m.

2.2.3 Functions of the SP

There are many factors affecting frost heave of soil. Likewise, the SP will depend upon the following factors:

[2.11] $\mathrm{SP} = \mathrm{SP}(\text{soil type, porosity, pore fluid, } P_0, \text{ cooling rate}, \sigma_{ov}, \mathrm{OCR}, N, \ldots)$

where σ_{ov} = overburden pressure at the segregation freezing front; OCR = overconsolidation ratio; and N = the number of freeze-thaw cycles.

The first three factors in the list relate basically to properties of the porous medium. Soil type includes all of the physical properties, such as gradation, mineralogy of the fines fraction, specific surface area, and surface charge density. The porosity reflects the degree of soil density. The pore fluid reflects the concentration of solute.

As shown in eq. [2.10], the water-intake rate decreases with decreasing suction pressure at the freezing front, and the SP decreases as well. Seto and Konrad (1994) directly measured the suction pressure at the freezing front during step-freezing frost-heave tests with applied back-pressure, and verified the effect against SP.

A relationship between cooling rate (or frost-penetration rate) and heave rate has been studied. Conclusions from these studies showed contradictions, however. Beskow (1935) concluded that, at a constant load on the soil, the heave rate is independent of the cooling rate. Loch (1979) showed that the heave rate did depend on the cooling rate for Norwegian silty soil. There existed a peak heave rate obtained at a certain value or range of cooling rate. Konrad and Morgenstern (1982b) defined the cooling rate as the change in average temperature of the frozen fringe per unit time. The SP for Devin silt showed a dependency on the cooling rate in step-freezing tests. The data indicated that the SP for Devin silt increased with decreasing cooling rate to some maximum value, and then began to decrease as shown in Figure 2.6.

It has been well documented that applied external load inhibits frost-heave susceptibility since Beskow's (1935) initial work. Konrad and Morgenstern (1982a) confirmed that T_s decreased with increasing overburden pressure in step-freezing frost-heave tests at the formation of the final ice lens. It is reasonable to define P_i equal to σ_{ov} for laboratory frost-heave tests. Eq. [2.1] is changed as shown below:

[2.12] $$P_w = \frac{L_w}{\overline{V}_w}\frac{T_s - T_0}{273.16 + T_0} + \frac{\overline{V}_i}{\overline{V}_w}\sigma_{ov}$$

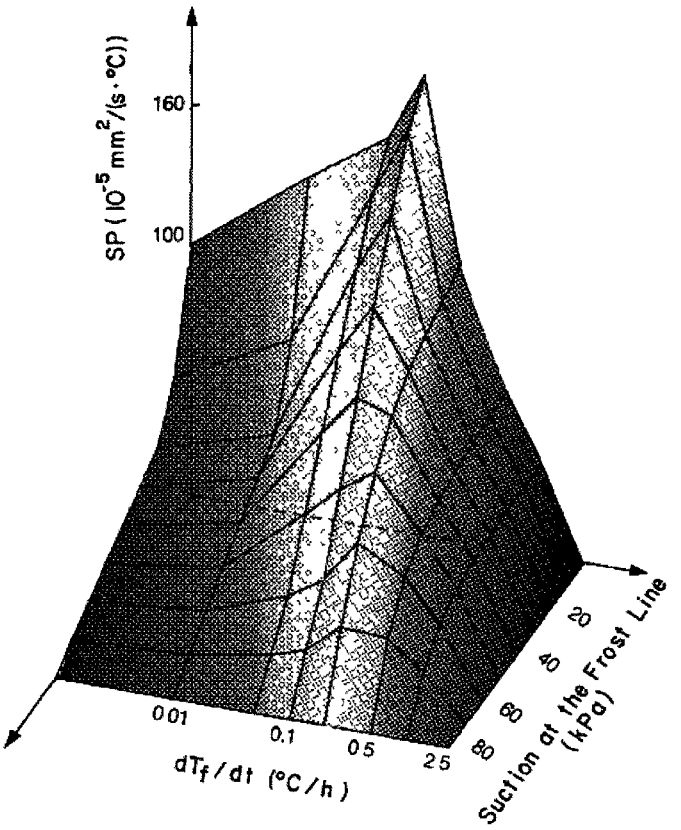

Figure 2 6 Characteristic frost-heave surface for Devin silt (Konrad and Morgenstern 1982b)

With decreasing T_s due to the overburden pressure loads, the thickness of the frozen fringe increases, therefore, overall hydraulic conductivity of the frozen fringe decreases according to the SP concept The effect of overburden pressure against SP is accounted empirically as

[2 13] $SP = SP_0 \exp(-b \times \sigma_{ov})$

where SP_0 = the maximum value of segregation potential, and b = a soil constant

With increasing OCR, smaller SP values are determined by laboratory frost-heave tests (Konrad 1989c) This trend is explained as the result of a decrease of T_s and a concomitant decrease of the overall frozen-fringe hydraulic conductivity In addition, with increasing OCR, the void ratio decreases, and the pore pressure at the freezing front increases However, if all other factors are kept

the same, the SP increases with increasing OCR. Konrad (1989c) explained the result by hypothesizing that the unfrozen water increases when the particles are packed closer together, and in consequence OCR increases. The more unfrozen water exists, the more water may possibly migrate within the frozen fringe.

Repeated freeze-thaw cycles reduced the SP value of saturated clay, and the SP converged to a certain value (Konrad 1989a). Although consolidation is induced in unfrozen soil during freezing due to frost heaving, the effect of freeze-thaw cycles is different from that of OCR. The freeze-thaw cycles show dependency over a range of OCR. Konrad (1989a) concluded that freeze-thaw cycles caused significant changes in the soil structure; the change of the soil structure reduced the SP values.

The effect of pore-water salinity on the SP concept was investigated with laboratory frost-heave experiments using saturated clayey silt at various pore-water of salinities and overburden pressures. Figure 2.7 shows the relationships between SP, overburden pressure, and pore-water salinity. For instance, a pore-water salinity of 35g/liter is the same as sea water salinity. With increasing salinity, SP decreased and showed slightly higher overburden pressure dependency. As shown in eq. [1.14], heaving pressure decreases with increasing solute concentration, decreasing frost-heave susceptibility. The experimental data confirmed that the SP concept established for saline-free soils could be extended to saline soils.

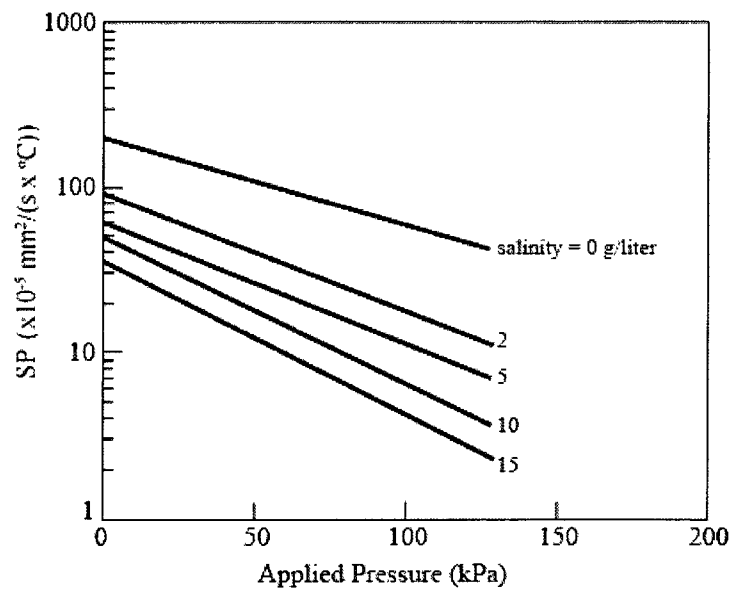

Figure 2.7 Summary of saline dependency in terms of the relationship between SP and applied pressure (modified from Konrad 1990).

2.3 Improvements to the SP frost-heave test equipment

Two types of frost-heave test equipment, single-cell and quadric-cell, were used in this study.

Single-cell frost-heave test equipment

The single-cell frost-heave test equipment used in the study is shown in Figure 2.8. The equipment consists of the following components:

- Frost heave cell,
- Two thermal baths to control pedestal temperatures,
- One thermal bath to induce ice nucleation,
- Laser linear voltage displacement transducer (laser LVDT),
- Differential pressure transducer,
- Air pressure loading system, and
- Data acquisition system.

The single-frost-heave cell was fabricated by the University of Laval, Quebec, Canada to determine the SP values by conducting step-freezing frost-heave tests. The single-cell apparatus was modified for this study as follows:

The single-freezing cell consists of a 102mm inner diameter PVC cylinder, with 50mm wall thickness and 337mm length. Stainless steel porous plates are used to improve thermal response. Overburden pressure applied to the sample is measured using an air pressure cell. The inside of the cell wall is greased with silicon vacuum grease to minimize friction during frost-heave tests. Top and bottom pedestal temperatures are controlled by circulating anti-freeze fluid from the thermal baths.

The soil temperature profiles are measured by seven evenly-spaced thermistors mounted at 18.3mm intervals along the cell sidewall. All of the thermistors are calibrated in an ice bath, in which a mixture of distilled ice and water co-exist to maintain a constant temperature of precisely 0°C. There was some uncertainty of temperature measurements in the original frost-heave cell because the original thermistor setup measured the inner walls of the frost-heave cell, not the exact temperature inside the specimen. With that in mind, these thermistors were directly attached to the soil sample. Furthermore, the frost-heave cell is covered with insulation consisting of fiber glass and a sheet of aluminum-coated insulation to prevent lateral heat flow and radiant effects.

Total sample displacement is recorded with a laser LVDT (Keyence LK-081), which has a precision of 0.003mm. A double-walled burette is connected to the top pedestal. Water intake/outflow is measured using a differential-pressure transducer (Validyne DP-10). The accuracy of the differential pressure transducer is 0.05ml. This is approximately equal to 0.006mm heave for a 100mm

diameter sample. The pressure head difference between inside the burette and pedestal is approximately 80cm (= 7.8kPa). Pore pressure at the end of the soil sample is assumed to be equal to atmospheric pressure, because the pressure-head difference is canceled out by the friction between the pedestal and the cell wall. These precise measurements make it possible to assess the formation of the final ice lens using both total heave and water intake data.

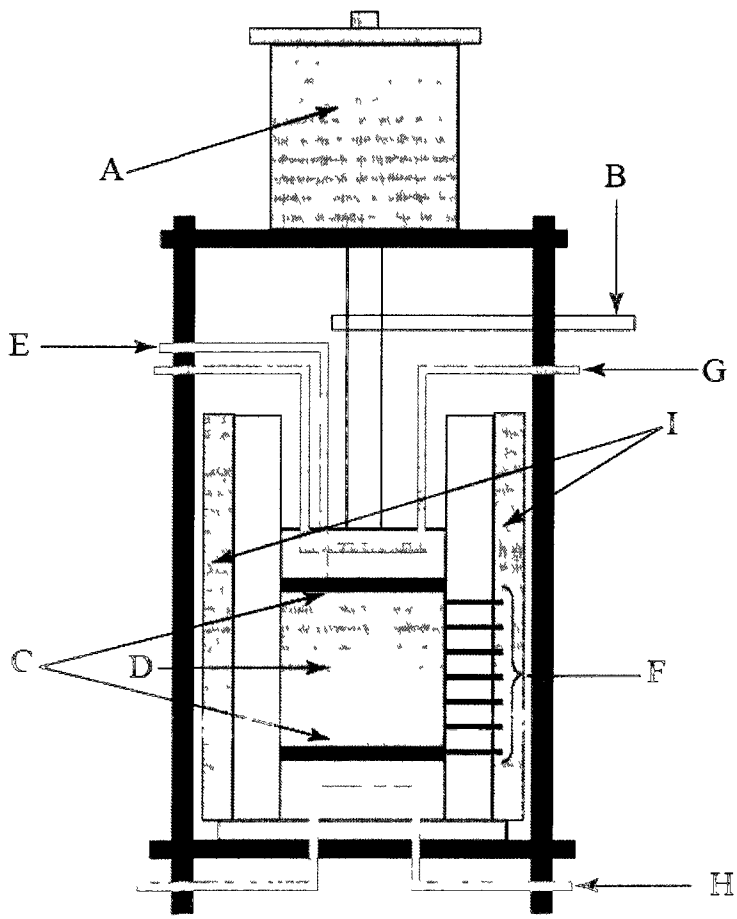

A) air pressure loading, B) horizontal arm for laser LVDT, C) porous metals, D) soil sample, E) water intake/outtake, F) thermistors, G) upper pedestal circulating fluid inlet and outlet, H) bottom pedestal circulating fluid inlet and outlet, and I) insulation

Figure 2.8 Schematic diagram of single-frost-heave cell.

Quadric-cell frost-heave test equipment

The configuration of the quadric-frost-heave cell, which was located at Hokkaido University in Japan, is shown in Figure 2.9. The quadric-cell was originally fabricated to make frozen sand samples under similar temperature conditions by Professor Akagawa. The equipment consists of the following items:

- Quadric-frost-heave cell,
- Two thermal baths to control pedestal temperatures,
- Linear voltage displacement transducer (LVDT),
- Differential pressure transducer,
- Free weight loading, and
- Data acquisition system.

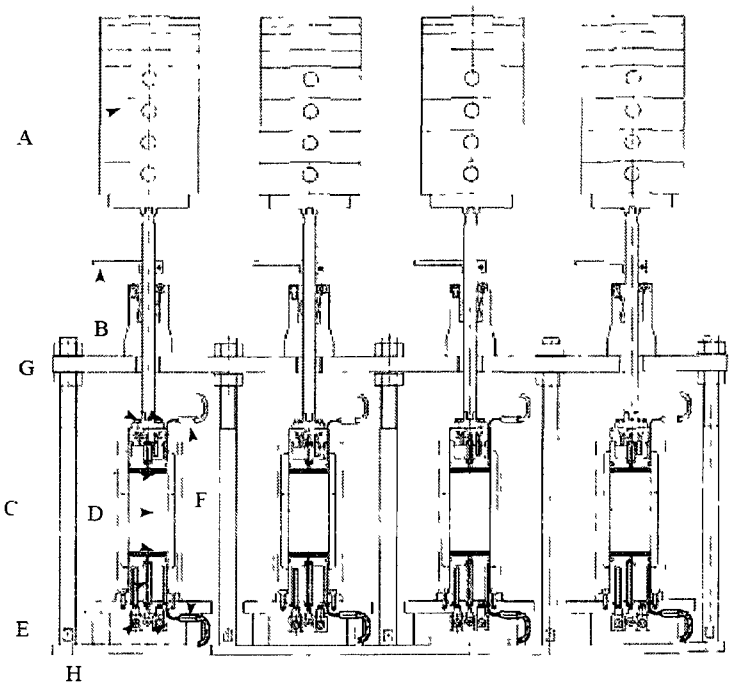

A) overburden pressure weight, B) horizontal arm for LVDT, C) porous stones, D) soil sample, E) water intake/outflow, F) platinum thermistors, G) upper pedestal circulating fluid inlet and outlet, and H) bottom pedestal circulating fluid inlet and outlet

Figure 2.9 Schematic diagram of quadric-frost-heave cell (modified from Akagawa, personal communication 2005).

The quadric-freezing cell consists of 50.2mm inner diameter acrylic cylinders; each cell has 7.5mm thick walls and is 100mm long. Porous stone plates are placed above and below the soil sample. An overburden pressure can be applied to the sample using a dead weight. The inside of the cell wall is greased to minimize friction during frost-heave tests. The top and bottom pedestal temperatures are controlled by circulating anti-freeze fluid from the thermal baths and measured by platinum resistance temperature detectors.

Total sample displacement is recorded with a LVDT. A double-walled burette is connected to the bottom pedestal. Water intake/outflow is measured using a differential pressure transducer.

2.4 Sample preparation and properties

Undisturbed soil samples were taken twice from the UAF frost-heave experiment site on the Chena Hot Spring Road, east of Fairbanks, Alaska. Initial sampling was conducted during the site construction in December 1999. Undisturbed soil samples were taken from just beneath the pipe using core samplers. Frost-heave tests were conducted using those undisturbed soil samples (Kim 2003). After the frost-heave tests, the undisturbed soil samples were remolded at 60kPa consolidation pressure. The remolded soil samples were trimmed for the quadric-frost-heave cell. Figure 2.10 shows the Fairbanks silt grain-size distribution curve and Table 2.1 shows the soil properties of the first soil samples taken in December 1999.

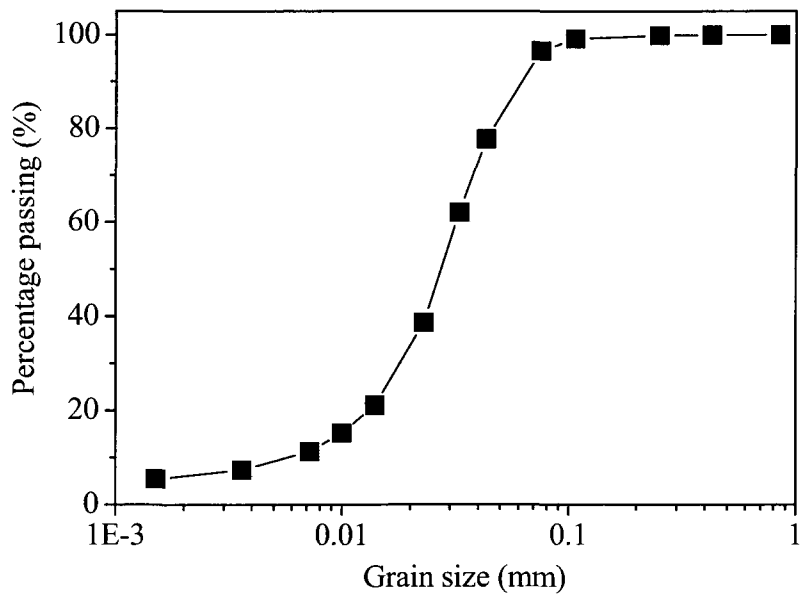

Figure 2.10 Gradation distribution of Fairbanks silt (Kim 2003).

Table 2.1 Soil properties (Kim 2003)

Soil density	Soil classification	Consistency properties			Consolidation yield stress	Compression index	Gram size distribution			
							Gravel fraction	Sand fraction	Silt fraction	Clay fraction
(kg/m^3)		Liquid limit	Plastic limit	Plasticity index	(kPa)		2~75mm (%)	0.075~2mm (%)	0.005~0.075mm (%)	less than 0.005mm (%)
2746	Clayey silt (Cs)	NP	NP	NP	99	0.1359	0	3.5	87.5	9

The second sampling was conducted in September 2005, after operation of the UAF frost-heave experiment was completed. The undisturbed soil sample was taken along the thermal fence, TFA-S1. The sample location was at 1.8m depth, and 1m south from the center of the pipe. The sample was fully saturated by applying vacuum pressure. The fully-saturated-sample was trimmed to 100mm diameter and 115mm initial height for the single-frost heave cell. The average gravimetric water content measured in the trimmed excess was 32.5%.

2.5 Testing program and procedures

The single-cell frost-heave test equipment was used for a series of step-freezing tests (STEP), and the quadric-cell frost-heave test equipment was for the JGST-freezing tests (JGST). Using the undisturbed soil sample, four step-freezing tests were conducted by changing thermal boundary conditions (e.g. temperature gradient and cooling rate) and overburden pressure. The undisturbed soil sample was enclosed in the single-frost-heave cell, and then cooled to approximately the warm-end pedestal temperature. An overburden pressure was applied to the top pedestal in each test. After consolidation, a falling-head hydraulic-conductivity test was conducted in the single-frost-heave cell. The frost-heave cell was covered with insulation consisting of fiber glass and a sheet of aluminum-coated insulation. The frost-heave cell was placed in a refrigerator, which was maintained at 1.5±0.25°C.

When the specimen temperature reached a steady state, anti-freeze fluid (-10°C) was circulated from the ice nucleation thermal bath through the bottom pedestal. After the ice nucleation was observed by temperature increase due to latent heat release, the test program started. After the freezing test, the sample was thawed by raising the temperature at the cold end to the warm-end temperature and the temperature in the refrigerator to the room temperature (approximately 25°C). The applied load was maintained during thawing. After thawing, the next step-freezing test was conducted using the same procedure.

A complete test on the sample consisted of four cycles of freezing, thawing, and over-consolidation. Table 2.2 lists the conditions of a series of step-freezing tests.

Table 2.2 Conditions of a series of step-freezing tests

Test No	Thermal bath temperature for bottom pedestal (°C)	Thermal bath temperature for top pedestal (°C)	Overburden pressure (kPa)	Hydraulic conductivity of unfrozen soil (cm/sec)	Cycles
STEP-1	-5	1 5	85	2 4x10-5	1
STEP-2	-5	1 5	160	1 7x10-5	2
STEP-3	-5	1 5	20	1.8x10-5	3
STEP-4	-3.5	3	50	1.7x10-5	4

Using the remolded soil samples, twelve JGST-freezing tests were conducted by changing the thermal boundary (i.e., cooling rate) and overburden pressure. The remolded soil samples were enclosed in the quadric-frost-heave cell. The quadric-frost-heave cell was placed in a cold room, which was maintained at 4±1.5°C. The soil samples were cooled to approximately the warm-end pedestal temperature. After the ice nucleation was determined by temperature rise due to latent heat release, the test programs started. Table 2.3 summarizes the test conditions of a series of JGST-freezing tests. The quadric-frost-heave cell has an advantage when used to evaluate the effect of overburden pressure, because four freezing tests under different overburden pressure conditions can be operated in the same thermal boundary conditions.

Table 2.3 Conditions of a series of JGST-freezing tests

Test No	Linear reduction of top pedestal temperature(°C)	Average bottom pedestal temperature(°C)	Operation time (hr)	Overburden pressure (kPa)	Initial height (mm)	Initial gravimetric water contents (%)
JGST-1	-0 14 → -3 86	0 22	80	30	29 4	30 4
JGST-2	-0 13 → -3 87	0 22		40	30 1	29 7
JGST-3	-0 17 → -3 86	0 43		60	30 9	29 9
JGST-4	-0 13 → -3 81	0 43		80	30 2	29 4
JGST-5	-0 25 → -4 35	0 33	60	30	31 5	32 2
JGST-6	-0 18 → -4 23	0 17		40	30	32 2
JGST-7	-0 24 → -4 29	0 32		60	32 6	32 2
JGST-8	-0 22 → -4 26	0 31		80	26 6	32 2
JGST-9	-0 26 → -3 93	0 31	40	30	31 4	32 2
JGST-10	-0 19 → -3 80	0 16		40	29 9	32 2
JGST-11	-0 26 → -3 86	0 32		60	28 1	32 2
JGST-12	-0 24 → -3 84	0 29		80	26 3	32 2

2.6 Results of step-freezing tests

Analysis of step-freezing tests data was conducted to determine the SP values. The determination requires defining the water intake rate (v_{sp}) and the temperature gradient of the frozen fringe, as well as cooling rate and pore-water pressure at a given time t, with measurements taken at every time increment Δt. All data were acquired at 5-minute intervals.

The water intake rate at time t can be directly calculated using the reading from the differential transducer as:

$$[2.14] \quad v_{sp}(t) = \frac{V(t-\Delta t) - V(t)}{A \times \Delta t}$$

where $V(t)$ = volume of the water in the burette at time t; and A = cross section area of the soil sample ($7.85 \text{x} 10^3 \text{mm}^2$).

The segregation heave (h_{sp}), which is the heave due to water migration through the unfrozen soil, is calculated by multiplying 1.09 by v_{sp} as:

$$[2.15] \quad h_{sp}(t) = 1.09 \times v_{sp}(t)$$

The total heave (h_t) is obtained directly from the laser LVDT reading. Using the total heave and the segregation heave, the *in-situ* heave (h_{in}) is calculated as:

$$[2.16] \quad h_{in}(t) = h_t(t) - h_{sp}(t)$$

On the other hand, the water-intake rate based on the reading from the laser LVDT (v_t) is calculated as:

$$[2.17] \quad v_t(t) = \frac{h_t(t) - h_t(t-\Delta t)}{1.09 \times \Delta t}$$

The temperature distribution can be used to calculate the temperature gradient of the frozen fringe ($gradT_{ff}$) and frozen depth (X_0).

Within a wide range of T_s, the SP itself is steady, and shows an acceptable accuracy for engineering purposes (Konrad and Morgenstern 1980). Therefore, assuming T_s = -0.1°C, $gradT_{ff}$ is calculated.

The cooling rate of the frozen fringe ($\dot{T}_{ff}$) is calculated as:

$$[2.18] \quad \dot{T}_{ff}(t) = gradT_{ff}(t + \Delta t) \times \frac{\Delta X_0(t)}{\Delta t}$$

where $X_0(t)$ = frozen depth at time t.

SP is defined as (Konrad and Morgenstern 1980):

$$[2.19] \quad \text{SP}(t) = \frac{v_{sp}(t)}{gradT_{ff}(t)}$$

The pore-water pressure at the freezing front (P_0) is calculated by applying Darcy's Law to the unfrozen soil as:

$$[2.20] \quad P_0(t) = \left|P_0(t) - 0\right| \times \rho_w g = \frac{v_{sp}(t) \times l_u(t)}{\kappa_u} \times \rho_w g$$

where κ_u = the hydraulic conductivity of the unfrozen soil; and $l_u(t)$ = the length of unfrozen soil at time t.

In early studies by Konrad and Morgenstern (1980, 1981, 1982b, 1982a), the SP concept was demonstrated from theoretical considerations that the freezing characteristics of a soil under constant boundary conditions are a unique function of the average suction, cooling rate, and temperature gradient across the frozen fringe. At the formation of the final ice lens, the experimental cooling rate could reproduce the extremely slow cooling rate found in field conditions. Therefore, the time at the formation of the final ice lens could be determined in a series of laboratory frost-heave tests. It must be emphasized that the analysis of frost-heave test data in terms of SP applies only for transient freezing. For growth of the final ice lens, the SP concept is not applicable as shown by Ishizaki and Nishio (1985).

The formation of a final ice lens was estimated by two different procedures using results from a step-freezing test, STEP-3, at a 20kPa overburden pressure.

The first procedure is based on temperature measurements. The cold-end temperature was maintained at -5°C and the warm-end at +1.5°C. In step-freezing tests, transient freezing occurred first. During the transient freezing, the calculated cooling rate steadily decreased toward the point of final ice lens formation. The segregation heave started when the calculated cooling rate became lower than 0.1°C/hr as shown in Figure 2.11.

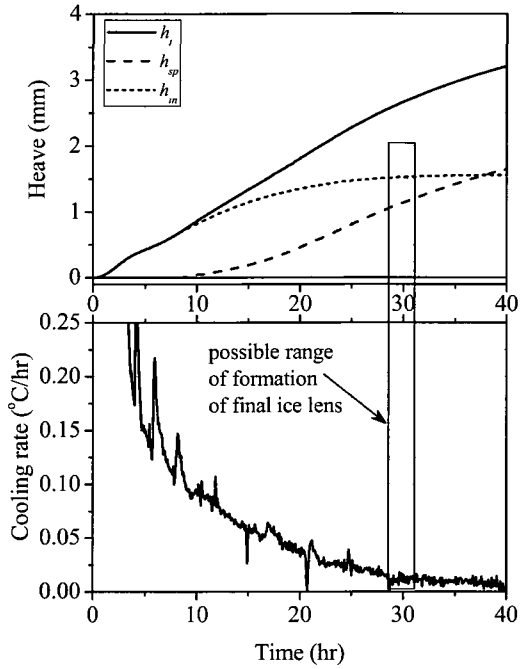

Figure 2.11 Histories of total heave, segregation heave, and *in-situ* heave from a step-freezing test, STEP-3.

The *in-situ* heave reached a constant in response to a cooling rate asymptotically close to 0°C/hr. After the formation of the final ice lens, *in-situ* heave stopped. The possible time range for forming the final ice lens was between 29 and 31hr.

The second procedure was conducted according to the relationship between v_t and v_{sp}. After the formation of the final ice lens, v_t should theoretically equal v_{sp}. As shown in Figure 2.12, v_t, which was from the laser LVDT output, fluctuated erratically with an amplitude of approximately +/- 0.01mm in raw data. v_{sp}, which was from the differential pressure transducer, also fluctuated with an amplitude of approximately +/-0.015mm and is of same order of amplitude as v_t. First Fourier Transform smoothing was applied to avoid misinterpretation of the results at 5 data points per 5 minutes. The smoothed results made it possible to determine the formation of the final ice lens with adequate accuracy. Each smoothed datum became equal asymmetrically between 29 and 31hr, corresponding to the result estimated by the first procedure.

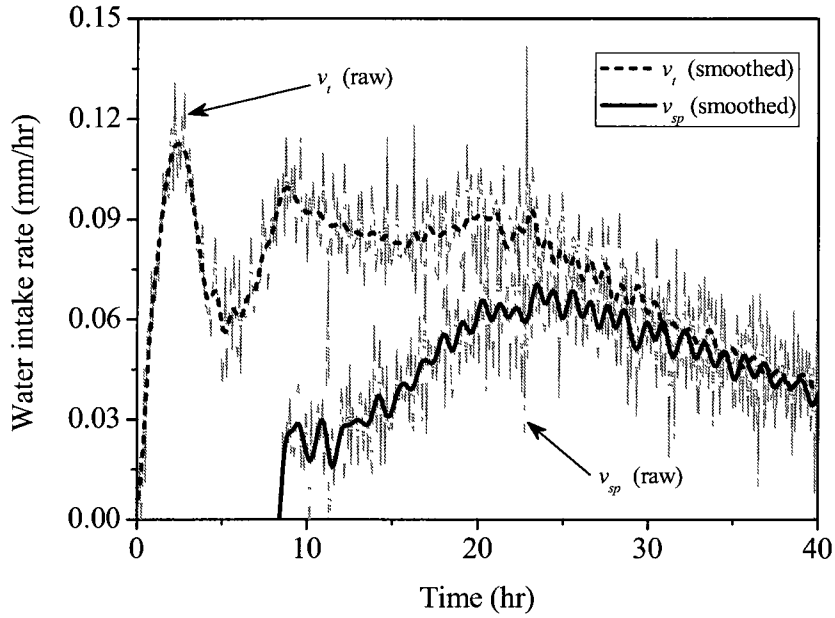

Figure 2.12 History of water flow rates from step-freezing test, STEP-3.

The laboratory frost-heave test data were analyzed in terms of SP, cooling rate, and P_0 as shown in Figure 2.13. The smoothed v_{sp} was used to calculate SP. Once the cooling rate became smaller than 0.1°C/hr, water intake started. Within the cooling rate range of 0.1 to 0.025°C/hr, the SP value increased as the cooling rate decreased. The maximum SP value was obtained at the cooling rate of approximately 0.025°C/hr. The SP value started to decrease after the peak. The values of P_0 varied within a very narrow range between 0 and -0.05kPa. This occurred because the hydraulic conductivity of the unfrozen soil was at a high value of 1.7×10^{-5}cm/sec indicating that the effect of P_0 is not sufficient to characterize the SP value for the *in-situ* Fairbanks silt. The SP value was evaluated as approximately 33×10^{-5}mm^2/(sec x °C) within the determined possible range of final ice lens formation.

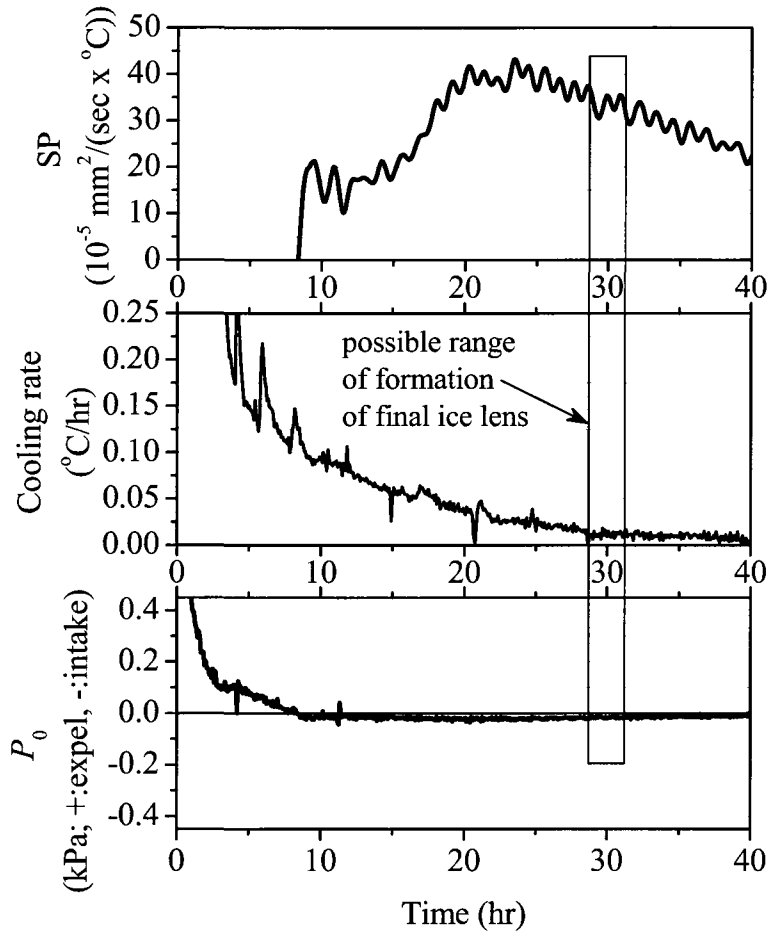

Figure 2.13 Results of frost-heave data analysis from a step-freezing test, STEP-3.

Some assumptions are made in a series of step-freezing tests. The Fairbanks silt used in the tests exhibits low compression characteristics as shown in Table 2.1. Because of the low frost-heave susceptibility and the high hydraulic conductivity of the unfrozen soil, pore-water pressure was nearly zero at the freezing front. For these reasons above, the effects of OCR, freeze-thaw cycle, and consolidation in the unfrozen zone were assumed to be negligible. However, this is only valid for a soil with a high hydraulic conductivity like Fairbanks silt.

The other three step-freezing tests at 50, 85, and 160kPa overburden pressures were analyzed as shown in Figures 2.14a, 2.14b, and 2.14c, respectively. The formation of the final ice lens was

obviously determined by water intake rates. The SP values showed pressure dependency; SP values decreased with increasing overburden pressure. The correlation between the SP value and overburden pressure is shown in Figure 2.15. The SP parameters for the undisturbed Fairbanks silt were determined by the least square regression analysis as $SP_0 = 41.3x10^{-5}mm^2/(sec\ x\ °C)$, $b = 0.0156kPa^{-1}$, and $R^2 = 0.99$, at the formation of the final ice lens.

The test results from each step-freezing test are presented in Appendix B and summarized in Table 2.4, respectively.

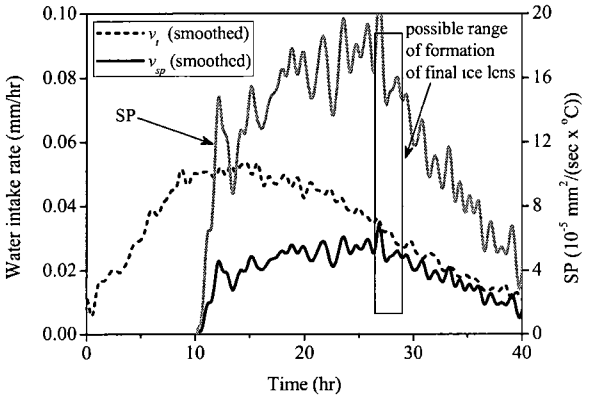

(a) at 50kPa (STEP-4)

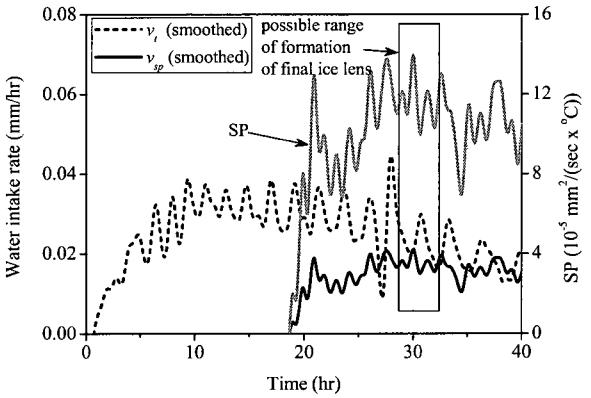

(b) at 85kPa (STEP-1)

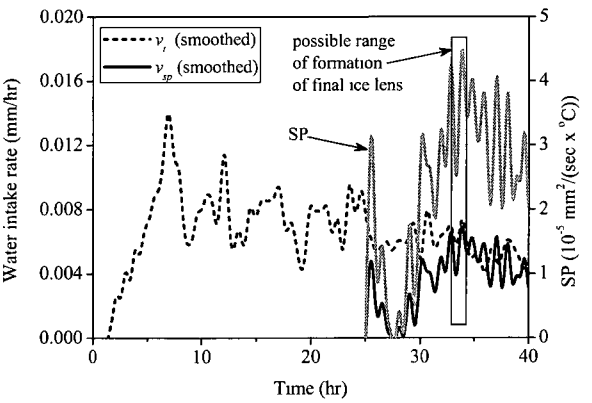

(c) at 160kPa (STEP-2)

Figure 2.14 Results of frost-heave data analysis from step-freezing tests.

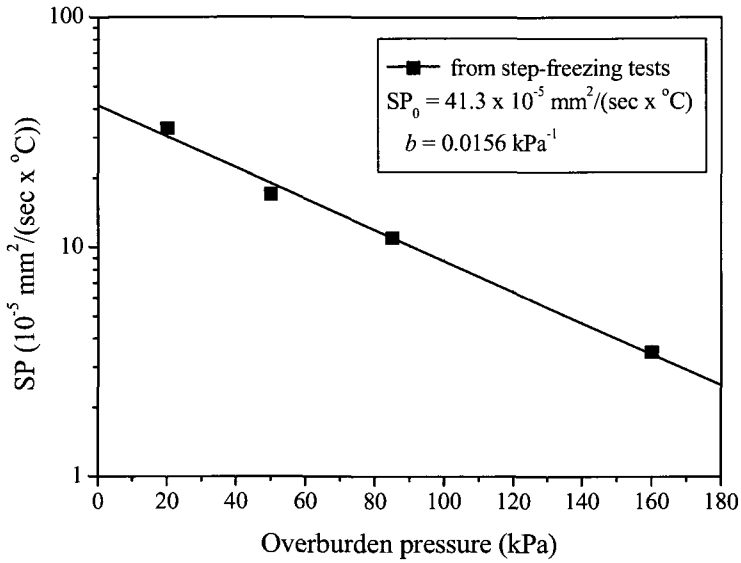

Figure 2.15 Segregation potential of undisturbed Fairbanks silt determined by step-freezing tests at the formation of the final ice lens.

Table 2.4 Results of a series of step-freezing tests

Test No.	Overburden pressure (kPa)	SP (10^{-5} mm^2/(sec x oC))	SP_0 (10^{-5} mm^2/(sec x oC))	b (kPa^{-1})	R^2
STEP-1	85	11			
STEP-2	160	3.5	41.3	0.0156	0.993
STEP-3	20	33			
STEP-4	50	17			

2.7 Results of JGST-freezing tests

The SP values were also determined by a series of JGST-freezing tests. One of the JGST-freezing test results at a 30kPa overburden pressure, JGST-9, is shown here as an example. Figure 2.16 shows the top and bottom pedestal temperatures, T_{cold} and T_{warm}, respectively. The top pedestal temperature was uniformly ramped down by -0.09°C/hr during 40hr, and the bottom pedestal temperature was set at a constant +0.31°C. Figure 2.17 shows the total heave (h_t), segregation heave (h_{sp}), and *in-situ* heave (h_{in}). The total heave is obtained directly from the LVDT reading. The segregation heave is calculated by the reading of the differential transducer multiplied by 1.09 and divided by the cross sectional area of the soil samples (approximately 1.96x10^{3}mm^2).

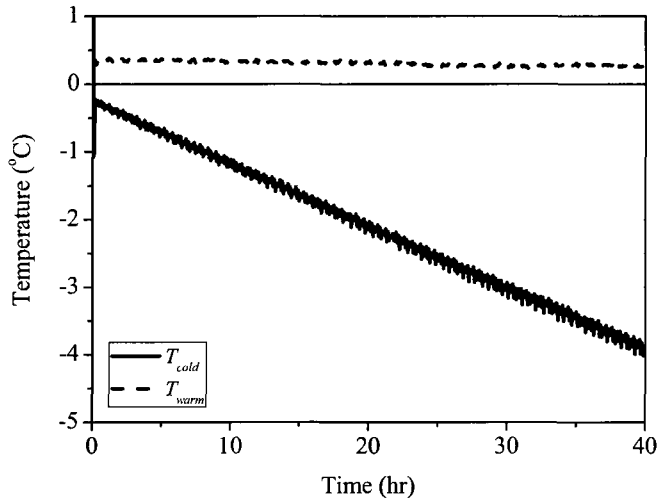

Figure 2.16 Results of temperature boundary condition from the JGST-freezing test, JGST-9.

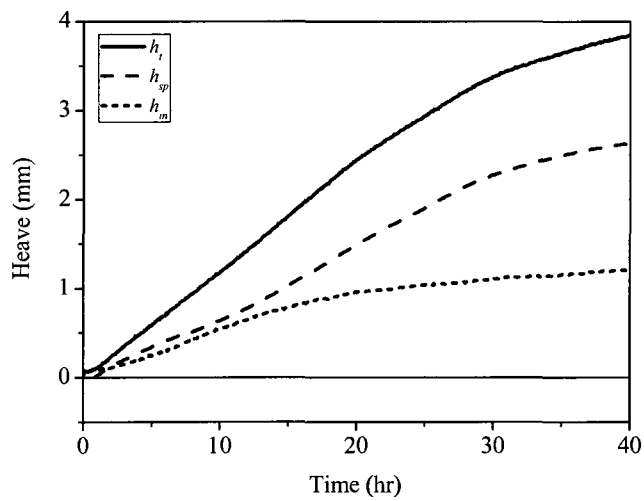

Figure 2.17 History of total heave, segregation heave, and *in-situ* heave from the JGST-freezing test, JGST-9.

The water intake rates were calculated based on the reading from the differential pressure transducer and the LVDT by eqs. [2.14] and [2.17], respectively. As shown in Figure 2.18a, v_t, which was from the LVDT output, fluctuates randomly; the raw data exhibit an amplitude of approximately +/-0.1mm. As shown in Figure 2.18b, v_{sp}, obtained from the differential pressure transducer, also fluctuates within approximately +/-0.075mm, thus showing better accuracy than v_t. Because of these fluctuations, the water intake data were smoothed by the First Fourier Transform method taking at 5 data points per 5minutes.

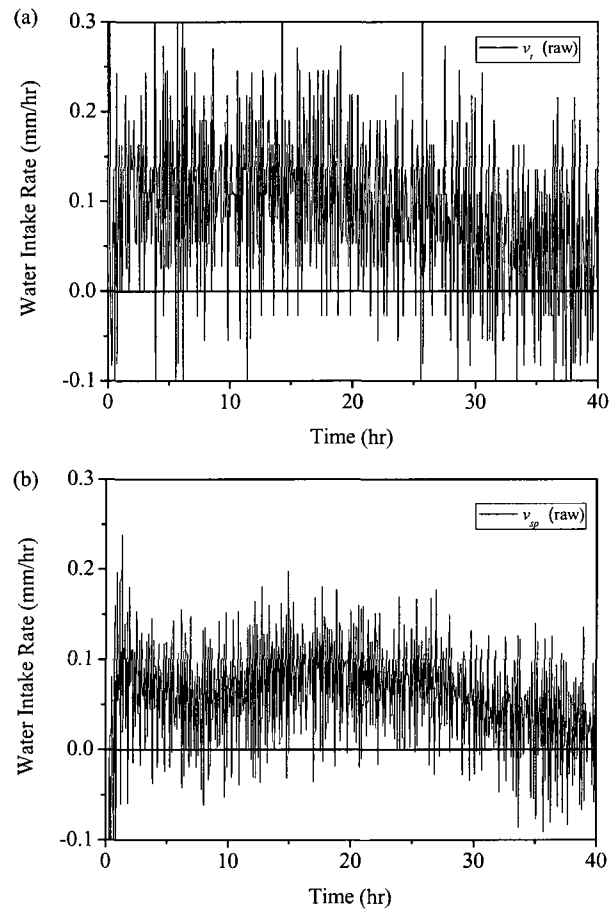

Figure 2.18 Comparison of output from (a) LVDT and (b) differential pressure transducer from JGST-freezing test, JGST-9.

Figure 2.19 shows the results of the frost-heave test analysis. During transient freezing conditions, v_t was greater than v_{sp}, whereas v_t came to equal v_{sp} when the final ice lens initiated. The water-intake rates suggested that the time required to form the final ice lens could be estimated as 21 to 23hr. Since soil temperatures were not measured in a series of JGST-freezing tests, an assumption was made to evaluate $gradT_{ff}$. When a ramped temperature below freezing was applied to the top of a soil sample, unsteady heat flow was initiated. The progress of a freezing front is a function of the imbalance of the heat removed. Heat associated with cooling was assumed to be negligible compared with that associated with the latent heat of freezing water. The thermal conductivities (λ_f = thermal conductivity of frozen soil, and λ_u = thermal conductivity of unfrozen soil) were determined based on the thermal conductivity needle probe method (Kim 2003). Satisfying continuity of temperature and heat flux at the frozen fringe, the relationship is shown as:

$$[2.21]\quad \lambda_f \frac{T_{cold}(t)-T_s}{0-X_s(t)} - \lambda_u \frac{T-T_{warm}(t)}{X_x(t)-(h_0+h_t(t))} = v_{sp}(t)L + \delta w_0 L \frac{\Delta X_s(t)}{\Delta t}$$

where λ_f = 2.11W/(m x °C); λ_u = 1.19W/(m x °C); $X_s(t)$ = the location of segregation freezing front; h_0 = the initial height of the soil sample; δ = a fraction taking into account the portion of unfrozen water in frozen soil; w_0 = unfrozen water content at freezing point; and L = volumetric latent heat of soil.

The right-hand term in eq. [2.21] represents the heat liberated by freezing of migrating water and *in-situ* water in the frozen fringe. When the final ice lens forms, the heat due to *in-situ* water on the right of the equal sign is assumed as zero. The location of the segregation freezing front is determined based on the assumptions above. Since thermal conductivity of the frozen fringe is assumed to be equal to that of the unfrozen soil, the temperature gradient of the frozen fringe is equal to that of the unfrozen soil at the start of the final ice lens formation, expressed as:

$$[2.22]\quad gradT_{ff}(t) = \frac{T_s - T_{warm}(t)}{X_0(t)-(h_0+h_t(t))}$$

The $gradT_{ff}$ at the formation of the final ice lens was calculated as 0.12°C/mm, and the SP was determined as $19\text{x}10^{-5}$mm^2/(sec x °C) in the possible range of the formation of the final ice lens.

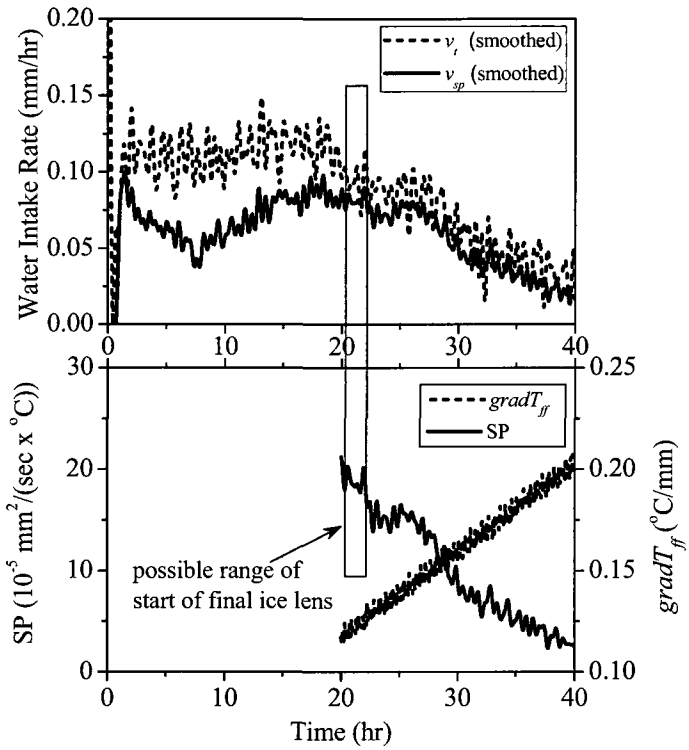

Figure 2.19 Results of frost heave data analysis from the JGST-freezing test, JGST-9.

The three other JGST-freezing tests, JGST-10, JGST-11, and JGST-12, were conducted at 40, 65, and 80kPa overburden pressures, and the same ramping temperature rate, 0.09°C/hr. The results are analyzed as shown in Figures 2.20a, 2.20b, and 2.20c, respectively. In the JGST-12 case, v_{sp} did not equal v_t but was slightly smaller than v_t after the formation of the final ice lens. This was contrary to the other JGST-freezing test results. Mageau and Morgenstern (1980) found that moisture transfer was much reduced in a passively-frozen system due to very low hydraulic conductivity of the frozen soil, and the effect on total heave was negligible in laboratory conditions. It is considered that a small amount of unfrozen water in the frozen soil and the frozen fringe gradually decreased in response to the JGST-freezing mode after the formation of the final ice lens.

The test results from each JGST-freezing test are presented in Appendix B and summarized in Table 2.5.

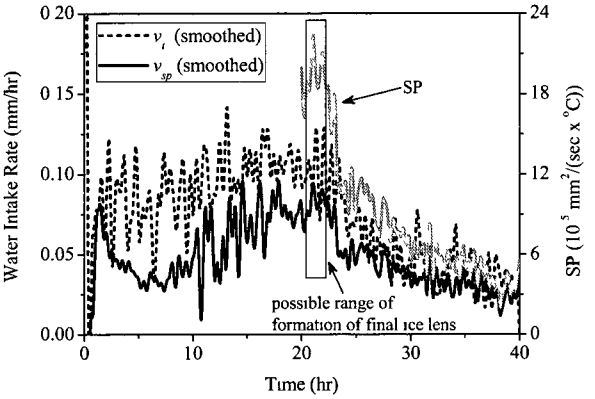

(a) at 40kPa (JGST-10)

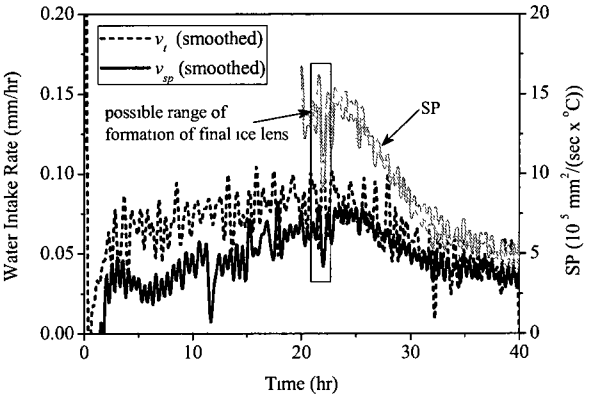

(b) at 60kPa (JGST-11)

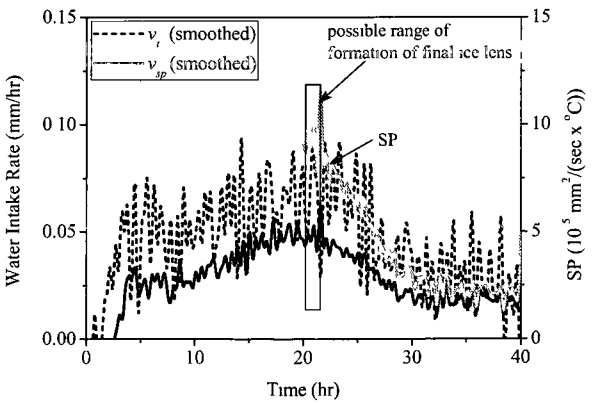

(c) at 80kPa (JGST-12)

Figure 2.20 Results of frost-heave data analysis from JGST-freezing test.

Table 2.5 Results of a series of JGST-freezing tests

Test No.	Overburden pressure (kPa)	SP (10^{-5} mm^2/(sec x °C))	SP_0 (10^{-5} mm^2/(sec x °C))	b (kPa^{-1})	R^2
JGST-1	30	28			
JGST-2	40	24	63.2	0.0243	0.93
JGST-3	60	18			
JGST-4	80	8			
JGST-5	30	24			
JGST-6	40	18	40.6	0.0190	0.99
JGST-7	60	13			
JGST-8	80	9			
JGST-9	30	19			
JGST-10	40	19	31.7	0.0145	0.95
JGST-11	60	14			
JGST-12	80	9.5			
		Total:	43.3	0.0192	0.88

The SP values determined in two different freezing modes are compared as shown in Figure 2.21. The SP values of JGST-freezing tests were more scattered than those of the step-freezing tests. The least-square regression analysis was conducted for the results from 12 JGST-freezing tests. The SP values for the remolded Fairbanks silt were defined as $SP_0 = 43.3 \times 10^{-5}$mm^2/(sec x °C) and $b = 0.0192$kPa^{-1} with a demonstrated R^2 of 0.88.

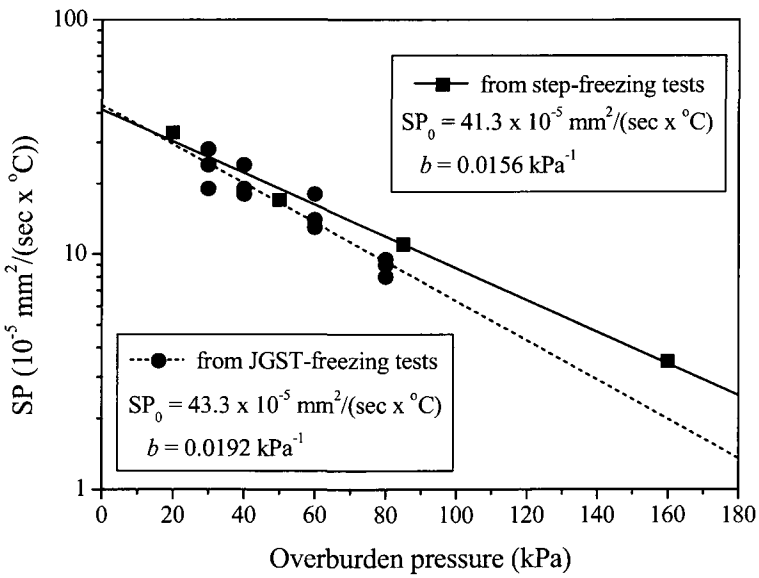

Figure 2.21 Segregation potential comparisons between step-freezing tests and JGST-freezing tests at the formation of the final ice lens.

The SP_0 determined from the JGST-freezing tests was very close to the value obtained from the step-freezing tests; the differences varied by less than 5%. The pressure dependency obtained from the JGST-freezing tests was greater than that from the step-freezing tests. The difference might be due to the assumption made in calculating $gradT_{ff}$ in a series of JGST-freezing tests. The difference between test results may not be significant, but it may indicate that the assumed $gradT_{ff}$ is not as reliable as the temperature measurements.

2.8 Discussion

Although the SP value was successfully determined in two different freezing modes, for a standard test to determine frost-heave susceptibility, the selected cooling rate should reflect the field condition. In the UAF frost-heave experiment, freezing-front penetration rates were very small, approximately 0.28mm/hr during the first 150 days and only approximately 0.07mm/hr after 500days (Kim et al. 2008). The actual temperature gradients of frozen fringe were also very small, ranging from approximately 0.002 to 0.0005°C/mm. Using these results, the cooling rate was calculated at 0.00056°C/hr or less. Penner (1986) conducted a ramped-freezing test simulating a cooling rate in field conditions of approximately 0.0008°C/hr; the test took 240 to 360hrs using a 10cm-high sample. The ramped-freezing test was expensive to conduct due to considering the long operational time involved.

There are two advantages of using step-freezing tests. The first is the short duration of testing, and the second is the simplicity of the frost-heave test apparatus and testing procedure. It should be emphasized that the step-freezing test provides a full range of cooling rates. The cooling rate is very high at the beginning of freezing, decreases rapidly with time, and approaches zero asymptotically as shown in Figure 2.13. Therefore, it is reasonable for the SP value at the formation of the final ice lens to be applied to frost-heave prediction in field conditions.

2.9 Summary and conclusion

A series of step-freezing and JGST-freezing tests were conducted to determine the SP values. Significant findings from this study are:

1) Improvements were made to a step-freezing test to facilitate a consistent and reproducible evaluation of the SP values. The improvements included the use of a differential transducer to measure precise water intake rate, the well-controlled environmental chamber and insulation for precise temperature measurement, and an additional thermal bath for ice nucleation.

2) The SP values were determined using an undisturbed Fairbanks silt sample by a series of step-freezing tests. The SP values were the most expensive parameters to obtain, and yet the most reliable parameters to use for SP predictions.
3) A series of JGST-freezing tests were conducted using remolded Fairbanks silt samples. SP values were obtained at the formation of the final ice lens that were consistent compared with step-freezing tests.

The advantage of continuous-heave and water-intake measurements to determine the formation of the final ice lens was demonstrated. Overall, it has been concluded that a step-freezing test should be conducted with a continuous water intake/outlet, soil heave, and temperature distribution monitoring system. With these improvements, consistent SP values were obtained for the UAF frost-heave experiment. The obtained SP values will be used for the proposed frost-heave model that is presented in the following chapter.

CHAPTER 3: EFFECT OF COOLING RATE AND OVERBURDEN PRESSURE

3.1 Introduction

A large number of studies have sought to establish the relationship between frost-heave susceptibility and cooling rate or freezing-front penetration. There appears to be a consensus that a maximum heave rate is obtained at a certain cooling rate or within a certain range of values (e.g. Horiguchi 1978; Loch 1979).

The influences of cooling rate on the segregation potential (SP) values have been evaluated (e.g. Konrad and Morgenstern 1982b; Konrad 1987a), but those tests were subjected to no external loading. The effect of overburden pressure on the SP values of *in-situ* Fairbanks silt was successfully evaluated at the formation of the final ice lens, under a near-steady-state condition (see Chapter 2). In this chapter, the author discusses the effects of overburden pressure on the SP values of *in-situ* Fairbanks silt during transient freezing.

In the following sections, the effects of cooling rate and overburden pressure on the SP values of *in-situ* Fairbanks silt are first evaluated by a proposed fitting method under transient conditions. Next, the SP values are characterized by a relationship between the SP values, the cooling rate of frozen fringe, and overburden pressure; this relationship is called the "characteristic frost-heave surface". Finally, the applicability of the developed characteristic frost-heave surface is discussed.

3.2 Segregation potential during transient freezing with overburden pressure

When applying freezing boundary conditions in step-freezing, an unsteady heat flow is initiated. The progress of freezing-front penetration is a function of the imbalance between the heat supplied and the heat removed. The final ice lens will form at the moment when the thermal steady-state condition is reached. Konrad and Morgenstern (1981) concluded that at the formation of the final ice lens, the water-intake rate was a function of the temperature gradient within the frozen fringe and the pore-water pressure at the freezing front. Also, the SP value decreases with increasing overburden pressure load (Konrad and Morgenstern 1982a).

However, the SP value determined at the formation of a final ice lens is not sufficiently accurate to predict the variation of frost heave observed during transient freezing. Because frost heave in a step-freezing test can be described as a moisture transfer process to a growing ice lens past the layered frozen fringe and unfrozen soil, the pore-water pressure at the freezing front continuously changes due to changes in the unfrozen soil length during transient freezing. In addition, the

characteristics of frozen fringe are dependent upon cooling rate. For instance, segregation freezing temperature decreases with increasing cooling rate for Devin silt (Konrad 1989b). The reduction of segregation-freezing temperature directly accounts for the decrease of hydraulic conductivity of the frozen fringe.

Konrad and Morgenstern (1982b) described the characteristic of the frozen fringe during transient freezing by determining the cooling rate of frozen fringe under zero-overburden pressure. Because it is very difficult to precisely measure the temperature distribution in the frozen fringe, the cooling rate of the frozen fringe ($\dot{T}_{ff}$) is approximated by considering the change of temperature per unit time at the level of the freezing front as shown in Figure 3.1. The average temperature change of the frozen fringe per unit time Δt is defined as:

$$[3.1] \qquad \dot{T}_{ff}(t) = gradT_{ff}(t+\Delta t) \times \frac{\Delta X_0(t)}{\Delta t}$$

where $gradT_{ff}(t)$ = temperature gradient of the frozen fringe at time t; and $X_0(t)$ = freezing-front penetration at time t.

With an accurate measurement of water-intake rate (v_{sp}) in a series of step-freezing tests as discussed in Chapter 2, the SP at any time t is directly defined as:

$$[3.2] \qquad \mathrm{SP}(t) = \frac{v_{sp}(t)}{gradT_{ff}(t)}$$

The variation of pore-water pressure at the freezing front (P_0) is determined by applying Darcy's Law to the unfrozen soil. Since the hydraulic conductivity of the unfrozen soil is known, P_0 is calculated as:

$$[3.3] \qquad P_0(t) = \frac{v_{sp}(t) \times l_u(t)}{\kappa_u} \times \rho_w g$$

where κ_u = the hydraulic conductivity of the unfrozen soil; and l_u = the length of the unfrozen soil.

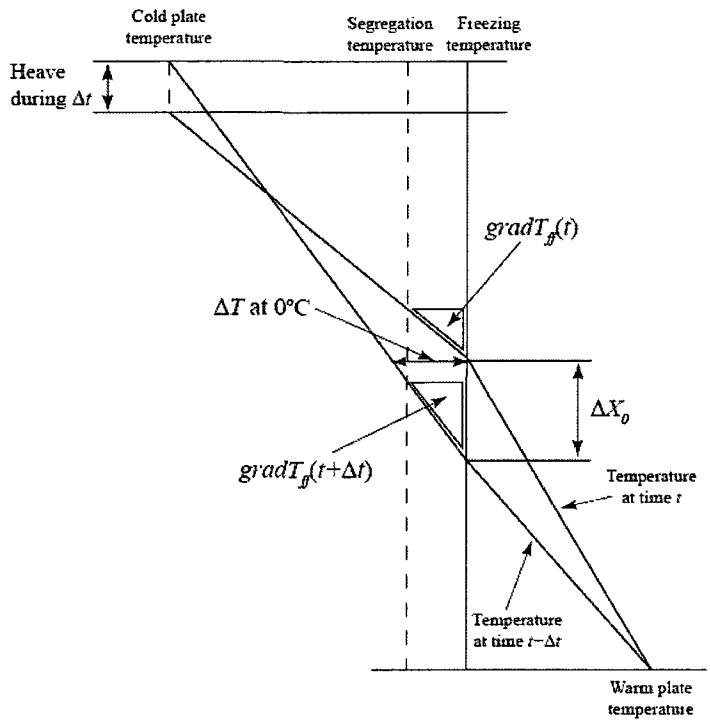

Figure 3.1 The cooling rate of the frozen fringe during transient freezing (modified from Konrad 1987a).

Results of the step-freezing test conducted at a 50kPa overburden pressure, STEP-4, are summarized in Figure 3.2 as an example of the SP analysis during transient freezing. Figure 3.2a shows the variation of SP and the cooling rate. For the *in-situ* Fairbanks silt, no water intake occurs when cooling rate is greater than approximately 0.075°C/hr. Within a range of cooling rates from 0.075 to 0.03°C/hr, the SP value increased as the cooling rate decreased. The maximum SP value was obtained in a cooling rate range of 0.03 to 0.017°C/hr. After the rate reached 0.017°C/hr, the SP value decreased with decreasing cooling rates. The final ice lens formed at the cooling rate of 0.015°C/hr.

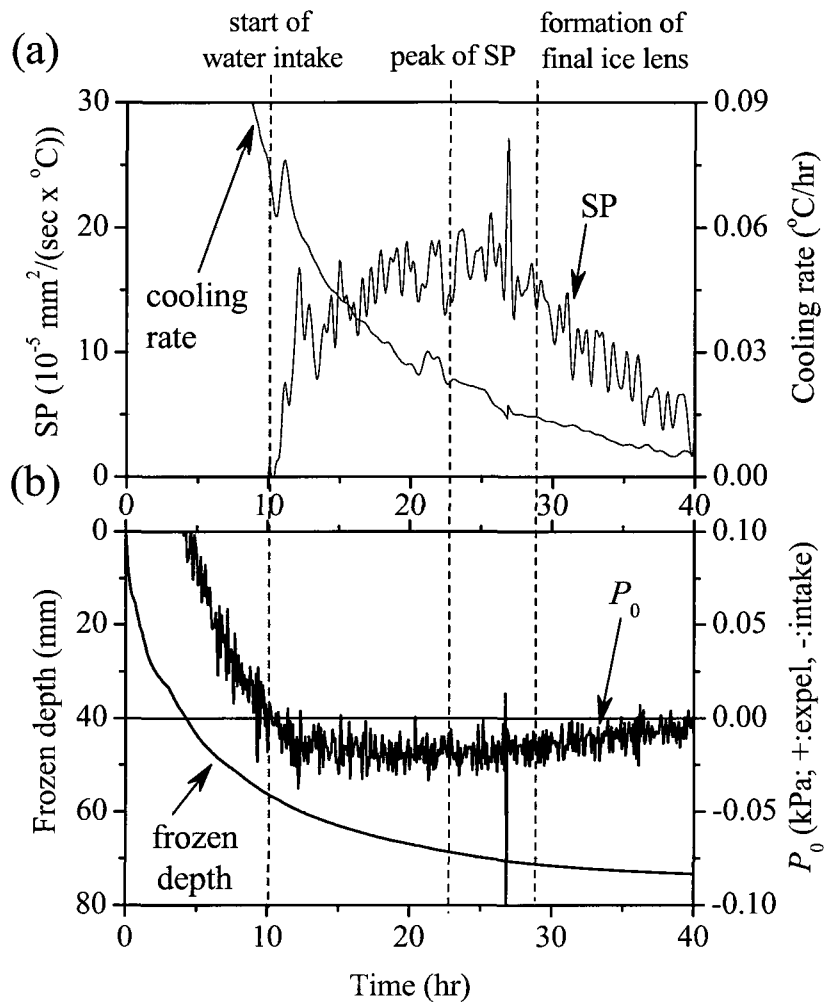

Figure 3.2 Example of typical data from test STEP-4 (at 50kPa applied pressure): (a) variation of SP and rate of cooling; (b) variation of freezing-front penetration and the pore-water pressure at the freezing front.

Figure 3.2b shows the variation of freezing-front penetration and P_0. It can be seen that water is expelled from the freezing front in the first 10hr, after which water intake begins. As the freezing-front penetration continues, P_0 decreases due to shortening of the unfrozen soil. However, the values

of P_0 vary in a very narrow range between 0 and -0.05kPa. This is because the hydraulic conductivity of the unfrozen soil is at a high value of 1.7×10^{-5}cm/sec.

The SP values for *in-situ* Fairbanks silt are apparently dependent upon cooling rate, as shown in Figure 3.2a. The tendency of the relationship between observed SP values and cooling rates is quantified by a function as:

$$[3.4] \quad \mathrm{SP} = SP_m \times \left(\frac{\dot{T}_{ff} + \dot{T}_0}{\dot{T}_m + \dot{T}_0} \right)^2 \times \exp\left(1 - \left(\frac{\dot{T}_{ff} + \dot{T}_0}{\dot{T}_m + \dot{T}_0} \right)^2 \right)$$

where SP_m = the maximum SP value; $\dot{T}_{ff}$ = cooling rate at any time; $\dot{T}_m$ = the cooling rate at which the maximum SP value occurs; and $\dot{T}_0$ = parameter to satisfy the SP at the formation of the final ice lens.

As a result of the step-freezing test at 50kPa overburden pressure, the following values for eq. [3.4] are determined: $SP_m = 18 \times 10^{-5}$mm^2/(sec x °C), $\dot{T}_m = 0.03$°C/hr, and $\dot{T}_0 = 0.0025$°C/hr.

In order to validate the proposed fitting method, the observed and predicted SP values are evaluated using linear regression analysis at four specific cooling rates: at the formation of the final ice lens, at the maximum SP, at one-half of the maximum SP, and at the start of water intake. The predicted SP value does not agree with the observed SP value at the start of water intake, as shown in Figure 3.3. Excluding the SP at the start of water intake, predicted SP values agree well with observed SP values, with $R^2 > 0.99$. A sudden increase of the SP value is observed at the start of water intake (see Figure 3.2a). To compensate for the nonconformity, the SP value is considered as zero when the cooling rate is higher than the critical rate of cooling (CRC). The CRC is defined as 0.075°C/hr for the *in-situ* Fairbanks silt at 50kPa overburden pressure. Figure 3.4 summarizes the result of the proposed fitting analysis in this case.

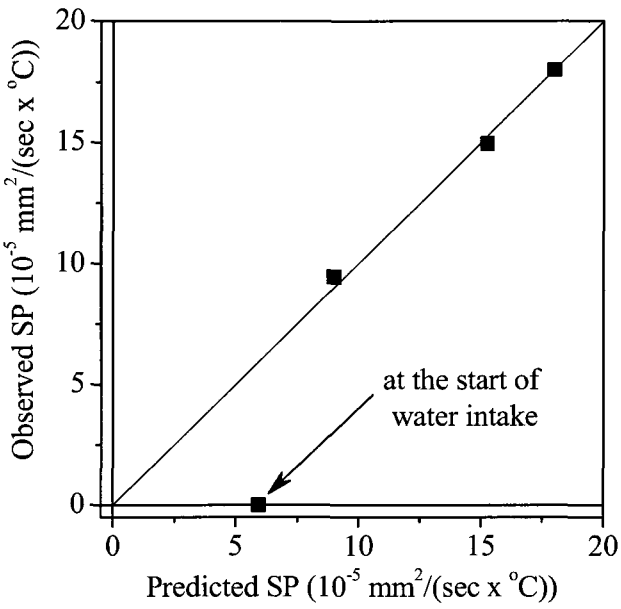

Figure 3.3 Comparison of SP as predicted by the proposed fitting with observed SP at 50kPa applied pressure (STEP-4).

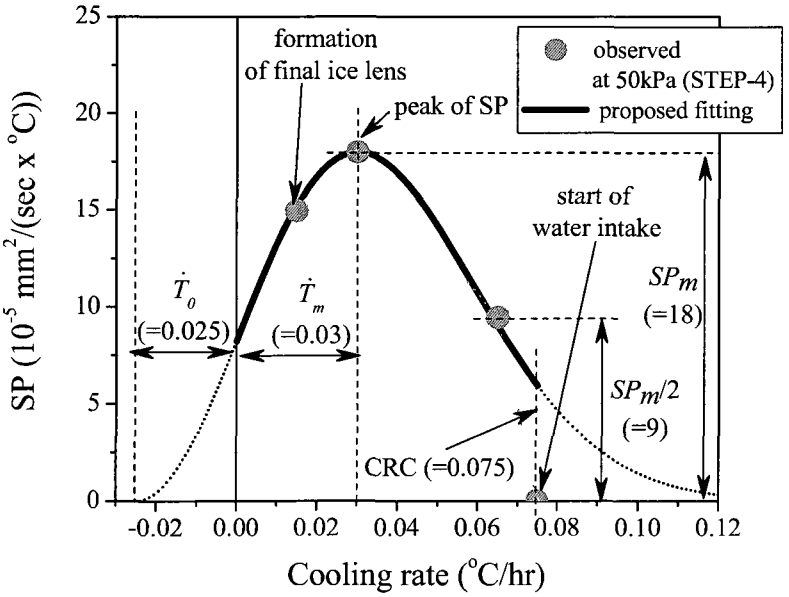

Figure 3.4 Relationship between SP and cooling rate for *in-situ* Fairbanks silt predicted by the proposed fitting method.

3.3 Characteristic frost-heave surface with effect of overburden pressure

Konrad and Morgenstern (1982b) found a unique relationship regarding the frost-heave characteristics of Devin silt under zero overburden pressure during transient freezing. The relationship, termed the "characteristic frost-heave surface", exists between SP, cooling rate of frozen fringe, and pore-water pressure at the freezing front. It was suggested that the characteristic frost-heave surface is also unique to an overburden pressure. However, the effect of overburden pressure is only verified at the formation of the final ice lens, not during the wide range of transient freezing (Konrad and Morgenstern 1982a). This section is devoted to evaluating the effect of overburden pressure over the entire range of step-freezing tests for *in-situ* Fairbanks silt.

For *in-situ* Fairbanks silt, water intake started when the cooling rate became smaller than the CRC (= 0.075°C/hr) at 50kPa overburden pressure (see Figure 3.2a). The SP values at the start of water intake during a series of step-freezing tests are summarized in Figure 3.5. The diagram indicates that the higher the overburden pressure, the smaller the CRC. To investigate the effect of overburden pressure on the CRC, a first-order exponential decay analysis was performed. The resulting first-order exponential decay analysis for the CRC at four different overburden pressures (σ_{ov}) is:

[3.5] $$CRC = 0.1637 \times \exp(-0.015 \times \sigma_{ov})$$

The CRC is highly related to overburden pressure with a demonstrated $R^2 > 0.99$.

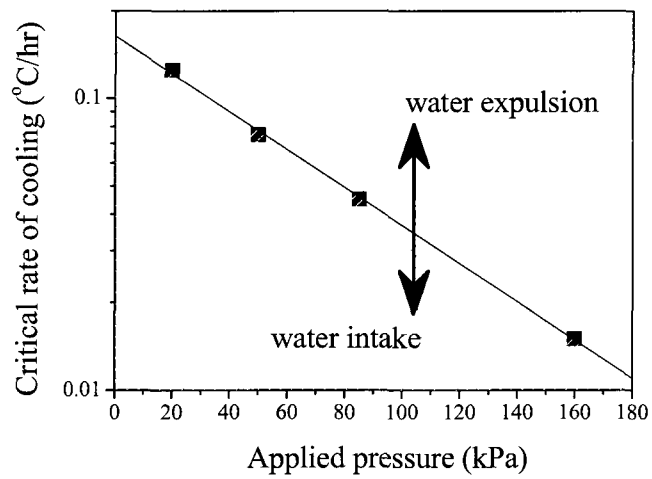

Figure 3.5 Critical rate of cooling with the effect of applied pressure.

The proposed fitting method is applied to a series of step-freezing tests at different overburden pressures. Table 3.1 summarizes the results, showing SP_m, $\dot{T}_m$, and $\dot{T}_0$ for each of the four different step-freezing tests. The CRCs are included as well.

Table 3.1 Parameters for the proposed fitting method

Test	Applied pressure (kPa)	SP_m (10^{-5} mm^2/(sec x °C))	$\dot{T}_m$ (°C/hr)	$\dot{T}_0$ (°C/hr)	CRC (°C/hr)
STEP1	85	13	0.017	0.015	0.045
STEP2	160	4	0.0067	0.0028	0.015
STEP3	20	40	0.0375	0.0575	0.125
STEP4	50	18	0.03	0.025	0.075

The SP values predicted by the proposed fitting analysis were compared with the observed SP values at three cooling rates: at the formation of the final ice lens, at the maximum SP, and at a value one-half of the maximum SP. The results of linear regression analysis at the three different overburden pressures, 20, 80, and 160kPa, are shown in Figures 3.6a, 3.6b, and 3.6c, respectively. Each linear regression analysis has $R^2 > 0.99$.

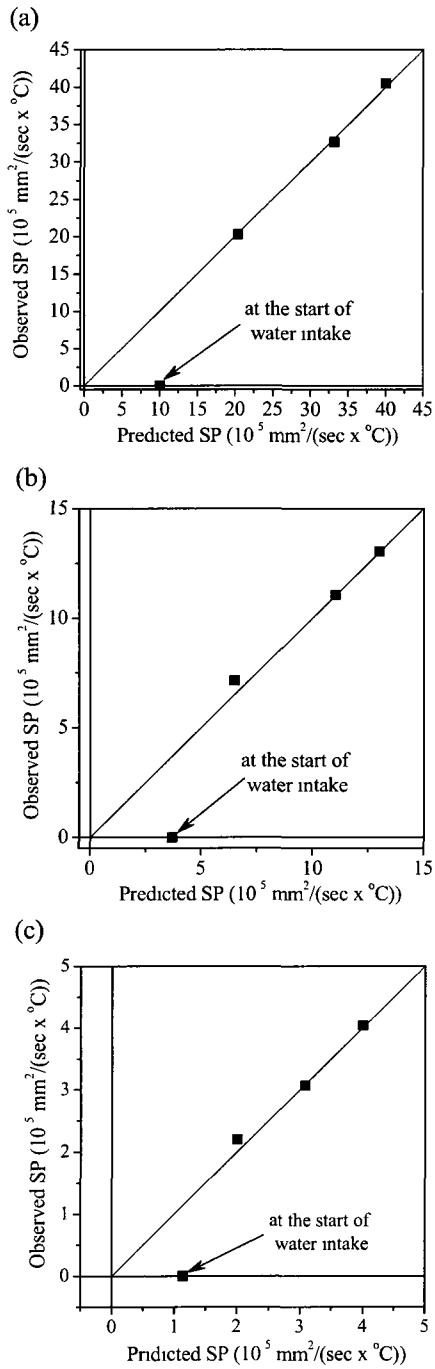

Figure 3.6 Comparison of predicted with observed SP values by the proposed fitting method: (a) at 20kPa (STEP-3); (b) at 85kPa (STEP-1); and (c) at 160kPa (STEP-2).

Figure 3.7 shows the results of the proposed fitting analysis for a series of step-freezing tests at each overburden pressure. In addition, the CRCs are considered. The diagram indicates that *in-situ* Fairbanks silt has a dependency upon overburden pressure, not only at the formation of the final ice lens but also during transient freezing. The *in-situ* Fairbanks silt exhibits a peak SP value at a given overburden pressure. Both the peak SP value and the corresponding cooling rate decrease as the overburden pressure increases, indicating that both parameters are dependent upon overburden pressure.

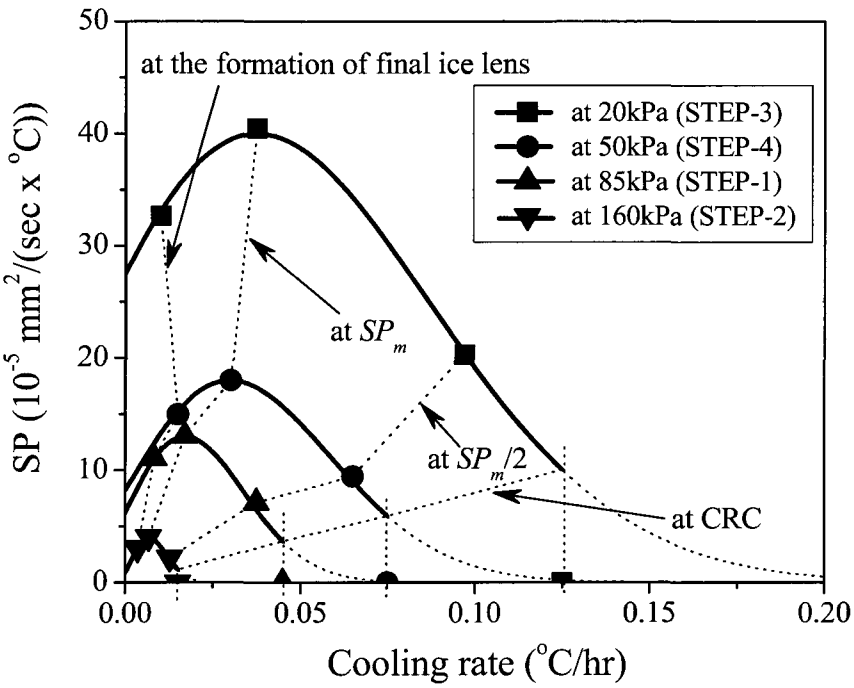

Figure 3.7 Effect of rate of cooling and applied pressure on SP values predicted by the proposed fitting method.

To investigate the effect of overburden pressure on each parameter for the proposed fitting, the first-order exponential decay analysis was conducted for SP_m and $\dot{T}_0$ (see Figure 3.8a and Figure 3.8c, respectively). Also, linear regression analysis of $\dot{T}_m$ at the four different overburden pressures was conducted (see Figure 3.8b).

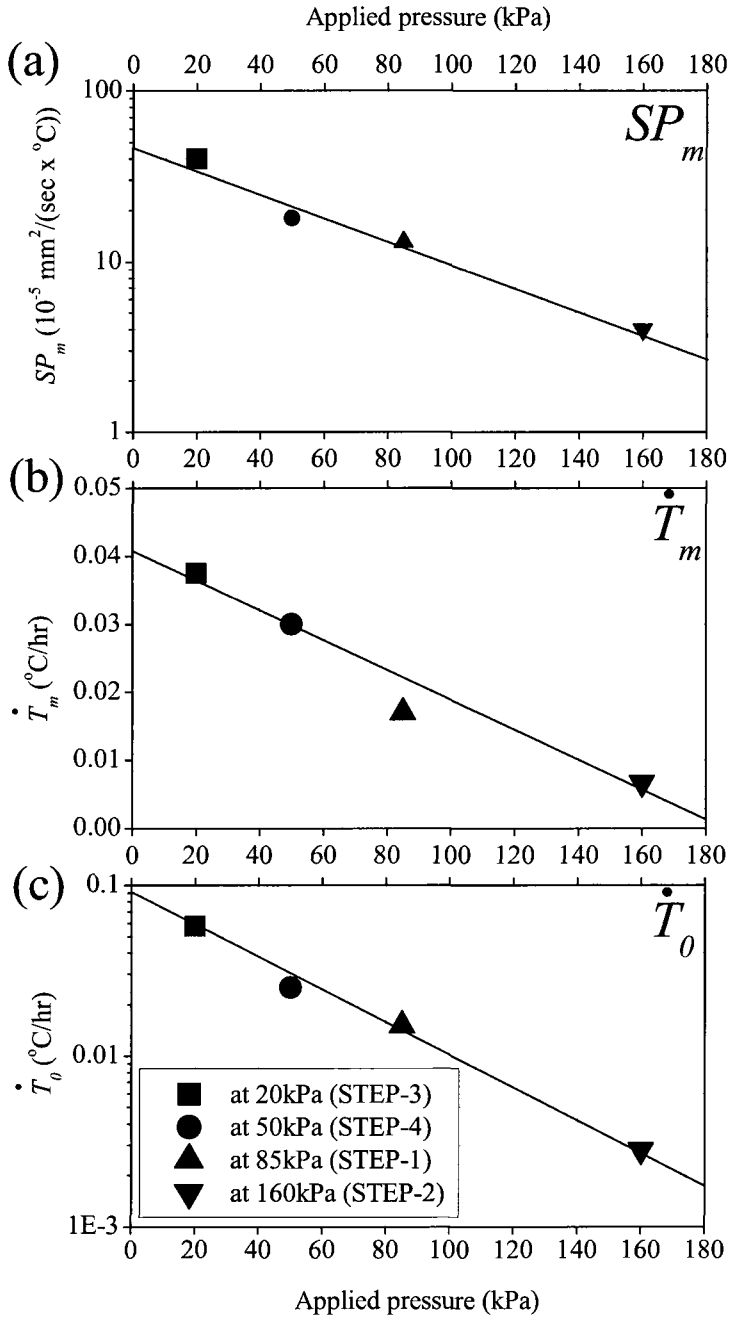

Figure 3.8 Relationship between parameters for the proposed fitting method and applied pressure.

SP_m is highly correlated to the overburden pressure with a demonstrated R^2 = 0.98. The resulting first-order exponential decay analysis for SP_m at the four different overburden pressures (σ_{ov}) is:

[3.6] $$SP_m = 47.801 \times \exp(-0.0158 \times \sigma_{ov})$$

$\dot{T}_m$ is also highly correlated to overburden pressure, with a demonstrated R^2 = 0.95. The resulting linear-regression analysis for $\dot{T}_m$ at the four different overburden pressures (σ_{ov}) is:

[3.7] $$\dot{T}_m = -0.0002 \times \sigma_{ov} + 0.0402$$

Similarly, $\dot{T}_0$ is highly correlated to overburden pressure with a demonstrated R^2 = 0.99. The resulting first-order exponential decay analysis for $\dot{T}_0$ at the four different overburden pressures (σ_{ov}) is:

[3.8] $$\dot{T}_0 = 0.0823 \times \exp(-0.0211 \times \sigma_{ov})$$

From eqs. [3.4] through [3.8], the SP value for Fairbanks silt during transient freezing is successfully determined with a relationship between SP, cooling rate, and overburden pressure.

Because the hydraulic conductivities of the frozen soil at each overburden pressure were high (e.g. from 1.7×10^{-5} to 2.4×10^{-5}cm/sec), the effect of pore-water pressure at the freezing front is considered negligible.

Finally, the characteristic frost-heave surface for *in-situ* Fairbanks silt is modified using the relationship between SP, cooling rate, and overburden pressure as shown in Figure 3.9. The SP value was treated as zero, when the cooling rate was smaller than the CRC according to eq. [3.5]. The characteristic frost-heave surface can provide input SP values at any cooling rate and overburden pressure for numerical simulations.

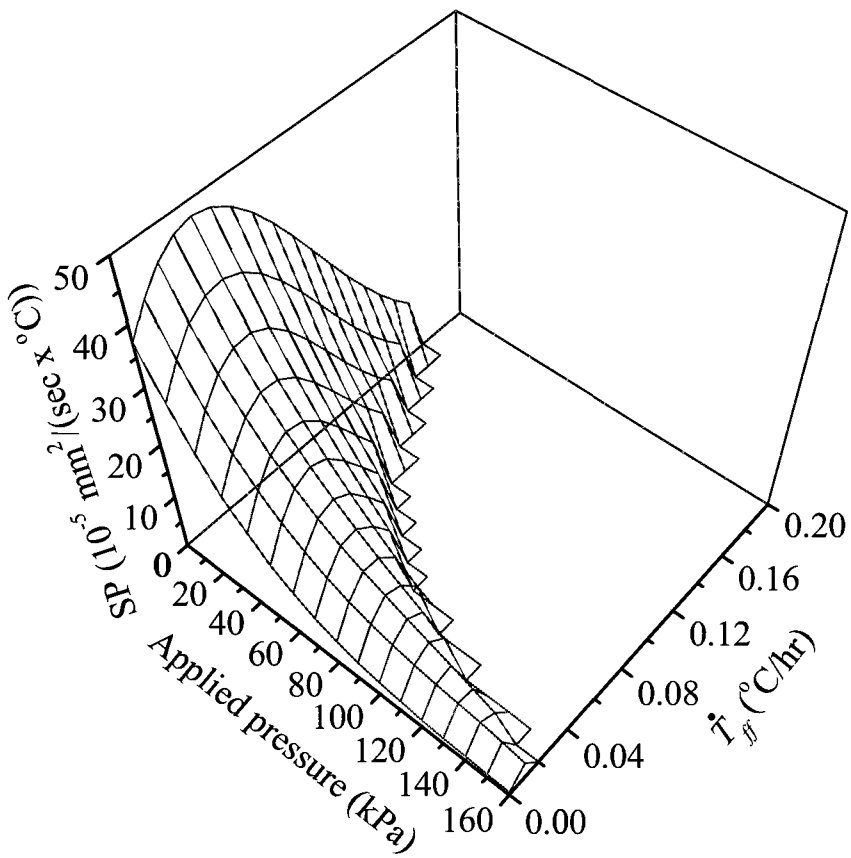

Figure 3.9 Characteristic frost-heave surface for *in-situ* Fairbanks silt.

3.4 Limitations of the proposed fitting method and the characteristic frost heave surface

The variation of the SP value for *in-situ* Fairbanks silt was successfully evaluated during transient freezing with different overburden pressures using a regression analysis. Furthermore, the characteristic frost-heave surface was developed by expanding the proposed fitting method. The limitations of the proposed evaluation methods are stated here.

The SP concept was found to be applicable during transient conditions, that is, by the time at the formation of the final ice lens in step-freezing tests with different overburden pressures for *in-situ* Fairbanks silt. After the formation of the final ice lens, the thermal condition approaches a steady state. When freezing-front penetration stops, the difference between heat flow out of and into the soil sample is balanced with the latent heat liberated by the migrating water due to frost heave; this state is defined as a quasi-steady state. Ishizaki and Nishio (1985) indicated that the SP concept was not applicable to prediction of final ice lens growth at a quasi-steady state.

Figure 3.10 shows the comparison between the observed and the predicted SP values at 50kPa overburden pressure. Contrary to the proposed fitting method based on the transient phase, the observed SP value decays after the formation of the final ice lens. Akagawa et al. (1985) observed variable SP decay for 100 to 1000hr after the final ice-lens formation; their SP values reached a constant magnitude at the quasi-steady state. They concluded that the constant SP value at quasi-steady state is approximately 20% of the SP value at the formation of the final ice lens. Unfortunately, the frost-heave equipment used in this dissertation could not be used to conduct tests of such a long duration. Therefore, this proposed fitting method and the characteristic frost-heave surface do not include the ability to predict the frost heave after the formation of the final ice lens.

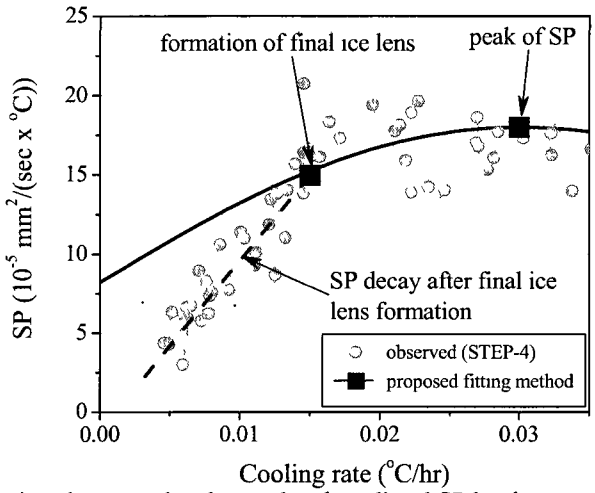

Figure 3.10 Comparison between the observed and predicted SP by the proposed fitting method after the formation of the final ice lens at 50kPa applied pressure.

3.5 Summary and conclusion

The effects of cooling rate and overburden pressure on SP values for *in-situ* Fairbanks silt were evaluated during transient freezing. Significant findings from this study are:

1) The *in-situ* Fairbanks silt showed dependency upon cooling rate during transient freezing. A fitting method, which has three parameters, was developed to quantify the effect of cooling rate on the SP value.
2) Water was either attracted to or expelled from the freezing front due to frost heave, depending upon cooling rate and overburden pressure. The cooling rate at the start of water intake was defined as the critical rate of cooling, CRC. The CRC was used to define the range of water intake for the proposed fitting method.
3) The effects of overburden pressure on three parameters used in the proposed fitting method and on the CRC were evaluated. The characteristics of frost heave for *in-situ* Fairbanks silt were successfully related to SP, cooling rate, and overburden pressure. This relationship is also termed the "characteristic frost-heave surface".
4) The proposed fitting method and the characteristic frost-heave surface were only available during transient freezing. They do not have the ability to predict the final ice lens growth.

The SP values obtained by the proposed fitting method will be used as input parameters for the developed frost-heave model, which will be presented in the following chapter.

CHAPTER 4: FROST HEAVE MODELING

4.1 Introduction

Taber (1929, 1930) first recognized that frost heave requires the flow of unfrozen water towards the freezing front and is different from the pore-water expansion due to freezing. The suction force that moves the unfrozen water is termed "cryogenic suction". Radd and Oertle (1973) proved that the cryogenic suction is governed by the Generalized Clausius-Clapeyron Equation. Many frost-heave theories and models have been developed applying the Generalized Clausius-Clapeyron Equation. For instance, the secondary frost-heave theory (Miller 1978) explained the mechanics of discrete ice-lens formation based on well-established soil physics, and was developed into the Rigid Ice Model by O'Neill and Miller (1985).

A complete analysis of multi-dimensional frost-heave problems must be able to deal with the coupling of heat transfer, moisture transfer, and mechanical analysis. The Rigid Ice Model has received great praise when used in microscopic approaches because it accurately simulates an individual ice lens. However, to produce quantitative results, especially for multi-dimensional frost-heave problems in frozen-ground engineering, the microscopic approach of the Rigid Ice Model may not be most reliable. This is often true in field conditions, in which empirical models based on laboratory frost-heave test results are far more useful for predicting multi-dimensional frost heave and induced load than are the microscopic models, which require more numerous and more complicated input parameters. A good example of an empirical concept is the segregation potential (SP) concept.

The SP concept prevails because of its considerable simplifications. The concept simplifies the frost-heave theory by allowing heat and moisture transfer to be considered as a coupled process, for which the mechanical analysis is independent. Consequently, the pressure acting on the frozen fringe is simply equal to the overburden pressure using a non-deforming mesh (e.g. Konrad and Morgenstern 1984; Kim et al. 2008). However, the SP frost-heave models using the non-deforming mesh cannot respond to an induced stress due to frost-heave displacement. Therefore, it is necessary to develop a more-advanced frost-heave relationship involving thermal and mass transfer and stress coupling to enable understanding of the multi-dimensional pressure effect on the SP using a deforming mesh.

This chapter has two objectives. The first is to develop a consecutive frost-heave model applying the SP concept in a finite-element application with deforming mesh. Also, it was found that the development of freezing within *in-situ* Fairbanks silt is dependent upon cooling rate and applied

pressure, as presented in Chapter 3. The other objective is to verify the developed frost-heave model using the SP values, which were obtained by the proposed fitting method.

In the following sections, the fundamental function used in the developed frost-heave model is described first. A description of the heat-transfer model and the basic assumptions and implementation procedure of the developed frost-heave model follow. Finally, verification of the developed frost-heave model against a laboratory frost heave test is presented with the effect of cooling rate and overburden pressure.

4.2 SP porosity growth function

Blanchard and Fremond (1985) were among the first individuals to propose a multi-dimensional frost-heave model for coupling heat transfer, moisture transfer, and mechanical analysis. Simulation of an individual ice lens was not considered in their model; instead, ice-lens growth was modeled as a volume increase of the soil-ice-water mixture.

Ideas that have been accepted by many frost heave studies include the control volume finite-element method (Coutts 1991), porosity rate function (Michalowski 1993), and modified porosity rate function (Michalowski and Zhu 2006). These earlier works are expanded in this study.

First, a volumetric expansion zone is considered in this model. As discussed in the previous chapters, frost heave can be described as a problem of moisture transfer to a growing ice lens past the layered frozen fringe and the unfrozen soil. From an engineering point of view, the zone that is colder than the growing ice lens is defined as a passive system. Moisture migrations were observed under temperature gradients in the passive system (e.g. Hoekstra and Chamberlain 1964; Ishizaki et al. 1985). However, moisture transfer was much reduced in the passive system due in part to very low hydraulic conductivity of the frozen soil; consequently, the contribution to total heave is negligible in both laboratory conditions (Mageau and Morgenstern 1980) and field conditions (Slusarchuk et al. 1978). Therefore, only active system volume expansion is considered in this study. The active system is described in Figure 4.1. Schematically, the active system is composed of growing ice lens and frozen fringe. As the active system is assumed to be fully saturated, the active system is modeled as a mixture of soil-ice-water.

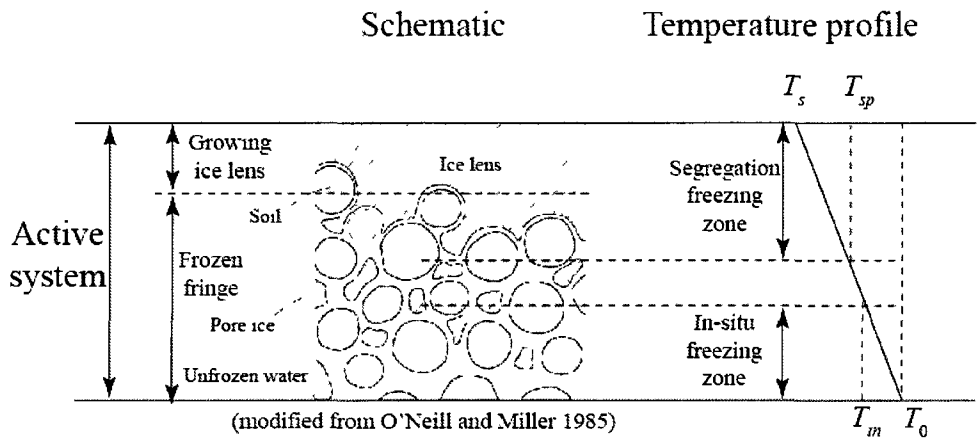

Figure 4.1 Active system of the proposed frost heave model.

Next, the active system has two volumetric expansion zones: namely, the *in-situ* freezing zone and segregation freezing zone. The expansion due to *in-situ* heave occurs in the *in-situ* freezing zone, which exists between freezing temperature (T_0) and *in-situ* freezing temperature (T_{in}). The *in-situ* heave is intended to account for the *in-situ* pore-water expansion due to freezing. Therefore, it is directly related to the fraction of unfrozen water in the *in-situ* freezing zone. With accurate water-intake rate measurements in a series of step-freezing tests shown in Chapter 2, the portion of unfrozen water is directly determined from those test results as follows:

$$[4.1] \qquad \delta(t) = \frac{h_{in}(t) - h_{in}(t-\Delta t)}{0.09 \times n_{ini} \times \left(X_0(t) - X_0(t-\Delta t)\right)}$$

where $\delta(t)$ = fraction of unfrozen water, which changes into *in-situ* freezing at time t; $h_{in}(t)$ = *in-situ* heave at time t; n_{ini} = initial porosity; and $X_0(t)$ = depth of freezing-front penetration at time t.

The maximum value of δ was 0.9 in a series of step-freezing tests for the *in-situ* Fairbanks silt. This means that a maximum of 90% of the pore-water can freeze during the freezing process. Assuming that all *in-situ* heave occurred within the *in-situ* freezing zone, the unfrozen water contents (w) - temperature (T) relationship is described as:

$$[4.2] \qquad w = w_0 + \frac{w_0 - w_u}{T_0 - T_{in}} \times \left(T - T_0\right)$$

where w_0 = unfrozen water content at the freezing point; w_u = residual unfrozen water content; and T_{in} = temperature at the end of *in-situ* freezing.

Figure 4.2 shows the comparison between the calculated unfrozen water content curve and the measured results of Fairbanks silt at the University of Alaska Fairbanks (UAF) frost-heave experiment site (Huang et al. 2004).

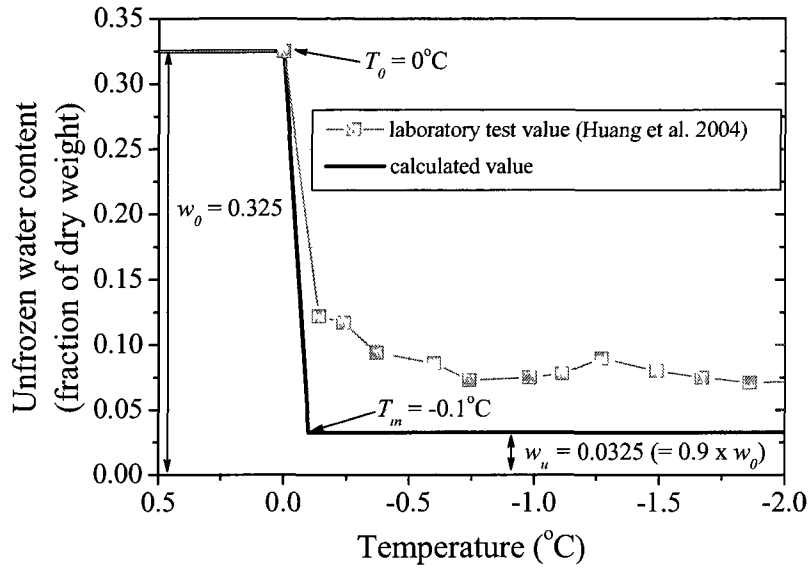

Figure 4.2 Unfrozen water characteristic curve for *in-situ* Fairbanks silt.

The segregation freezing zone is between a location in frozen fringe (T_{sp}) and the warmest growing ice lens temperature (T_s) as shown in Figure 4.1. Excess pore ice will occur in the segregation freezing zone due to the migrating water. Since it is assumed that all *in-situ* heave occurs within the *in-situ* freezing zone, the masses of soil and unfrozen water are constant in the segregation freezing zone. Therefore, the incremental change of porosity in the segregation freezing zone is identical to the incremental change in volumetric ice content in response to the migrating water.

The incremental change in total porosity (Δn_t) is composed of porosity growth due to *in-situ* heave plus that due to segregation heave. Defining the initial water content at time t as $w(t)$, the porosity growth due to *in-situ* heave (Δn_{in}) at time $t+\Delta t$ can be expressed as:

$$[4.3] \quad \Delta n_{in} = -0.09 \times \theta_w(t) \times \frac{w(t+\Delta t) - w(t)}{w(t)}$$

where $\theta_w(t)$ = volumetric fraction of water at time t.

To predict the segregation heave, the SP concept is applied to the developed frost-heave model. At each time step, the water migrating rate (v) is calculated as:

[4.4] $$v = \mathrm{SP}\left(\sigma_{ov}, \dot{T}_{sp}, P_0\right) \times gradT_{sp}$$

where SP = segregation potential; σ_{ov} = the stress acting on the segregation freezing zone; $\dot{T}_{sp}$ = cooling rate of the segregation freezing zone; P_0 = pore-water pressure at the freezing front; and $gradT_{sp}$ = temperature gradient in the segregation freezing zone.

The amount of migrating water is converted to volume strain. The thermal solution gives the effective area of the segregation freezing zone (A_{sp}) and determines the effective width of the segregation freezing zone in the element (l_{sp}). Thus, the porosity growth due to segregation heave (Δn_{sp}) is calculated as:

[4.5] $$\Delta n_{sp} = \frac{1.09 \times l_{sp} \times v}{A_{sp}} \times \Delta t = \frac{1.09 \times l_{sp} \times \mathrm{SP}\left(\sigma_{sp}, \dot{T}_{sp}, P_0\right) \times gradT_{sp}}{A_{sp}} \times \Delta t$$

where Δn_{sp} is defined as the SP porosity growth function.

The total porosity growth (Δn_t) is obtained by adding eqs. [4.3] and [4.4]:

[4.6] $$\Delta n_t = \Delta n_{in} + \Delta n_{sp}$$

The incremental change in total porosity is identical to the incremental change in volumetric strain. Assuming the initial porosity at time step t is $n(t)$, the new porosity at time $n(t+\Delta t)$ is updated as:

[4.7] $$n(t+\Delta t) = \frac{n(t) + \Delta n_t}{1 + \Delta n_t}$$

The time-dependent volumetric fractions (θ) of the three-phase relations were defined as shown in Figure 4.3 and calculated as below:

[4.8] $$\begin{cases} \theta_s(t+\Delta t) = 1 - n(t+\Delta t) \\ \theta_w(t+\Delta t) = \dfrac{\rho_s}{\rho_w} w(t+\Delta t)\{1 - n(t+\Delta t)\} \\ \theta_i(t+\Delta t) = n(t+\Delta t) - \dfrac{\rho_s}{\rho_w} w(t+\Delta t)\{1 - n(t+\Delta t)\} \end{cases}$$

where ρ = density; and subscripts s, w, and i = soil, water, and ice, respectively.

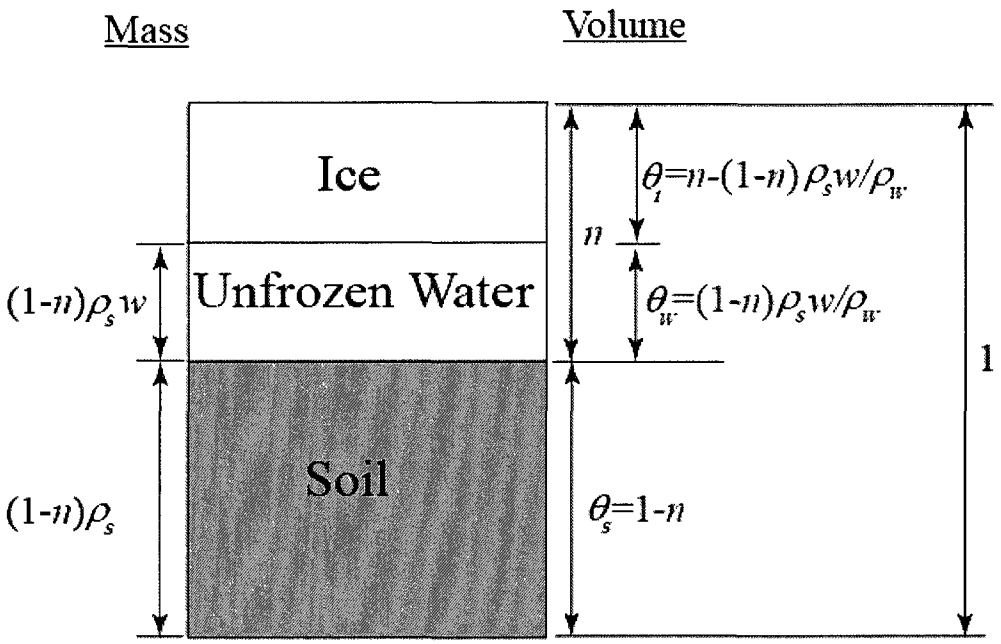

Figure 4.3 Three-phase relations of the modeled fully-saturated soil.

4.3 Basic equation for heat transfer

The three basic modes of heat transfer are conduction, radiation, and convection. Radiation components contribute almost nothing to the amount of heat transferred; radiation accounts for < 1% of the total heat transfer in sands and even less in fine-grained soils (Farouki 1981).

Although heat convection was considered in some models (e.g. Harlan 1973), it is usually of negligible importance in soil heat transfer studies. For instance, Nixon (1975) determined that, for most one-dimensional thaw calculations, the effects of convective heat transfer could be neglected without significant loss in accuracy using a mathematical solution.

Nixon's mathematical approach was applied to verify the effect of water migration due to frost heave on heat transfer in soils. The moisture migration in the frozen zone on the cold side of the active ice lens is assumed to be negligible because of the extremely low hydraulic conductivity. Moisture migration occurs only in frozen fringe and unfrozen soil. One-dimensional heat transfer taking into account the convective component in the frozen fringe can be written as:

$$[4.9] \quad C_{ff}\frac{\partial T}{\partial t} = \lambda_{ff}\frac{\partial^2 T}{\partial x^2} - C_w v(x,t)\frac{\partial T}{\partial x}$$

where C_{ff} = volumetric heat capacity of frozen fringe; C_w = volumetric heat capacity of water; λ_{ff} = thermal conductivity of frozen fringe; and v = water migration rate.

The rate of water migration is written using the frost-heave strain parameter (FH) as:

$$[4.10] \quad v(x,t) = FH\frac{dX_0(t)}{dt}$$

where $X_0(t)$ = depth of freezing-front penetration at time t.

Eq. [4.10] states that when a unit depth of soil freezes, the water migration that occurs will equal FH. Substituting eq. [4.10] in eq. [4.9] yields:

$$[4.11] \quad \frac{\partial T}{\partial t} = \frac{\lambda_{ff}}{C_{ff}}\frac{\partial^2 T}{\partial x^2} - \frac{C_w}{C_{ff}}FH\frac{dX_0(t)}{dt}\frac{\partial T}{\partial x}$$

The thermal boundary condition simulates the segregation freezing temperature (T_s) as:

$$[4.12] \quad \text{at } x = 0; T = T_s; t \geq 0$$

The initial temperature is assumed to be equal to the freezing point (T_0) as:

$$[4.13] \quad \text{at } x = X_0(t); T = T_0; t = 0$$

When the initial temperature is close to the freezing point, the effect of the initial temperature can be ignored without significant loss in accuracy, unlike the effect of latent heat, which is more significant and cannot be ignored (Nixon and McRoberts 1973).

The solution for the movement of the freezing front and the associated temperature fields was developed by Neumann in the 1860's and is presented by Carslaw and Jaeger (1947). Assuming that all the latent heat is liberated at the freezing front, the rate of movement of the freezing front is solved at the freezing front as:

$$[4.14] \quad \lambda_{ff}\frac{\partial T}{\partial x} = L\frac{\partial X_0(t)}{\partial t}$$

where L = volumetric latent heat of soil.

To solve eq. [4.11] subjecting it to a boundary condition described in eq. [4.12], the freezing front penetration is given by:

$$[4.15] \quad X_0(t) = PR\sqrt{t}$$

where PR = freezing rate parameter.

The solution to eq. [4.11] subject to the boundary conditions described in eqs. [4.12] and [4.13] is found as:

$$[4.16]\quad T = T_s + \frac{(T_0 - T_s)\left\{\operatorname{erf}\left(\frac{x}{2\sqrt{\lambda_{ff}/C_{ff}\,t}} + FH\frac{PR}{2\sqrt{\lambda_{ff}/C_{ff}}}\right) - \operatorname{erf}\left(FH\frac{PR}{2\sqrt{\lambda_{ff}/C_{ff}}}\right)\right\}}{\operatorname{erf}\left(\frac{PR}{2\sqrt{\lambda_{ff}/C_{ff}}} + FH\frac{PR}{2\sqrt{\lambda_{ff}/C_{ff}}}\right) - \operatorname{erf}\left(FH\frac{PR}{2\sqrt{\lambda_{ff}/C_{ff}}}\right)}$$

Substitution of eqs. [4.15] and [4.16] into eq. [4.14] yields an expression for the freezing-front penetration parameter in eq. [4.15] as:

[4.17]

$$\frac{\exp\left\{-\left(\frac{PR}{2\sqrt{\lambda_{ff}/C_{ff}}} + FH\frac{PR}{2\sqrt{\lambda_{ff}/C_{ff}}}\right)^2\right\}}{\operatorname{erf}\left(\frac{PR}{2\sqrt{\lambda_{ff}/C_{ff}}} + FH\frac{PR}{2\sqrt{\lambda_{ff}/C_{ff}}}\right) - \operatorname{erf}\left(FH\frac{PR}{2\sqrt{\lambda_{ff}/C_{ff}}}\right)} = PR\frac{L\sqrt{\pi}}{2\sqrt{\lambda_{ff}C_{ff}}(T_0 - T_s)}$$

Once the thermal properties are known in eq. [4.17], this equation is expressed in terms of the single unknown, *PR*. The units of *PR* are m/sec$^{0.5}$. The parameter becomes dimensionless when divided by 2 x $(k_{ff}/C_{ff})^{0.5}$. The dimensionless freezing-rate parameter in eq. [4.17] is then a function of two variables: $C_{ff}(T_s\text{-}T_0)/L$ and *FH*. The former function is referred to as the Stefan Number. The latter function expresses the amount of heat transfer taking place due to water migration, which is heat convection due to frost heave. The effect of convection on the rate of freezing-front penetration is examined by plotting the dimensionless freezing-rate parameter vs. the Stefan Number. In the UAF frost-heave experiment, segregation heave was determined to be 0.05m in response to 3.5m freezing front penetration over 3 years of observation (Kim et al. 2008). The frost-heave strain was calculated as *FH* = 0.05/3.5/1.09 = 0.025. This is a typical case of low frost-heave susceptibility. A case of high frost-heave susceptibility was also considered, a 100 times greater frost-heave strain of *FH* = 2.5, which was one of a series of JGST-freezing tests. Material properties, λ_{ff} = 2.11W/(m x °C); C_{ff} = 2.2 MJ/(m^3 x °C); and *L* = 142 MJ/m^3, were used for the analysis.

Figure 4.4 shows the effect of convective heat transport on the dimensionless freezing-rate parameter across the practical range of frozen fringe temperatures. The range of Stefan Number between 0.001 and 0.01 corresponds to a T_s of between -0.06 and -0.65°C. With *FH* = 0.025, the effect of convection was less than 0.03% through the entire temperature range. The effect of convective heat transfer was noticeable with *FH* = 2.5. Although the greatest difference was observed at Stefan

Number = 0.01, it was still less than 6%. Therefore, the effect of convective heat transfer on the temperature distribution can be negligible for frost-heave simulations.

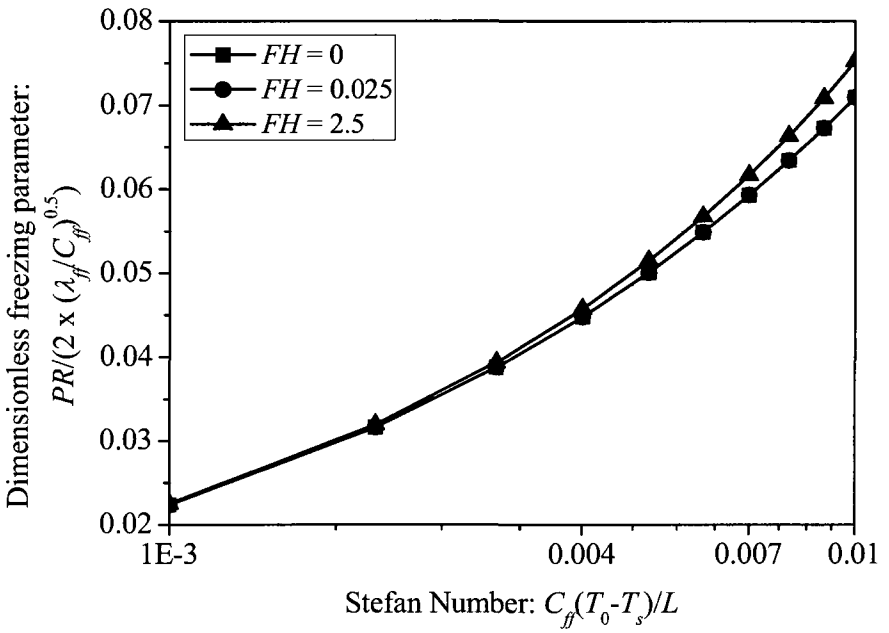

Figure 4.4 Effect of water migration in the frozen fringe on the dimensionless freezing parameter.

It is concluded from the results of the parametric study that the effect of convective heat transfer in the frozen fringe can be ignored in most engineering simulations without the risk of incurring errors of more than a few percent. Because of this result, the developed frost-heave model with isotropic thermal properties is based on conduction only and is governed by the following equation:

$$[4.18] \quad C\frac{\partial T}{\partial t} - L_w \rho_i \frac{\partial \theta_i}{\partial T} = \lambda\left(\frac{\partial^2 T}{\partial x^2} + \frac{\partial^2 T}{\partial y^2} + \frac{\partial^2 T}{\partial z^2}\right)$$

where C = volumetric heat capacity of soil; L = volumetric latent heat of soil; T = temperature; and λ = thermal conductivity.

The thermal conductivity of a soil mixture is determined by Johansen's method (Johansen 1977). The volumetric heat capacity of a soil mixture is calculated as the sum of the volumetric heat capacities of the four phases multiplied by their volumetric fractions (Kay et al. 1977) as below:

[4.19] $$C = \rho_s c_s \theta_s + \rho_w c_w \theta_w + \rho_i c_i \theta_i + \rho_a c_a \theta_a$$

where ρ = density; c = mass heat capacity; θ = volumetric fraction; and subscripts, s, w, i, a = soil, water, ice, and air, respectively.

Alternatively, eq. [4.18] can be expressed as:

[4.20] $$C_{ap} \frac{\partial T}{\partial t} = \lambda \left(\frac{\partial^2 T}{\partial x^2} + \frac{\partial^2 T}{\partial y^2} + \frac{\partial^2 T}{\partial z^2} \right)$$

where C_{ap} = apparent volumetric heat capacity of soil.

In this study, the unfrozen water effect is directly taken into account in the phase change (e.g. Nixon 1983; Shen 1988) as:

[4.21] $$C_{ap} = C - L_w \rho_i \frac{\partial \theta_i}{\partial T}$$

where L_w= latent heat of fusion per unit mass of water.

4.4 Implementation of the frost-heave model

The developed frost heave model applying the SP porosity growth function is implemented by ABAQUS software. ABAQUS/CAE (computer aided engineering) and ABAQUS/Standard were used for modeling; ABAQUS/CAE is the user interface and ABAQUS/Standard is the solver. ABAQUS/CAE creates an input file. The input file is composed of the following tasks: generation of finite-element mesh, assignment of material properties, and the definition of boundary conditions. The created input file is submitted to ABAQUS/Standard. The results are visualized in ABAQUS/CAE. The solution created by the ABAQUS/Standard solver is based on the combination of a finite element method and a finite-difference method. The Galerkin finite-element solution (e.g. Reddy 2005) is used in the spatial domain, and the Crank-Nicolson finite-difference scheme (Crank and Nicholson 1947) uses a backward algorithm in time domain. Iso-parametric elements are used for simulations.

ABAQUS/Standard employs a user-defined subroutine function to extend the capabilities of the applications; the flow chart of this subroutine is shown in Figure 4.5. The user-defined subroutine is called at all integration points of elements at each time step, and then is linked to the ABAQUS/Standard implementation. The user-defined subroutine is composed of four components -

SDVINI, HETVAL, USDFLD, and UEXPAN. The user-defined subroutines are written in the FORTRAN language.

First, SDVINI is used to define the initial material properties. For any particular time step, temperature distribution is first calculated using the user-defined subroutine HETVAL with an iterative procedure. The thermal results are used to determine the location of the active system. Once the location of the active system is determined, the change of unfrozen water content and $gradT_{sp}$ are calculated. Next, stress state is called from the previous time step using USDFLD. The user-defined function UEXPAN is then used to calculate the volumetric increase of ice due to both *in-situ* and segregation heave. The volumetric increase is passed to the next time step to carry out the thermal analysis.

The porosity increment occurs due to the growth of ice within the active system. The rate of water migration is governed by the SP porosity growth function instead of the Darcy's Law. It must be emphasized that the porosity growth rate is calculated assuming that the pore-water pressure at the freezing front, P_0, is zero. From eq. [4.4], the frost-heave susceptibility decreases with increasing P_0. However, in most field conditions, P_0 is fairly small because of the small water-intake rate. Furthermore, Fairbanks silt showed a very narrow range variation of P_0 between 0 and -0.05kPa because of its high hydraulic conductivity in a series of step-freezing tests. The SP porosity growth function also does not account for the effect of consolidation in unfrozen soil in response to the water migration due to frost heave. However, any errors due to the lack of consolidation effect will introduce a conservative estimation of the frost-heave amount.

Consequently, it should be noted that the SP porosity growth function will not be able to simulate laboratory frost-heave tests using soil which has low hydraulic conductivity and high compressibility such as a clayey soil.

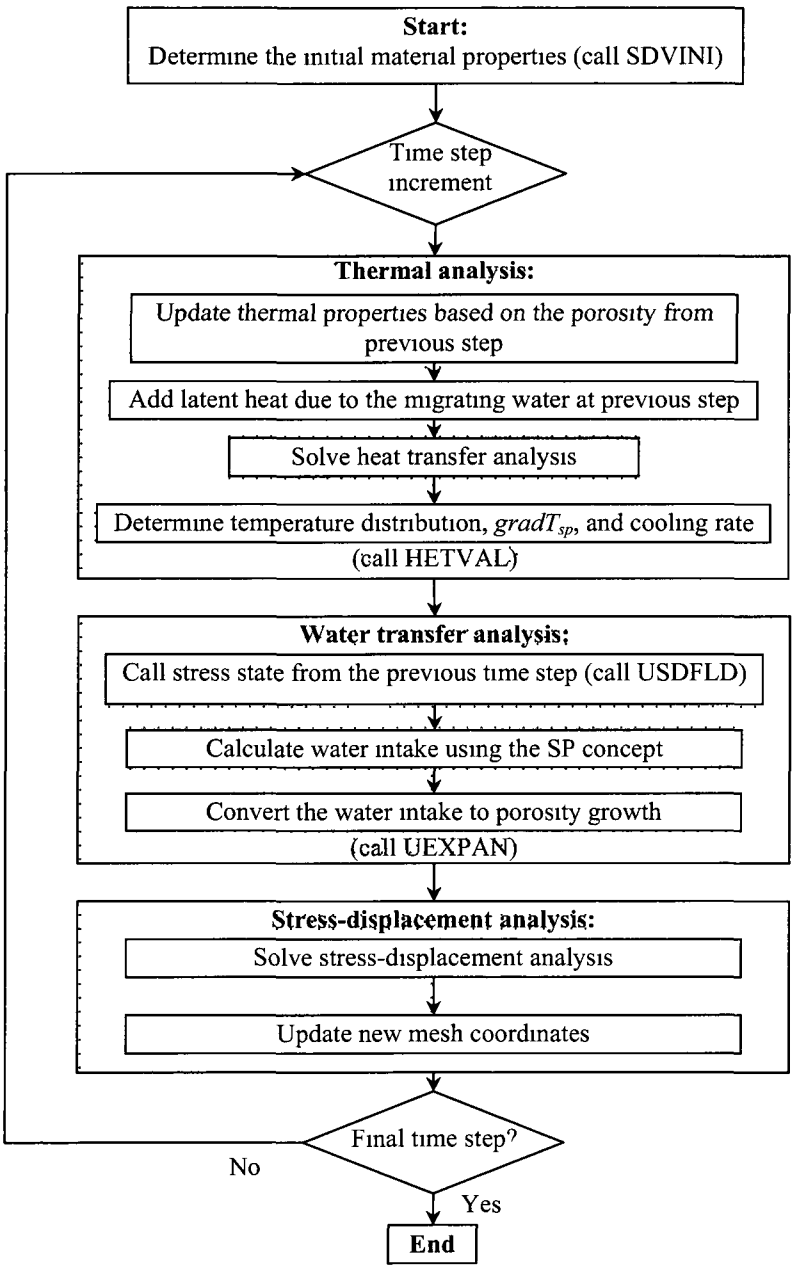

Figure 4 5 Flow chart of the user-defined subroutine which is composed of four components, SDVINI, HETVAL, USDFLD, and UEXPAN These components are discussed in the following text.

4.5 Basic assumptions for the developed frost-heave model

In order to solve this complex coupled process, several basic assumptions are necessary in this modeling study. They are summarized as follows:

- The soil is fully saturated (air does not exist);
- Pore-water pressure at the freezing front is zero;
- Moisture migration occurs only in the active system and unfrozen soil. The moisture migration in the frozen zone on the cold side of the active ice lens is negligible;
- The unfrozen soil remains fully saturated regardless of the moisture migration;
- Moisture migration occurs only in a liquid water form. The air phase and vapor transportation are not considered;
- The effect of salt exclusion is negligible;
- The effect of consolidation in unfrozen soil due to frost heave is negligible;
- The volume of soil particles remains constant during the freezing process;
- The effect of the freeze-thaw cycle is negligible; and
- Segregation-freezing point depression under loading is negligible.

4.6 Validation of the developed frost-heave model

The developed frost-heave model was verified against a series of step-freezing tests using *in-situ* Fairbanks silt. The soil sample was in 100mm diameter and 115mm in initial height. The boundary conditions are shown in Figure 4.6. Also, the initial and boundary conditions for the tests are summarized in Table 4.1.

A two-dimensional finite-element mesh was generated to simulate a series of step-freezing tests. The mesh consisted of a single column of 1mm-square elements. The vertical boundaries were adiabatic and no displacement was allowed in the horizontal direction. Therefore, this two-dimensional finite-element analysis was treated as a one-dimensional thermal-displacement analysis.

The soil sample was assumed to be fully saturated. The initial gravimetric water content was 0.325. The parameters for the unfrozen water characteristics curve (eq. [4.2]) were defined as: w_0 = 0.325 and w_u = 0.0325 (= 0.1 x w_0). The parameters for the frozen fringe were defined as: T_0 = 0 °C, T_{in} = -0.1 °C, T_{sp} = -0.15 °C, and T_s = -0.35°C.

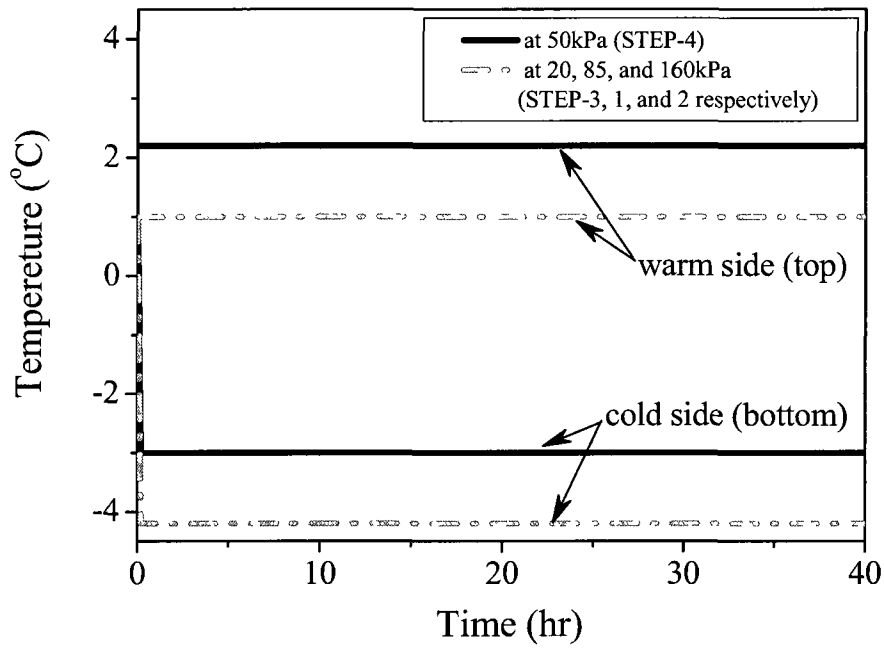

Figure 4.6 Boundary conditions for simulated processes.

Table 4.1 Boundary and initial conditions of simulations for a series of step-freezing tests

Tests	Applied pressure (kPa)	Cold side temperature (Bottom) (°C)	Warm side temperature (Top) (°C)	Initial temperature (°C)
STEP-1	85	-4 2	1	1 (=uniform)
STEP-2	160	-4 2	1	1 (=uniform)
STEP-3	20	-4 2	1	1 (=uniform)
STEP-4	50	-3	2.2	constant gradient (1°C bottom and 2 2°C top)

Volumetric heat capacities were calculated by eq. [4.19]. The values of thermal properties are listed in Table 4.2. Thermal conductivity of the soil sample was 1.19W/(m x °C) for the unfrozen state and 2.11W/(m x °C) for the frozen state. The thermal conductivities were obtained by the thermal conductivity needle-probe method (Kim 2003), and calibrated using the correlations of Johansen (1977). The initial dry density and initial porosity of soil were calculated to be 1451kg/m^3 and 0.472, respectively.

Table 4.2 Thermal properties (Johnston 1981)

	Density ρ (kg/m^3)	Mass heat capacity c (J/(kg x C))	Latent heat L_w (J/kg)
Fairbanks silt	2746*	800	
Water	1000	4200	333700
Ice	917	2090	333700
Air	1.25	1000	

* measured data (Kim 2003)

The SP values, which were obtained by the fitting method proposed in Chapter 3, were utilized for the simulations. The SP values are calculated by:

$$[4.22]\quad \mathrm{SP} = SP_m \times \left(\frac{\dot{T}_{sp} + \dot{T}_0}{\dot{T}_m + \dot{T}_0}\right)^2 \times \exp\left(1 - \left(\frac{\dot{T}_{sp} + \dot{T}_0}{\dot{T}_m + \dot{T}_0}\right)^2\right) \quad \left(0 \le \dot{T}_{sp} \le \mathrm{CRC}\right)$$

where SP_m = the maximum SP value; $\dot{T}_m$ = the cooling rate at which the maximum SP value occurs; $\dot{T}_0$ = the cooling rate required to satisfy the SP at the formation of the final ice lens; and CRC = the critical rate of cooling at which water intake starts. Figure 3.7 shows the relationship between the SP values and the cooling rate at different applied pressures. The parameters for eq. [4. 22] are summarized in Table 4.3.

In the simulations, it was assumed that all porosity growth was predominantly in the direction of the one-dimensional heat flow, and instead of the SP value, a no-overburden pressure condition was applied at certain applied pressures. Therefore, the total strain increment in this simulation consisted of the porosity growth only. However, an examination of multi-dimensional frost-heave problems indicated that the deformations in orthogonal directions will influence the extent of frost-heave development in the predominant direction. Additionally, multi-directional constraints will produce

stress within the soil matrix. Detailed aspects of the anisotropy and the mechanical analysis coupling will be presented in the next chapter.

Table 4.3 Input SP parameters for simulated step-freezing tests

Test	Applied pressure (kPa)	SP_m (10^{-5} mm^2/(sec x °C))	$\dot{T}_m$ (°C/hr)	$\dot{T}_0$ (°C/hr)	CRC (°C/hr)
STEP-1	85	13	0.017	0.015	0.045
STEP-2	160	4	0.0067	0.0028	0.015
STEP-3	20	40	0.0375	0.0575	0.125
STEP-4	50	18	0.03	0.025	0.075

The result of a step-freezing test at a 50kPa overburden pressure, STEP-4, is shown in Figure 4.7 as a simulation example. An initial, constant temperature gradient existed from 1°C at the bottom to 2.2°C at the top.

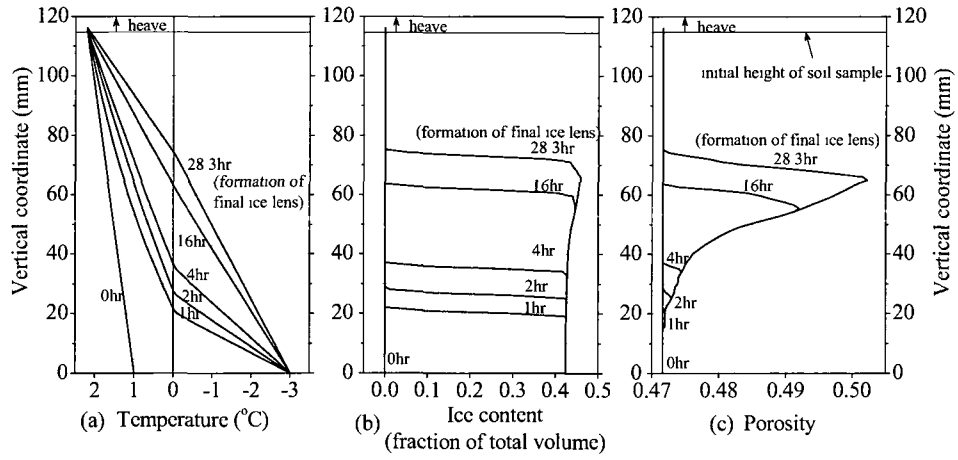

Figure 4.7 Freezing process for the STEP-4 step-freezing test at 50kPa applied pressure: (a) distribution of temperature; (b) ice content; and (c) porosity.

Figures 4.7a, b, and c show the variation of temperature, ice content, and porosity distributions, respectively, in the soil sample at different times during the step-freezing process. The results are given for the following instances (in hr): 0, 1, 2, 4, 16, and 28.3 (at the formation of the final ice lens).

Despite increasing ice content, porosity hardly grew at all during first 1hr despite a high cooling rate. When the freezing-front penetration was delayed due to latent heat release, porosity began to increase in response to *in-situ* heave. Once the cooling rate became smaller than the CRC, porosity increased rapidly. After 16 hrs the curve representing the porosity increase curved up into a bulb shape. The increasing trend in porosity distribution indicates the rhythmic ice-lens banding. The coordinate system was updated at each step, taking into account the heave by deforming the mesh.

The stress acting on the segregation heave zone is simply equal to the applied pressure in this one-dimensional analysis. The effect of pore-water pressure at the freezing front is negligible for the *in-situ* Fairbanks silt because of the high hydraulic conductivity of the unfrozen soil. Therefore, calculating the cooling rate according to eq. [4. 22] is most important in order to determine the SP value for *in-situ* Fairbanks silt.

The detailed analyses of segregation heave are shown in Figure 4.8. The variation of the simulated cooling rate is compared with that of the observed rate. The simulated values agreed well with the observed rates, as shown in Figure 4.8b. In response to the cooling rate, the simulated SP values are in agreement with the observed measurements during the growth of ice lenses (see Figure 4.8c).

The SP value started to increase at approximately 10hr in response to cooling having reached the CRC. The simulated SP value gradually increased as the cooling rate decreased. The maximum SP value was obtained at approximately 20hr. After the peak, the SP value began to decrease. The SP concept is not able to predict the final ice-lens growth, as discussed in Chapter 3. Beyond the formation of the final ice lens, the simulated segregation heave is overestimated (see Figure 4.8a).

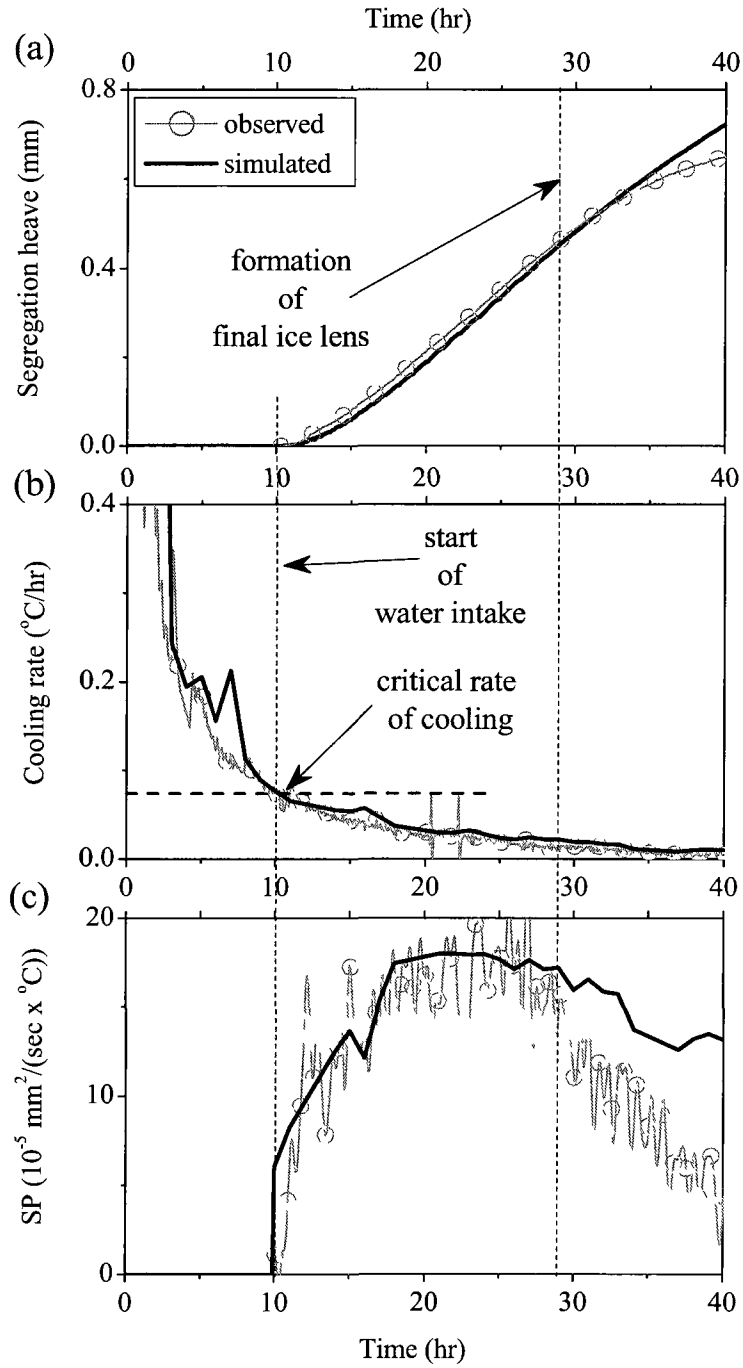

Figure 4.8 Freezing process for a step-freezing test at 50kPa applied pressure: (a) variation of segregation heave; (b) cooling rate; and (c) SP.

The segregation heave was successfully simulated at 50kPa applied pressure by considering the effect of cooling rate during the transient condition. The step-freezing tests at the other, different applied pressures were simulated as well. The variation of simulated total heaves appears to fit the observed ones in each step-freezing test (see Figure 4.9a). The amounts of simulated total heaves at the formation of final ice lens agreed well with those of observed heaves (see Figure 4.9b). The simulated total heave decreased with increasing applied pressure. The proposed fitting method was also valid for the effect of the applied pressure.

The significance of this simulation is that a trial-and-error approach was not needed to adjust input parameters in order to obtain a good match with the observed measurements. The verification results of a series of step-freezing tests confirm the validity of the developed frost-heave model and the SP values obtained by the proposed fitting method.

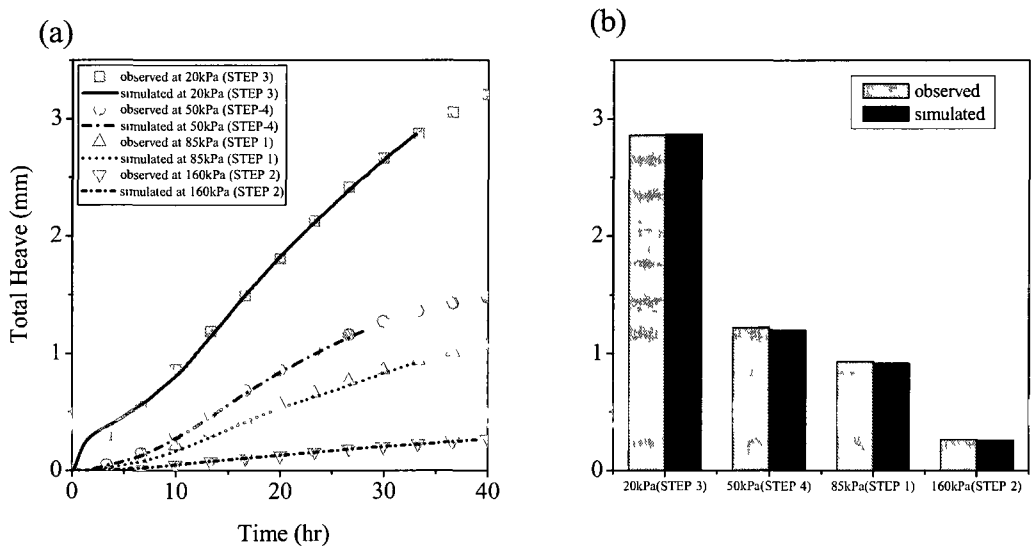

Figure 4.9 Comparison of total heave between simulated and observed for a series of step-freezing tests at different applied pressures: (a) variation; and (b) total heave amount at the formation of the final ice lens.

4.7 Summary and conclusion

A frost-heave model was developed by applying the SP concept. Significant findings from this study are:

1) The volume expansion is considered in the active system, which simulates the growing ice lens and the frozen fringe. Furthermore, the active system has two volumetric expansion zones: the *in-situ* freezing zone and the segregation freezing zone. The proposed model was able to reproduce the cooling rate of the segregation freezing zone.
2) The SP porosity growth function is created by considering the effects of cooling rate and applied pressures. The proposed fitting method can be applied to obtain the input SP values. The simulated SP values agreed well with the observed values in a series of step-freezing tests during transient freezing conditions.

The developed frost heave model, which applies the SP porosity growth function, simulated a series of step-freezing tests with remarkably accurate results. The model was implemented by applying a deforming mesh in a finite element code, ABAQUS. The developed frost-heave model will be used for multi-dimensional frost-heave simulations in the following chapters.

CHAPTER 5: EFFECTS OF RATE-DEPENDENT SOIL PROPERTIES

5.1 Introduction

A one-dimensional frost-heave model applying the segregation potential (SP) concept was successfully developed, and the results were presented in the previous chapter. However, many field problems are multi-dimensional. For instance, the frost-heave problem is one of the most clearly-foreseen issues for a buried chilled gas pipeline in an arctic region. Therefore, the developed one-dimensional frost-heave model has been expanded into a two-dimensional model.

In the following sections, the two-dimensional frost-heave model with SP porosity growth function is described first. Next, the developed frost-heave model is verified by the UAF frost-heave experiment and is used to predict the pipe heave of a well-documented Calgary frost-heave experiment. Finally, the numerical simulation investigates the influence of strain-rate-dependent soil properties and the induced stress field on frost-heave susceptibility.

5.2 Two-dimensional frost-heave modeling with SP porosity growth function

A complete analysis of two-dimensional frost-heave problems must be able to deal with the coupling of heat transfer, moisture transfer, and mechanical analysis. The coupled heat transfer, moisture transfer, and stress fields in the soil are mutually inclusive. The heat-transfer analysis determines the temperature distribution, and in turn determines how much the soil expands due to frost heave. The expansion of the soil changes the volumetric composition of the soil matrix. The results change thermal properties and affect the heat-transfer analysis in the subsequent time step. The stress field also changes as the soil heaves, which affects further frost heave.

The two-dimensional coupling process for frost-heave modeling takes several factors into consideration, such as:

1) Coupled processes of thermal condition and moisture transportation within frozen fringe and unfrozen soil;
2) The moving boundary associated with the penetration of a freezing front;
3) The mechanical behavior of frozen and unfrozen soil; and
4) The growth of ice lenses in an anisotropic fashion.

The coupled process of heat and moisture transfer for the developed frost-heave model is discussed first, to deal with factors 1) and 2). The constitutive model is described next, to deal with factors 3) and 4).

5.2.1 Coupled processes of heat and moisture transfer

5.2.1.1 Unfrozen water content

The unfrozen water content in frozen soils is part of the constitutive frost-heave model in order to solve the moving-boundary problem associated with the penetration of a freezing front. The unfrozen water content (w) and temperature (T) relationship has been defined in the previous chapter as:

[5.1] $$w = w_0 - \frac{w_0 - w_u}{T_0 - T_{in}} \times (T_0 - T)$$

where w_0 = unfrozen water content at the freezing point; w_u = residual unfrozen water content; T_0 = freezing temperature; and T_{in} = temperature at the end of *in-situ* freezing.

5.2.1.2 Heat Transfer

The heat conduction, considered as the only form of energy exchange in the soil, is described as:

[5.2] $$\left(C - L_i \rho_i \frac{\partial \theta_i}{\partial T}\right)\frac{\partial T}{\partial t} = C_{ap}\frac{\partial T}{\partial t} = \lambda\left(\frac{\partial^2 T}{\partial x^2} + \frac{\partial^2 T}{\partial y^2} + \frac{\partial^2 T}{\partial z^2}\right)$$

where C = volumetric heat capacity of soil; L = volumetric latent heat of soil; ρ_i = density of ice; θ_i = volumetric fraction of ice; T = temperature; C_{ap} = apparent volumetric heat capacity of soil; and λ = thermal conductivity.

The volumetric heat capacity, C, is defined as:

[5.3] $$C = \rho_s c_s \theta_s + \rho_w c_w \theta_w + \rho_i c_i \theta_i + \rho_a c_a \theta_a$$

where ρ = density; c = mass heat capacity; θ = volumetric fraction; and subscripts s, w, i, a = soil, water, ice, and air, respectively.

The thermal conductivity of the soil mixture is calculated by Johansen's method (Johansen 1977). The material properties used in this chapter are summarized in Table 5.1.

Table 5 1 Thermal properties of several example soils and materials

	Density ρ (kg/m^3)	Mass heat capacity c (J/(kg x C))	Latent heat L_w (J/kg)
Fairbanks silt	2746*	800	
Calgary silt	2700**	800	
Lanzhou sand	2650***	800	
Water	1000	4200	333700
Ice	917	2090	333700
Air	1 25	1000	

* Kim, 2003
** Northern Engineering Services Company Ltd, 1975
*** Zhu et al , 1988

5.2.1.3 SP porosity growth function

Frost heave can be described as a problem of moisture transfer to a growing ice lens past the layered frozen fringe and the unfrozen soil However, it is extremely difficult to measure the hydraulic conductivity over a range of temperatures within the frozen fringe To overcome the difficulty, Konrad and Morgenstern (1980, 1981) developed an empirical concept, called the SP concept A porosity growth function was successfully applied using the SP concept to numerical calculation in one dimension Volume strain increment is considered only in the active system, which simulates the frozen fringe and growing ice lens The active system has two volumetric expansion zones, namely the *in-situ* freezing zone and the segregation freezing zone, as shown in Figure 4 1 At each time step, the thermal solution gives the temperature distribution Using the result, the location of the active system is determined

Defining the water content at time t as $w(t)$, the porosity growth due to *in-situ* heave (Δn_{in}) at time $t+\Delta t$ can be expressed as

$$\Delta n_{in} = 0.09 \times \theta_w(t) \times \frac{w(t) - w(t+\Delta t)}{w(t)} \quad [5\,4]$$

where $\theta_w(t)$ = volumetric fraction of water at time t

The porosity growth due to segregation heave (Δn_{sp}) is calculated as

[5.5] $$\Delta n_{sp} = \frac{1.09 \times l_{sp} \times v}{A_{SP}} \times \Delta t$$

with

[5.6] $$v = \mathrm{SP} \times gradT_{sp}$$

where l_{sp} = the effective width of the segregation freezing zone in the element; v = the rate of migrating water; A_{sp} = the effective area of the segregation freezing zone; SP = segregation potential; and $gradT_{sp}$ = temperature gradient in the segregation freezing zone.

The $gradT_{sp}$ in eq. [5.6] is taken in direction *1* in Figure 5.1, which is the direction of heat flow and

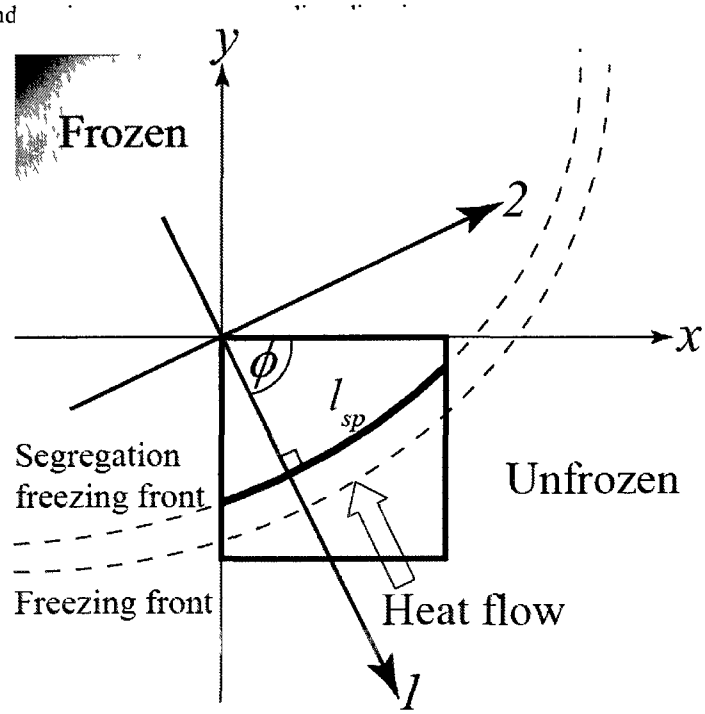

Figure 5.1 Coordinate system of an anisotropic heave element.

The $gradT_{sp}$ is determined as:

[5.7] $$gradT_{sp} = \sqrt{\left(\frac{\partial T}{\partial x}\right)^2 + \left(\frac{\partial T}{\partial y}\right)^2}$$

where $\partial T/\partial x$ and $\partial T/\partial y$ are temperature gradients along the horizontal and vertical directions, respectively.

The SP value is dependent on the following variables (Konrad and Morgenstern 1982a):

[5.8] $$\mathrm{SP} = \mathrm{SP}\left(\sigma_t, \dot{T}_{sp}, P_0\right)$$

where σ_t is the effective stress acting on the segregation freezing zone.

The effect of the effective stress is accounted for empirically as:

[5.9] $$\mathrm{SP} = \mathrm{SP}_0 \exp\left(-b \times \sigma_t\right)$$

where b = a soil constant; and SP_0 = the maximum value of segregation potential that occurs at zero external pressure.

$\dot{T}_{sp}$ is the cooling rate of the active system. When the SP concept is applied to predict frost heave in field problems, the SP values should be carefully obtained from laboratory frost-heave tests that have considered the dependency of SP upon cooling rate. The dependency on cooling rate has been misinterpreted by some practitioners. For instance, Svec (1989) suggested using the "critical" SP value as a measure of the highest possible value that could occur during the laboratory frost-heave test, regardless of the dependency upon the rate of cooling. The maximum SP value is approximately 30% higher than the SP value at the formation of the final ice lens at 20kPa applied pressure for the *in-situ* Fairbanks silt. Svec's interpretation potentially overestimates the amount of frost heave for engineering problems under relatively low effective stress (i.e. highway design or buried chilled gas pipeline). Since the cooling rate in the field is extremely slow, it is justified to predict frost heave in field conditions using the SP concept when the SP values are obtained from step-freezing tests at the formation of the final ice lens, which is initiated when the rate of cooling approaches zero. The SP values at the formation of the final ice lens in step-freezing tests have been used to predict field-scale pipeline experiments (e.g. Konrad and Morgenstern 1984; Carlson and Nixon 1988).

P_0 is the pore-water pressure at the freezing front. The SP value decreases with decreasing P_0. In most field conditions, P_0 is fairly small because of the small water- intake rate. It is reasonable to use the SP value determined by a laboratory frost-heave test in which the warm-plate temperature is close to the freezing point, because the thermal boundary condition creates a small P_0 value due to the short unfrozen soil sample.

The total porosity growth (Δn_t) is obtained by adding eqs. [5.4] and [5.5]:

[5.10] $$\Delta n_t = \Delta n_{in} + \Delta n_{sp}$$

5.2.2 Constitutive model for soil deformation

5.2.2.1 Mechanical modeling of frozen and unfrozen soil

Mechanical properties of frozen soils depend upon factors such as soil type, density, ice content, unfrozen water content, cryostructure, strain rate, etc. Frost heave has a strong dependency upon stress condition, and has been coupled with stress condition in frost-heave models. For instance, Coutts (1991) used linear elastic constitutive laws for both unfrozen and frozen soils. However, Coutts revealed that use of the linear elastic constitutive laws was unsuitable because unrealistic induced stresses lead to an excessive reduction of frost-heave susceptibility. Konrad and Shen (1996) approximated the ductile deformation of frozen soil by a bilinear elastic law to simulate the stress field. In this study, the bilinear elastic law is modified to consider the failure condition, as shown in Figure 5.2. Strain-rate dependency has also been accounted for. The details of mechanical properties will be discussed later.

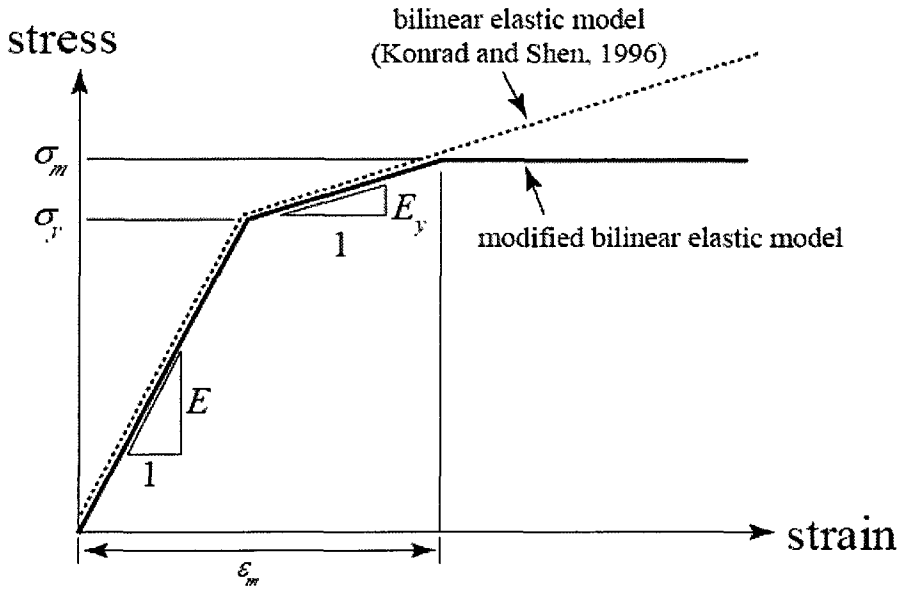

Figure 5.2 Modified bilinear stress-strain relationship for soil mechanical model (modified from Konrad and Shen 1996).

5.2.2.2 Anisotropic deformation of soil

The multi-dimensional concept of the total porosity growth tensor $(\Delta n_t)_{ij}$ is modeled as:

[5.11] $$(\Delta n_t)_{ij} = \Delta n_t \times a_{ij}$$

where

[5.12] $$a_{ij} = \begin{vmatrix} a_{11} & a_{12} & a_{13} \\ a_{21} & a_{22} & a_{23} \\ a_{31} & a_{32} & a_{33} \end{vmatrix} = \begin{vmatrix} \zeta & 0 & 0 \\ 0 & (1-\zeta)/2 & 0 \\ 0 & 0 & (1-\zeta)/2 \end{vmatrix}$$

The unit growth tensor (a_{ij}) in eq. [5.12] is specified such that direction *1* shown in Figure 5.1 is the major principal growth direction, which coincides with the heat flow direction. ζ is a dimensionless quantity. When $\zeta = 1/3$, porosity growth is isotropic, whereas one-dimensional porosity growth takes place when $\zeta = 1$. No induced stress was produced in the simulation of step-freezing tests, which was unconfined with $\zeta = 1$, as discussed in the previous chapter. However, multi-dimensional freezing and anisotropic porosity-growth processes in which displacements are restrained by boundary conditions will lead to an increase in stress and possibly restrain the SP porosity growth according to eq. [5.9].

The total strain increment ($\Delta\varepsilon$) is composed of two components: the modified bilinear elastic strain increment ($\Delta\varepsilon^{el}$) and the strain due to the total porosity growth ($\Delta\varepsilon^{sp}$) function, described as:

[5.13] $$\Delta\varepsilon = \Delta\varepsilon^{el} + \Delta\varepsilon^{sp}$$

The incremental isotropic modified bilinear strain-stress relationship is defined as:

[5.14] $$\Delta\varepsilon^{el} = [D] \cdot \Delta\sigma$$

where $[D]$ = elasticity tensor; and $\Delta\sigma$ = total stress.

The local coordinating system coincides with the direction of the heat flow as shown in Figure 5.1. Introducing the coordinating system with i = 1, 2, and 3 denoting the three principal axis directions eq. [5.13] is written as:

$$[5.15]\quad \begin{cases} \Delta\varepsilon_{11} = \dfrac{1}{E}\{\Delta\sigma_{11} - \mu(\Delta\sigma_{22} + \Delta\sigma_{33})\} + \zeta\Delta n_t \\ \Delta\varepsilon_{22} = \dfrac{1}{E}\{\Delta\sigma_{22} - \mu(\Delta\sigma_{11} + \Delta\sigma_{33})\} + \dfrac{1}{2}(1-\zeta)\Delta n_t \\ \Delta\varepsilon_{33} = \dfrac{1}{E}\{\Delta\sigma_{33} - \mu(\Delta\sigma_{11} + \Delta\sigma_{22})\} + \dfrac{1}{2}(1-\zeta)\Delta n_t \\ \Delta\varepsilon_{12} = \dfrac{2(1+\mu)}{E}\tau_{12} \\ \Delta\varepsilon_{23} = \dfrac{2(1+\mu)}{E}\tau_{23} \\ \Delta\varepsilon_{31} = \dfrac{2(1+\mu)}{E}\tau_{31} \end{cases}$$

where; τ = shear stress; E = Young's modulus; and μ = Poisson's ratio.

For plane strain problems, $\Delta\varepsilon_{33} = \Delta\varepsilon_{23} = \Delta\varepsilon_{31} = 0$, and

$$[5.16]\quad \Delta\sigma_{33} = \mu(\Delta\sigma_{11} + \Delta\sigma_{22}) - \frac{1}{2}(1-\zeta)\Delta n_t$$

Substituting eq. [5.16] into the first equations of eq. [5.15], the total strain increments for plane strain problems can be written as:

$$[5.17]\quad \begin{cases} \Delta\varepsilon_{11} = \dfrac{1-\mu^2}{E}\left(\Delta\sigma_{11} - \dfrac{\mu}{1-\mu}\Delta\sigma_{22}\right) + \left\{\zeta + \mu\dfrac{1}{2}(1-\zeta)\right\}\Delta n_t \\ \qquad = \dfrac{1}{E}(\Delta\sigma_{11} - \mu\times\Delta\sigma_{22}) + \left\{\xi + \mu\dfrac{1}{2}(1-\zeta)\right\}\Delta n_t \\ \Delta\varepsilon_{22} = \dfrac{1}{E}(\Delta\sigma_{22} - \mu\times\Delta\sigma_{11}) + \dfrac{1}{2}(1+\mu)(1-\zeta)\Delta n_t \\ \Delta\varepsilon_{12} = \dfrac{2(1+\mu)}{E}\tau_{12} \end{cases}$$

The first term on the right-hand side of each equation in eq. [5.17] is a bilinear elastic strain increment, and the second term is due to porosity growth. The strain increment due to porosity growth is described as:

$$[5.18]\quad \begin{Bmatrix} \Delta\varepsilon_{11} \\ \Delta\varepsilon_{22} \\ \Delta\varepsilon_{12} \end{Bmatrix} = \begin{Bmatrix} \zeta + \mu\dfrac{1}{2}(1-\zeta) \\ \dfrac{1}{2}(1+\mu)(1-\zeta) \\ 0 \end{Bmatrix}\Delta n_t$$

The component of the strain increment due to porosity growth in the global x, y coordinating system (plane strain) is obtained by the following transformation rule:

$$\begin{Bmatrix} \Delta\varepsilon_x^{sp} \\ \Delta\varepsilon_y^{sp} \\ \Delta\varepsilon_{xy}^{sp} \end{Bmatrix} = \begin{vmatrix} \cos^2\phi & \sin^2\phi & -2\sin\phi\cos\phi \\ \sin^2\phi & \cos^2\phi & 2\sin\phi\cos\phi \\ \sin\phi\cos\phi & -\sin\phi\cos\phi & \cos^2\phi-\sin^2\phi \end{vmatrix} \begin{Bmatrix} \Delta\varepsilon_{11}^{sp} \\ \Delta\varepsilon_{22}^{sp} \\ \Delta\varepsilon_{12}^{sp} \end{Bmatrix}$$

[5.19]

$$= \begin{Bmatrix} \cos^2\phi\times\left\{\zeta+\mu\frac{1}{2}(1-\zeta)\right\}+\sin^2\phi\times\frac{1}{2}(1+\mu)(1-\zeta) \\ \sin^2\phi\times\left\{\zeta+\mu\frac{1}{2}(1-\zeta)\right\}+\cos^2\phi\times\frac{1}{2}(1+\mu)(1-\zeta) \\ \frac{1}{2}\sin\phi\cos\phi(3\zeta-1) \end{Bmatrix}\Delta n_t$$

where ϕ = the angle the x axis makes with the heat flow direction 1 as defined in Figure 5.1.

5.3 Verification for full-scale frost-heave experiments

One of the major sources of induced load to the pipelines is the differential heave near the interface between two types of soils with different frost-heave susceptibility or between frozen and unfrozen soils. In order to understand the complex pipeline-freezing soil interaction due to frost heave, it is reasonable to examine and predict the frost-heave amount in two dimensions at a place where the influence of the pipeline in frozen ground is negligible. Such a place is an area free of the influence of pipe restraint, and hence is known as the free-field area (Figure 5.3).

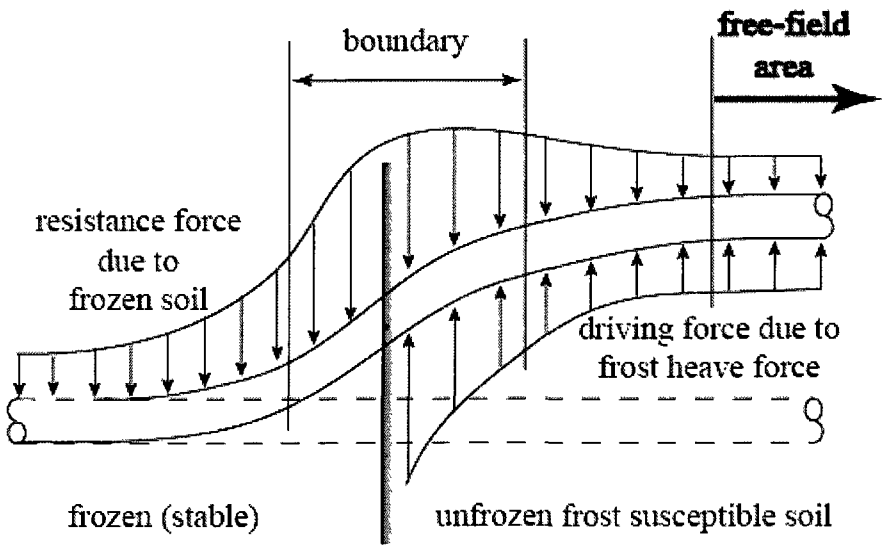

Figure 5.3 Differential heaves along a pipeline (Kim et al. 2008).

The developed two-dimensional frost heave model was verified using two well-documented frost-heave field experiments, which are the UAF and Calgary frost-heave experiments, respectively.

5.3.1 UAF frost-heave experiment

Huang et al. (2004) has described the UAF frost-heave experiment facility in detail. As indicated by Huang et al. (2004), a 0.914m diameter, 105m long chilled pipeline with X65 grade and 9mm wall thickness was used. The first 30m of the pipeline were in a shallower supra-permafrost-table area and the remaining 75m were in unfrozen ground, which consisted of a deeper supra-permafrost-table area. The pipe was covered with approximately 0.9m of *in-situ* soil. The reference elevation was defined as 1.00m. Thermal fence A (TFA) was located 58m from the inlet riser, approximately 30m from the frozen-unfrozen boundary, and was assumed to be in the free-field area. There were six thermistor strings with depths ranging from 0.8 to -7.3m in elevation. The thermistor spacing varied between 0.25 and 1.0m. A finer spacing was used as the thermistor strings became closer to the pipeline (Figure 5.4).

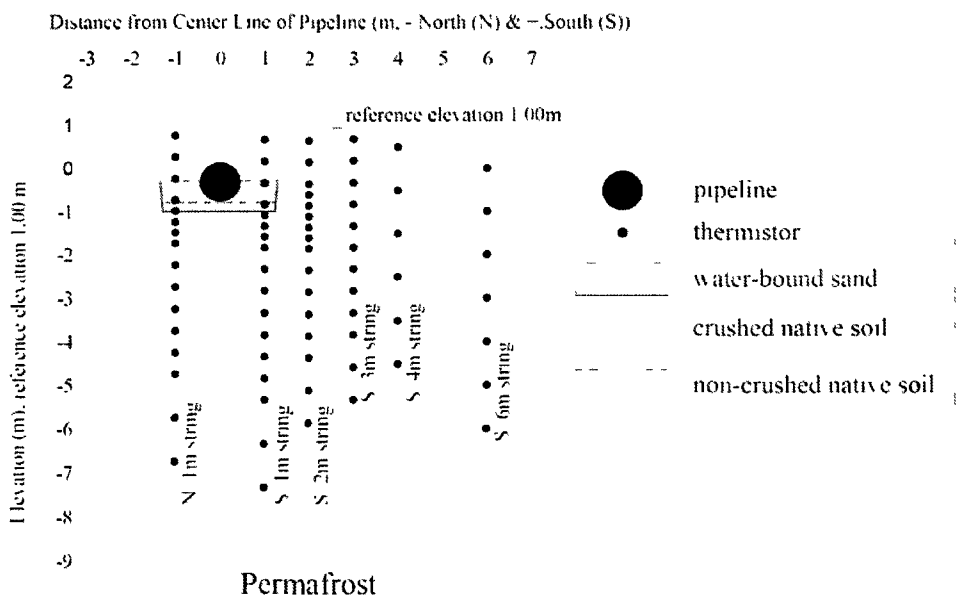

Figure 5.4 Cross-section of TFA showing the placement of thermistor beads and the generalized backfill materials (modified from Bray 2003).

Additional thermistors were placed on the top of the pipeline. The thermistor 65m from the inlet riser, which was the closest to TFA, was used as the reference pipeline temperature for TFA. Pipeline movement was monitored by 28 heave rods (HRs) welded directly to the top of the pipeline. In this study, the vertical displacement of the pipeline was determined by HR-25, which was located at 58.805m from the inlet riser. The depth to the groundwater table was monitored by an open standpipe near TFA.

5.3.1.1 Geometry

The geometry and boundary conditions are illustrated in Figure 5.5a. The pipe was buried with 0.9m overburden pressure. The frost bulb was observed 3.5m vertically and 4m laterally from the center of the pipeline at TFA through the operation (Huang et al. 2004). The dimensions of the soil region were modeled as 15m x 20m, an area 4 times greater than the area of frost bulb influence.

Figure 5.5b shows the finite-element discretization of the simulation. The model consisted of 864 elements. An implicit scheme was used for the time step.

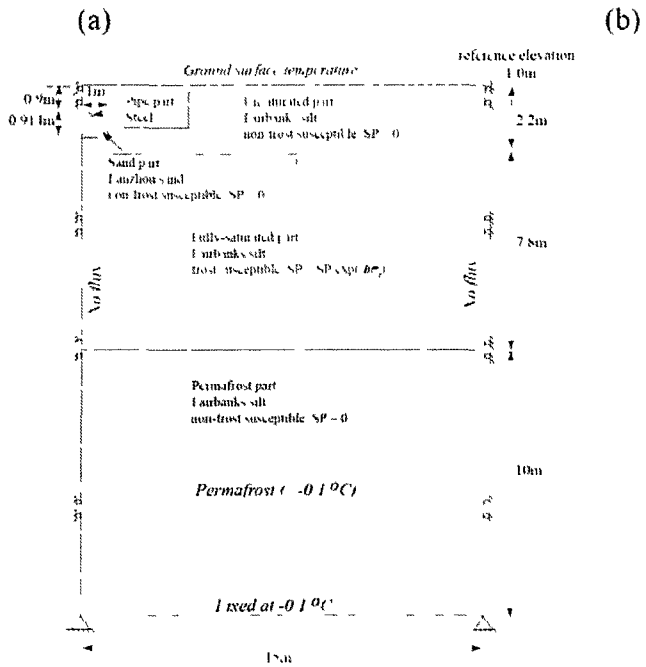

Figure 5.5 (a) Initial and boundary conditions and (b) finite-element mesh of the UAF frost-heave experiment.

Initial dry densities of the Fairbanks silt and Lanzhou sand were calculated as 1308 and 1894kg/m^3, respectively The unsaturated, permafrost, and sand layers in the mesh were modeled as non-frost-susceptible The thermal properties of unsaturated parts were calculated by eq [5 3] using w_0 = 0 318 and w_u = 0 07 The properties of the trench fraction were calculated using w_0 = 0 14 and w_u = 0 01, and those of the permafrost and fully-saturated fractions were calculated using w_0 = 0 4 and w_u = 0 07 The *in-situ* freezing temperature and freezing temperature for soils were defined as -0 1 and 0°C, respectively The calculated thermal properties for the simulation of the UAF frost-heave experiment are summarized in Table 5 2

Table 5 2 Thermal properties for simulation of the UAF frost-heave experiment

Part	Volumetric heat capacity C (kJ/(m^3 x °C))		Thermal conductivity λ (W/(m x °C))		Phase change temperature (°C)	
	Unfrozen	Frozen	Unfrozen	Frozen	Freezing	In-situ freezing
Unsaturated	2762	2094	1 38	2 17	0	-0 1
Fully saturated and Permafrost	3245	2260	1 52	2 74	0	-0 1
Sand	2629	2110	1 40	2 17	0	-0 1
Pipe	3520		40			

A series of step-freezing tests were conducted using undisturbed soil samples as described in previous chapters The SP values were determined to be SP_0 = 41 3 x 10^5 mm^2/(sec x °C) and b = 0 0156kPa^{-1} In addition, Nixon (2003) reported SP characteristics for the Fairbanks frost-heave experiment, which was conducted at the same site as that used by the UAF frost-heave experiment in the 1970s Variations of the SP values were reported because of variations in the clay fractions of different undisturbed soil samples obtained at the site Nixon (2003) reported values of SP_0 = 262 x 10^5 mm^2/(sec x °C) and b = 0 02596kPa^{-1} These results are shown in Figure 5 6 Nixon's SP values were used in preliminary frost-heave simulations (Kim et al 2008) In order to allow comparison between the preliminary simulations, Nixon's SP values were utilized for the simulation Furthermore, Nixon's SP values will introduce a more conservative estimate of the frost-heave amount than would the step-freezing tests SP values

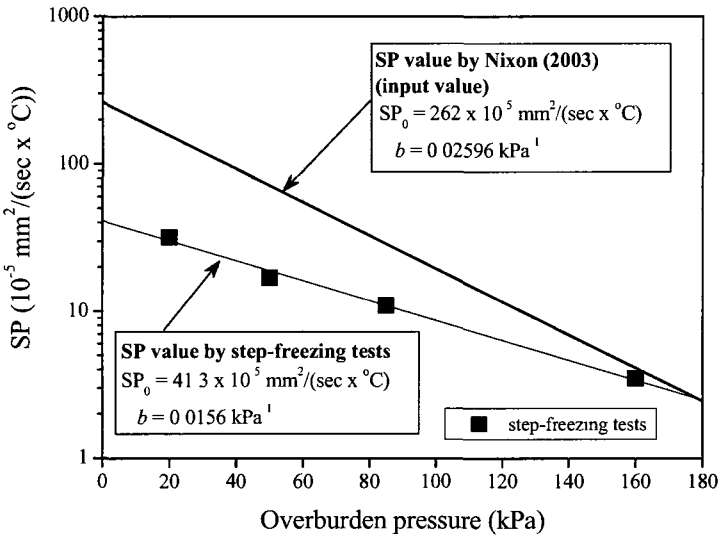

Figure 5.6 Segregation potential of Fairbanks silt.

5.3.1.2 Boundary conditions and initial conditions

The pipe temperature throughout the operation averaged -8.5°C, but it fluctuated somewhat with time; therefore, a step temperature was applied to the numerical simulation. The phases were divided into 60-day intervals. The average temperature during each phase was defined as input pipeline temperature as shown in Figure 5.7.

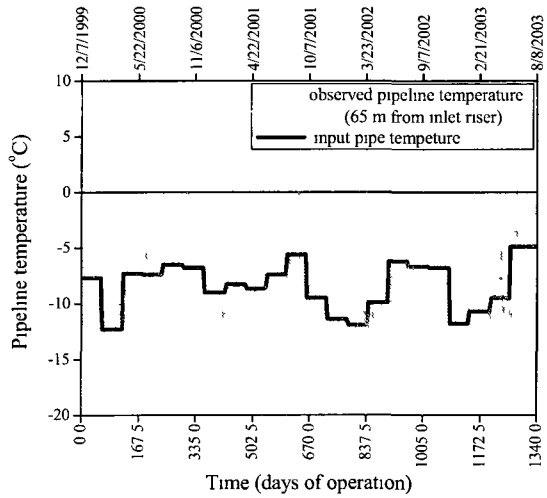

Figure 5.7 History of the input pipe temperature (Huang et al. 2004).

The air temperature was converted to the ground-surface temperature by using an n-factor. Zero heat flux was applied at the vertical boundary, which was 15m from the pipe center. Horizontal displacements are not allowed along vertical sides, while the bottom is fixed in both horizontal and vertical directions. Air pressure within the pipeline was assumed to be 1.4MPa based on the field data (Kim et al. 2005).

The initial ground temperature was created by the following procedure. First, a temperature of +1°C was applied to all nodes from the ground surface to 10m deep. The temperature of the bottom horizontal boundary (20m below the ground surface) was fixed at -0.1°C. The same temperature, -0.1°C, was also applied to all nodes below 10m to simulate the existence of permafrost. Then, the model was executed without pipe temperature input for 3 years. Finally, -1°C was applied to an area 1m wide and 1.8m deep at the center, to simulate the condition of excavating the pipe trench during wintertime.

Groundwater levels were measured starting in the year 2000, which was the second winter. Measurements of the first year cycle were extrapolated from the third-year-cycle data. Figure 5.8 shows the variation of the groundwater table and the freezing-front penetration at 6m from the center of the pipe (TFA-S6). In the early part of the summers, the groundwater level showed an abrupt change. The abrupt changes ended when the frozen layer disappeared. The temperature data indicate that the aquifer was confined by the frozen layer during winter. When the segregation freezing zone was below the groundwater table, calculation of segregation heave started. The groundwater table data were also used to calculate the overburden pressure of soil for numerical simulation. The soil pressure acted on the segregation freezing zone; thus, σ_l was composed of two components: (1) induced soil stress due to frost heave at the previous time step (σ_{sp}), and (2) overburden pressure of the soil above the segregation freezing zone (σ_{ov}). The overburden pressure was assumed to be a function of freezing depth, bulk and buoyant weights of soil, and groundwater table elevation. The overburden pressure is evaluated as following:

$$
\begin{cases}
\text{When } X_s(t) < W(t) \\
\sigma_{ev}(t) = \gamma_t(t) \times X(t) \\
\\
\text{When } X_s(t) \geq W(t) \\
\sigma_{ev}(t) = \gamma_t(t) \times W(t) + \gamma_b(t) \times (X(t) - W(t)) \\
\\
\gamma_t(t) = \gamma_d(t) \times (1 + w(t)) \\
\gamma_b(t) = \gamma_d(t) \times (1 + w(t)) - r_w
\end{cases}
\qquad [5.20]
$$

where $W(t)$ = the depth of the groundwater table from the ground surface; $X_s(t)$ = the depth of the segregation freezing zone from the ground surface; $\gamma_d(t)$ = dry soil unit weight; γ_w = water unit weight; $\gamma_t(t)$ = bulk soil unit weight; and $\gamma_b(t)$ = buoyant soil unit weight.

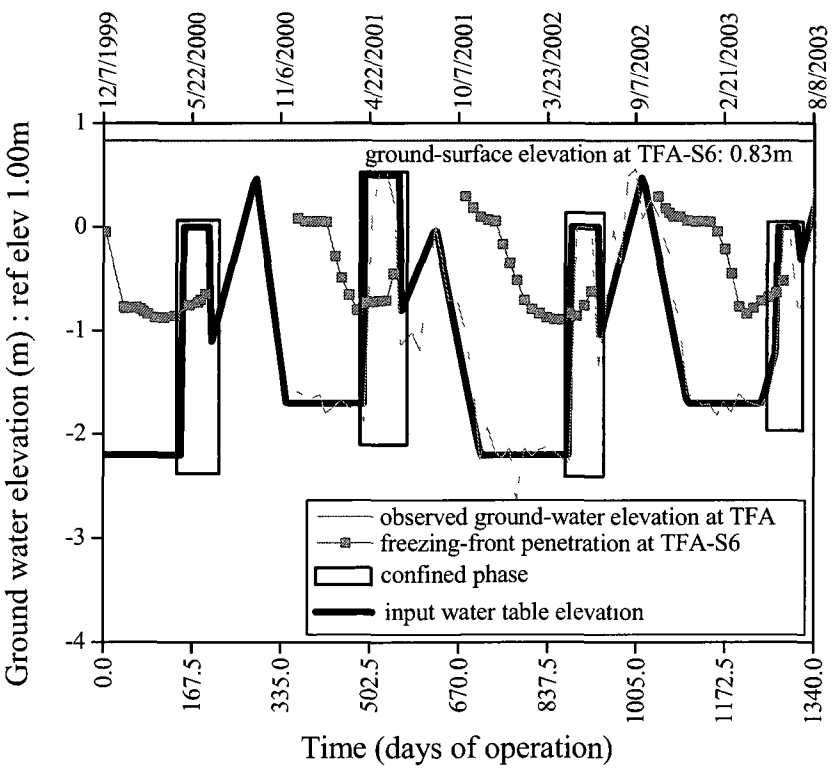

Figure 5.8 History of the groundwater table elevation (Bray 2003).

5.3.1.3 Mechanical properties

Fairbanks silt:

The strain-rate-dependent frozen-soil properties have been considered in frost heave models (e.g. Shen and Ladanyi 1991; Selvadurai and Shinde 1993; Selvadurai et al. 1999b). Konrad and Shen (1996) simply applied long-term strength as yield strength. For the proposed bilinear elastic model, long-term creep strength was applied to the peak strength (σ_m). The strain rate of the UAF frost-heave experiment was defined first. The incremental frost heave per freezing-front penetration is illustrated in Figure 5.9.

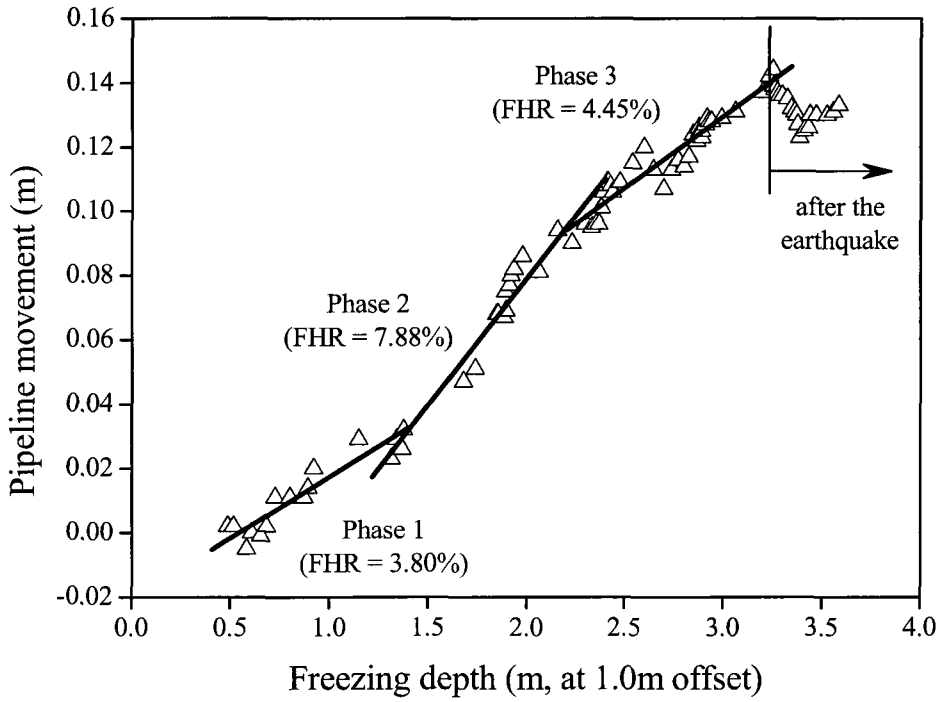

Figure 5.9 Observed pipeline movement vs. freezing depth of UAF frost-heave experiment (Bray 2003).

The ratio of these two quantities was defined as frost-heave ratio (FHR). Field observations indicated that a large amount of settlement occurred after day 1062, possibly caused by an M7.9 earthquake in interior Alaska on November 3, 2002 (Huang et al. 2004). To avoid the influence of this

unusual event, three phases were defined that were free from the effect of the earthquake. Then, the average fractional increase of the soil volume during each phase of the freezing process was defined as the strain rate of the UAF frost-heave experiment; the strain rates are summarized in Table 5.3.

Table 5.3 Field strain rates of the UAF frost-heave experiments

	Days of operation		FHR	Strain rate
	Starting	Ending	(%)	(1/sec)
Phase1	0	162	3.80	2.71E-09
Phase2	162	507	7.88	2.64E-09
Phase3	507	1060	4.45	9.31E-10

The strain-rate-dependent mechanical properties of remolded Fairbanks silt were studied from a series of constant-strain-rate uniaxial compressive tests (Zhu and Carbee 1987). The series of tests were conducted under different strain rates (from 6.2×10^{-2} to 1.1×10^{-6} 1/sec), temperatures (from -0.5 to -10°C), and dry density (from 1080 to 1430kg/cm^3). The Fairbanks silt used in the study was obtained from the CRREL permafrost tunnel, Fox, Alaska. Bray (2008) studied the strain-rate dependency using a series of relaxation tests to simulate a range of low strain rates (from 1.1×10^{-4} to 1.1×10^{-12} 1/sec). Undisturbed and remolded samples from the CRREL permafrost tunnel were used for the relaxation tests. The remolded samples (RMs) were created by reproducing the medium-density (1180 to 1230kg/cm^3) samples made by Zhu and Carbee (1987). The RMs and medium-density samples, which did not have micro-lenticular cryostructure, were used for the input parameters.

Figure 5.10 shows typical strain rate vs. creep strength (σ_r) curves at various temperatures for the RMs from relaxation tests. The creep strength obviously increased with decreasing test temperatures. The logarithmic plots of strain rate vs. creep strength showed a change in slope at a strain rate of approximately 1.1×10^{-6} 1/sec. The strain rate at the transition point was described as the critical strain rate of the RM (Bray 2008). Strain rates above the critical strain rate are considered "short-term strength", and below this value are termed "long-term strength".

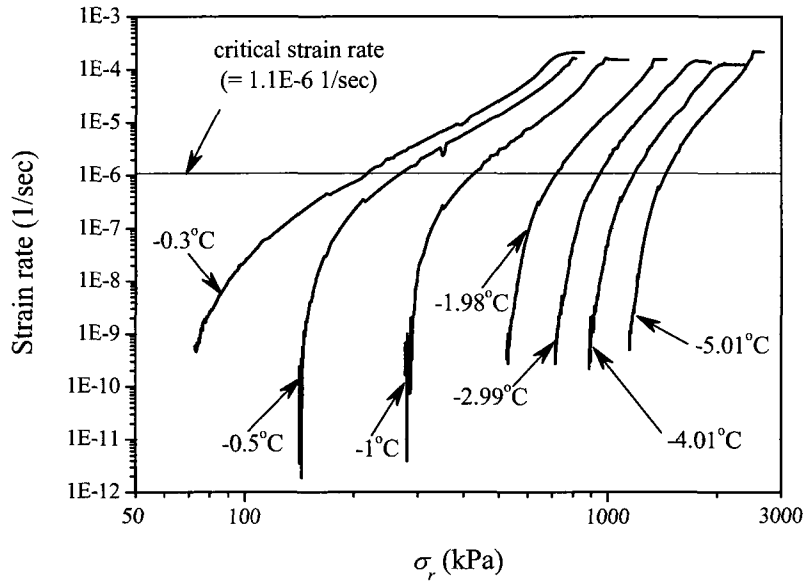

Figure 5.10 Relationship between strain rate and creep strength for RMs at various temperatures (Bray 2008).

Figure 5.11 shows the relaxation data plotted as strain rate vs. creep strength for RM, undisturbed vertical micro-lenticular (vml), and undisturbed horizontal micro-lenticular (hml) samples at -1°C. The curves suggest that very similar strain rates exist at a given creep strength above the critical strain rate; however, the undisturbed samples with micro-lenticular cryostructure showed faster strain rates at a given stress than did the RM below the critical strain rate. Bray (2008) interpreted the difference between the data curves representing RMs and undisturbed samples as being due to the existence of micro-lenticular cryostructure. Because of no micro-lenticular cryostructure exists in an RM, friction of soil particles significantly dominated RM creep strength below the critical strain rate. Therefore, the transition into the steeper section of the RM curve could be interpreted to represent the activation of a long-term resistance caused by soil particles. The section below the critical strain rate was defined as a "damped creep stage".

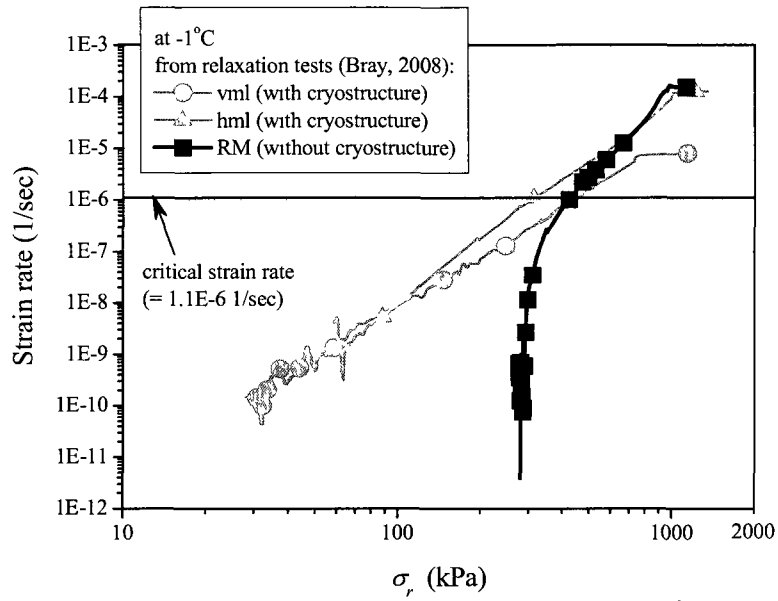

Figure 5.11 Relationship between strain rate and creep strength for RMs at -1°C and comparison with vml and hml samples at -1°C (Bray 2008).

The long-term creep strength of a frozen soil without micro-lenticular cryostructure could be considerably higher than that of a frozen soil with micro-lenticular cryostructure. For instance, in the UAF frost-heave experiment, a strain-rate two or three orders of magnitude lower than the critical strain rate was induced in the frozen soil during the process of frost heave, as shown in Table 5.3. Furthermore, the frozen soil around the frozen fringe will exhibit a micro-lenticular crystructure due to frost heave.

Bray (2008) created the power law relation between strain rate ($\dot{\varepsilon}$) and creep strength (σ_r) for RMs using the data of creep strength above the critical strain rate, excluding the damped creep stage as:

[5.21] $\dot{\varepsilon} = Y \times \sigma_r^{\ s}$

where Y and s = empirical coefficients. The values of eq. [5.21] for RMs at various temperatures are summarized in Table 5.4.

Table 5.4 Creep rate coefficients for the RM samples derived from relaxation tests (Bray 2008)

No.	T (°C)	σ_{range} (kPa)	s	Y (sec^{-1} x kPa^{-s})	R^2	$\sigma_{full\ range}$ (kPa)
51	-1	400-983	5.4330	6.133E-21	0.995	204-1327.2
52	-1.98	700-1613	7.1053	7.072E-27	0.992	526.7-1613.6
55	-2.99	900-1700	8.3914	1.463E-31	0.958	714.8-1909.3
56	-0.5	200-750	4.2462	5.189E-17	0.992	141.6-1044.8
58	-0.3	150-822	3.8380	1.216E-15	0.994	72.7-953.9
61	-4.01	1100-2371	8.2672	6.067E-32	0.982	888.5-2371.2
62	-5.01	1400-2588	8.6396	8.781E-34	0.991	1146.8-2749.8

note: Equation 5.21, $\varepsilon = Y \sigma_r^{\ s}$. T is temperature in degrees C, σ_{range} is the stress range from which s and Y were determined from relaxation test, s and Y are empirical coefficients, and $\sigma_{full\ range}$ is the total range of applied stress experienced by the sample over the course of the relaxation test.

Figure 5.12 shows the relationship between strain rate and creep strength (σ_r) from relaxation tests (creep tests) and peak strength (σ_m) from constant-strain-rate uniaxial compressive tests (strength tests) at -1°C. The trend of strain rate vs. σ_r (or σ_m) plots from these two types of tests showed a good similarity at higher-stress conditions. For instance, the parameters in eq. [5.21] had the values of s = 5.4330, $Y = 6.133 \times 10^{-21}$ sec^{-1} x kPa^{-s}, and $R^2 = 0.995$ by power-law regression analysis for relaxation tests, and s = 5.0911, $Y = 7.3736 \times 10^{-20}$ sec^{-1} x kPa^{-s}, and $R^2 = 0.9508$ for uniaxial compressive tests. As shown in Table 5.3, strain rates of the UAF frost-heave experiments are below the critical strain rate, such a low strain rate is extremely difficult to reproduce by constant-strain-rate uniaxial compressive tests. Therefore, the creep strengths of the RMs determined using relaxation tests were applied to the peak strengths of the proposed bilinear elastic model to simulate the UAF frost-heave experiment.

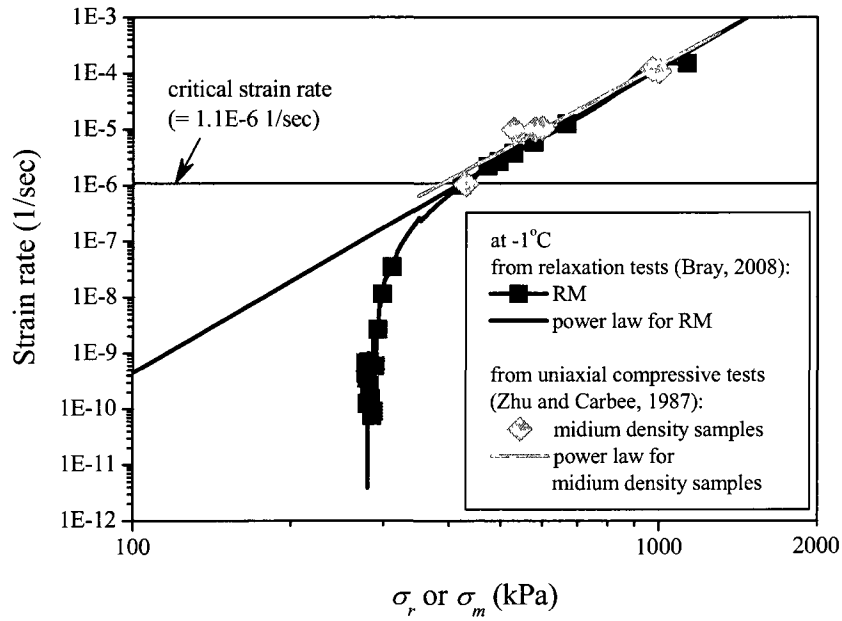

Figure 5.12 Power law relationships between strain rate and stress based on relaxation and uniaxial compressive tests at -1°C.

As reported by Sayles and Haines (1974), the temperature dependency of the peak strength at certain strain rates can be determined by:

[5.22] $\sigma_m = \sigma_0(-T)^m$

where σ_0 and m = empirical coefficients.

The peak strengths for each phase and the critical strain rate were calculated by eq. [5.21]. A plot of log peak strengths vs. log (-T) is shown in Figure 5.13, and the values for eq. [5.22] are summarized in Table 5.5. The calculated peak strengths were used to determine the mechanical properties of fully-saturated permafrost in the simulation mesh. When the temperature was warmer than -0.1°C, the peak strength at -0.1°C was used for the value of Fairbanks silt.

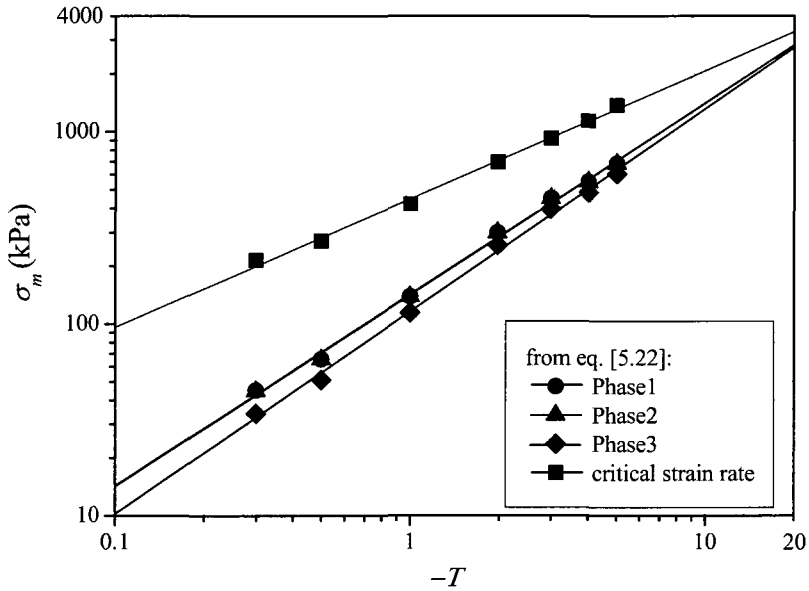

Figure 5.13 A plot of log σ_m vs. log (-T) of Fairbanks silt for various strain rates.

Table 5.5 Values in Equation 5.22 for Fairbanks silt

	Strain rate (1/sec)	σ_0 (kPa)	m	R^2
In Equation 5.22:				
Phase1	2.71E-09 (= $\dot{\varepsilon}_{UAF1}$)	142.27	0.996	0.997
Phase2	2.64E-09 (= $\dot{\varepsilon}_{UAF2}$)	141.55	0.998	0.997
Phase3	9.31E-10 (= $\dot{\varepsilon}_{UAF3}$)	116.02	1.055	0.997
Critical strain rate	1.10E-06 (= $\dot{\varepsilon}_{critical}$)	447.00	0.667	0.996

Zhu and Carbee (1987) reported that the saturation degree might significantly influence the peak strength of Fairbanks silt. For instance, the peak strengths of the partially-saturated samples were approximately 7-20% less than those of fully-saturated soils, even though the degree of saturation for the partially-saturated soil was only 3-4% less than for the fully-saturated soil. The unsaturated zone

of the mesh was assumed to represent 78% saturation. The peak strength for the unsaturated soil was modeled as 50% of the fully-saturated zone.

The yield stress (σ_y) can be simply estimated in terms of dry density (Zhu and Carbee 1987) as:

[5.23] $$\sigma_y = (2.150 - 0.00115 \times \rho_d) \times \sigma_m$$

The initial dry density value of 1308kg/m^3 (=*const*) was applied to eq. [5.23].

The failure strain (ε_m) for the medium-density samples (Zhu and Carbee 1987) was 0.0913; this value was applied to the model.

The 50% peak strength modulus (E_{50}) at the critical strain rate was used as Young's modulus (E). Young's modulus of unfrozen Fairbanks silt was assumed to be constant and equal to 11.2MPa, which was a typical value for silts (e.g. Shen and Ladanyi 1991; Konrad and Shen 1996; Selvadurai et al. 1999b). Zhu and Carbee (1987) reported the temperature-dependent E_{50} of the Fairbanks silt at the critical strain rate as:

[5.24] $$E = E_{50} = E_{50}' \times (1.1 \times 10^{-3})^{0.122} \times (-T)^{0.624}$$

where E_{50}' = 740MPa for the medium-density samples.

When Young's modulus of frozen Fairbanks silt determined by eq. [5.24] was smaller than 11.2MPa, the value was assumed to be equal to 11.2MPa. Poisson's ratio was taken as $\mu = 0.3$ for both the frozen and the unfrozen cases.

Sand:

The strain rate and temperature dependencies of Lanzhou sand were reported by Zhu et al. (1988). Lanzhou sand showed a change in slope at a strain rate of approximately 1.0x10^{-6} 1/sec of logarithmic plots of strain rate vs. stress, similar to Fairbanks silt. The properties below 1.0x10^{-6} 1/sec became constant and were defined as long-term properties. The long-term properties of Lanzhou sand were used for the trench part of the simulation mesh.

The long-term yield strength and elastic modulus depending upon temperature were reported as:

[5.25] $$\begin{cases} \sigma_y = 3800 \times (-T)^{0.466} \times (0.33 \times 10^{-2})^{0.204 + 0.0066 \times T} \\ E = 44 \times (-T)^{0.684} \end{cases}$$

where σ_y was in kPa, and E was in MPa.

When the temperature was warmer than -0.1°C, the peak strength of Lanzhou sand at -0.1°C was used. Young's modulus of unfrozen Lanzhou sand was assumed to be constant and equal to

20MPa. When Young's modulus of frozen Lanzhou sand determined by eq. [5.25] was smaller than 20MPa, the value was assumed to be equal to 20MPa.

The post-yield modulus of Lanzhou sand was modeled as zero. Poisson's ratio was taken as $\mu = 0.3$ for both the frozen and the unfrozen case.

Steel:

The mechanical properties of steel (Kim 2003) were specified as:

$$[5.26] \quad \begin{cases} \sigma_y = 482\ \text{MPa} \\ E = 206\ \text{GPa} \end{cases}$$

The post-yield modulus of steel was modeled as zero. Poisson's ratio was taken as $\mu = 0.3$.

5.3.1.4 Effect of the change of anisotropic expansion parameter

Although it is known that the ice lens grows mostly perpendicular to the direction of heat flow, the anisotropic expansion parameter ζ is difficult to determine. Therefore, a sensitivity analysis was conducted to evaluate how the developed model responds to the variation of this parameter. The concept of Rosenblueth's method was applied (Rosenblueth 1975).

The value of $\zeta = 0.75$ was adopted as the mean value. The coefficient of variation of the anisotropic expansion parameter (COV_ζ) was assumed to be 20%, and the standard deviation was calculated as 0.15.

The strain rate of Phase 2 in Table 5.3 represents the field strain used to calculate the peak strength. Figure 5.14 shows the comparison between the simulated and observed pipeline movement caused by the M7.9 earthquake. During freezing in the first winter (132.75 days), the simulated heaves were very close to each other regardless of the expansion parameters used. The simulated heave curves started to separate after the first winter. h^+ is the simulated total heave increased by one standard deviation ($\zeta = 0.9$), and h^- is decreased by one standard deviation ($\zeta = 0.6$). h^+ and h^- were calculated as 0.145m and 0.135m, respectively. The coefficient of variation of the simulated total heave (COV_h) was calculated as:

$$[5.27] \quad \text{COV}_h = \frac{h^+ - h^-}{h^+ + h^-} \times 100\%$$

If the COV_h is larger than the COV_ζ, the developed model will be mathematically unstable to the effect of the anisotropic expansion parameter. The COV_h was calculated as 3.6%, which was six times smaller than the COV_ζ of 20%. The uncertainty in the value of the anisotropic expansion

parameter was reflected in the different simulated total heaves, but the possible inaccuracy of the parameter did not amplify the error in the response. The result in the model response was mathematically stable. Although further study of the anisotripic frost heave is required, ζ was empirically identified as 0.9 here for Fairbanks silt in the UAF frost-heave experiment.

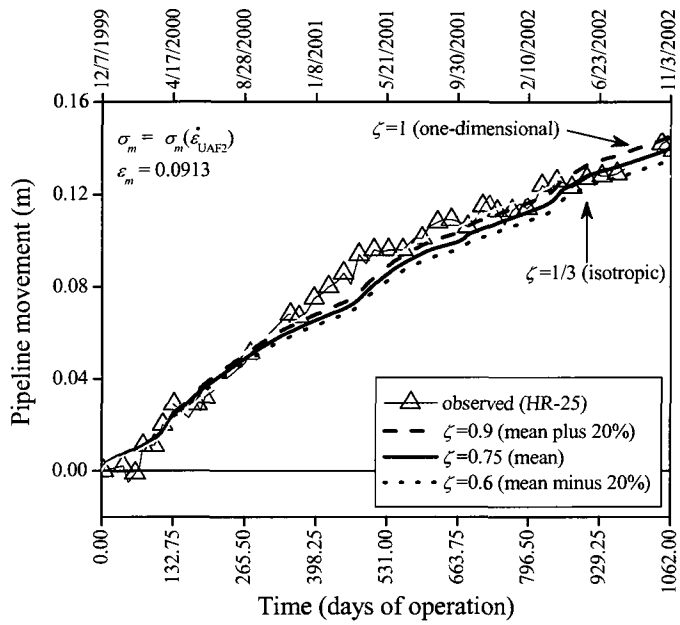

Figure 5.14 Comparison between the observed (Huang et al. 2004) and the simulated pipe displacement using isotropic and anisotropic heave elements for the UAF frost-heave experiment.

5.3.1.5 Results

Figure 5.15 shows the simulated (a) freezing depth and (b) temperature gradient of the segregation freezing zone at 1m from the center line of the pipe for the anisotropic expansion case. The overall simulated results agreed well with the observation. The moving boundary condition and input parameter $gradT_{sp}$ for the SP porosity growth function were successfully modeled.

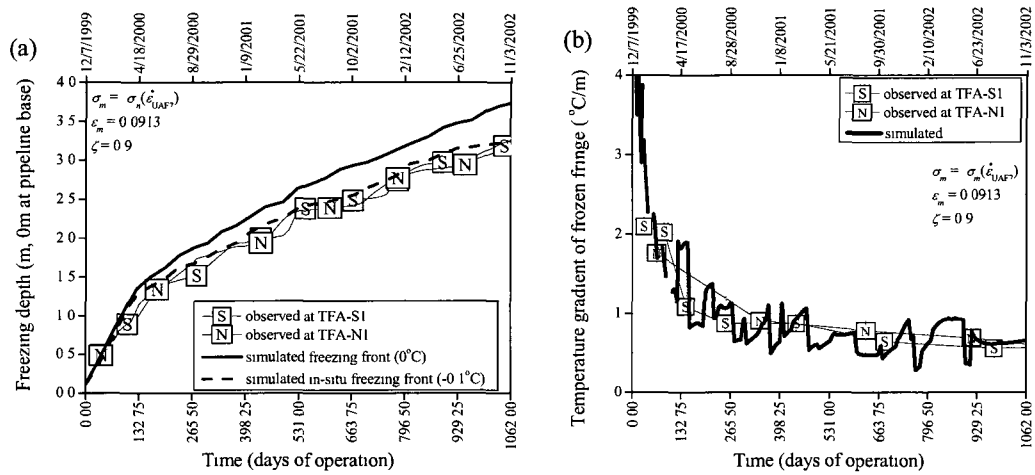

Figure 5.15 Comparison between the observed (Huang et al. 2004) and the simulated results of (a) freezing depth and (b) temperature gradient of frozen fringe at 1m from the center of the pipe.

5.3.2 Calgary frost-heave experiment

A research program involving a field-test facility and laboratory testing was conducted in Calgary in early 1970s. Four separate sections of using 1.22m-diameter pipe with 1cm thick walls, each 12.2m long were buried under different conditions. The four separate sections were referred to as the control, deep burial, restrained, and gravel sections. Measured data have been widely reported (e.g. Northern Engineering Services Company Ltd 1975; Slusarchuk et al. 1978; Carlson and Ellwood 1982; LEC Engineering Ltd 1984; Carlson and Nixon 1988).

The developed two-dimensional frost-heave model was verified against the deep burial section of the Calgary frost-heave experiment.

5.3.2.1 Geometry and boundary conditions

The geometry and boundary conditions used to simulate the deep burial section are illustrated in Figure 5.16a. The frost bulb was observed 3m vertically and 3m laterally from the center of the pipeline. in the deep burial section through the operation (Slusarchuk et al. 1978). The dimensions of the soil region were modeled as 15m x 20m, an area more than 5 times the size of the observed frost bulb. The model consisted of 584 elements as shown in Figure 5.16b. The pipe was buried with 1.7m

overburden. The pipe was assumed to be located in a free-field area. Horizontal displacements are not allowed along vertical sides; the bottom is fixed in both horizontal and vertical directions.

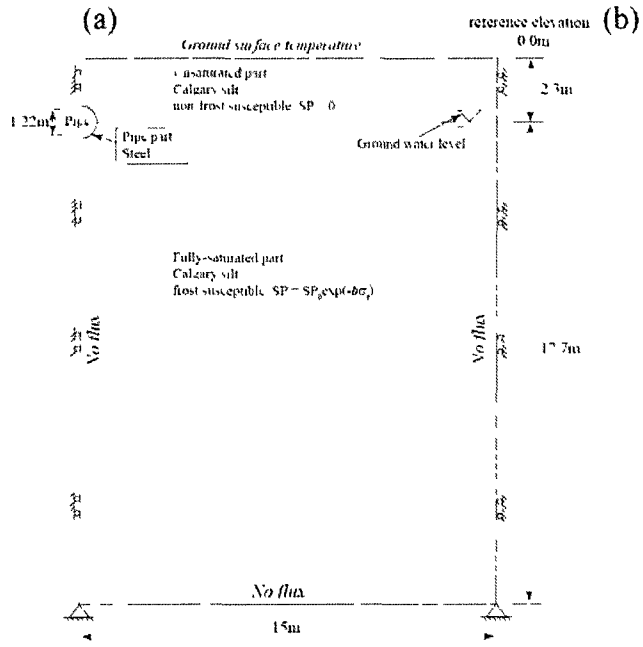

Figure 5.16 (a) Initial and boundary conditions and (b) finite-element discretion of the Calgary frost-heave experiment.

The groundwater table elevation was set at a constant -2.3m. The soil above the water table was assumed to be partially saturated (50% saturation) and not frost-susceptible, while soil below the groundwater table was assumed to be fully saturated and frost-susceptible.

The initial dry density of Calgary silt was determined as 1753kg/m^3 (Northern Engineering Services Company Ltd 1975). Thermal properties were calculated by eq. [5.3] using $w_0 = 0.1$ and $w_u = 0.02$ for the unsaturated part, and $w_0 = 0.2$ and $w_u = 0.02$ for the fully-saturated part. The thermal conductivities of frozen and unfrozen soil were taken as 1.8 and 1.5W/(m x °C), respectively, for both unsaturated and fully saturated parts (Konrad and Morgenstern 1984). The thermal properties are summarized in Table 5.6.

A mean value of -8.5°C was chosen to represent the input pipe temperature. Furthermore, during the first 50 days of simulation, the input pipe temperature decreased from -3.2 to -8.5°C, which closely represents the actual conditions.

The air temperature was converted to the ground surface temperature by using the n-factor. Zero heat flux was applied at the vertical and bottom boundaries. Inline pipe air pressure was atmospheric pressure.

The initial ground temperature was created by the following procedure. First, a temperature of +5°C was applied to all nodes. Then, the model was executed without pipe temperature input for 3 years.

Table 5.6 Thermal properties for simulation of the deep burial section, Calgary frost-heave experiment

Part	Volumetric heat capacity C (kJ/(m^3 x °C))		Thermal conductivity λ (W/(m x °C))		Phase change temperature (°C)	
	Unfrozen	Frozen	Unfrozen	Frozen	Freezing	In-situ freezing
Unsaturated	2139	1843	1.5*	1.8*	0	-0.1
Fully saturated	2875	2155	1.5*	1.8*	0	-0.1
Pipe	3520		40			

* Konrad and Morgenstern (1984)

A series of frost-heave tests were conducted using undisturbed soil samples from the Calgary frost-heave experiment site by Northern Engineering Services Company Ltd (1975) and analyzed by Konrad and Morgenstern (1984). The SP values were apparently scattered as shown in Figure 5.17. Compared with other Calgary silts sampled at different locations (Ueda and Penner 1977), the Calgary silt were highly variable with different clay contents. The appreciable scatter could be explained by variations in clay fraction in the different undisturbed soil samples obtained at different depths. Values of $SP_0 = 300x10^{-5}mm^2/(sec\ x\ °C)$ and $b = 0.0095kPa^{-1}$ were utilized for the simulation analysis.

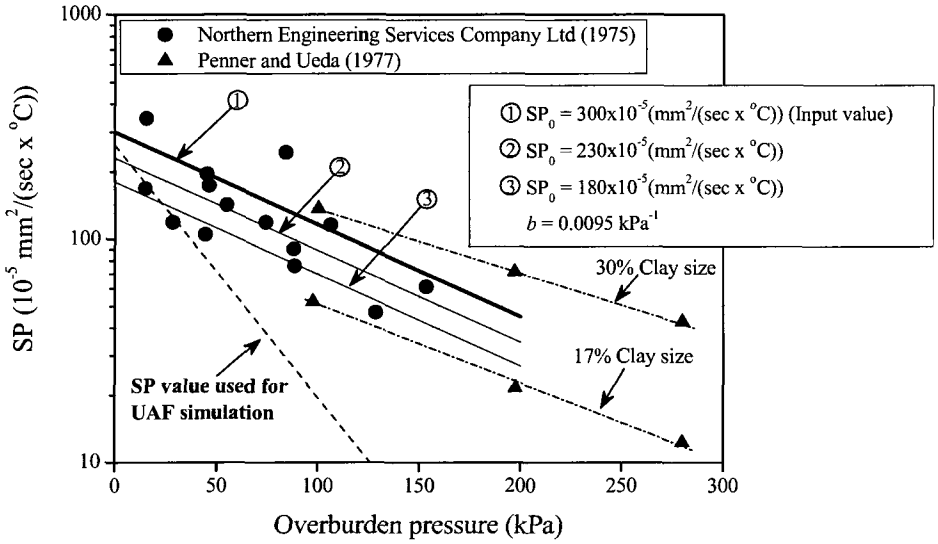

Figure 5.17 Segregation potential of Calgary silt.

5.3.2.2 Mechanical properties

The frost-heave ratio for the deep burial section was reported as shown in Figure 5.18. As the freezing front propagated, the freezing-front penetration rates decreased, then finally slowed to zero at approximately 1050 days. After 1050 days, the frost-heave ratio reached the theoretical limit of 100% because the final ice lens had formed. Since the SP concept is not available to predict final ice-lens growth (Ishizaki and Nishio 1985), three phases were defined during the transient condition. The average increase of the soil volume during each phase of the freezing process was used as a strain rate to simulate the deep burial section; this information is summarized in Table 5.7.

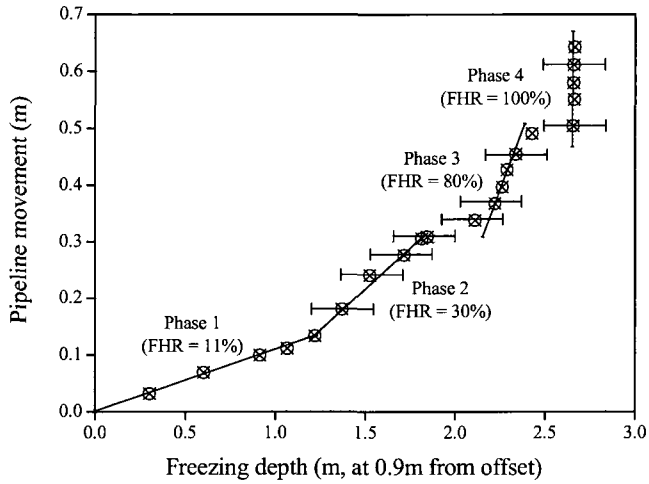

Figure 5.18 Pipeline movement vs. freezing depth measured during the Calgary frost-heave experiment (LEC Engineering Ltd 1984).

Table 5.7 Field strain rates of the deep burial section, Calgary frost-heave experiment

	Days of operation		FHR	Strain rate
	Starting	Ending	(%)	(1/sec)
Phase1	0	165	11	7.72E-09
Phase2	165	450	30	1.22E-08
Phase3	450	1015	80	1.64E-08

Long-term creep properties of Calgary silt have not been reported in the literature. The peak strength of Calgary silt was calculated by eqs. [5.21] and [5.22]. The values for eq. [5.22] are summarized in Table 5.8. Yield strength was calculated by eq. [5.23] using an initial dry density of 1753kg/cm^3 (=*const*). Since the initial dry density of 1753kg/cm^3 was higher than that of the middle-density samples, failure strain and elastic modulus were calculated using the properties of high-density Fairbanks silt (Zhu and Carbee 1987). The failure strain was determined as 0.1868. The elastic modulus was calculated by eq. [5.24] using E_{50}' as 120MPa. Poisson's ratio was taken as $\mu = 0.3$ for both the frozen and the unfrozen cases.

The properties of steel used for the UAF frost-heave experiment were used for the Calgary frost-heave experiment as well.

Table 5.8 Values in Equation 5.22 for Calgary silt

	Strain rate (1/sec)	σ_0 (kPa)	m	R^2
In Equation 5.22:				
Phase1	7.72E-09 (= $\dot{\varepsilon}_{CAL1}$)	173.62	0.939	0.998
Phase2	1.22E-08 (= $\dot{\varepsilon}_{CAL2}$)	189.42	0.914	0.998
Phase3	1.64E-08 (= $\dot{\varepsilon}_{CAL3}$)	200.44	0.898	0.998
Critical strain rate	1.10E-06 (= $\dot{\varepsilon}_{critical}$)	447.00	0.667	0.996

5.3.2.3 Results

As discussed above, the peak strength of Fairbanks silt was applied to the Calgary frost-heave simulations regardless of differences in soil types. The sensitivity of frost-heave simulations was investigated for different values of peak strength. In order to proceed in a simple manner, the peak strength was modified by using the multiplication factor α while using the strain rate of Phase2 shown in Table 5.8. The parametric study shows that the two-dimensional frost-heave simulations are sensitive to the stress field, and that setting the value of α equal to 0.5 produced a good approximation of the observed heave as shown in Figure 5.19.

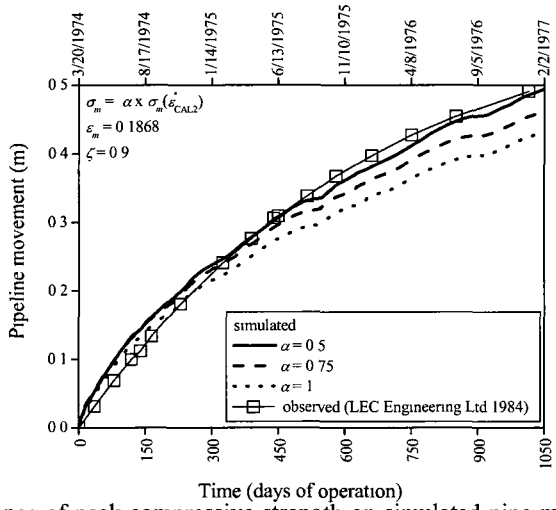

Figure 5.19 Influence of peak compressive strength on simulated pipe movement during the Calgary frost-heave experiment.

The stress dependency was evaluated using the slope of the post-yield relationship as follows:

[5.28] $E_y = \beta \times E$

where β = a multiplication factor used to test the effect of post-yield stress-strain characteristics. Figure 5.20 summarizes the relationship between β and temperature. A α value of 0.5 corresponds to a β value between 0.02 and 0.04. Konrad and Shen (1996) also suggested that setting the value of β equal to 0.05 or even slightly smaller produced the best post-yield characteristics for simulating the deep burial section of the Calgary frost-heave experiment.

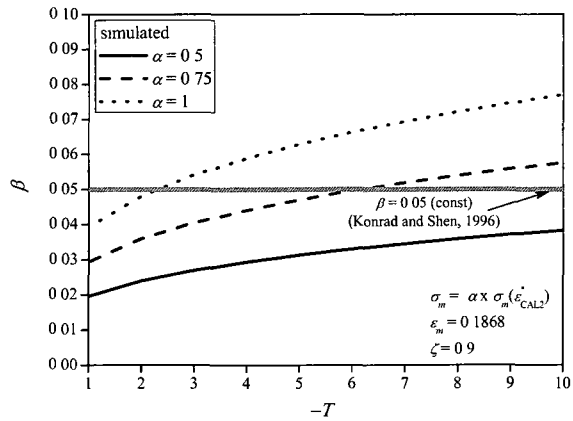

Figure 5.20 Influence of peak compressive strength on the relationship between β and temperature.

Figure 5.21 shows simulated and (a) freezing-front penetration and (b) thermal analysis, using α as 0.5 at a 0.91m offset from the center. The simulated freezing depth was shallower (i.e. 25% less after 150 days) than the observed value. Otherwise, the trend of simulated $gradT_{sp}$ was similar to that of the observed. Figure 5.22 shows the distribution of gravimetric water content at the center line of the pipe. The simulation predicted an increase in gravimetric water content from approximately 20 to 45% toward the base of the frost bulb at 1050 days. This trend was similar to the observations reported by Carlson and Nixon (1988) following excavation of the frost bulb in the deep burial section.

Judging from the above, the modified peak strength determined by the parametric study was suitable for simulating the deep burial section.

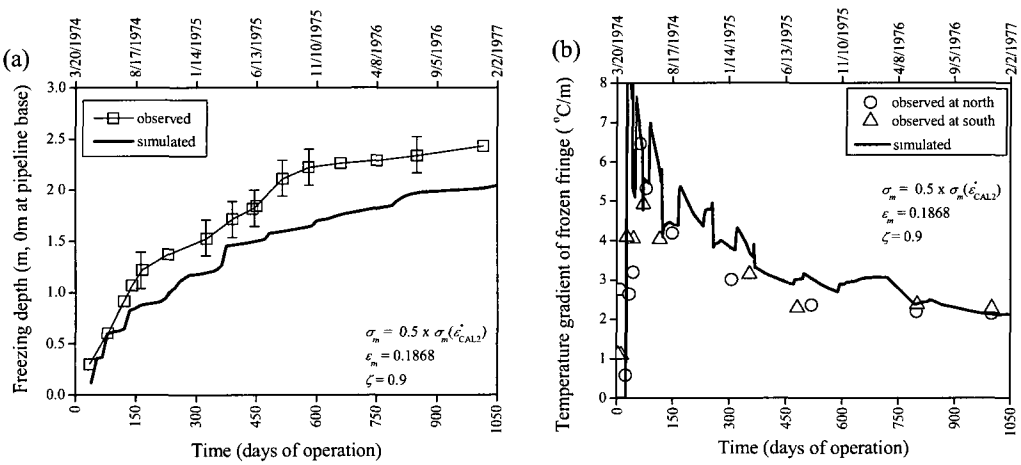

Figure 5.21 Comparison between the observed (LEC Engineering Ltd 1984) and the simulated results of (a) frost depth and (b) temperature gradient of frozen fringe at 0.9m from the center of the pipe.

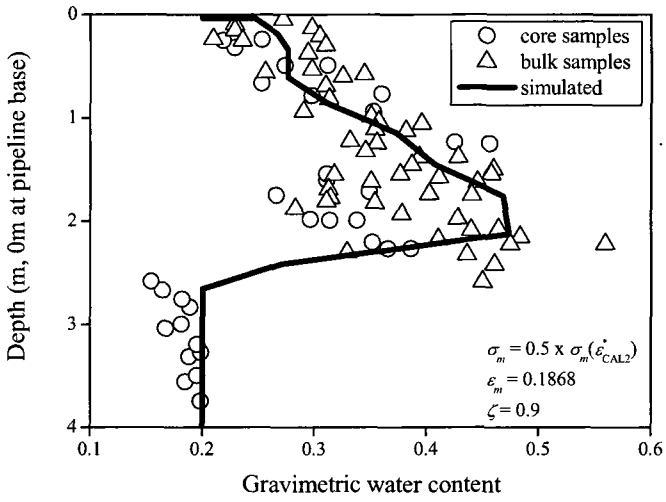

Figure 5.22 Comparison between the observed (Carlson and Nixon 1988) and the simulated distribution of gravimetric water content at the center line of the pipe.

5.4 Effect of soil strain-rate properties and induced stress on frost heave

The developed two-dimensional SP porosity growth model reasonably estimated the pipeline movement and temperature fields using long-term creep strength data. The effect of simulated strain-rate-dependent material properties were tested against observations from the UAF frost-heave experiment. The peak strengths were calculated using the strain rate at each phase and the critical strain rates are summarized in Table 5.3. As shown in Figure 5.23, the simulated results agreed well with the observed values at location HR-25 using the field-strain rates. For instance, the difference between the Phase2 and Phase3 cases was only 0.004m by day 1062, and the Phase1 case almost overlapped the Phase2 case. However, when the critical strain was applied to the frost-heave simulation, the simulated total heave was 0.11m at the end of simulation; this value was approximately 75% of the observed heave. This indicates that induced stress in the segregation freezing zone for the critical strain rate case was significantly different from the field-strain rates.

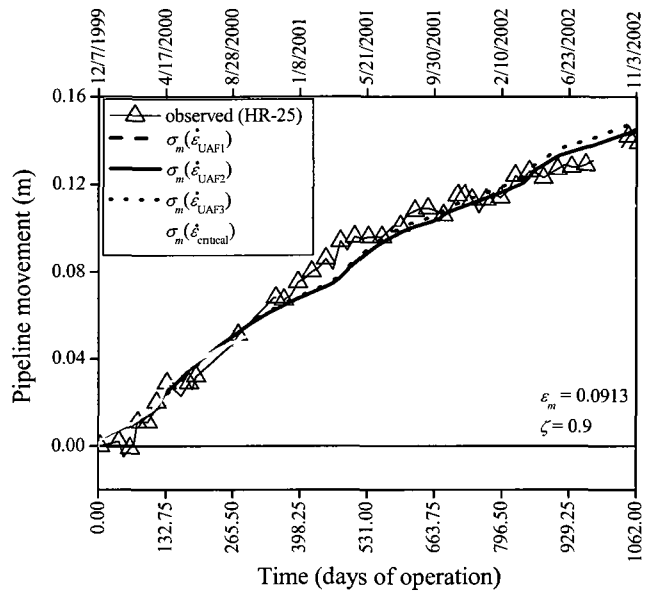

Figure 5.23 Influence of strain-rate dependency on pipeline movement.

The induced-stress distributions were compared next. The third freeze cycle was selected at operational days 724, 899, and 1020, and the results are shown in Figures 5.24, 5.25, and 5.26, respectively. The freeze-thaw cycle was simulated as follows. The frozen layer existed at the shoulder of the frost bulb (Figure 5.24). The deepest penetration of the freezing isotherm at the shoulder occurs in early spring due to the latent heat release, despite the thawing from the ground surface (Figure 5.25). The frozen layer thaws near the end of summer (Figure 5.26).

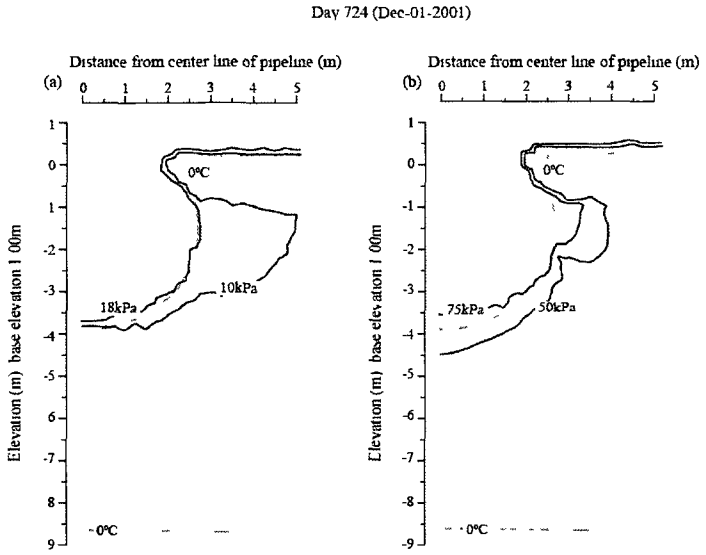

Figure 5.24 Simulated induced-stress distribution around the UAF test pipe in early December of the third cycle, with comparison between using (a) field strain rate and (b) critical strain rate.

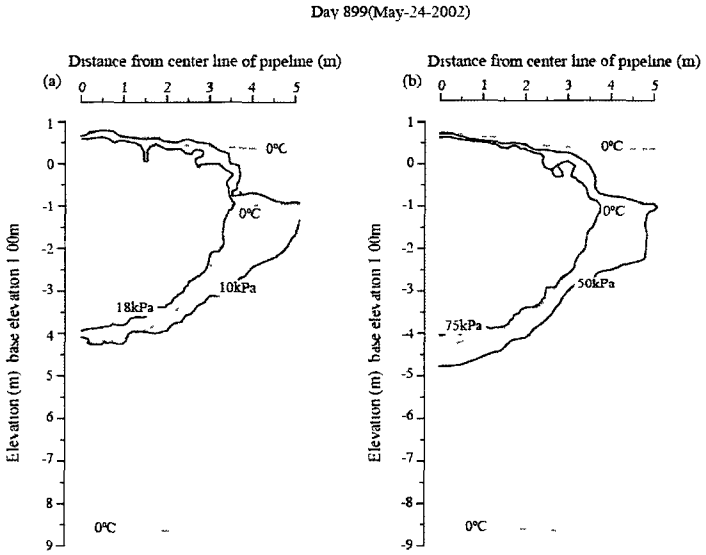

Figure 5.25 Simulated induced-stress distribution around the UAF test pipe in late May of the third cycle, with comparison between using (a) field strain rate and (b) critical strain rate.

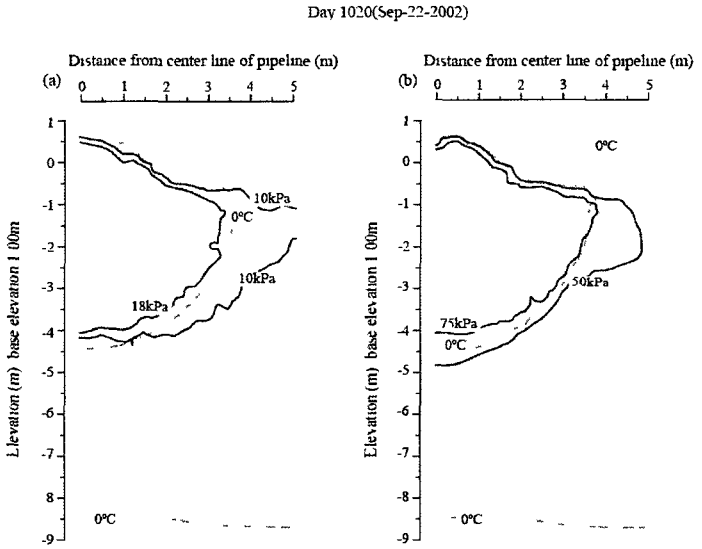

Figure 5.26 Simulated induced-stress distribution around the UAF test pipe in early September of the third cycle, with comparison between using (a) field strain rate and (b) critical strain rate.

Higher stress was induced in the horizontal direction than the vertical direction in both cases. Significant stress concentration occurred in the critical strain rate case at the centerline because of the induced stress in the horizontal direction. Regardless of the existence of the frozen layer, the induced stress in the segregation freezing zone was approximately 75kPa at the center line using the critical strain rate, which is four times higher than the field strain rate case in which the strain rate of Phase2 was used.

Estimating the mechanical properties using the critical strain rate resulted in an over-estimation of the stress field and an under-prediction of the frost heave. Using this factor could, therefore, result in an underestimation of frost heave, with potential consequences of damage to both the pipeline and the environment. The effect of strain-rate-dependent mechanical properties used to reproduce field conditions will, therefore, undoubtedly be an important factor to arctic gas pipeline design.

5.5 *Effect of frozen layer on resistance to upward motion of the frost bulb*

The developed two-dimensional finite-element (FE) frost-heave model predicted a relatively constant stress field induced by frost heave despite the existence of a frozen layer in the third freeze-thaw cycle. The effect of the frozen layer on resistance to upward motion of the frost bulb was studied in detail. A quasi two-dimensional finite-difference (FD) frost-heave model was developed by Kim et al. (2008) to predict the UAF frost-heave experiment at the free-field area. The FD frost-heave model ignored the stresses and strains at the frozen-unfrozen interface and resistance of the frozen layer; that is to say, the soil pressure acting on the segregation freezing zone was simply assumed to be equal to the overburden pressure in eq. [5.8]. Figure 5.27 presents the comparison between observed and simulated heave predicted by both the FE and the FD frost-heave models. The FD frost heave model simulation predicted approximately 0.4m more heave than was predicted by the FE frost-heave model.

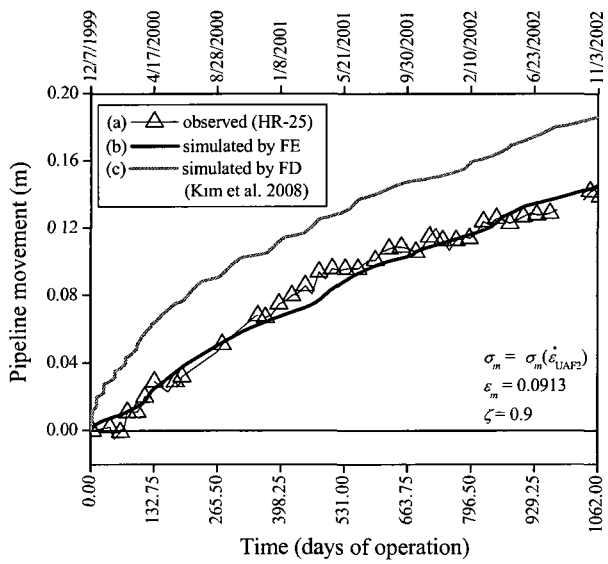

Figure 5.27 Comparison of pipeline movement among (a) observed (Huang et al. 2004), (b) simulated by FE model, and (c) simulated by FD model (Kim et al. 2008).

The simulated heaves were evaluated by heave rate (HRR). The least square regression analysis was applied in phases, which were defined in Table 5.3. The results are summarized in Table 5.9 and shown in Figure 5.28.

As shown in Figure 5.28, Phase1 was characterized by a higher observed heave rate; it was followed by Phase2 and Phase3 with lower rates of observed heave. The same trend was seen in simulated heaves. The heave rate simulated by the FD frost-heave model was approximately two times higher than the observed value in Phase1. Five heave gages monitored foundation heave within the first 1m of native soil below the base of the pipeline (Huang et al. 2004). Within the first 1m, foundation movement could be directly compared with pipeline movement. The detailed heave analysis was conducted in Phase1 using a heave gage.

Table 5.9 Analysis of heave rate for the UAF frost-heave experiment

	Days of operation		Observed	R^2	Simulated by FE	R^2	Simulated by FD	R^2
	Starting	Ending	HRR (mm/day)		HRR (mm/day)		HRR (mm/day)	
Phase1	0	162	0.208	0.874	0.173	0.976	0.382	0.994
Phase2	162	507	0.207	0.993	0.139	0.994	0.156	0.994
Phase3	507	1060	0.082	0.975	0.108	0.997	0.104	0.996

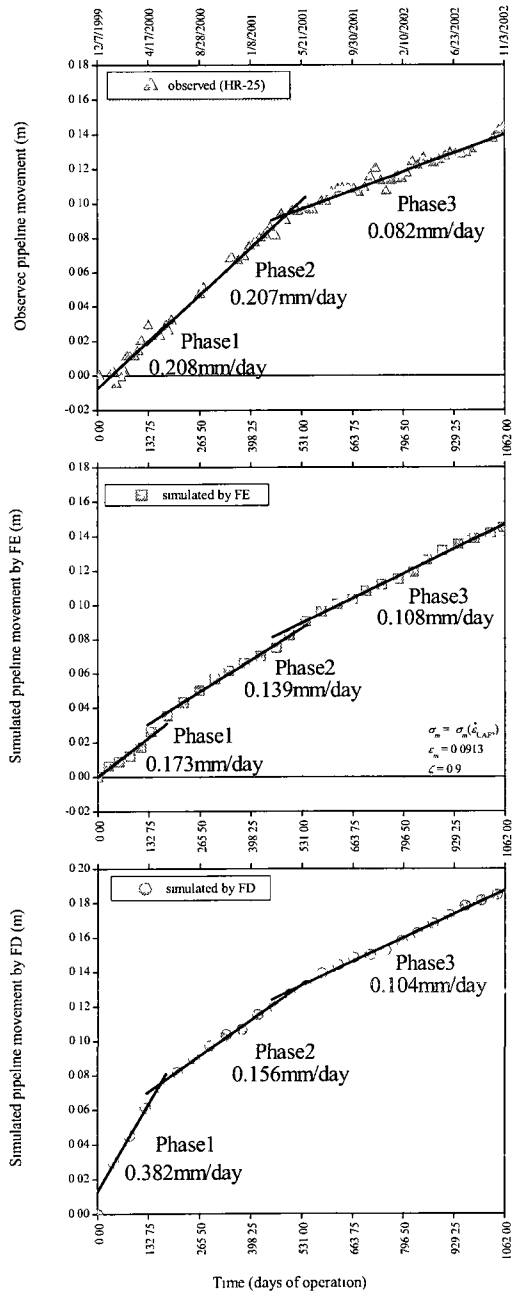

Figure 5.28 Pipeline movement vs. time with comparison between observed (top) (Huang et al. 2004), simulated by the FE model (middle), and simulated by the FD model (bottom) (Kim et al. 2008).

Figure 5.29 shows the relationship between the pipeline movement (HR-25 at 58.805m), foundation heave (HG-5 at 68.85m), and simulated heaves. The heave simulated by the FD frost-heave model was simply correlated to *in-situ* heave due to the freezing-front penetration because stress-strain analysis was not coupled. The FE simulation exhibited a trend and magnitude similar to that of the observed pipeline heave by day 90, which was the approximate time after which no further foundation heave was recorded. Although the pipe movement fluctuated due to pipe temperature oscillation, the heave simulated by the FE frost-heave model showed good agreement with the observed pipe movement.

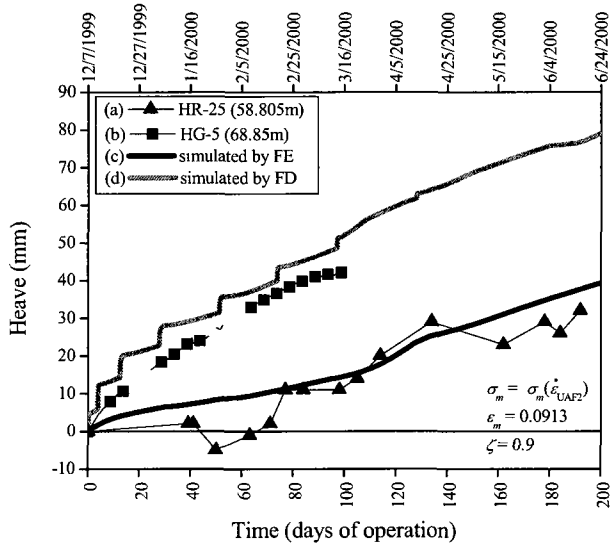

Figure 5.29 Relationships between (a) pipeline movement (HR) (Huang et al. 2004), (b) foundation heave (HG) (Huang et al. 2004), (c) pipeline movement simulated by a finite element model (FE), and (d) pipeline movement simulated by a finite difference model (FD) (Kim et al. 2008).

The effect of the frozen layer was evaluated by the post-yield strain data. Figure 5.30a shows temperature and post-yield strain distributions in a 5m by 5m area close to the pipe on day 120. Because the frozen soil layer had high strength in wintertime, it resisted the upward motion of the frost bulb. Consequently, the distribution of post-yield strain of 0.0025 was induced in unfrozen soil below the pipe. The frozen part expanded due to frost heave, while at the same time the unfrozen part was compressed by the resistance of the frozen layer during the first 120 days. Figure 5.30b shows

distribution of post-yield strain on day 125. Between days 120 and 125, the post-yield strain of 0.0025 was exerted in the frozen layer when the frozen-layer temperature became warmer than -0.5°C. Figure 5.30c shows the distribution on day 193, at which time the temperature of the frozen layer was very close to 0°C. The post-yield strain significantly increased in the frozen layer instead of in the unfrozen soil immediately beneath the surface. This indicates that with increasing surface temperature, the strength of the frozen layer decreased. Furthermore, the resistance force of the frozen layer decreased once the strain phase reached the post-yield strain.

The difference of total heave simulated by the FE and FD frost heave models was approximately 0.4m on day 120 at the time the post-yield strain occurred in the frozen layer; this difference was also approximately 0.4m on day 1162, which was the end of the simulation. Also, the heave rates simulated by both models exhibited similar trends in Phases 2 and 3 as shown in Figure 5.28, which had post-yield strain in the frozen layer. The results indicate that the resistance to upward motion of the frost bulb was nearly negligible at the free-field area after the post-yield strain had occurred in the frozen layer.

There were difficulties in the FE frost-heave model with simulation time and in the FD model with stress-strain analysis coupling in early-stage operation. The developed FE frost-heave model required considerable simulation time, for instance, approximately 12hrs for a 3-year simulation using a high-performance workstation or a super computer. Furthermore, numerical instabilities arose because of the complicated coupling process. The FD simulation of the UAF frost-heave experiment took only a half hour or less of computing time by a personal computer under the same geometry and boundary conditions, and the FD frost-heave model was able to predict the total heave amount during the major portion of the operation except in the early stage. Therefore, it might be appropriate to simulate the early-stage operation using the FE frost-heave model and the remaining operation using the FD frost-heave model. By combining the results from the two types of simulations, a more efficient and practical "complete" two-dimensional frost-heave prediction can be produced for arctic pipeline design.

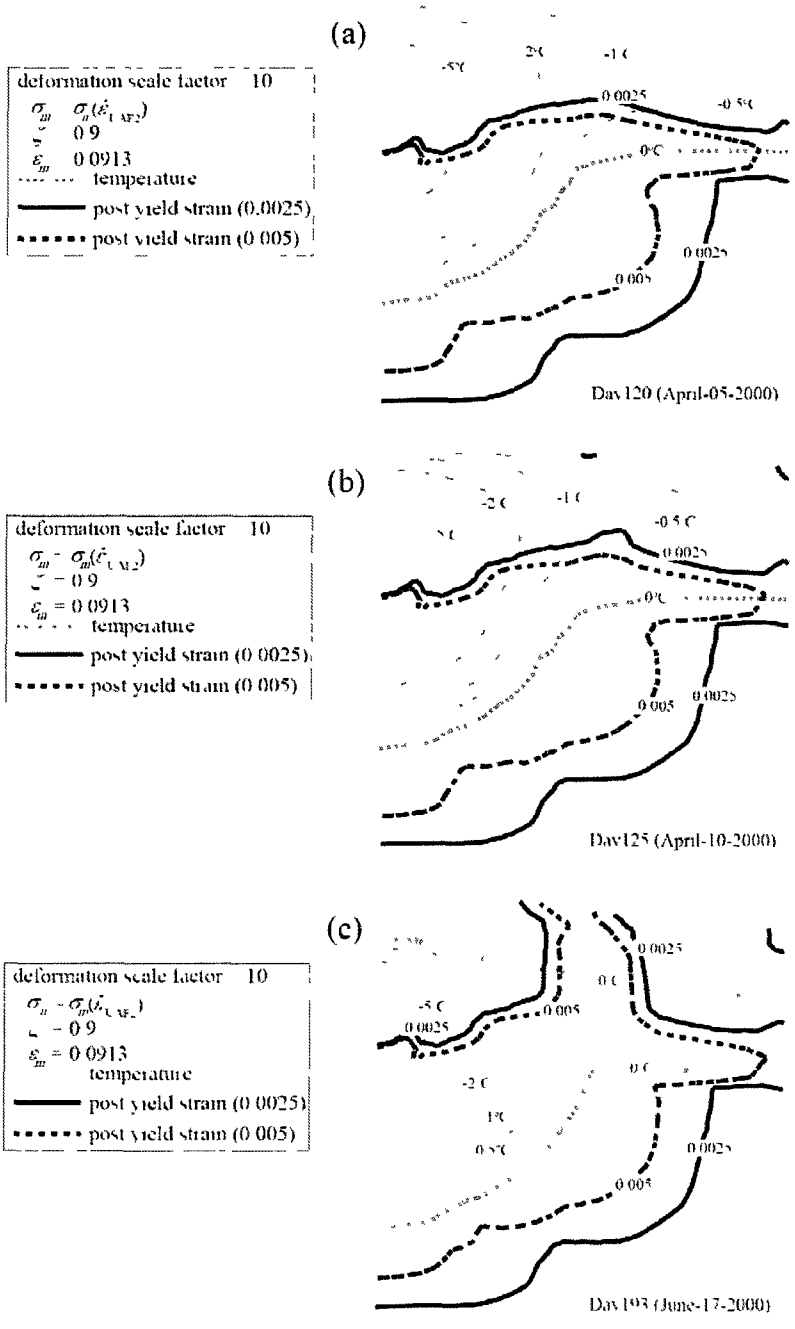

Figure 5.30 Simulated temperature and post-yield strain distribution in the early stage of the UAF frost-heave experiment at (a) day 120, (b) day 125, and (c) day 193.

5.6 Summary and conclusion

A two-dimensional SP porosity frost-heave model was developed with fully-coupled thermal and moisture transfer and mechanical behaviors. A deforming finite element and nonlinear material properties were applied to the model. Although individual ice-lens distribution could not be reproduced, the effect of cryostructure was accounted for in the mechanical model.

Significant findings from this study are:

1) The anisotropic deformation was verified against the UAF frost-heave experiment. The anisotropic deformation of soil was modeled by simulating the phenomenon of ice-lens growth mostly perpendicular to heat-flow direction, yielding 90% of the ice-lens expansion parallel to, and the remaining 10% perpendicular to the direction of heat flow.
2) Post-yield characteristics of the frozen soil were modeled by a modified bilinear elastic model. The sensitivity of the post-yield characteristics was evaluated by a multiplication factor β. The post-yield ability to simulate the deep burial section of the Calgary frost-heave experiment was represented by β values between 0.02 and 0.04.
3) The numerical simulation suggested the use of mechanical properties applying field-strain rates for the two-dimensional frost heave prediction of pipeline at free-field area.
4) Estimating mechanical properties using the critical strain rate resulted in an unrealistic stress buildup, and an under-prediction of the frost heave. Using this factor could, therefore, result in an underestimation of frost heave, with potential consequences of damage to both the pipeline and the environment.
5) The existence of a frozen layer significantly reduced the frost heave in the early stage of simulation. However, once post-yield strain had been induced in the frozen layer, the resistance to upward motion of the frost bulb was nearly negligible at the free-field area after the post-yield strain had occurred in the frozen layer.

CHAPTER 6: THREE-DIMENSIONAL SIMULATION USING THE SP POROSITY GROWTH FUNCTION

6.1 Introduction

One of the major sources of induced load to arctic gas pipelines is the differential heave near the interface between two types of soil with different frost-heave susceptibilities or between frozen and unfrozen soils.

Several researchers have used Winkler models to predict differential frost heave (e.g. Nixon et al. 1983; Rajani and Morgenstern 1992, 1993, 1994; Razaqpur and Wang 1996). For instance, Rajani and Morgenstern (1992) created a Winkler model, which assumed the ice-rich permafrost to be an elastic-plastic foundation. The Winkler model was applied to two small-scale steel pipes (diameter x thickness = 38.1 mm x 0.889mm and 50.8mm x 4.9mm) embedded in polycrystalline ice, and satisfactory comparisons were obtained between the observations and the simulations (Rajani and Morgenstern 1993). The same Winkler model also simulated the differential frost heave observed during the Caen frost-heave experiment which used a pipe, diameter x thickness = 0.273m x 5mm (Rajani and Morgenstern 1994). Despite its simplicity, the developed Winkler model could predict the overall pipe defects and induced stresses discovered during the Caen frost-heave experiment. However, Winkler models have limitations. Since Winkler models use springs to account for the axial and radial restraints by surrounding soil, the soil pressure was only characterized in terms of the absolute pipe displacement. Furthermore, the Winkler model neglects the impact of rigid body movements of the soil and the interaction through the soil from location to location.

Selvadurai et al. (1999b) developed a more rigorous continuum modeling of soil-pipeline interaction due to differential frost heave. The continuum approach was established to model the interaction induced by the three-dimensional time-dependent growth of a frost bulb around the chilled pipeline, and the stress-dependent expansion of the frost-susceptible soil. The developed three-dimensional frost-heave model could simulate the behavior of a buried pipeline in the Caen frost-heave experiment. However, this three-dimensional approach modeled the pipe as a one-dimensional beam element that might influence the thermal analysis and the soil-pipeline interaction induced by axial, shear, and flexural stiffness characteristics. Furthermore, the continuum model has not yet been applied to analyze large-diameter pipelines subjected to differential frost heave.

Upheaval buckling can also lead to large upward movement of arctic pipelines as reported for the Norman Wells oil pipeline in Canada (Nixon and Burgess 1999). Upheaval movement was modeled as the interaction between the longitudinal compressive force present during operation and

overbend irregularities in the profile due to thaw settlement and/or frost heave (Palmer and William 2003).

The purpose of this chapter is two-fold. First, the development of a three-dimensional frost-heave model using the SP porosity growth function to predict the soil-pipeline interaction due to differential frost heave will be explained. Subsequently, the developed model will be verified by observations from the University of Alaska Fairbanks (UAF) frost-heave experiment regarding the responses of a large-diameter pipeline, diameter x thickness = 0.914m x 9mm, due to differential frost heave. Second, an abrupt-upheaval pipeline movement that was observed in the UAF frost-heave experiment will be evaluated based on the existing upheaval buckling model.

In the following sections, first the three-dimensional frost-heave model is described. A description of the UAF frost-heave experiment at Fairbanks, Alaska follows. Verification of the three-dimensional frost-heave model against the UAF frost-heave experiment is presented. Next, a quantitative analysis of the abrupt pipeline uplift is conducted. Finally, support for the contention that the developed three-dimensional frost-heave model can predict pipe movement and induced bending due to differential frost heave in a 20-year period is presented.

6.2 Three-dimensional SP porosity growth function

The segregation potential (SP) concept is a macroscopic semi-empirical model based on laboratory observations and theoretical considerations such as the validity of the Generalized Clausius-Clapeyron Equation at the active ice lens. In frost-susceptible soils, volume change occurs as a result of ice-lens formation as *in-situ* pore water and migratory water freeze at the segregation freezing front. The stress-strain behavior of frozen soils depends mainly upon factors such as soil type, mineralogical composition, ice content, temperature, and strain rate. In freezing soils, stresses are applied slowly since the heave rates are usually small, on the order of tenths of millimeters per day, for example, in the UAF frost-heave experiment (Kim et al. 2008). The frozen soils then deform in a ductile manner and the stress-strain relationship is approximated by a modified bilinear law.

As described in the previous chapters, the SP porosity growth function was modeled as porosity increment due to frost heave. The total porosity increment (Δn_t) was clearly composed of two components: *in-situ* heave and segregation heave.

Defining the water content at time t as $w(t)$, the porosity growth due to *in-situ* heave (Δn_{in}) at time $t+\Delta t$ can be expressed as:

$$\Delta n_{in} = 0.09 \times \theta_w(t) \times \frac{w(t) - w(t+\Delta t)}{w(t)} \quad [6.1]$$

where $\theta_w(t)$ = volumetric fraction of water at time t.

The porosity growth due to segregation heave (Δn_{sp}) is calculated as:

$$[6.2] \quad \Delta n_{sp} = \frac{1.09 \times \Lambda_{sp} \times v}{V_{sp}} \times \Delta t$$

with

$$[6.3] \quad v = \mathrm{SP}(\sigma_t) \times gradT_{sp}$$

where Λ_{sp} = the effective area of the segregation freezing temperature in the element; v = the rate of migrating water; V_{sp} = the effective volume of the segregation freezing zone; SP = segregation potential; σ_t = soil pressure acting on the segregation freezing zone; and $gradT_{sp}$ = temperature gradient in the segregation freezing zone.

The $gradT_{sp}$ in eq. [6.3] is taken in direction *1* in Figure 6.1, which is the direction of heat flow and the maximum temperature gradient direction, and is determined as:

$$[6.4] \quad gradT_{sp} = \sqrt{\left(\frac{\partial T}{\partial x}\right)^2 + \left(\frac{\partial T}{\partial y}\right)^2 + \left(\frac{\partial T}{\partial z}\right)^2}$$

where $\partial T/\partial x$, $\partial T/\partial y$, and $\partial T/\partial z$ are temperature gradients in the x, y, and z directions of the global coordinating system, respectively.

The SP porosity growth function was obtained by adding eqs. [6.1] and [6.2]:

$$[6.5] \quad \Delta n_t = \Delta n_{in} + \Delta n_{sp}$$

The total strain increment ($\Delta\varepsilon$) was modeled to consist of two components: the modified bilinear elastic strain increment ($\Delta\varepsilon^{el}$) and the strain increment due to the total porosity growth function ($\Delta\varepsilon^{sp}$) as:

$$[6.6] \quad \Delta\varepsilon = \Delta\varepsilon^{el} + \Delta\varepsilon^{sp}$$

The strain increment due to the total porosity growth function was modeled as anisotropic. The three-dimensional anisotropic strain increments could be written using an orthogonal matrix as:

$$[6.7] \quad \left[\Delta\varepsilon^{sp}\right] = \begin{bmatrix} \Delta\varepsilon_{11}^{sp} & \Delta\varepsilon_{12}^{sp} & \Delta\varepsilon_{13}^{sp} \\ \Delta\varepsilon_{21}^{sp} & \Delta\varepsilon_{22}^{sp} & \Delta\varepsilon_{23}^{sp} \\ \Delta\varepsilon_{31}^{sp} & \Delta\varepsilon_{32}^{sp} & \Delta\varepsilon_{33}^{sp} \end{bmatrix} = \begin{bmatrix} \zeta & 0 & 0 \\ 0 & \frac{1}{2}(1-\zeta) & 0 \\ 0 & 0 & \frac{1}{2}(1-\zeta) \end{bmatrix} \Delta n_t$$

where ζ = a dimensionless value between 1/3 and 1, representing conditions ranging between the isotropic (ζ = 1/3) and one-dimensional (ζ = 1) cases. The direction *1* was specified as the major principal direction in eq. [6.7].

The component of the strain increment due to the three-dimensional SP porosity growth function in a global *x-y-z* coordinating system is obtained by the following transformation rule:

$$[6.8] \quad \begin{bmatrix} \Delta\varepsilon_{xx}^{sp} & \Delta\varepsilon_{xy}^{sp} & \Delta\varepsilon_{xz}^{sp} \\ \Delta\varepsilon_{yx}^{sp} & \Delta\varepsilon_{yy}^{sp} & \Delta\varepsilon_{yz}^{sp} \\ \Delta\varepsilon_{zx}^{sp} & \Delta\varepsilon_{zy}^{sp} & \Delta\varepsilon_{zz}^{sp} \end{bmatrix} = [B] \cdot \begin{bmatrix} \Delta\varepsilon_{11}^{sp} & \Delta\varepsilon_{12}^{sp} & \Delta\varepsilon_{13}^{sp} \\ \Delta\varepsilon_{21}^{sp} & \Delta\varepsilon_{22}^{sp} & \Delta\varepsilon_{23}^{sp} \\ \Delta\varepsilon_{31}^{sp} & \Delta\varepsilon_{32}^{sp} & \Delta\varepsilon_{33}^{sp} \end{bmatrix} \cdot [B]^{-1}$$

with

$$[6.9] \quad [B] = \begin{bmatrix} \sin\psi\cos\varphi & -\sin\varphi & \cos\psi\cos\varphi \\ \sin\psi\sin\varphi & \cos\varphi & \cos\psi\sin\varphi \\ \cos\psi & 0 & -\sin\psi \end{bmatrix}$$

where ψ = the angle that the *x* axis makes with the reflection of heat flow direction *1* on the *x-y* plane; and φ = the angle that the *z* axis makes with heat flow direction *1* as defined in Figure 6.1.

The developed three-dimensional SP porosity growth function is applied to examine the soil-pipeline interaction induced by differential frost heave in a full-scale frost-heave experiment.

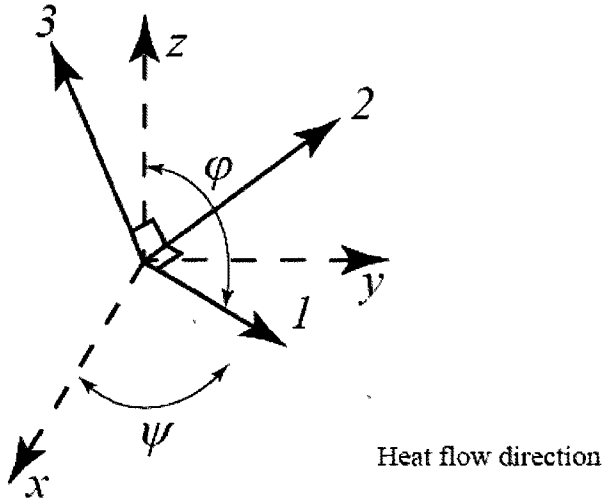

Figure 6.1 Three-dimensional coordinate system of an anisotropic element.

6.3 UAF frost-heave facility

The UAF and Hokkaido University, Japan, conducted a full-scale field experiment from December 1999 to August 2003 to determine the differential heave of a 105m long pipe near a frozen-unfrozen boundary.

In this section, the UAF frost-heave experiment is briefly described. Figure 6.2 shows the initial permafrost conditions along the pipeline; a rapid deepening of the permafrost table at 30m from the inlet riser can be seen. The reference elevation was defined as 1.00m. The pipeline crossed a boundary between permafrost and unfrozen ground. A 0.914m diameter, 105m long pipe with X65 grade and 9mm wall thickness was used. The first 30m of the pipe were in a shallower supra-permafrost table area and the remaining 75m were in unfrozen ground - a deeper supra-permafrost table area. The pipeline trench was backfilled with sand to the top of the pipeline in the shallower supra-permafrost area, and to the spring line of pipes in the deeper supra-permafrost table area. After the sand was bounded by water, the pipeline was covered with approximately 0.9m of *in-situ* crushed soil.

Figure 6.2 also shows the instrumentation and monitoring. The depth to the groundwater table was monitored by three open standpipes; Well #1, 2, and 3 were located approximately 104m, 113m, and 58m from the inlet riser, respectively. In order to monitor the heave of the soil directly beneath the pipeline, five heave gauges (HGs) were installed. The HGs were located at 27.85, 30.96, 32.33, 37.04, and 68.85m from the inlet riser, and monitored movement of the first 1m of soil underneath the pipeline.

Pipeline movement was monitored by 28 heave rods (HRs) welded directly to the top of the pipe. Eleven stations along the pipeline were used to monitor the pipe strain. Forty weldable strain gauges (SGs) were placed on the outside surface of the pipeline. The results derived from the UAF frost-heave experiment were fully documented by Bray (2003) and Huang et al. (2004). The results will be presented, where appropriate, in the subsequent sections.

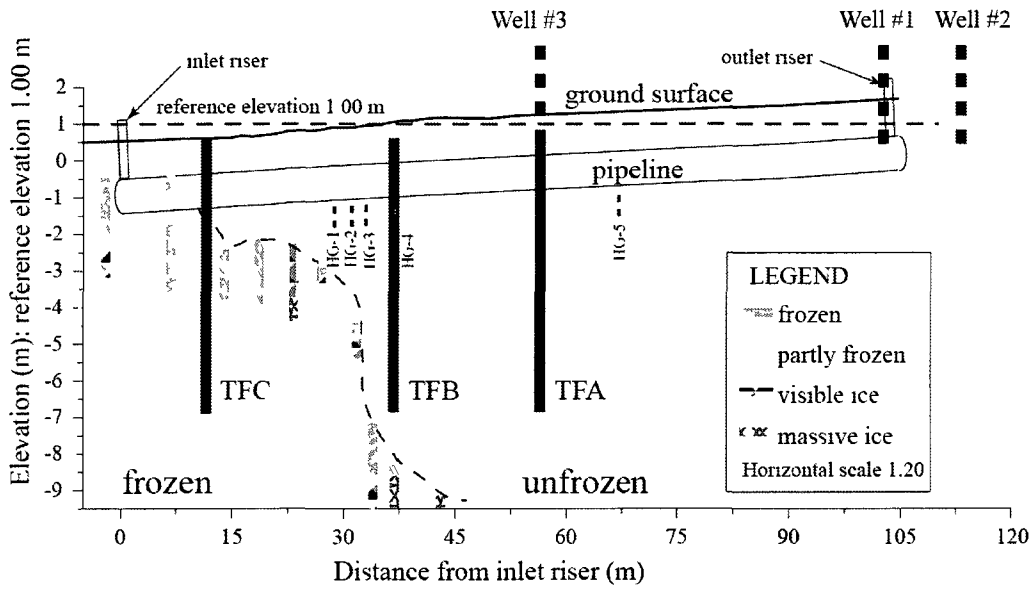

Figure 6.2 Initial permafrost condition, instrumentation, and monitoring of the UAF frost-heave experiment (modified from Kim et al. 2008).

Three thermal fences (TFs) were designed to monitor changes in the thermal regime of the soil system. TFA and TFB were placed in the deeper supra-permafrost area and TFC was located in the shallower supra-permafrost area. Figures 6.3a and 6.3b show the location and spacing of the thermistors for TFB and TFC, which were located at 36.5m and 13m from the inlet riser, respectively. TFB included three thermistor strings located between 1 and 3 m from the pipeline centerline with depths ranging from 0.09 to 7.76m (elevation 1.09 to -6.87 m) beneath the ground surface. Thermistor spacing ranged from 0.25 to 1.0m. TFC contained four thermistor strings with thermistor depths ranging from 0.04 to 7.00m (elevation 0.54 to -6.42m) beneath the ground surface. Thermistor spacing ranged from 0.5 to 1.0m. Pipeline temperatures were monitored by 9 thermistors placed along the outside of the pipeline.

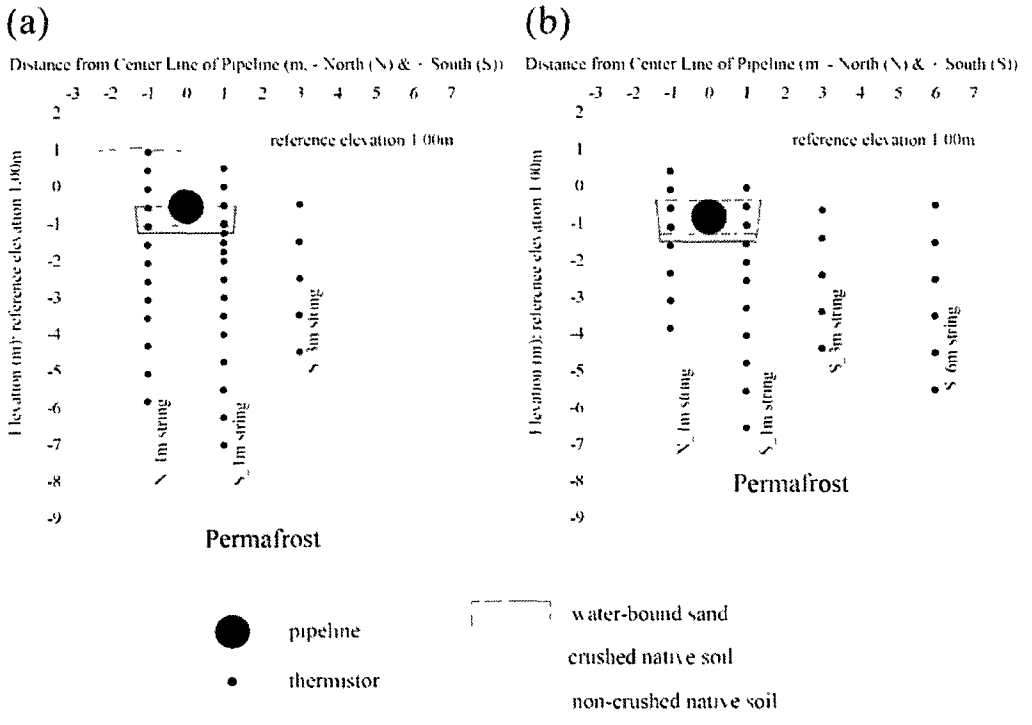

Figure 6.3 Cross section of (a) TFB and (c) TFC showing the placement of thermistor beads and the generalized backfill materials (modified from Bray 2003).

6.4 Modeling of the buried chilled gas pipeline problem

6.4.1 Geometry

Figure 6.4a shows the pipeline movement profile for various days between day 4 and 1340. Day 4 on December 11, 1999 was the first day of the survey; day 1340 on August 8, 2003 was the last day of the survey. Up to day 50, the pipeline experienced settlement. The initial settlement was possibly due to the thermal disturbance that occurred during excavation and to the increased overburden pressure from the pipeline and berm. The shallower supra-permafrost area experienced approximately 0.025m of initial settlement, while the deeper supra-permafrost area showed less settlement. The largest heave rate was observed between days 50 and 266. After day 266, lack of heave was observed at HR-26 and HR-27, which were located 74.04m and 89.275m, respectively, from the inlet riser. One possible explanation was simply that the soil in that vicinity was less

susceptible to frost heave. Alternatively, the groundwater condition could be locally different. Figure 6.4b shows the groundwater table fluctuations over a period of slightly less than two years instead of three, because groundwater levels were measured starting in the second winter in 2000. Well #3 constantly showed a higher water table than did the other wells. The lower groundwater might be responsible for the lack of heave at HR-26 and HR-27. Reduced heave also was observed at HR-28, which was at the end of the test section at 105m. The observed reduced heave might be due to boundary effects. At the end of the test section, a vertical riser took the chilled air from the test section back to the refrigeration units via an aboveground pipe. Since there was no chilling of the ground beyond the end of the pipeline test section, only a limited frost bulb and resulting heave developed. After day 1060, the pipeline experienced a slow rate of settlement and little heave. These phenomena continued until the end of the monitoring. The settlement occurred not only in the deeper supra-permafrost area but also in the shallower area. The reason for this settlement behavior is unknown; however, this settlement occurred right after an M7.9 earthquake in interior Alaska on November 3, 2002 (Huang et al. 2004).

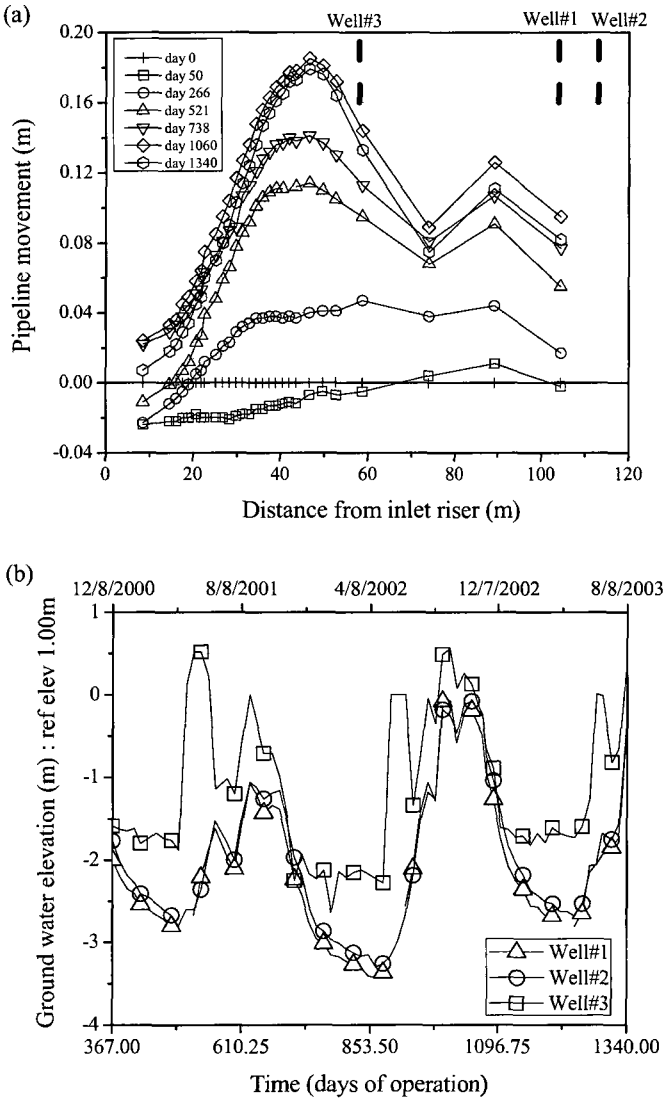

Figure 6.4 Observations (Huang et al. 2004) of (a) pipeline movement profile along the length of the pipeline, and (b) groundwater table elevations.

The main purpose of this study is to predict and examine the soil-pipeline interaction due to differential frost heave, which occurs because the pipeline traverses areas of different permafrost

conditions, by applying a three-dimensional frost-heave model which was developed in this study. Therefore, the area between the shallower and the deeper supra-permafrost area in the UAF frost-heave experiment was chosen for verifying the simulation. The dimensions (x, y, z) of the ground were modeled as 15m x 20m x 50m as shown in Figures 6.5a, 6.5b, and 6.5c. Because of symmetry about the center line, only half of the actual geometry was modeled. For the sake of more reasonable simulations, in this study the pipe was modeled as an octagonal shape using solid mesh.

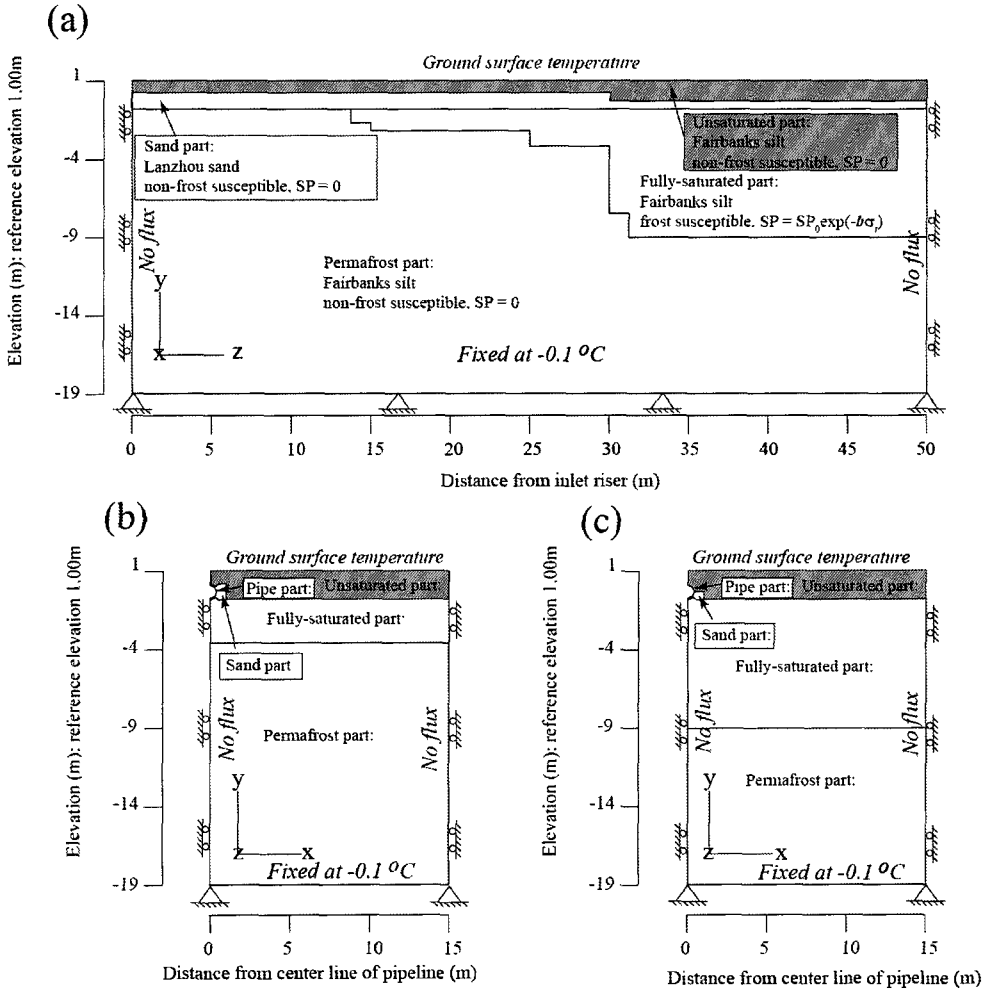

Figure 6.5 The geometry (a) in the longitudinal direction; (b) of the cross section at the rapidly-deepening area (at 30m from the inlet riser); and (c) of the cross section in the deeper supra-permafrost area (beyond 30m from the inlet riser).

The simulations were conducted with a mesh characterized by 11088 rectangular elements and 12913 nodes as shown in Figure 6.6.

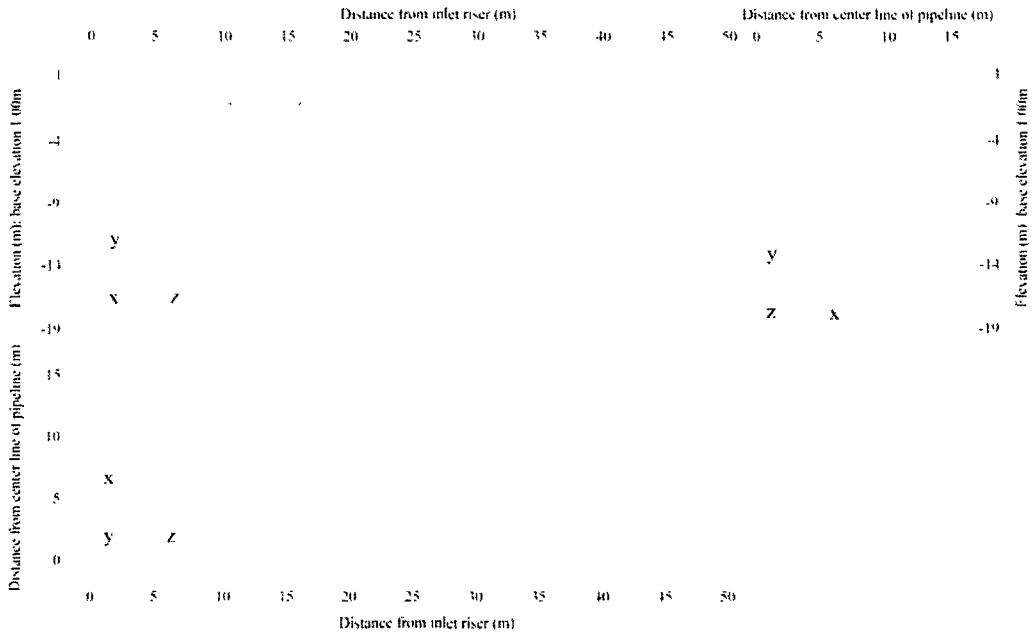

Figure 6.6 The finite-element mesh of the three-dimensional simulation.

6.4.2 Boundary conditions and initial conditions

The types of boundary conditions used for the simulation are illustrated in Figures 6.5a, 6.5b, and 6.5c. Horizontal displacements are not allowed along vertical sides, and the bottom is fixed in both horizontal and vertical directions. The pipeline temperature data collected at 5 points, 2m, 15m, 25m, 40m, and 50m from the inlet riser, were used for the simulation. Since the pipe temperature fluctuated with time, a step temperature was applied to the numerical simulation. The phases were divided into 60-day bins. The average temperature during each phase was defined as input pipeline temperature. With increasing distance from the inlet riser, the pipeline temperature increased. For instance, the input pipeline temperature at 2m from the inlet riser was usually 2°C colder than that at 50m. The 50m modeled pipeline was divided into 10m sections. The input pipeline temperatures were applied to each section uniformly as shown in Figure 6.7.

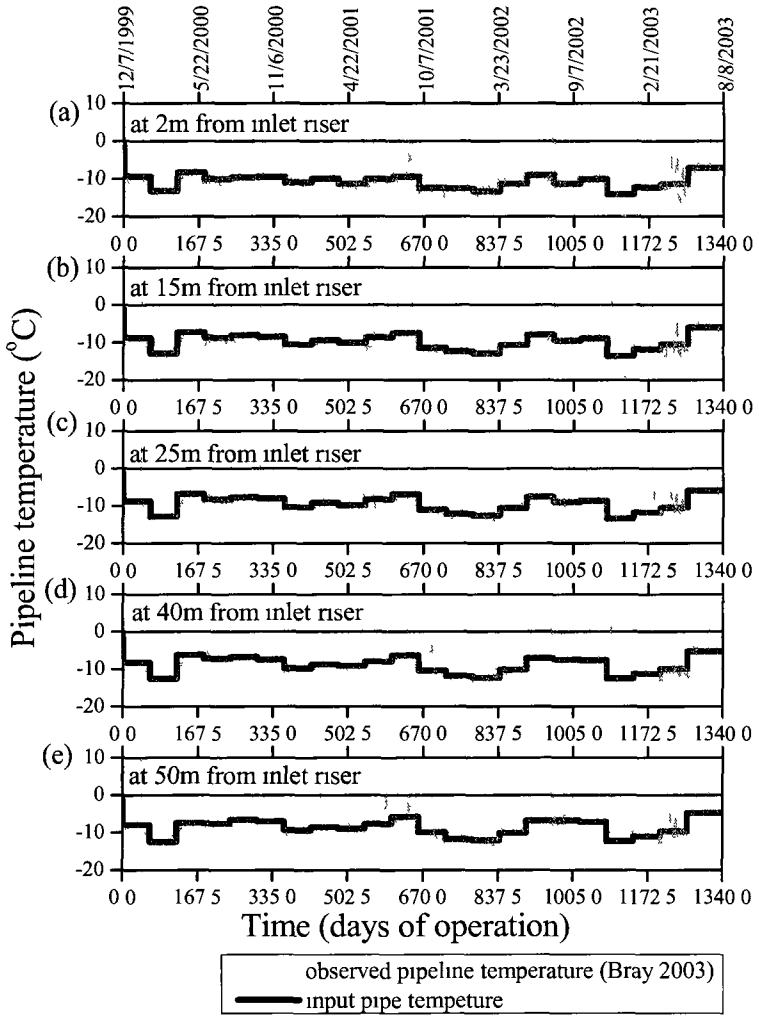

Figure 6 7 Input pipe temperatures (a) from 0 to 10m, (b) from 10 to 20m, (c) from 20 to 30m, (d) from 30 to 40m, and (e) from 40 to 50m

The air temperature was converted to the ground surface temperature by using an n-factor Zero heat flux was applied at the vertical boundaries The initial ground temperature was created by the following procedure First, a temperature of -0 1°C was applied to all nodes in the permafrost part, and 1°C was applied to the rest of the mesh nodes The temperature of the bottom horizontal boundary (20m below the ground surface) was fixed at -0 1°C Then, the simulation was executed without pipe

temperature input for 3 years. Finally, -1°C was applied to an area 1m wide and 1.8m deep at the center. This temperature was assumed because the trench for the pipe was excavated during wintertime.

Figure 6.8a shows an example of foundation heave versus time for three heave gauges, HG-2, HG-4, and HG-5. The heave trend was essentially linear up to day 110, which suggests simple linear volumetric pore-water expansion. An initial stabilization period was observed after day 110. As the freezing front penetrated and passed through the anchor of the heave gauge, the heave gauges could no longer detect any movement between the plate and the anchor. The first plateau occurred in response to the latent heat release of pore water below the groundwater table. Following day 130, HG-2 and HG-4 experienced abrupt jumps caused by ice segregation, but HG-5 did not experience any additional jump in total heave amount (Huang et al. 2004). The observations suggest that in mid-April the groundwater level existed at approximately -1.7m at HG-2 and HG-3, which are located in the shallower supra-permafrost area, and at approximately -2.2m at HG-5, which is located in the deeper supra-permafrost area.

The groundwater table input for the three-dimensional simulation was created using observations at Well #3 located approximately 58m from the inlet riser. In the early part of the summers, an abrupt change of groundwater level was observed. The abrupt change occurred as a result of the release of groundwater that had been confined by the frozen layer during winter. No monitor wells were installed closer than 58m from the inlet riser. However, temperature data from TFC indicated that the active layer completely froze in the shallower supra-permafrost area, suggesting that the groundwater within the shallower supra-permafrost area was also seasonally confined to summer months. Figure 6.8b shows the variation of the groundwater data input for the three-dimensional simulation. Measurement of the first-year cycle was extrapolated using data from the third-year cycle, and a -1.7m elevation was applied to the stabilization period between mid-December and mid-April of the first-year cycle according to the HG analysis presented above. Calculation of segregation heave started when the segregation freezing zone reached the groundwater table.

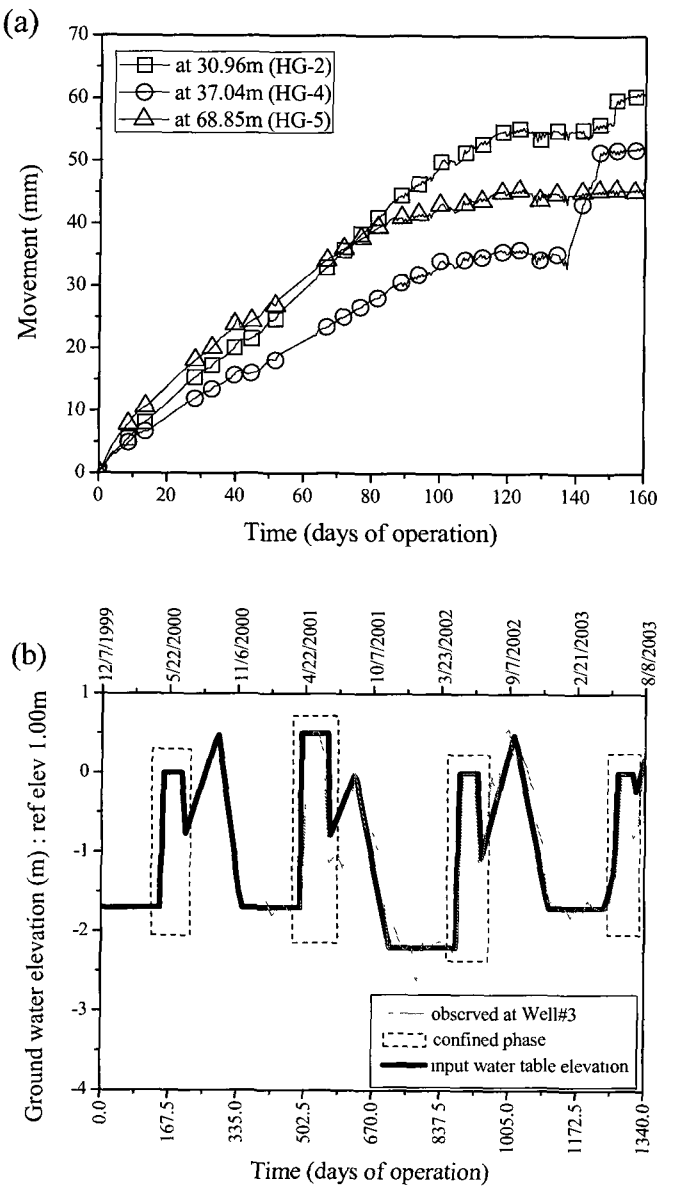

Figure 6.8 (a) HG data showing the foundation heave within the first 1m of native silt below the bottom of the pipeline (Huang et al. 2004); and (b) variation of the input groundwater table elevation.

As shown in eq. [6.3], moisture migration depends not only on $gradT_{sp}$ but also on the stress field. The soil pressure acting on the segregation freezing zone, or σ_t, is composed of two components: (1) induced soil stress due to frost heave at previous time step (σ_{sp}), and (2) overburden pressure of the soil above the segregation freezing zone (σ_{ov}). The overburden pressure is assumed to be a function of freezing depth, bulk and buoyant weights of soil, and groundwater table elevation. The overburden pressure was evaluated as follows:

$$
\begin{cases}
\text{When } X_s(t) < W(t) \\
\sigma_{ov}(t) = \gamma_t(t) \times X(t) \\
\\
\text{When } X_s(t) \geq W(t) \\
\sigma_{ov}(t) = \gamma_t(t) \times W(t) + \gamma_b(t) \times (X(t) - W(t)) \\
\\
\gamma_t(t) = \gamma_d(t) \times (1 + w(t)) \\
\gamma_b(t) = \gamma_d(t) \times (1 + w(t)) - \gamma_w
\end{cases}
\qquad [6.10]
$$

where $W(t)$ = the depth of the groundwater table below the ground surface; $X_s(t)$ = the depth of the segregation freezing zone below the ground surface; $\gamma_d(t)$ = dry soil unit weight; γ_w = water unit weight; $\gamma_t(t)$ = bulk soil unit weight; and $\gamma_b(t)$ = buoyant soil unit weight.

Inline pipe air pressure of 1.4MPa was applied based on the field data (Kim et al. 2005).

6.4.3 Material properties

The simulation domain consisted of frost-susceptible and non-frost-susceptible materials. The initial permafrost conditions were reproduced in response to the permafrost condition. The fully-saturated zone was modeled as frost-susceptible, and the other zones as non-frost-susceptible.

The material properties of the UAF frost-heave experiment were described in previous chapters. Initial dry densities of the Fairbanks silt and Lanzhou sand were calculated as 1308 and 1894kg/m^3, respectively. The thermal material properties were summarized in Table 5.2.

The following temperature- (T-) dependent mechanical properties were used for the bilinear elastic stress-strain relationships shown in Figure 5.2.

Fairbanks silt:

The temperature of the Fairbanks silt at peak strength (σ_m) was determined as:

[6.11] $$\sigma_m = \left(2.64\times10^{-9}\right)\times\left(-T\right)^{0.998}$$

where σ_m was in kPa. The peak strength of the unsaturated part was modeled as 50% of the peak strength of the fully-saturated part.

The yield stress (σ_y) was estimated in terms of the initial dry density (ρ_d = 1308kg/m^3) as:

[6.12] $$\sigma_y = \left(2.150 - 0.00115\times\rho_d\right)\times\sigma_m$$

The temperature-dependent Young's modulus (E) of Fairbanks silt was determined as:

[6.13] $$E = 740\times\left(1.1\times10^{-3}\right)^{0.122}\times\left(-T\right)^{0.624}$$

where E was in MPa.

When Young's modulus of frozen Fairbanks silt as determined by eq. [6.13] was smaller than 11.2MPa, the value was assumed to be equal to 11.2MPa. Poisson's ratio was taken as μ = 0.3 for both the frozen and unfrozen case.

Sand:

The long-term yield strength and elastic modulus are temperature-dependent and were determined as:

[6.14] $$\begin{cases}\sigma_y = 3800\times\left(-T\right)^{0.466}\times\left(0.33\times10^{-2}\right)^{0.204+0.0066\times T}\\ E = 44\times\left(-T\right)^{0.684}\end{cases}$$

where σ_y was in kPa, and E was in MPa.

When the temperature was warmer than -0.1°C, the peak strength of Lanzhou sand at -0.1°C was used. Young's modulus of unfrozen Lanzhou sand was assumed to be constant and equal to 20MPa. When Young's modulus of frozen Lanzhou sand determined by eq. [6.14] was smaller than 20MPa, the value was assumed to be equal to 20MPa.

The post-yield modulus of Lanzhou sand was modeled as zero. Poisson's ratio was taken as μ = 0.3 for both the frozen and unfrozen cases.

Steel:

The mechanical properties of steel were specified as:

[6.15] $$\begin{cases}\sigma_y = 482\ \text{MPa}\\ E = 206\ \text{GPa}\end{cases}$$

The post-yield modulus of steel was modeled as zero. Poisson's ratio was taken as μ = 0.3.

6.4.4 SP values

Nixon (2003) reported that the relationship between SP and soil pressure was established for the undisturbed Fairbanks silt as:

$$[6.16] \quad SP = 262 \times 10^{-5} \exp(-b \times \sigma_t) \qquad (\text{in mm}^2/(\text{sec} \times {}^\circ\text{C}))$$

where $b = 0.02596\text{kPa}^{-1}$; and σ_t is in kPa.

Using the SP values in eq. [6.16], the author successfully simulated the pipeline movement in two-dimension at TFA compared with the field-heave measurements of HR-25, which was located 58m from the inlet riser (Kim et al. 2008). However, pipeline heave was non-uniform along the pipe axis as shown in Figure 6.4a. For instance, the heave at HR-22, was located 46.615m from the inlet riser, was greater than that at any other location. It is common that considerable variation in field conditions can exist even within a small geographical area, albeit the soils may be categorically classified as belonging to the same group. Although most soil profiles are layered and non-uniform, they are often represented by a uniform soil profile with average properties as shown in Figures 6.5a, 6.5b, and 6.5c. In this simulation, SP_0 was evaluated by using a multiplication factor $SI = 1.0$, 1.5, and 2.0, and by using a constant b value for the three-dimensional frost-heave simulations.

Figures 6.9a and 6.9b show a comparison of observed and simulated pipeline movement at HR-16 and HR-22, located at 35.945m and 46.615m from the inlet riser, respectively. HR-16 was located at TFB and the maximum heave was observed at HR-22. An anisotropic expansion parameter $\zeta = 0.9$ was used for the simulations. Two unexpected settlements were observed: initial pipeline settlement, which continued up to day 90, and settlement at a slow rate after day 1060, possibly due to a large earthquake. The proposed model did not predict those two events. Although the proposed model exhibited these shortcomings, the maximum pipeline movements observed on day 1060 were estimated well. The maximum amount of the simulated heave using $SI = 1.5$ was only 1.56% smaller than the observation at HR-16 and 2.14% smaller at HR-22 on day 1060. As expected, the simulations showed higher heave with increasing SI values. However, the simulated heave at $SI = 2.0$ was approximately 40% higher than the heave at $SI = 1.0$ despite the twice of the SP value.

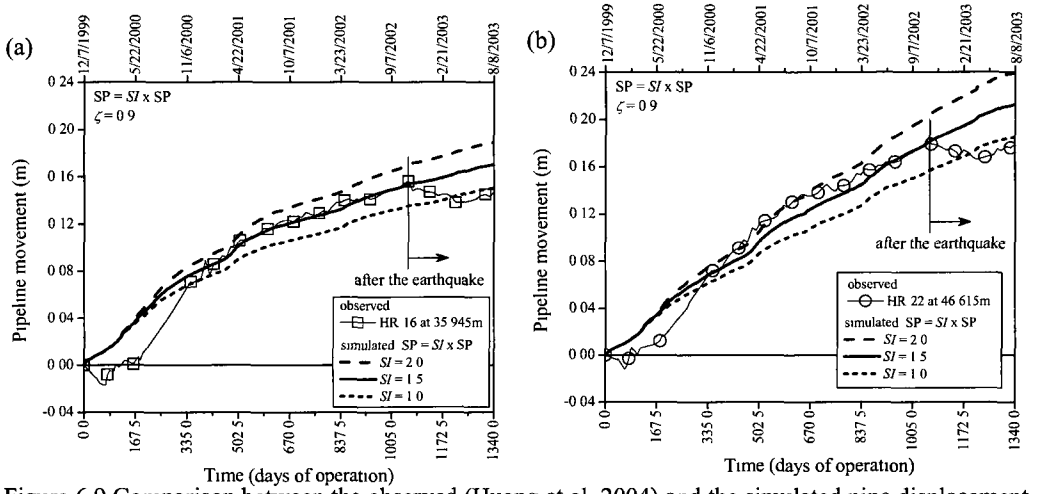

Figure 6.9 Comparison between the observed (Huang et al. 2004) and the simulated pipe displacement using different SP values for the UAF frost-heave experiment: (a) at HR-16 (TFB); and (b) at HR-22.

Figures 6.10a and 6.10b summarize the simulated freezing depth and temperature gradient of the segregation freezing zone ($gradT_{sp}$) at 1m from the centerline of the pipe using SI = 1.5. The simulated freezing depth agreed well with the observations. The $gradT_{sp}$ is required by the SP porosity growth function. The $gradT_{sp}$ obtained from the simulations also agreed fairly well with the observed values. Therefore, the SP values were utilized with SI = 1.5 in this study.

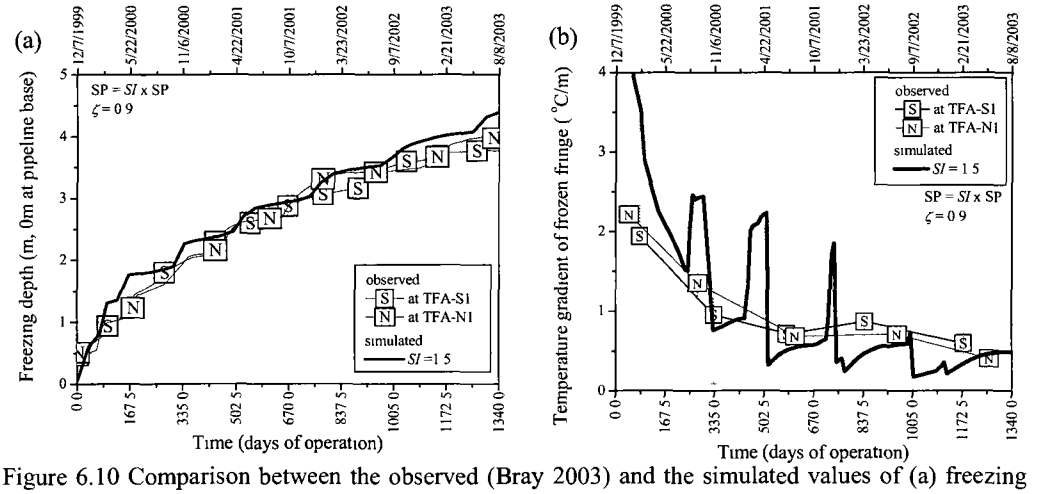

Figure 6.10 Comparison between the observed (Bray 2003) and the simulated values of (a) freezing depth and (b) temperature gradient of frozen fringe at 1m from the pipeline center at TFB.

6.4.5 Effect of the change of anisotropic expansion parameter

The anisotropic expansion parameter, ζ, was empirically determined as 0.9 in the two-dimensional simulations. A sensitivity analysis was conducted to evaluate how the developed model responds to the variation of the anisotropic parameter in the three-dimensional simulations. The coefficient of variation of the simulated total heave (COV_h) was calculated using eq. [5.27]. The mean value of ζ and the coefficient of variation of the anisotropic expansion parameter (COV_ζ) were assumed as 0.75 and 20%, respectively.

Figures 6.11a and 6.11b show the comparison between the simulated and observed pipeline movement presumably caused by the M7.9 earthquake at HR-16 and HR-22, which were the locations of the TFB and the maximum observed heave, respectively. The variations of the simulated heaves were very close to each other regardless of the type of volumetric expansion. The COV_h was calculated as 1.39% and 2.06% at HR-16 and HR-22, respectively. Since the COV_h were one order of magnitude smaller than the COV_ζ (= 20%), the result in the model response was mathematically stable. ζ = 0.9 was empirically identified in both the three-dimensional and the two-dimensional frost-heave simulations.

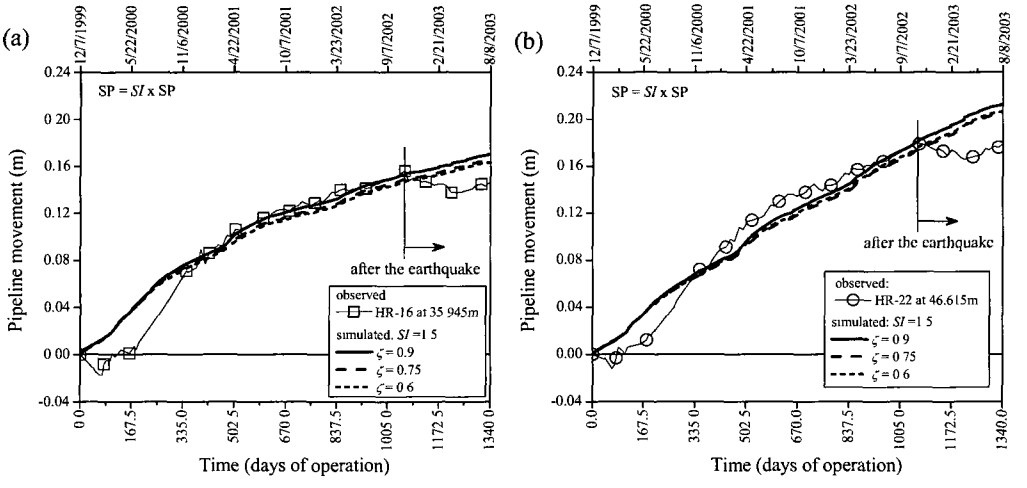

Figure 6.11 Influence of strain-rate dependency on pipeline movement: (a) at HR-16 (TFB); and (b) at HR-22.

6.5 Thermal analysis

The developed three-dimensional model was based on only conduction in heat transfer analysis, with isotropic thermal properties. Temperature distribution and freezing-front penetration in the deeper supra-permafrost area were compared using TFB data. Figures 6.12, 6.13, and 6.14 show the comparison between observed and simulated temperature profiles of TFB in mid-December for 3 years. During the first year of operation, the soil mass beneath the pipe underwent progressive cooling resulting in a uniform temperature near freezing. After the first year of operation, no significant cooling of the soil mass beyond the frost bulb occurred. The simulated progressive cooling effect was verified by the distributions of the isotherms at 0.15°C above freezing (i.e. the solid line in Figures 6.12, 6.13, and 6.14). Although there were no direct temperature measurements deeper than -7.0m, the simulated results showed a similar temperature trend.

Since the thermistor distribution was coarse above the pipe at 3m south of the center line, the observed temperature distribution deviated from the simulated results near the surface (Figure 6.3a). However, the frost-bulb shape was reproduced according to the freezing-front distribution that existed at depths deeper than the pipeline. The simulated -1, -3, and -5°C isotherms agreed with the field observations that were made at depths deeper than the pipeline as well.

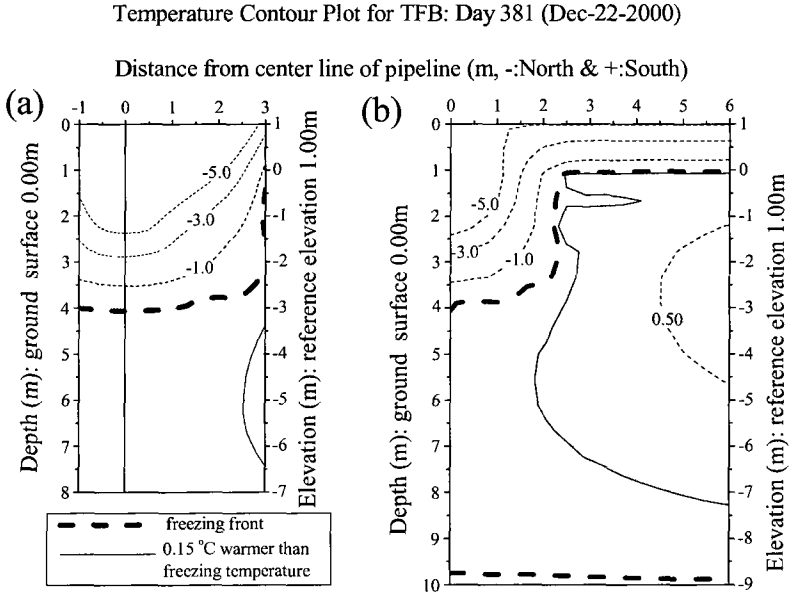

Figure 6.12 Temperature distribution at TFB in early December of the first year cycle with comparison between (a) the observed (Bray 2003) and (b) the simulated results.

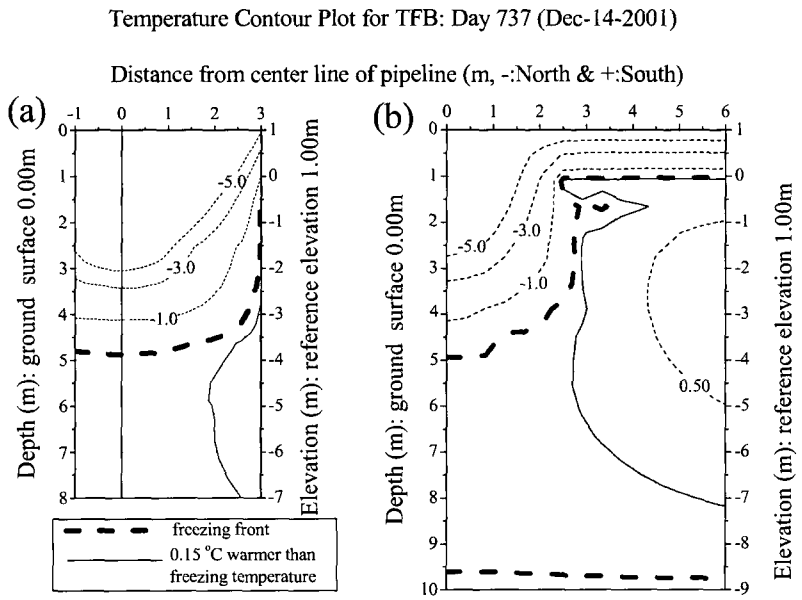

Figure 6.13 Temperature distribution at TFB in early December of the first-year cycle with comparison between (a) the observed (Bray 2003) and (b) the simulated results.

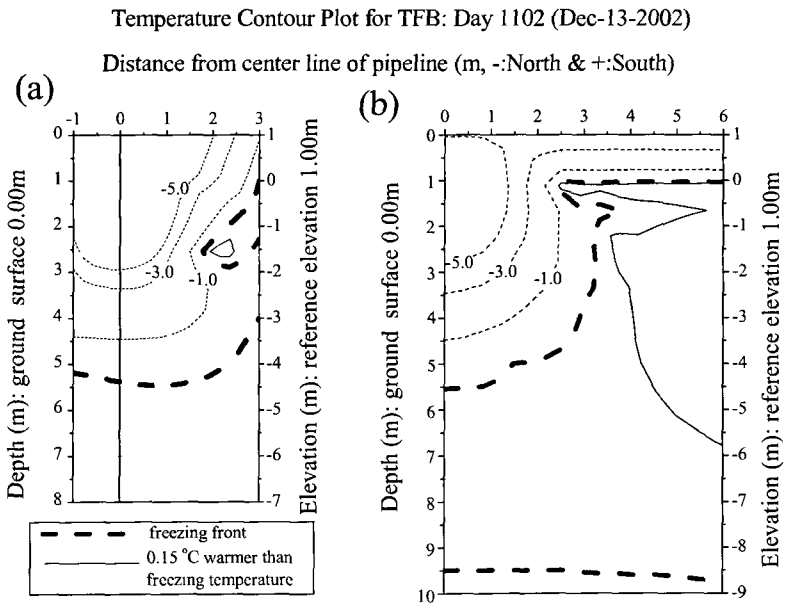

Figure 6.14 Temperature distribution at TFB in early December of the second-year cycle with comparison between (a) the observed (Bray 2003) and (b) the simulated results.

Next, temperature distributions were compared in the shallower supra-permafrost area using TFC data. Figures 6.15, 6.16, and 6.17 show the comparison between observed and simulated temperature contour profiles of TFC in the middle of December for 3 years. The rate of thermal influence at TFC was much greater than that at TFB because the latent heat effect was less significant in the initially-frozen soil than in the initially-unfrozen soil. For instance, the isotherm propagation of "-0.3°C colder than freezing temperature" reached 6m from the center line in the second-year cycle (i.e. solid lines in Figures 6.15, 6.16, and 6.17). Furthermore, it can be seen that the permafrost region cooled down and became more thermally stable as freezing propagated from the observed thawed layer.

The overall distributions of each isotherm indicated by the simulation were consistent with the observations at both TFB and TFC. Therefore, the initial permafrost condition and boundary conditions for the simulation were assumed to be reasonable.

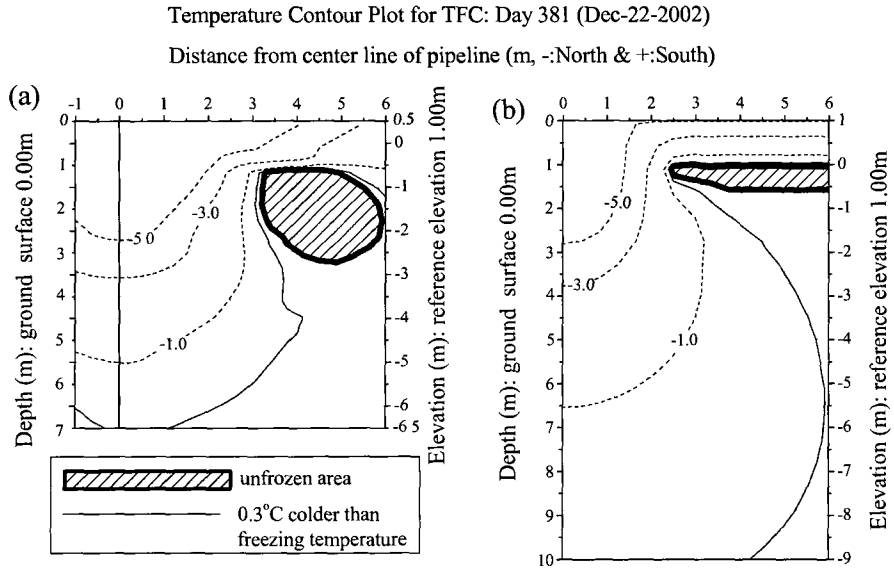

Figure 6.15 Temperature distribution at TFC in early December of the first-year cycle with comparison between (a) the observed (Bray 2003) and (b) the simulated results.

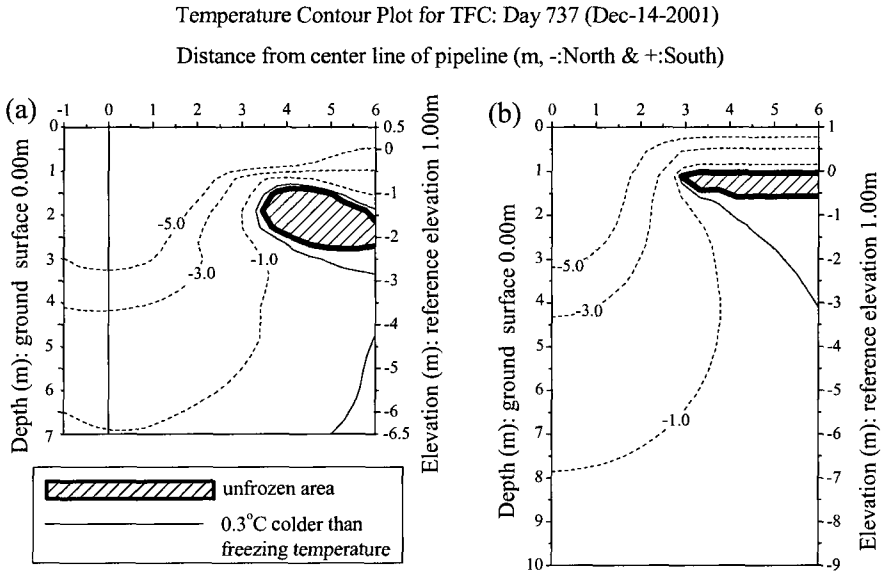

Figure 6.16 Temperature distribution at TFC in early December of the second-year cycle with comparison between (a) the observed (Bray 2003) and (b) the simulated results.

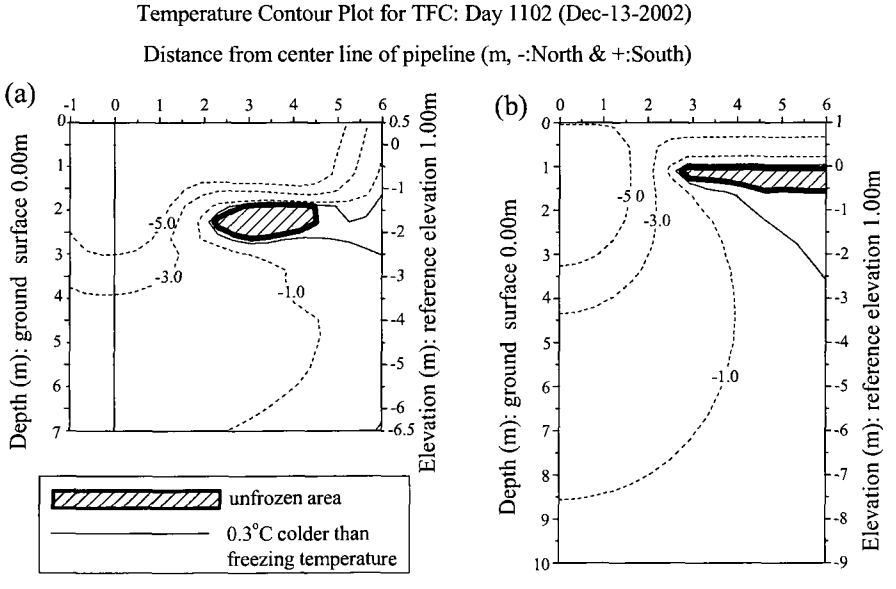

Figure 6.17 Temperature distribution at TFC in early December of the third-year cycle with comparison between (a) the observed (Bray 2003) and (b) the simulated results.

Since the distances between the thermal fences were too large, a detailed analysis could not be performed using the observed longitudinal (parallel to the longitudinal axis of the pipeline) thermal data. Therefore, Figure 6.18 shows only the simulated longitudinal temperature contour plots along the pipeline center line.

The freezing front did not reach the material boundary, and the *in-situ* freezing zone widely distributed between 25 and 30m from the inlet riser in the first-year cycle (Figure 6.18a). The *in-situ* freezing zone is in an unstable, quasi-steady thermal state that is very sensitive to changes in the surface conditions. As the existence of the chilled pipeline prevented the soil mass beneath the pipeline from warming up throughout the experiment, the size of the *in-situ* freezing zone decreased with increasing time (Figures 6.18b and 6.18c). A distinct vertical thermal boundary developed 30m from the inlet riser. The vertical thermal boundary stabilized in the first-year cycle and hardly penetrated the unfrozen soil after stabilization because of the effect of latent heat release.

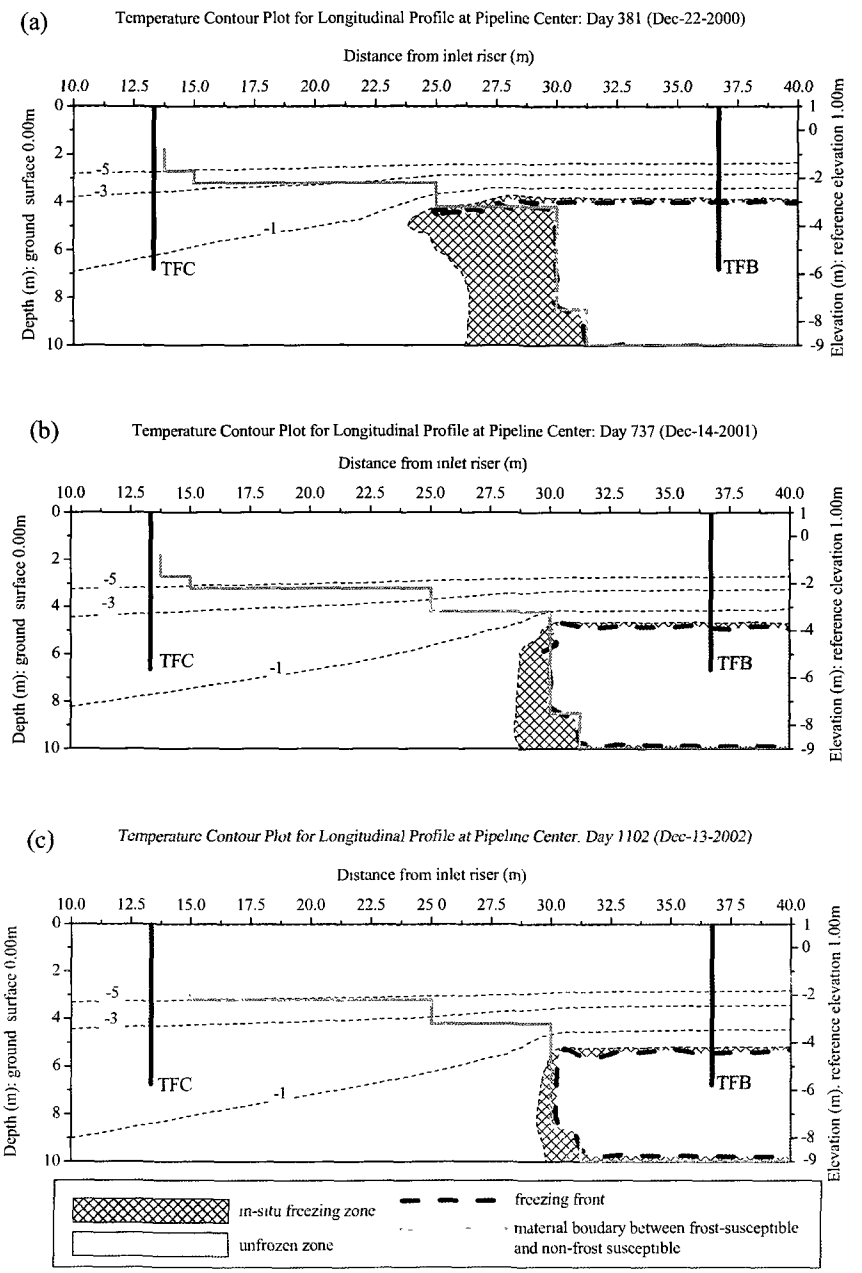

Figure 6.18 Distribution of simulated temperature at the center line in early December of (a) the first-year cycle, (b) the second-year cycle, and (c) the third-year cycle.

6.6 Differential frost heave analysis

Deeper supra-permafrost area:

The analysis of the simulation is now extended to accommodate constitutive responses of the soils in the frost-susceptible and non-frost-susceptible areas and the flexural response of the buried pipeline.

Figure 6.19 shows the comparison between observed and simulated pipeline movement in the deeper supra-permafrost area. Differential frost heave was analyzed using HR data. HR-14, HR-16, and HR-19 (i.e. located 32.9m, 35.945m, and 40.515m from the inlet riser, respectively) were chosen as representative points for pipeline movements in the deeper supra-permafrost area. The simulated results had some shortcomings. The simulation did not predict the initial settlement, which occurred until day 90. Also, from day 90 until day 400, the heave rates calculated by the proposed model were lower than the observations. This is probably because of the different frost-heave susceptibilities of different soil layers.

Differential pipeline movements were observed after day 400. The main objective of this study is to examine pipeline movement due to differential frost heave. When the segregation freezing zone reached the permafrost table between 25m and 30m from the inlet riser, the frost-susceptible zone did not experience any more volumetric expansion. Therefore, pipeline movements in the deeper supra-permafrost area were anchored by the frozen soil. As shown in Figure 6.18a, only a small frost-susceptible layer remained unfrozen in place between 25m and 30m from the inlet riser on day 381. Therefore, the proposed model could likely simulate the beginning of the differential pipeline movement. The simulated heave rate agreed well with the observation at each HR after day 381. On day 1060, HR-14, HR-16, and HR-19 showed maximum heaves of 0.136m, 0.156m, and 0.172m, respectively. The maximum pipeline heaves were simulated to be 0.126m, 0.154m, and 0.170m at each HR location, in good agreement with the observations on day 1060. As mentioned above, the pipeline experienced a slow rate of settlement after day 1060 until the end of the experiment; this was possibly due to the earthquake, which the proposed model could not simulate. Although the proposed model showed some limitations, it should be noted that the proposed model could simulate the differential pipeline movements in the deeper supra-permafrost area.

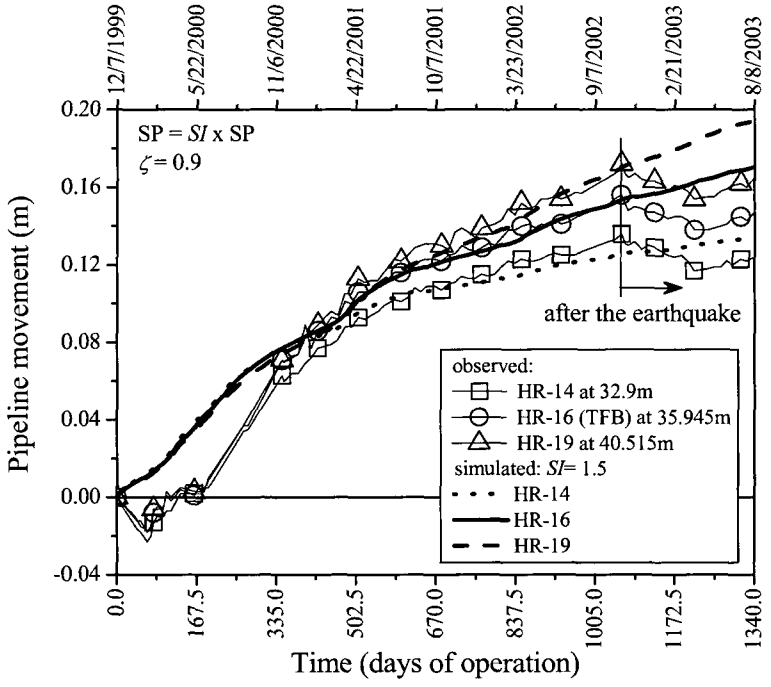

Figure 6.19 Comparison between the observed (Huang et al. 2004) and the simulated pipe displacement in the deeper supra-permafrost area.

Shallower supra-permafrost area:

Figure 6.20a shows the comparison between observed and simulated pipe movement in the shallower supra-permafrost area. HR-1 and HR-2 (i.e. located 8.53m and 14.63m from the inlet riser, respectively) were chosen as representative points for pipeline movement in the shallower supra-permafrost area. The HRs in the shallower supra-permafrost area experienced initial settlement similar to that of HRs in the deeper supra-permafrost area. The initial settlement of approximately 0.025m was followed by a period of very slow upward heaving that lasted until day 510. In between day 510 and day 542, an abrupt upheaval was observed in the shallower supra-permafrost area as shown in Figure 6.20b. After this abrupt upheaval, only a small amount of upward pipeline movement occurred of less than 0.005m until the date of the earthquake. After the earthquake, no additional heave occurred; rather, there was a gradual settlement. The simulated heave at TFC (i.e. located at 13m from the inlet riser) was less than 0.002m throughout the experiment; the simulation did not predict the subtle variations of the observed heaves.

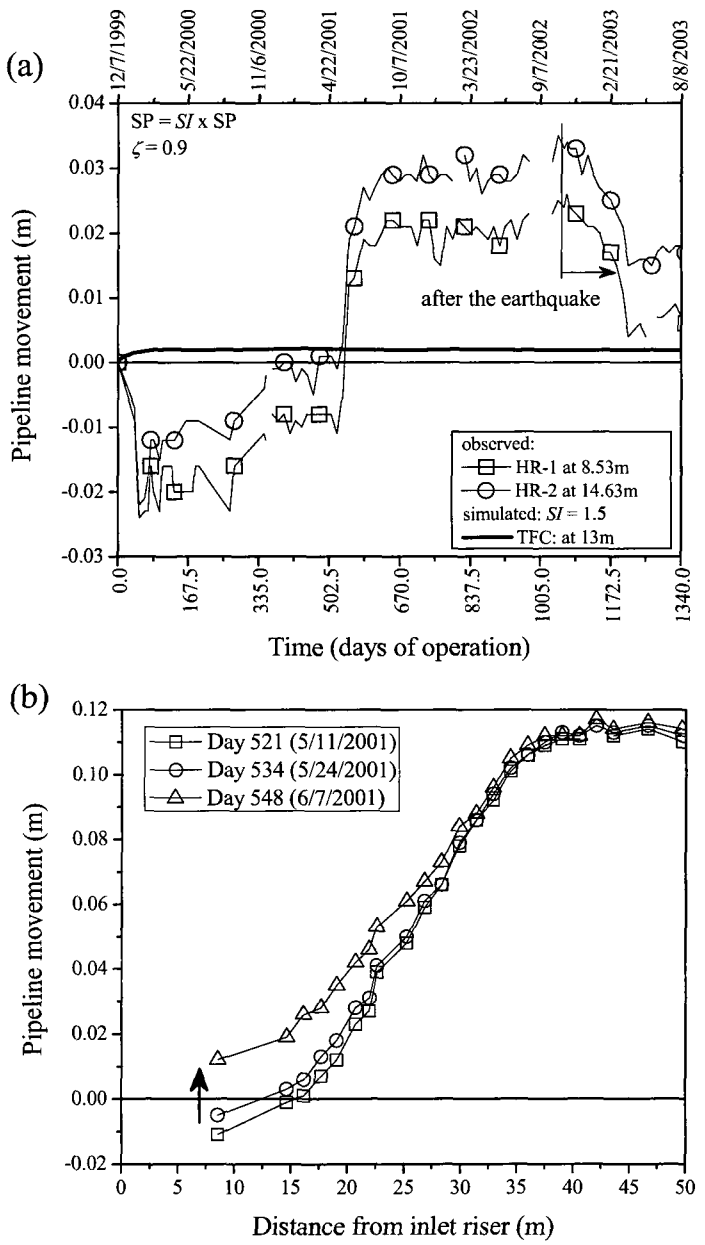

Figure 6.20 (a) Comparison between the observed (Huang et al. 2004) and the simulated pipe displacement in the deeper supra-permafrost area; and (b) pipeline movement profile during the abrupt upheaval in the shallower supra-permafrost area.

6.7 Quantitative analysis of abrupt pipeline upheaval movement in shallower supra-permafrost area

Although pipeline movement is of importance, it is even more important for pipeline designers to know what the bending moment will be. Six-order polynomial fitting analyses were performed using the pipeline movement results. Then the bending moment due to differential frost heave could be determined from the second derivative of the fitted pipeline profiles.

Figure 6.21a shows the comparison between observed and simulated profiles of pipeline movement on day 521, before the abrupt upheaval in the shallower permafrost area. The simulated results agreed well with the observed results. The bending moment profiles determined by the fitting procedure were in agreement with the profile determined from SG data measured in the longitudinal direction at 9 locations (i.e. 18.53, 22.1, 24, 26.24, 30.68, 32.16, 33.51, 36.8, and 42.75m from the inlet riser) as shown in Figure 6.21b.

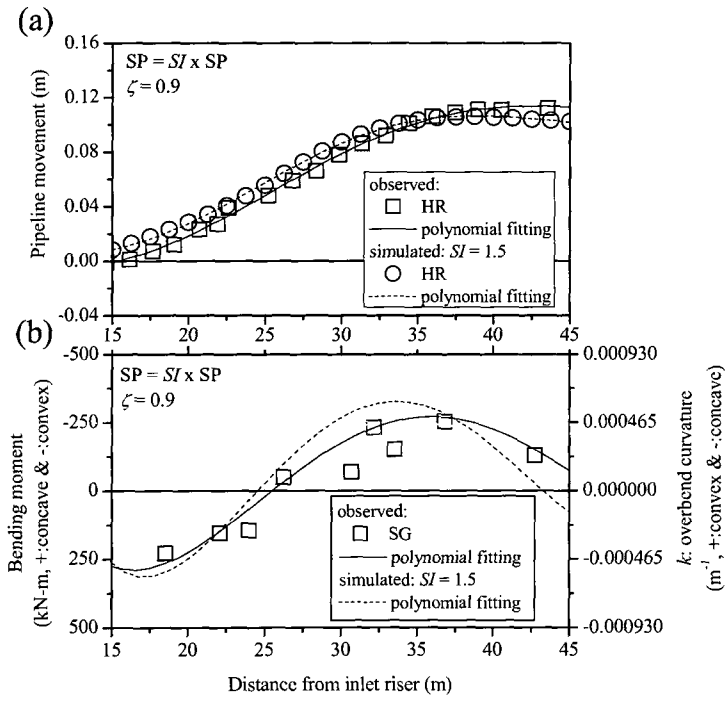

Figure 6.21 Comparison between observed (Huang et al. 2004) and simulated distribution of (a) pipe movement; and (b) bending moment along the pipeline on day 521, before the abrupt upheaval event.

Figures 6.22a and 6.22b show the comparison between observed and simulated profiles of pipeline movement and bending moment, respectively, on day 548, after the abrupt upheaval movement. The bending moment profiles from observations show that the pipeline experienced relaxation in the shallower supra-permafrost area due to the abrupt upheaval, and the simulated bending moment in the shallower supra-permafrost area was approximately three times larger than the observations.

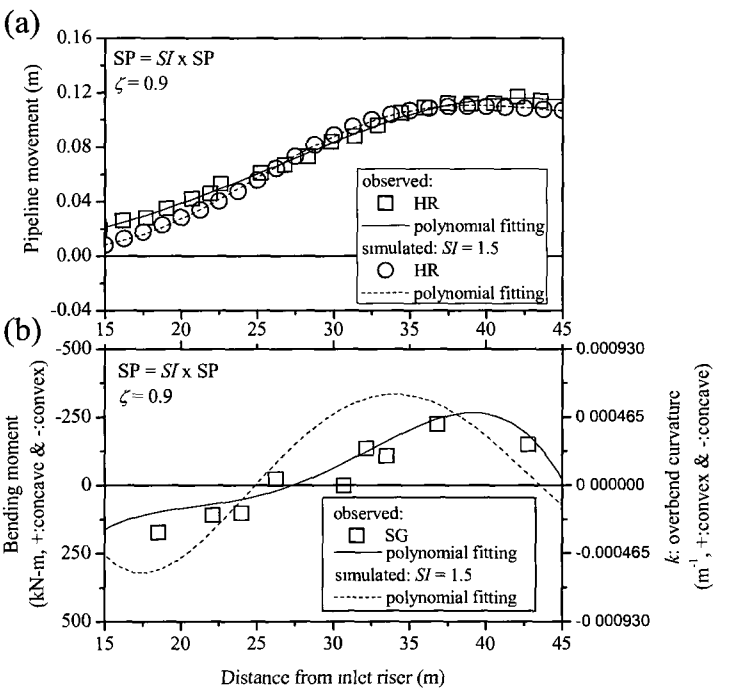

Figure 6.22 Comparison between observed (Huang et al. 2004) and simulated distribution of (a) pipe movement; and (b) bending moment along the pipeline on day 534, which is after the abrupt upheaval event.

The most likely explanation for the abrupt pipeline movement in the shallower permafrost area is uplift buckling. Palmer and Williams (2003) developed a simple model to evaluate abrupt upheaval movement of a pipeline. Uplift buckling is caused by high axial stresses in the pipe resulting from a large difference between installation and operation temperatures, coupled with soil resistance that is inadequate to resist the tendency for the pipe to buckle upwards. The mechanism for abrupt

upheaval movement was modeled as a combination of longitudinal compressive stress and overbend irregularities in the profile. In the model, the pipeline was assumed to be a thin-walled cylindrical shell, and to remain elastic. The induced longitudinal stress has two components: inline pipe air pressure and thermal expansion. Following the customary sign convention in this study, compression is considered as positive.

Consider an element of pipeline in an arbitrary profile defined by a vertical distance y (y: measured positive upwards from a datum), which is a function of longitudinal distance z. In Figure 6.23, p is the longitudinal stress, S is the shear force, q is the external vertical force per unit length, and M is the bending moment.

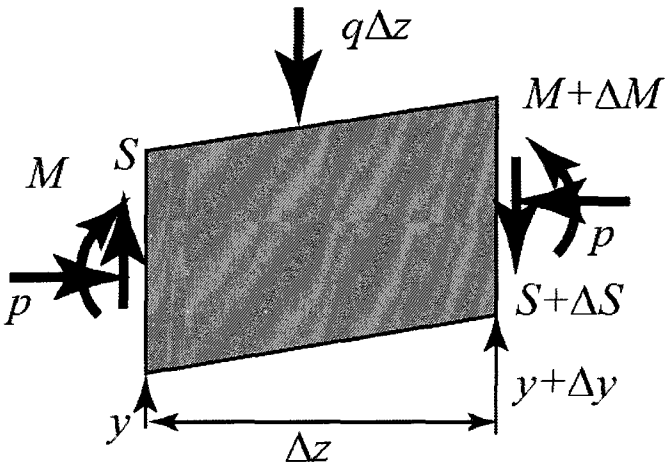

Figure 6.23 Pipeline element (modified from Palmer and William 2003).

The vertical force on the element is described as:

$$[6.17] \quad q = -\frac{\Delta S}{\Delta z}$$

Then, the moment equilibrium of the element is described as:

$$[6.18] \quad p\frac{\Delta y}{\Delta z} + \frac{\Delta M}{\Delta z} - S = 0$$

Differentiating eq. [6.18] and substituting it into eq. [6.17] yields the following;

$$[6.19] \quad q = -p\frac{\Delta^2 y}{\Delta z^2} - \frac{\Delta^2 M}{\Delta z^2}$$

if the pipe remains elastic,

$$[6.20] \quad M = F\frac{\Delta^2 y}{\Delta z^2}$$

where flexural rigidity (F) for a thin-walled elastic cylinder with elastic modulus (E) is given by,

$$[6.21] \quad F = \frac{\pi\Theta^3 \vartheta E}{8}$$

where Θ = mean diameter (twice the mean radius, measured from the center to halfway through the wall); and ϑ = wall thickness.

And then,

$$[6.22] \quad q = -p\frac{\Delta^2 y}{\Delta z^2} - F\frac{\Delta^4 y}{\Delta z^4}$$

In eqs. [6.19] and [6.22], the first term on the right is a curvature term, the product of the longitudinal stress and the curvature $\Delta^2 y/\Delta z^2$, which is positive for concave curvature and negative for convex curvature. The pipeline tends to push upwards due to frost heave, and therefore a positive value of q is required to hold it down. The less obvious second term is proportional to changes in shear force, and vanishes when the curvature is uniform.

When frost heave lifts the pipeline, the deflection profile from the initial position is idealized as an arc of a circle with uniform overbend curvature k (so that $\Delta^2 y/\Delta z^2$ is $-k$ and the overbend radius is $1/k$).

The force per unit length available to hold the pipeline down is the sum of the pipeline weight per unit length (ω) and the uplift resistance per unit length provided by the overburden pressure. The uplift resistance per unit length (η) is calculated as:

$$[6.23] \quad \eta = \gamma_t \Theta \Xi \left(1 + f\frac{\Xi}{\Theta}\right)$$

where Ξ = the thickness of the overburden pressure (measured from the top of the pipeline to the ground surface); and f = an uplift resistance coefficient determined experimentally.

Assembling the results from eqs. [6.19], [6.22], and [6.23], the pipe becomes unstable when

$$[6.24] \quad -p\frac{\Delta^2 y}{\Delta z^2} = q > \omega + \eta$$

$$[6.25] \quad \frac{\pi\Theta^2}{4}(1-2\mu)pk > \omega + \gamma_t \Theta \Xi \left(1 + f\frac{\Xi}{\Theta}\right)$$

which can be rewritten as:

$$[6.26] \quad k > \frac{1}{1-2\mu}\frac{\gamma_t}{p}\left[\frac{\omega}{\frac{\pi\Theta^2\gamma_t}{4}} + \frac{4}{\pi}\frac{\Xi}{\Theta}\left(1+f\frac{\Xi}{\Theta}\right)\right]$$

The non-dimensional term $\omega/(\pi\Theta^2\gamma_t/4)$ in eq. [6.26] has a simple physical interpretation; it is the relative density of the pipeline, relative to the soil it is buried in. The last term highlights the importance of the ratio of overburden pressure cover thickness to pipeline diameter.

As an example, Figure 6.24 presents observations at 24m from the inlet riser between day 518 and day 553, during which period the abrupt upheaval occurred. The 5-week history of pipeline temperature and inline pressure is shown in Figure 6.24a. Pipeline temperature suddenly increased from approximately -10°C on day 531 to 6°C on day 537. The axial stress increased in response to the pipeline temperature fluctuation during this time, as shown in Figure 6.24b. As the test was operated at a relatively constant pressure of approximately 1.4MPa during this period of time, it is safe to say that the compressive axial stress was induced mainly due to thermal expansion.

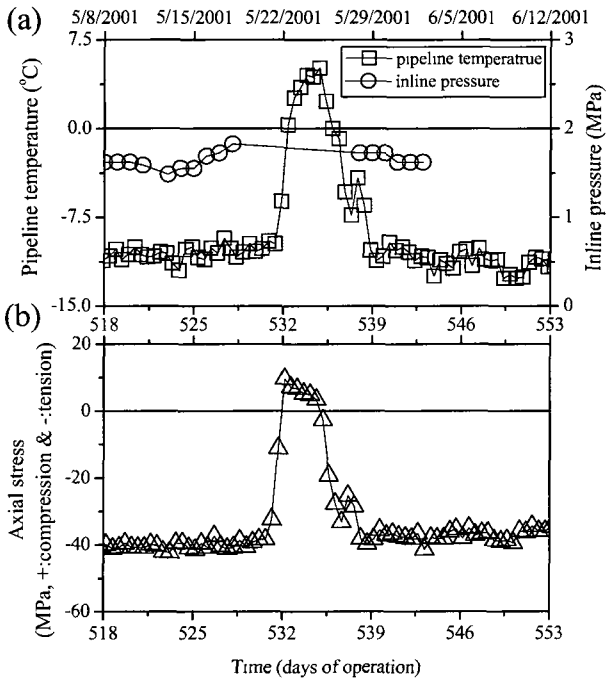

Figure 6.24 History of (a) the observed pipeline temperature and inline pipe air pressure; and (b) axial stress at 24m from the inlet riser during the abrupt upheaval event.

For the evaluation of the abrupt uplift in the shallower permafrost area, the input values for eq. [6.26] were determined as: γ_t = 18kN/m^3, p = 10MPa, ω = 2.0kN/m, Ξ = 0.9m, Θ = 0.905m, μ = 0.3, and f = 0.5 (Palmer and William 2003). The calculated overbend curvature at which the pipeline becomes unstable is 0.0093m^{-1}. On day 543, the observed maximum overbend curvature was induced around 35m from the inlet riser as approximately 0.000465m^{-1}, which is one order of magnitude smaller than the calculated value at which instability occurs. Furthermore, as shown in Figure 6.20b, little upheaval occurred around 35m from the inlet riser between day 521 and day 548. However, at the location close to the inlet riser, larger upheaval was observed. The maximum movement was approximately 0.025m around 15m from the inlet riser.

Figure 6.25 shows a schematic of abrupt upheaval: as the longitudinal compressive stress is induced, the pipe moves inward against the longitudinal resistance of the surrounding soil; then the upheaval grows in the shallower supra-permafrost area. Since the first station of pipeline movement (HR-1) was located 8.53m from the inlet riser, there were no direct measurements around the inlet pipeline riser. As shown in Figure 6.4a, the pipeline initially experienced non-uniform settlement; for instance, 0.02m at HR-1 and 0.01m at HR-2. Over the distance between the inlet riser and HR-1, the calculated curvature is 0.0093m^{-1}; at this curvature the pipeline becomes unstable using the input values above. This curvature corresponds to a 0.083m high "hill" profile. Any overbend that becomes more sharply curved than this will become unstable.

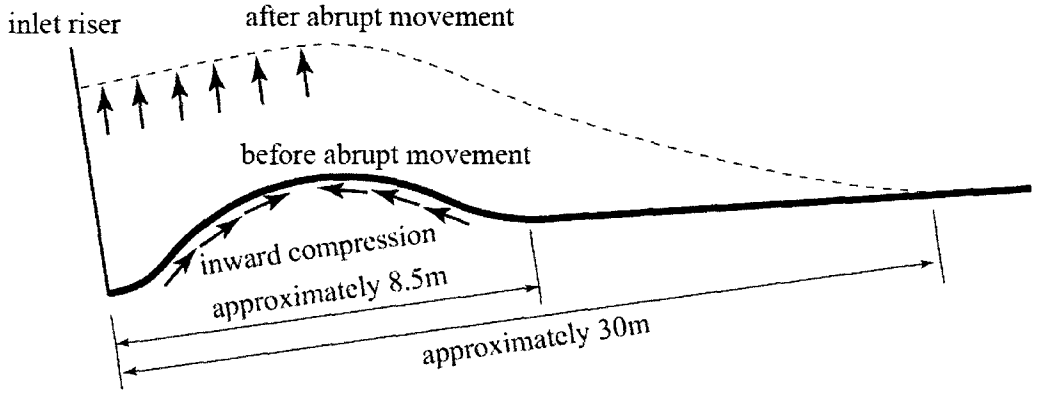

Figure 6.25 Schematic drawing of abrupt pipeline movement (not to scale).

Figures 6.26a and 6.26b show the comparison between observed and simulated profiles of pipeline movement and bending moment, respectively, on day 1060, which was two days before the M7.9 earthquake in interior Alaska on November 3, 2002. The simulated heave profile agreed well

with the observed profile in the deeper supra-permafrost area. Eventually, without considering the stress relaxation, the simulation overestimated the bending moment by about 60% in the shallower supra-permafrost area. The results suggest that the abrupt upheaval observed in the UAF frost-heave experiment gave a conservative estimate of pipeline bending. However, it is wrong to conclude that uplift buckling will always yield conservative results. For instance, uplift of 1.1m or more was observed at one location (kilometer post 5.2) of the Norman Wells oil pipeline (Nixon and Burgess 1999). This uplift event was extremely dramatic, resulting in the pipeline being exposed above the surrounding ground surface.

When pipeline temperature fluctuates during arctic pipeline operations, compressive longitudinal stress will likely be induced in the pipeline. Even though many numerical simulations have been done to predict vertical pipeline movement due to differential frost heave, it is undoubtedly critical for arctic pipeline designers to evaluate the effect of the longitudinal stress induced by temperature fluctuation on differential pipeline movement.

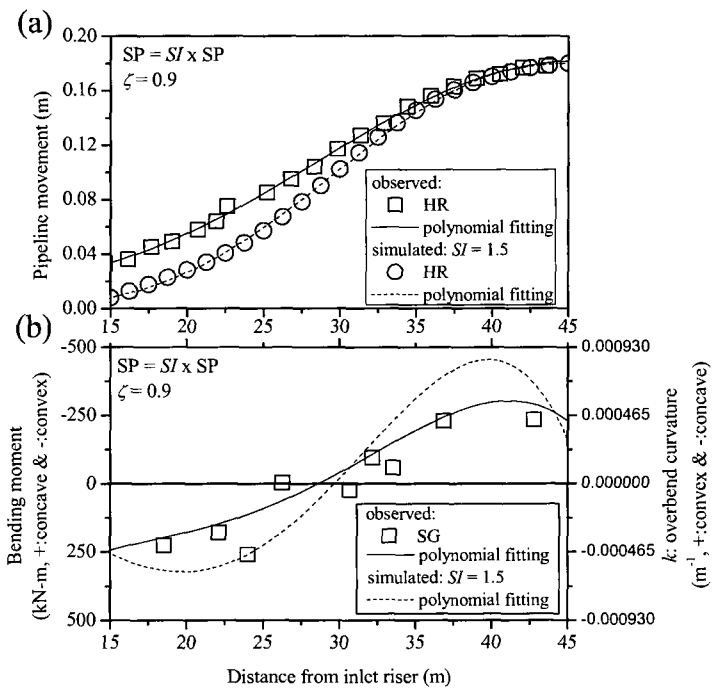

Figure 6.26 Comparison between observed (Huang et al. 2004) and simulated distribution of (a) pipe movement; and (b) bending moment along the pipeline on day 1060, which is two days before the earthquake.

6.8 Frost heave prediction in discontinuous permafrost

The verification analysis using results from the UAF frost-heave experiment supported the developed three-dimensional frost-heave model. A frost-heave prediction was conducted in order to answer two important questions. First, how much frost heave can be expected to occur over the lifetime of a pipeline? And second, how much induced bending will occur due to differential frost heave at the discontinuous permafrost boundary?

Although the UAF frost-heave experiment ceased on day 1340, a 20-year simulation was conducted to predict the differential frost heave. The same histories of air temperature and groundwater level were used repeatedly for the prediction. The 50m modeled pipeline was divided into 10m sections; then, the input pipeline temperatures were applied to each sections and pipe sections were set to constant temperatures of -10.8, -9.8, -9.5, -8.9, and -8.7°C. Figure 6.27 shows the variations in total heave and both freezing-front and *in-situ*-freezing-front penetration beneath the pipeline at HR-16. The permafrost table moved upward due to heat removal by the chilled pipeline. The freezing front reached the rising permafrost table in year 7. However, the simulated heaves did not stop when the *in-situ* freezing front arrived. The pipe heave leveled off at 0.3m when the *in-situ* freezing front reached the original permafrost table level in year 20.

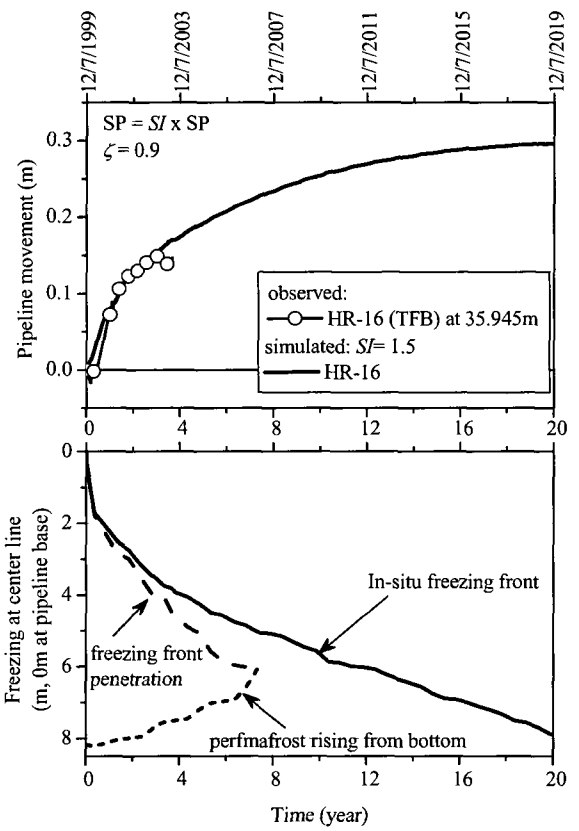

Figure 6.27 Prediction of pipe displacement due to differential frost heave.

The next analysis was performed in order to predict pipeline-permafrost interaction. As shown in Figure 6.2, a rapid deepening of the permafrost existed at 30m from the inlet riser, and the permafrost table gradually deepened from the shallower supra-permafrost area to the deeper supra-permafrost area in the UAF frost-heave experiment. After the segregation freezing zone reached the permafrost table between 25m and 30m from the inlet riser, the frost-susceptible zone ceased its volumetric expansion and became anchorage. Differential pipeline movement was induced in the deeper supra-permafrost area in response to the anchoring (Figure 6.19). Figure 6.28a shows the predicted profiles of pipeline movement at years 3, 6, 12, and 20. Hardly any simulated vertical movement was predicted to occur within 25m of the inlet riser after year 3. However, the soil anchorage was influenced by the differential pipeline movement at distances greater than 25m from the inlet riser.

The variations of the simulated bending moment along the pipeline are shown in Figure 6.28b. The bending moment increased in the vicinity of 25m from the inlet riser, reaching 220kN-m after year 3 of the simulation, and 900kN-m in year 20. The transition zone area, where the bending moment is zero, moved toward the deeper supra-permafrost area. After year 3 of the simulation, the transition zone was located 30m from the inlet riser, while after year 20 it was located 35m from the inlet riser. The simulated maximum bending moment was 1160kN-m 44m from the inlet riser after year 20. The maximum bending moment was equal to an overbend curvature of $0.0022m^{-1}$. The calculated maximum value was still smaller than the observed critical value of $0.0093m^{-1}$ for a 0.02m abrupt upheaval movement event in response to pipe temperature increase.

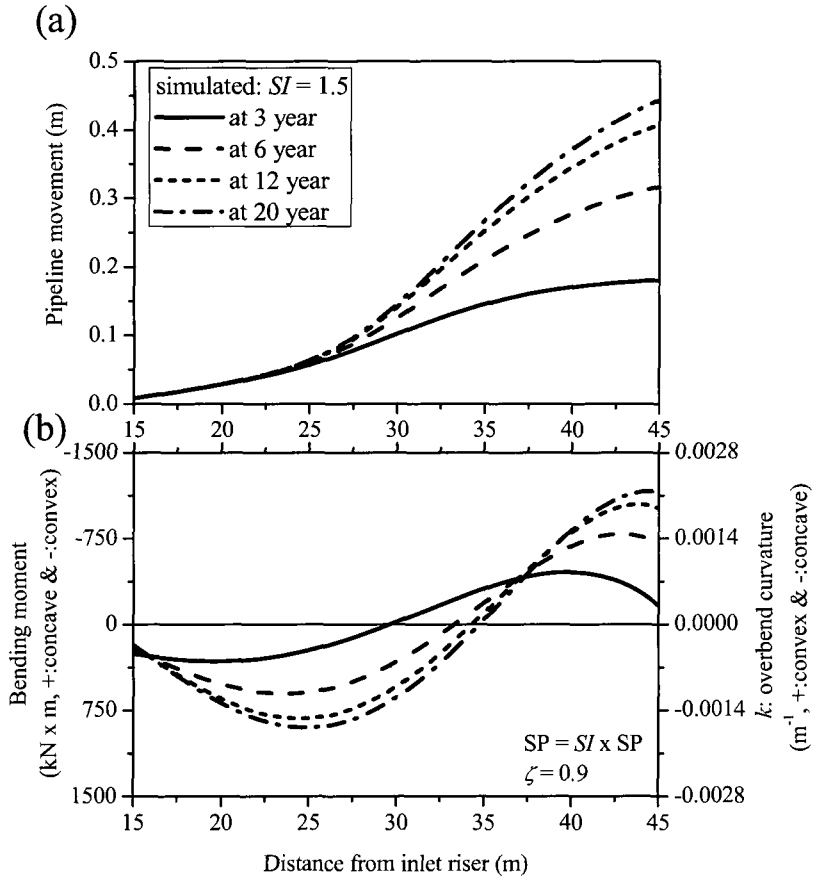

Figure 6.28 Distribution of simulated (a) vertical pipeline movement and (b) bending moment along the pipeline.

6.9 Summary and conclusion

A three-dimensional frost-heave model applying the SP porosity growth function was developed to simulate differential pipeline movement in the transition zone between a pre-frozen soil and an unfrozen frost-susceptible soil. Although some deviations were observed, the developed three-dimensional frost-heave model was verified using the results of the full-scale UAF frost-heave experiment, which employed a large-diameter pipe.

The developed three-dimensional frost-heave model had limitations and shortcomings. However, the overall simulated results agreed well with the trends presented by the full-scale experiment.

Significant findings from this chapter are:

1) Simulated temperature distributions were in a good agreement with observations in both the pre-frozen soil and the unfrozen frost-susceptible soil due to the effect of latent heat release.
2) The developed frost-heave model was modeled so that volumetric expansion due to frost heave only occurs in fully-saturated sections of the soil. After the segregation freezing zone reached the permafrost table between 25m and 30m from the inlet riser, differential pipeline movement started. The simulated results showed good agreement with observations.
3) Between day 510 and day 542, approximately 0.02m abrupt upheaval was observed in the shallower supra-permafrost area. It was postulated that the abrupt upheaval event occurred due to a combination of longitudinal compressive stresses induced by pipe temperature fluctuations.
4) In a 20-year prediction, the three-dimensional simulation indicated that pipe movement continued to be influenced by movement of the *in-situ* freezing front, and reached the elevation of the original permafrost table. The developed three-dimensional frost-heave model can predict pipe movements and induced bending moment due to differential frost heave.

CHAPTER 7: CONCLUSIONS AND RECOMMENDATIONS

7.1 Conclusions

Since the 1970s, numerous frost-heave models have been developed as a result of advancement in frost-heave theories and improvements in computer processing power. Although most frost-heave theories and numerical models consider heave as a one-dimensional process both experimentally and numerically, many field problems are multi-dimensional. For instance, one of the major sources of induced load to buried, chilled gas pipelines in arctic regions is the differential heave near the interface between two types of soil with different frost-heave susceptibilities or between frozen and unfrozen soils. A complete analysis of multi-dimensional frost-heave problems must be able to deal with the coupling of heat transfer, moisture transfer, and mechanical analysis. Development of a simple and yet practical multi-dimensional frost-heave model has been the goal of design engineers for a long time.

Frost heave can be described as a problem of moisture transfer to a growing ice lens passing through the layered frozen fringe and the unfrozen soil. The segregation potential (SP) concept could provide estimates of the frost-heave susceptibility of soils using the results of laboratory frost-heave tests. In the study, improvements were made to a step-freezing test to facilitate a consistent and reproducible evaluation of the SP values for Fairbanks silt. The advantage of continuous heave and water-intake measurements was demonstrated for determining the formation of the final ice lens using two different types of freezing tests; step-freezing tests and Japanese Geotechnical Standard Test (JGST)-freezing tests. At the formation of the final ice lens, the SP clearly decreased with increasing overburden pressure. The effect of overburden pressure on SP was accounted empirically as:

[7.1] $$SP = SP_0 \exp(-b \times \sigma_{ov})$$

Similar SP values were obtained at the formation of the final ice lens by both freezing tests; SP_0 = $41.3 \times 10^{-5} mm^2/(sec \times °C)$ and $b = 0.0156 kPa^{-1}$ from step-freezing tests, and $SP_0 = 42.8 \times 10^{-5} mm^2/(sec \times °C)$ and $b = 0.0189 kPa^{-1}$ from JGST-freezing tests.

Analysis of the laboratory frost-heave test results was conducted over a wide range of cooling rates. The analysis established a relationship between SP, overburden pressure, and cooling rate of the frozen fringe in *in-situ* Fairbanks silt using a fitting method. For *in-situ* Fairbanks silt, a critical rate of cooling of the frozen fringe was observed. When the cooling rate was higher than the critical value, water migration did not occur. The critical rate of cooling was a function of overburden pressure. Including the effect of the critical rate of cooling, a characteristic frost-heave surface for *in-situ*

Fairbanks silt was created to provide input SP values at any cooling rate and overburden pressure for numerical simulations.

A simple macroscopic approach has been developed, which assumes that ice-lens growth can be modeled as a volume expansion of the soil-ice-water mixture. The soil freezing process that occurs in a passive system was distinguished from that in an active system. The passive system was defined as the zone that is colder than the growing ice lens. The volume increase was only considered in the active system, which simulates the growing ice lens and the frozen fringe. The developed model was verified by a series of step-freezing tests in one dimension. The characteristic frost-heave surface was used as the input, taking into account the effects of cooling rate and overburden pressures. The developed frost-heave model could simulate a series of step-freezing tests with remarkable accuracy.

A two-dimensional frost-heave model was developed by applying the SP porosity growth function to simulate pipeline movement at a free-field area. Two field frost-heave experiments were used to verify the model. The anisotropic deformation of soil was modeled by simulating the phenomenon of ice-lens growth mostly perpendicular to the heat-flow direction, yielding 90% of the ice-lens expansion parallel to, and the remaining 10% perpendicular to the direction of heat flow. In multi-dimensional frost-heave simulations, the SP porosity growth function must take into account the interactions between soil stresses and SP on the one hand, and the relationship between stresses and strains at the frozen-unfrozen interface as a resisting force on the other hand. Therefore, the prediction of stress and deformation fields during frost heaving is considered to be of great importance in arctic pipeline design. In other words, it is assumed that the input mechanical properties, which are strain-rate dependent, are directly related to stress, deformation, and frost-heave susceptibilities. Estimating mechanical properties using the critical strain rate resulted in an unrealistic stress buildup and an under-prediction of observations from the University of Alaska Fairbanks (UAF) frost-heave experiment. The numerical simulation suggested that the use of field strain rate for mechanical properties applying field-strain rates. The existence of a frozen layer significantly reduced the frost heave in the early stage of simulation in the UAF frost-heave experiment. However, once post-yield strain was induced in the frozen layer, the resistance to upward motion of the frost bulb was nearly negligible at the free-field area after the post-yield strain had occurred in the frozen layer.

Finally, a three-dimensional frost-heave model was developed by applying the SP porosity growth function to simulate the soil-pipeline interaction near the boundary. Winkler models have been used to simulate differential pipeline movements. Since Winkler models use springs to account for the axial and radial restraints imposed by surrounding soil, they characterize soil pressure only in terms of the absolute pipe displacement. In contrast, the developed frost-heave model accounted for the impact of rigid body movements of the frozen soil and the interactions between different soil locations due to

movement and energy transmitted through the intervening soil. In the approach used in this model, the interaction is induced by the time-dependent growth of a frost bulb and the pressure-dependent volume expansion applying the SP porosity growth function. Simulated temperature distributions were in good agreement with observations in both the pre-frozen soil and the unfrozen frost-susceptible soil due to the effect of latent heat release. The developed frost-heave model could successfully simulate the differential pipeline movement at the boundary between pre-frozen and unfrozen soils in the frost-heave experiment. An abrupt pipeline upheaval event was observed in the UAF frost-heave experiment. The abrupt upheaval event was postulated to be the result of a combination of longitudinal compressive stresses induced by pipe temperature fluctuation.

In conclusion, it should be mentioned that the developed model is the first three-dimensional frost-heave model applying the SP concept considered with the effect of rate-dependent soil properties. The macroscopic approach avoided simulating individual ice-lens formation; this simplification could make it possible to easily predict differential pipeline movements for a 20-year period. From a theoretical and practical viewpoint, therefore, the developed model is believed to be an improvement over existing Winkler spring models for simulating soil-pipeline interactions. The developed model will be a powerful engineering tool for predicting differential pipeline movements due to frost heave at the boundary for the upcoming Alaska gas pipeline project.

7.2 Recommendations for future study

Overall, the simulated results agreed with the trends observed during the UAF frost-heave experiment using a large diameter pipe; the developed three-dimensional frost-heave model accurately predicted pipe movements and induced bending due to differential frost heave. However, there remains room for improving the accuracy of the frost-heave model.

Suggestions for further improvement of the developed three-dimensional frost-heave model are:

1) The developed SP porosity does not account for the effect of consolidation in unfrozen soil in response to water migration due to frost heave. For achieving accurate simulations using soils which have low hydraulic conductivity and high compressibility, such as clays, the future model should take into account the effects of consolidation.
2) A simulation adapting a combination of longitudinal stress and vertical pipeline bending stress due to differential frost heave in the soil profile is needed to simulate an abrupt upheaval event.

3) Future work should focus on the development of a comprehensive model coupled to freeze-thaw cycles in soils. A truly comprehensive model will include thaw weakening and settlement.

REFERENCES:

Aguirre-Puente, M., Vignes, M., and Viaud, P. (1973). "Study of the structural changes in soils during freezing." *Proceedings of the 2nd International Conference on Permafrost*, Yakutsk, USSR, 315-323.

Akagawa, S., Yamamoto, Y., and Hashimoto, S. (1985). "Frost heave characteristics and scale effect of stationary frost heave." *Proceedings of the 4th International Symposium on Ground Freezing*, Sapporo, Hokkaido, Japan, 137-143.

Beskow, G. (1935). "Soil freezing and frost heaving, with special applications to roads and railroads. (Translated in 1947 by J. Osterberg, Northwestern University Technological Institute, Evanston, III)." *Sveriges geologiska undersökning Serie C*, 375.

Biermans, M., Dijkema, K., and de Vries, D. A. (1976). "Water movement in porous media towards an ice front." *Nature*, 264, 166-167.

Biermans, M., Dijkema, K., and de Vries, D. A. (1978). "Water movement in porous media towards an ice front." *Journal of Hydrology*, 37(1-2), 137-148.

Black, P. B. (1995). "RIGIDICE model of secondary frost heave." *CRREL Report 95-12*, U.S. Army Cold Regions Research and Engineering Laboratory Hanover, NH, 41 pp.

Black, P. B., and Hardenberg, M. J. (1991). "Historical perspective of frost heave research: The early works of S. Taber and G. Beskow." *CRREL Special Report 91-23*, U.S. Army Cold Regions Research and Engineering Laboratory, Hanover, NH, 174 pp.

Black, P. B., and Miller, R. D. (1985). "A continuum approach to modelling of frost heaving." *Freezing and Thawing of Soil-water Systems*, ASCE, Technical Council on Cold Regions Monograph, 36-45.

Blanchard, D., and Fremond, M. (1985). "Soil frost heaving and thaw settlement." *Proceedings of the 4th International Symposium on Ground Freezing*, Sapporo, Japan, 209-216.

Bray, M. T. (2003). "Field observations of a large diameter chilled pipeline experiment, Fairbanks, Alaska." *Civil Engineering Department*, University of Alaska Fairbanks, Fairbanks, Alaska, M.S. Thesis, 150 pp.

Bray, M. T. (2008). "The influence of soil cryostructure on the creep and long term strength properties of frozen soils." *Civil Engineering Department*, University of Alaska Fairbanks, Fairbanks, Alaska, Ph.D. Thesis, 249 pp.

Brouchkow, A., and Griva, G. (2004). "Pipeline on Russian North: Review of problems of interaction with permafrost (in Japanese)." *Snow and Ice*, 66(2), 241-249.

Burt, T. P., and Williams, P. J. (1976). "Hydraulic conductivity in frozen soils." *Earth Surface Processes*, 1(4), 349-360.

Carlson, L. E., and Butterwick, D. E. (1983). "Testing pipeline techniques in warm permafrost." *Proceedings of the 4th International Conference on Permafrost*, Fairbanks, Alaska, 97-102.

Carlson, L. E., and Ellwood, J. R. (1982). "Field test results of operating a chilled, buried pipeline in unfrozen ground." *Proceedings of the 4th Canadian Permafrost Conference*, Calgary, Alberta, 475-480.

Carlson, L. E., and Nixon, J. F. (1988). "Subsoil investigation of ice lensing at the Calgary, Canada, frost heave test facility." *Canadian Geotechnical Journal*, 25(2), 307-319.

Carslaw, H. S., and Jaeger, J. C. (1947). *Conduction of heat in solids*, Clarendon Press, Oxforf, England, 386 pp.

Chalmers, B., and Jackson, K. A. (1970). "Experimental and theoretical studies of the mechanism of frost heaving." *CRREL Research Report 199*, U.S. Army Cold Regions Research and Engineering Laboratory Hanover, NH, 23 pp.

Christoffersen, P., and Tulaczyk, S. (2003). "Response of subglacial sediments to basal freeze-on 1. Theory and comparison to observations from beneath the West Antarctic Ice Sheet." *Journal of Geophysical Research*, 108(B4), 2222.

Christoffersen, P., Tulaczyk, S., Behar, A. E., and Carsey, F. D. (2007). "Reply to comment by A. W. Rempel et al. on 'A quantitative framework for interpretation of basal ice facies formed by ice accretion over subglacial sediment'." *Journal of Geophysical Research*, 112, F02037.

Christoffersen, P., Tulaczyk, S., Carsey, F. D., and Behar, A. E. (2006). "A quantitative framework for interpretation of basal ice facies formed by ice accretion over subglacial sediment." *Journal of Geophysical Research*, 111, F01017.

Coutts, R. J. (1991). "Development of two-dimensional finite element model to calculate temperatures and stresses in frost susceptible soils around a chilled pipeline." *Civil Engineering Department*, University of Waterloo, Ontario, Canada, M.S. Thesis, 113 pp.

Crank, J., and Nicholson, P. (1947). "A practical method for the numerical evaluation of solutions of practical differential equations of the heat conduction type." *Proceedings of the Cambridge Philosophical Society*, 43, 50-67.

Darrow, M. M., Huang, S. L., and Akagawa, S. (2009). "Adsorbed cation effects on the frost susceptibility of natural soils." *Cold Regions Science and Technology*, 55(3), 263-277.

Dash, J. G. (1989). "Thermomolecular pressure in surface melting: Motivation for frost heave." *Science*, 246(4937), 1591-1593.

Dash, J. G., Rempel, A. W., and Wettlaufer, J. S. (2006). "The physics of premelted ice and its geophysical consequences." *Reviews of Modern Physics*, 78, 695-741.

Edlefsen, N. E., and Anderson, A. B. C. (1943). "Thermodynamics of soil moisture." *Hilgardia*, 15(2).

Everett, D. H. (1961). "The thermodynamics of frost damage to porous solids." *Transactions of the Faraday Society*, 57, 1541-1551.

Evgin, E., and Svec, O. J. (1988). "Heat and moisture transfer characteristics of compacted Mackenzie silt." *Geotechnical Testing Journal*, 11(2), 92-99.

Farouki, O. T. (1981). "Thermal Properties of Soils." *CRREL Monograph 81-1*, U.S. Army Cold Regions Research and Engineering Laboratory, Hanover, NH, 136 pp.

Foothill Pipe Lines Ltd. (1981). "Plans for dealing with frost-heave and thaw settlement: Addendum to the environmental impact statement for the Yukon section of Alaska Highway Gas Pipeline." Calgary, Alberta, Canada, 1-46.

Fowler, A. C., and Krantz, W. B. (1994). "A generalized secondary frost heave model." *SIAM Journal on Applied Mathematics*, 54(6), 1650-1675.

Fukuda, M. (1983). "Experimental studies of coupled heat and moisture transfer in soils during freezing." *Contributions from the Institute of Low Temperature Science. Series A*, 31, 35-91.

Fukuda, M., Ohhun, M., and Luthin, J. N. (1980). "Experimental studies of coupled heat and moisture transfer in soil during freezing." *Cold Regions Science and Technology*, 3(2-3), 223-232.

Gas Arctic Systems Study Group. (1971). "Gas Arctic systems: Gas pipeline research in the Arctic environment." Gas Arctic Systems Study Group, 23 pp.

Gilpin, R. R. (1979). "A model of the "liquid-like" layer between ice and a substrate with applications to wire regelation and particle migration." *Journal of Colloid and Interface Science*, 68(2), 235-251.

Gilpin, R. R. (1980a). "A model for the prediction of ice-lensing and frost heave in soils." *Water Resources Research*, 16(5), 918-930.

Gilpin, R. R. (1980b). "Wire regelation at low temperatures." *Journal of Colloid and Interface Science*, 77(2), 435-448.

Gilpin, R. R. (1982). "A frost heave interface condition for use in numerical modelling." *Proceedings of the 4th Canadian Permafrost Conference*, Calgary, Alberta, 459-465.

Guymon, G L , and Hromadka, T V (1977) "Finite element model of transient heat conduction with isothermal phase change (two and three-dimensional) " *CRREL Research Special Report 77-38*, U S Army Cold Regions Research and Engineering Laboratory Hanover, NH, 146 pp

Guymon, G L , Hromadka, T V , and Berg, R L (1980) "A one dimensional frost heave model based upon simulation of simultaneous heat and water flux " *Cold Regions Science and Technology*, 3(2-3), 253-262

Guymon, G L , Hromadka, T V , and Berg, R L (1984) "Two-dimensional model of coupled heat and moisture transport in frost-heaving soils " *Journal of Energy Resources Technology*, 106(3), 336-343

Guymon, G L , and Luthin, J N (1974) "A coupled heat and moisture transport model for arctic soils " *Water Resources Research*, 10(5), 995-1001

Harlan, R L (1973) "Analysis of coupled heat-fluid transport in partially frozen soil " *Water Resources Research*, 9(5), 1314-1323

Henry, K S (2000) "A review of the thermodynamics of frost heave " *CRREL Technical Report 00-16*, U S Army Cold Regions Research and Engineering Laboratory Hanover, NH, 25 pp

Hoekstra, P (1969) "Water movement and freezing pressures " *Soil Science Society of America Proceedings*, 33, 512-518

Hoekstra, P , and Chamberlain, E J (1964) "Electro-osmosis in frozen soils " *Nature*, 203, 1406-1407

Hopke, S (1980) "A model for frost heave including overburden " *Cold Regions Science and Technology*, 3(2-3), 111-127

Horiguchi, K (1976) "Relations between the chemical composition and the heave amount of powder materials (in Japanese) " *Low Temperature Science Series A, Physical Sciences*, 34, 245-247

Horiguchi, K (1977) "Frost heave character in freezing of powder materials " *Proceedings of International Symposium on Frost Action in Soils*, Lulea, Sweden, 67-75

Horiguchi, K (1978) "Effects of the rate of heat removal on the rate of frost heaving " *Proceedings of the 1st International Symposium on Ground Freezing*, Bochum, W Germany, 25-30

Horiguchi, K (1987) "An osmotic model for soil freezing " *Cold Regions Science and Technology*, 14(1), 13-22

Horiguchi, K , and Miller, R D (1980) "Experimental studies with frozen soil in an "ice sandwich" permeameter " *Cold Regions Science and Technology*, 3(2-3), 177-183

Horiguchi, K , and Miller, R D (1981) "A note on an "ice sandwich" permeater (in Japanese) " *Low Temperature Science Series A Physical sciences*, 40, 137-145

Horiguchi, K , and Miller, R D (1983) "Hydraulic conductivity functions of frozen materials " *Proceedings of the 4th International Conference on Permafrost*, Fairbanks, Alaska, 504-508

Huang, S L , Bray, M T , Akagawa, S , and Fukuda, M (2004) "Field investigation of soil heave by a large diameter chilled gas pipeline experiment, Fairbanks, Alaska " *Journal of Cold Regions Engineering*, 18(1), 2-34

Ishizaki, T (1993) "Study of frost heave evaluation and test method (in Japanese) " *Low Temperature Science Series A Physical Sciences*, 51, 159-172

Ishizaki, T , and Kinoshita, S (1979) "Frost heave under overburden pressure (in Japanese) " *Low Temperature Science Series A, Physical Sciences*, 38, 169-178

Ishizaki, T , and Nishio, N (1985) "Experimental study of final ice lens growth in partially frozen saturated soil " *Proceedings of the 4th International Symposium on Ground Freezing*, Sapporo, Hokkaido, Japan, 71-79

Ishizaki, T , and Nishio, N (1988) "Experimental study of frost heaving of a saturated soil " *Proceedings of the 5th International Symposium on Ground Freezing*, Nottingham, England, 65-72

Ishizaki, T , Yoneyama, K , and Nishio, N (1985) "X-ray technique for observation of ice lens growth in partially frozen, saturated soil " *Cold Regions Science and Technology*, 11(3), 213-221

Ito, Y , Vinson, T S , Nixon, J F , and Stewart, D (1998) "An improved step freezing test to determine segregation potential " *Proceedings of the 7th International Conference on Permafrost*, Collection Nordicana, Yellowknife, Canada, 509-516

Jackson, R D (1965) "Water vapour diffusion in relatively dry soil IV Temperature and pressure effects on sorption diffusion coefficients " *Soil Science Society of America Proceedings*, 29, 144-148

Jame, Y W , and Norum, D I (1980) "Heat and mass transfer in a freezing unsaturated porous medium " *Water Resources Research*, 16(4), 811-819

Japan Geotechnical Society (2003) "Test method for frost heave suceptibility of soils 0172-2003 " Japan Geotechnical Society, Tokyo, Japan, 45-50

Johansen, O (1977) "Thermal conductivity of soils " *Draft translation 637*, U S Army Cold Regions Research and Engineering Laboratory, Hanover, NH, 291 pp

Johnston, G H (1981) *Permafrost Engineering design and construction*, John Wiley & Sons, Inc , New York, 540 pp

Kay, B C , Sheppard, M I , and Loch, J P G (1977) "A preliminary comparision of simulated and observed water redistribution in soils freezing under laboratory and field conditions " *Proceedings of International Symposium on Frost Action in Soils*, Lulea, Sweden, 102-111

Kim, K (2003) "Pipeline - permafrost interaction " *Civil Engineering department*, Hokkaido University, Sapporo, Hokkaido, Japan, unpublished M S Thesis, (in Japanese), 269 pp

Kim, K., Huang, S., Akagawa, S., and Kanie, S. (2005). "Field observation of pipe strain caused by soil pressure development in frost bulb." *Proceedings of the 40th U.S. Rock Mechanics Symposium*, Anchorage, Alaska, (CD-ROM).

Kim, K., Zhou, W., and Huang, S. (2008). "Frost heave predictions of buried chilled gas pipelines with the effect of permafrost." *Cold Regions Science and Technology*, 53(3), 382-396.

Konrad, J. M. (1987a). "The influence of heat extraction rate in freezing soils." *Cold Regions Science and Technology*, 14(2), 129-137.

Konrad, J. M. (1987b). "Procedure for determining the segregation potential of freezing soils." *Geotechnical Testing Journal*, 10(2), 51-58.

Konrad, J. M. (1989a). "Effect of freeze–thaw cycles on the freezing characteristics of a clayey silt at various overconsolidation ratios." *Canadian Geotechnical Journal*, 26(2), 217-226.

Konrad, J. M. (1989b). "Influence of cooling rate on the temperature of ice lens formation in clayey silts." *Cold Regions Science and Technology*, 16(1), 25-36.

Konrad, J. M. (1989c). "Influence of overconsolidation on the freezing characteristics of a clayey silt." *Canadian Geotechnical Journal*, 26(1), 9-21.

Konrad, J. M. (1990). "Segregation potential-pressure-salinity relationships near thermal steady state for a clayey silt." *Canadian Geotechnical Journal*, 27(2), 203–215.

Konrad, J. M. (1994). "Sixteenth Canadian Geotechnical Colloquium: Frost heave in soils: Concepts and engineering." *Canadian Geotechnical Journal*, 31(2), 223-245.

Konrad, J. M. (1999). "Frost susceptibility related to soil index properties." *Canadian Geotechnical Journal*, 36(3), 403-417.

Konrad, J. M. (2002). "Prediction of freezing-induced movements for an underground construction project in Japan." *Canadian Geotechnical Journal*, 39(6), 1231-1242.

Konrad, J M , and Morgenstern, N R (1980) "A mechanistic theory of ice lens formation in fine-grained soils " *Canadian Geotechnical Journal*, 17(4), 473-486

Konrad, J M , and Morgenstern, N R (1981) "The segregation potential of a freezing soil " *Canadian Geotechnical Journal*, 18(4), 482-491

Konrad, J M , and Morgenstern, N R (1982a) "Effects of applied pressure on freezing soils " *Canadian Geotechnical Journal*, 19(4), 494-505

Konrad, J M , and Morgenstern, N R (1982b) "Prediction of frost heave in the laboratory during transient freezing " *Canadian Geotechnical Journal*, 19(3), 250-259

Konrad, J M , and Morgenstern, N R (1984) "Frost heave prediction of chilled pipelines buried in unfrozen soils " *Canadian Geotechnical Journal*, 21(1), 100-115

Konrad, J M , and Nixon, J F (1994) "Frost heave characteristics of a clayey silt subjected to small temperature gradients " *Cold Regions Science and Technology*, 22(3), 299-310

Konrad, J M , and Shen, M (1996) "2-D frost action modeling using the segregation potential of soils " *Cold Regions Science and Technology*, 24, 263-278

Koopmans, R W R , and Miller, R D (1966) "Soil freezing and soil water characteristics " *Soil Science Society of America Proceedings*, 30, 680-685

Kuroda, T (1985a) "Theoretical study of frost heaving Kinetic process at a water layer between ice lens and soil particles (in Japanese) " *Low Temperature Science Series A Physical Sciences*, 44, 183-189

Kuroda, T (1985b) "Theoretical study of frost heaving Kinetic process at water layer between ice lens and soil particles " *Proceedings of the 4th International Symposium on Ground Freezing*, Sapporo, Hokkaido, Japan, 39-45

Ladanyi, B , and Shen, M (1989) "Mechanics of freezing and thawing in soils " *Proceedings of International Symposium on Frost in Geotechnical Engineering*, Saariselka, Finland, 73-103

LEC Engineering Ltd. (1984). "Analysis of data from the Calgary frost heave test facility." *Earth Physics Branch Open File Number 84-26*, Ottawa, Canada, 29 pp.

Loch, J. P. G. (1979). "Influence of the heat extraction rate on the ice segregation rate of soils." *Frost I Jord*, 20, 19-30.

Loch, J. P. G. (1980). "Frost actions in soils, state of the art." *Proceedings of the 2nd Inernational Symposium on Ground Freezing*, Trondheim, Norway, 581-596.

Lunardini, V. J. (1981). *Heat transfer in cold climates*, Van Nostrand Reinhold Company, New York, 731 pp.

Mageau, D. W., and Morgenstern, N. R. (1980). "Observations on moisture migration in frozen soils." *Canadian Geotechnical Journal*, 17(1), 54-60.

Michalowski, R. L. (1993). "A constitutive model of saturated soils for frost heave simulations." *Cold Regions Science and Technology*, 22(1), 47-63.

Michalowski, R. L., and Zhu, M. (2006). "Frost heave modelling using porosity rate function." *International Journal for Numerical and Analytical Methods in Geomechanics*, 30(8), 703-722.

Miller, R. D. (1972). "Freezing and heaving of saturated and unsaturated soils." *Highway Research Record*, 393, 1-11.

Miller, R. D. (1978). "Frost heaving in non-colloidal soils." *Proceedings of the 3rd International Conference on Permafrost*, Edmonton, Alberta, Canada, 707-713.

Miller, R. D. (1980). "Freezing phenomena in soils." *Applications of Soil Physics*, Hillel, D., ed., Academic Press, New York, 385 pp.

Miyata, Y. (1998). "A thermodynamic study of liquid transportation in freezing porous meda." *JSME International Journal Series B*, 41, 601-609.

Mizoguchi, M. (1993). "A derivation of matric potential in frozen soil." *The Bulletin of the Faculty of Bioresources, Mie University*, 10, 175-182.

Nakano, Y., and Tice, A. (1983). "Transport of water in frozen soil II. Effects of ice on the transport of water under isothermal conditions." *Advances in Water Resources*, 6(1), 15-26.

Nakano, Y., Tice, A., and Oliphant, J. (1984). "Transport of water in frozen soil: III. Experiments on the effects of ice content." *Advances in Water Resources*, 7(1), 28-34.

Nixon, J. F. (1975). "The role of convective heat transport in the thawing of frozen soils." *Canadian Geotechnical Journal*, 12(3), 425-429.

Nixon, J. F. (1983). "Practical applications of a versatile geothermal simulator." *Journal of Energy Resources Technology*, 105(4), 442-447.

Nixon, J. F. (1991). "Discrete ice lens theory for frost heave in soils." *Canadian Geotechnical Journal*, 28(6), 843-859.

Nixon, J. F. (2003). "Conceptual geotechnical/geothermal design basis." *Conceptual and Preliminary Engineering for Mackenzie Gas Project*, Imperial Oil Resources Ventures Limited, 90 pp.

Nixon, J. F., and Burgess, M. (1999). "Norman Wells pipeline settlement and uplift movements." *Canadian Geotechnical Journal*, 36(1), 119-135.

Nixon, J. F., and McRoberts, E. C. (1973). "A study of some factors affecting the thawing of frozen soils." *Canadian Geotechnical Journal*, 10(3), 439-452.

Nixon, J. F., Morgenstern, N. R., and Reesor, S. N. (1983). "Frost heave - pipeline interaction using continuum mechanics " *Canadian Geotechnical Journal*, 20(2), 251-261.

Northern Engineering Services Company Ltd. (1975). "Interim report on frost effects study." Northern Engineering Services Company Ltd, Calgary, Alberta, Canada, 111 pp.

Northwest Project Study Group. (1972). "Information file." Northwest Project Study Group, Calgary, Alberta, Canada, 12 pp.

O'Neill, K. (1983). "The physics of mathematical frost heave models: A review." *Cold Regions Science and Technology*, 6(3), 275-291.

O'Neill, K., and Miller, R. D. (1985). "Explorations of a rigid ice model of frost heave." *Water Resources Research*, 21(3), 281-296.

Ozawa, H., and Kinoshita, S. (1989). "Segregated growth on a microporous filter." *Journal of Colloid and Interface Science*, 132(1), 113-124.

Palmer, A. C., and William, P. J. (2003). "Frost heave and pipeline upheaval buckling." *Canadian Geotechnical Journal*, 40(5), 1033-1038.

Penner, E. (1959). "The mechanisms of frost heaving in soils." *Highway Research Board Bulletin*, 325, 1-22.

Penner, E. (1967). "Heaving pressure in soils during unidirectional freezing." *Canadian Geotechnical Journal*, 4(4), 398-408.

Penner, E. (1986). "Aspects of ice lens growth in soils." *Cold Regions Science and Technology*, 13(1), 91-100.

Penner, E., and Ueda, T. (1977). "The dependence of frost heaving on load applications: Preliminary results." *Proceedings of Inernational Symposium Frost Action in Soils*, Lulea, Sweden, 92-101.

Permafrost Subcommittee. (2005). *Multi-language glossary of permafrost and related ground-ice terms: Definitions*, National Snow and Ice Data Center/World Data Center for Glaciology, Boulder, CO, 90 pp.

Peterson, R. A., and Krantz, W. B. (2003). "A mechanism for differential frost heave and its implications for patterned-ground formation." *Journal of Geology*, 49(164), 69-80.

Radd, F. J., and Oertle, D. H. (1973). "Experimental pressure studies of frost heave mechanisms and the growth-fusion behavior of ice." *Proceedings of the 2nd International Conference on Permafrost*, Yakutsk, USSR, 377-383.

Rajani, B., and Morgenstern, N. R. (1992). "Behaviour of a semi-infinite beam in a creeping medium." *Canadian Geotechnical Journal*, 29(5), 779-788.

Rajani, B., and Morgenstern, N. R. (1993). "Uplift of model steel pipelines embedded in polycrystalline ice." *Canadian Geotechnical Journal*, 30(3), 441-454.

Rajani, B., and Morgenstern, N. R. (1994). "Comparison of predicted and observed responses of pipeline to differential frost heave." *Canadian Geotechnical Journal*, 31(6), 803-816.

Razaqpur, A. G., and Wang, D. (1996). "Frost-induced deformations and stresses in pipelines." *International Journal of Pressure Vessels and Piping*, 69(2), 105-118.

Reddy, J. N. (2005). *An Introduction to the finite element method*, McGraw-Hill, New York, NY, 755 pp.

Rempel, A. W. (2007). "Formation of ice lense and frost heave." *Journal of Geophysical Research*, 112, F02S21.

Rempel, A. W. (2008). "A theory for ice-till interactions and sediment entrainment beneath glaciers." *Journal of Geophysical Research*, 113, F01013.

Rempel, A. W., Wettlaufer, J. S., and Worster, M. G. (2004). "Premelting dynamics in a continuum model of frost heave." *Journal of Fluid Mechanics*, 498, 227-244.

Rempel, A. W., Wettlaufer, J. S., and Worster, M. G. (2007). "Comment on "A quantitative framework for interpretation of basal ice facies formed by ice accretion over subglacial sediment" by Poul Christoffersen et al." *Journal of Geophysical Research*, 112, F02036.

Rosenblueth, E. (1975). "Point estimates for probability moments." *Proceedings of the National Academy of Sciences*, 72(10), 3812-3814.

Sayles, F. H., and Haines, D. H. (1974). "Creep of frozen silt and clay." *CRREL Technical Report 252*, U.S. Army Cold Regions Research and Engineering Laboratory Hanover, NH, 54 pp.

Selvadurai, A. P. S., Hu, J., and Konuk, I. (1999a). "Computational modelling of frost heave induced soil-pipeline interaction: I. Modelling of frost heave." *Cold Regions Science and Technology*, 29(3), 215-228.

Selvadurai, A. P. S., Hu, J., and Konuk, I. (1999b). "Computational modelling of frost heave induced soil-pipeline interaction: II. Modelling of experiments at the Caen test facility." *Cold Regions Science and Technology*, 29(3), 229-257.

Selvadurai, A. P. S., and Shinde, S. B. (1993). "Frost heave induced mechanics of buried pipelines." *Journal of Geotechnical Engineering*, 119(12), 1929-1951.

Seto, J. T. C., and Konrad, J. M. (1994). "Pore pressure measurements during freezing of an overconsolidated clayey silt." *Cold Regions Science and Technology*, 24(3), 263-278.

Shar, K. R., and Razaqpur, A. G. (1993). "A two-dimensional frost-heave model for buried pipelines." *International Journal of Numerical Methods in Engineering*, 36(15), 2545-2566.

Shen, M. (1988). "Numerical analysis of temperature field in a thawing embankment in permafrost." *Canadian Geotechnical Journal*, 25(1), 167-172.

Shen, M., and Ladanyi, B. (1991). "Soil-pipe interection during frost heaving around a buried chilled pipeline." *Proceedings of the 6th International Specialty Conference.*

Slusarchuk, W. A., Clark, J. I., Nixon, J. F., and Morgenstern, N. R. (1978). "Field test results of a chilled pipeline buried in unfrozen ground." *Proceedings of the 3rd International Conference on Permafrost*, Edmonton, Alberta, Canada, 878-883.

Slusarchuk, W. A., Watson, G. H., and Speer, T. L. (1973). "Instrumentation around a warm oil pipeline buried in permafrost." *Canadian Geotechnical Journal*, 10(2), 227-245.

Svec, O. J. (1989). "A new concept of frost-heave characteristics of soils." *Cold Regions Science and Technology*, 16(3), 271-279.

Taber, S. (1929). "Frost heaving." *Journal of Geology*, 37(5), 428-461.

Taber, S. (1930). "The mechanics of frost heaving." *Journal of Geology*, 38(4), 303-317.

Takagi, S. (1980a). "The adsorption force theory of frost heaving." *Cold Regions Science and Technology*, 3(1), 57-81.

Takagi, S. (1980b). "Summary of the adsorption force theory of frost heaving." *Cold Regions Science and Technology*, 3(2-3), 233-235.

Takashi, T., Masuda, M., and Yamamoto, Y. (1974). "Experimental study on the influence of freezing speed upon frost heave ratio of soil under constant effective stress (in Japanese)." *Snow and Ice*, 36(2), 1-20.

Takashi, T., Ohrai, T., Yamamoto, Y., and Okamoto, J. (1981). "Upper limit of heaving pressure derived by pore-water pressure measurements of partially frozen soil." *Engineering Geology*, 18(1-4), 245-257.

Taylor, G. S., and Luthin, J. N. (1978). "A model for coupled heat and moisture transfer during soil freezing." *Canadian Geotechnical Journal*, 15(4), 548-555.

Ueda, T., and Penner, E. (1977). "Mechanical analogy of a constant heave rate." *Proceedings of Inernational Symposium on Frost Action in Soils*, Lulea, Sweden, 57-67.

Vignes, M., and Dijkema, K. (1974). "A model for the freezing of water in a dispersed medium." *Journal of Colloid and Interface Science*, 49(2), 165-172.

Watanabe, K., and Mizoguchi, M. (2000). "Ice configuration near a growing ice lens in a freezing porous medium consisting of micro glass particles." *Journal of Crystal Growth*, 213(1-2), 135-140.

Watson, G. H., Rowley, R. K., and Slusarchuk, W. A. (1973). "Performance of a warm-oil pipeline buried in permafrost." *Proceedings of the 2nd International Conference on Permafrost*, Yakutsk, USSR, 759-766.

Wettlaufer, J. S., Worster, M. G., Wilen, L. A., and Dash, J. G. (1996). "A theory of premelting dynamics for all power law forces." *Physical Review Letters*, 76(19), 3602-3605.

White, T. L. (2006). "Pipelines in permafrost and freezing ground, engineering resource library and database indexes." Permafrost Environmental Consulting Inc, Ottawa, Canada, 14 volumes, 1400 pp.

Wilen, L. A., and Dash, J. G. (1995). "Frost heave dynamics at a single crystal interface." *Physical Review Letters*, 74(25), 5076-5079.

Williams, P. J. (1986). *Pipilines and Permafrost*, The Carleton University Press, Ottawa, Canada, 129 pp.

Williams, P. J., and Burt, T. P. (1974). "Measurement of hyaraulic conductivity of frozen soils." *Canadian Geotechnical Journal*, 11(4), 647-650.

Zhu, Y., and Carbee, D. L. (1987). "Creep and strength behavior of frozen silt in uniaxial compression." *CRREL Report 87-10*, U.S. Army Cold Regions Research and Engineering Laboratory Hanover, NH, 67 pp.

Zhu, Y., Zhang, J., and Shen, Z. (1988). "Uniaxial compressive strength of frozen medium and under constant deformation rates." *Proceedings of the 5th International Symposium on Ground Freezing*, Nottingham, England, 225-232.

APPENDIX A: SUMMARY OF NOTATION AND SYMBOLS

Table A.1 Summary of notation and symbols

Notation and Symbol	Meaning	Unit dimension
ARSC	Arctic Region Supercomputing Center	
CAE	computer assisted engineering	
const	constant	
COV_h	coefficient of variation of the simulated (soil) total heave	
COV_γ	coefficient of variation of the anisotropic expansion parameter	
CRREL	U S Army Cold Regions Research and Engineering Laboratory	
EPSCoR	Experimental Program to Stimulate Competitive Research	
FD	finite difference	
FE	finite element	
FH	frost heave strain parameter	
FHR	frost heave ratio	
HG	heave gauge	
hml	horizontal micro-lenticular	
HR	heave rod	
HRR	heave rate	[L/T]
JGST	Japanese geotechnical standard test (method)	
LNG	liquid natural gas	
LVDT	linear voltage displacement transducer	
N W T	Northwest Territories, Canada	
OCR	overconsolidation ratio	
PR	freezing rate parameter	$[L/T^{0.5}]$
RM	remolded sample	
SG	strain gauge	
SI	multiplication factor	
SP	segregation potential	$[L^2/(T \times K)]$
SP_0	the maximum value of segregation potential	$[L^2/(T \times K)]$
TAPS	Trans Alaska Pipeline System	
TF	thermal fence	
UAF	University of Alaska Fairbanks	
vml	vertical micro-lenticular	
VSM	Vertical Support Member	
A	cross section area of the soil sample	$[L^2]$
γ	multiplication factor to test the effect of peak strength	
A_{sp}	effective area of segregation freezing zone	$[L^2]$
b	soil constant	[1/F]
γ	multiplication factor to test the effect of post-yield stress-strain characteristics	
C	volumetric heat capacity of soil	$[J/(K \times L^3)]$
γ	stress partition factor	
c_a	mass heat capacity of air	[J/(K x M)]
C_{ap}	apparent volumetric heat capacity of soil	$[J/(K \times L^3)]$
C_{ff}	volumetric heat capacity of frozen fringe	$[J/(K \times L^3)]$
c_i	mass heat capacity of ice	[J/(K x M)]
CRC	critical rate of cooling	[K/T]
c_s	mass heat capacity of soil particle	[J/(K x M)]

Dimension	Indicator	Example (SI units)
length	L	meter
mass	M	kilogram
time	T	second
temperature	K	degree Celsius
force	F	Pascal
energy	J	Joule

Table A.1 (continued) Summary of notation and symbols

Notation and Symbol	Meaning	Unit dimension
C_w	volumetric heat capacity of water	[J/(K x L^3)]
c_w	mass heat capacity of water	[J/(K x M)]
d	thickness of frozen fringe	[L]
D	elasticity tensor	
$\&$	fraction taking into account the portion of unfrozen water in frozen soil	
$\&_{max}$	maximum value of fraction of unfrozen water	
$\&n_{in}$	porosity growth due to *in-situ* heave	
$\&n_{sp}$	porosity growth due to segregation heave	
$\&n_t$	incremental change in total porosity	
E	Young's modulus	[F]
$\&$	total strain	
$\&$	strain rate	
E_{50}	50% peak strength modulus	[F]
$\&^{el}$	modified bilinear elastic strain	
$\&_f$	failure strain	
$\&^{gp}$	strain increment due to the total porosity growth function	
F	flexural rigidity for a thin-walled elastic cylinder	[F x L^2]
f	uplift resistance coefficient determined experimentally	
$\&$	the angle x axis makes with maximum heat flow direction	
G	Gibb's free energy	[J/M]
g	gravitational acceleration	[L/T^2]
$\&_b$	buoyant soil density	[F]
$\&_d$	dry soil density	[F]
G_i	Gibb's free energy of ice	[J/M]
$\&_{i\,w}$	chemical potential between ice and water at the onset of the growing ice lens	[J]
$gradT_{ff}$	temperature gradient in the frozen fringe	[K/L]
$gradT_{sp}$	temperature gradient in the segregation freezing zone	[K/L]
$\&_t$	bulk soil density	[F]
G_w	Gibb's free energy of water	[J/M]
$\&_w$	water density	[F]
H	total potential	[L]
$\&$	uplift resistance per unit length	[F/L]
h_0	initial height of the soil sample	[L]
h_{in}	*in-situ* heave	[L]
h_{sp}	segregation heave	[L]
h_t	total heave	[L]
J	diffusivity	[M/L^3]
$\&$	wall thickness	[L]
k	overbend curvature	[L^{-1}]
$\&_{ff}$	hydraulic conductivity of frozen fringe	[M/T]
$\&_u$	hydraulic conductivity of unfrozen soil	[M/T]
L	volumetric latent heat of fusion of soil	[J/L^3]
$\&$	thermal conductivity	[J/(T x M x K)]
$\&_f$	thermal conductivity of frozen soil	[J/(T x M x K)]
$\&_{ff}$	thermal conductivity of frozen fringe	[J/(T x M x K)]

Dimension	Indicator	Example (SI units)
length	L	meter
mass	M	kilogram
time	T	second
temperature	K	degree Celsius
force	F	Pascal
energy	J	Joule

Table A.1 (continued) Summary of notation and symbols

Notation and Symbol	Meaning	Unit dimension
l_{sp}	effective width of the segregation freezing zone	[M]
l_u	length of unfrozen soil	[M]
$>_u$	thermal conductivity of unfrozen soil	[J/(T x M x K)]
L_w	specific latent heat of fusion of pure water	[J/M]
M	bending moment	[F x L]
$>$	Poisson's ratio	
n	porosity	
$>$	number of freeze-thaw cycles	
n_{ini}	initial porosity	
P	pressure	[F]
p	longitudinal stress	[F/L^2]
$>$	osmotic pressure of water	[F]
P_0	suction pressure at the freezing front	[F]
P_i	ice pressure	[F]
P_w	pore water pressure	[F]
q	external vertical force per unit length	
$>$	mean diameter (twice the mean radius, measured from the center to halfway through the wall)	[L]
$>_i$	volumetric fraction of ice	
$>_s$	volumetric fraction of soil particle	
$>_u$	volumetric fraction of ice	
R_1	resistance in the freezing process of the water film	[J x T/L]
R_2	resistance in the suction process	[J x T/L]
$>_a$	density of air	[M/L^3]
$>_d$	dry density of soil	
$>_i$	density of ice	[M/L^3]
r_{iw}	radius of ice-water interface	[M]
$>_s$	density of soil particle	[M/L^3]
$>_w$	density of water	[M/L^3]
s	entropy	[J/M]
S	shear force	[F]
s_i	entropy of ice	[J/M]
SP_m	the maximum SP value at the peak	[L^2/(T x K]
s_w	entropy of water	[J/M]
T	temperature	[K]
t	time	[T]
$>$	shear stress	[F]
T_0	freezing temperature	[K]
$\dot{T}_0$	parameter to satisfy the SP at the formation of the final ice lens	[K/T]
T_{cold}	cold end temperature	[K]
$\dot{T}_{ff}$	cooling rate of frozen fringe	[K/T]
T_{in}	*in-situ* freezing temperature	[K]
$\dot{T}_m$	the cooling rate at which the maximum SP value occurs	[K/T]
T_s	segregation-freezing temperature	[K]
T_{sp}	temperature at a location in frozen fringe	[K]
$\dot{T}_{sp}$	cooling rate of the segregation freezing zone	[K/T]

Dimension	Indicator	Example (SI units)
length	L	meter
mass	M	kilogram
time	T	second
temperature	K	degree Celsius
force	F	Pascal
energy	J	Joule

Table A.1 (continued) Summary of notation and symbols

Notation and Symbol	Meaning	Unit dimension
T_{warm}	warm end temperature	[K]
U	freezing rate	[L/T]
U_0	soil constant	[L/T]
V	volume of the water in the burette	[L^2]
v	water migrating rate	[L/T]
$\overline{V_i}$	specific volume of ice	[$1/L^3$]
v_{sp}	water intake rate calculated using the reading from the differential transducer	[L/T]
V_{sp}	effective volume of segregation freezing zone	[L^3]
v_t	water intake rate calculated using the reading from the laser displacement transducer	[L/T]
$\overline{V_w}$	specific volume of water	[$1/L^3$]
W	depth of the groundwater table below the ground surface	[M]
	pipeline weight per unit length	[F/L]
w_0	unfrozen water content at freezing point	
w_u	residual unfrozen water content	
	the thickness of the cover (measured from the top of the pipeline to the ground surface)	[L]
	frost heave ratio	
X_0	depth of freezing front	[L]
	soil constant	
X_s	depth of segregation freezing front	[L]
	the angle that x axis makes with the reflection of the maximum heat flow on x-y plane	
	dimensionless quantity	
Λ_{sp}	effective area of the segregation freezing temperature in the element	[L^2]
φ	the angle z axis makes with maximum heat flow direction	
σ	total stress	[F]
σ_0	soil constant	[F]
σ_e	effective stress	[F]
σ_{iw}	surface tension of ice-water interface	[F x M]
σ_m	peak strength	[F]
σ_n	neutral stress	[F]
σ_{ov}	overburden pressure	[F]
σ_r	creep strength	[F]
σ_{sp}	induced soil stress due to frost heave	[F]
σ_t	effective pressure acting on the segregation freezing zone	[F]
σ_y	yield stress	[F]

Dimension	Indicator	Example (SI units)
length	L	meter
mass	M	kilogram
time	T	second
temperature	K	degree Celsius
force	F	Pascal
energy	J	Joule

APPENDIX B: GRAPHICAL PRESENTATION OF FROST HEAVE TEST RESULTS

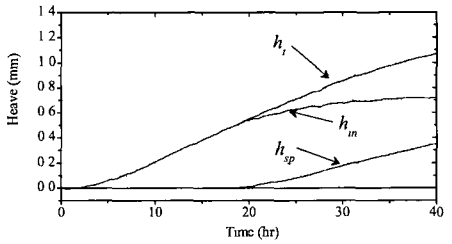

(a) Heave

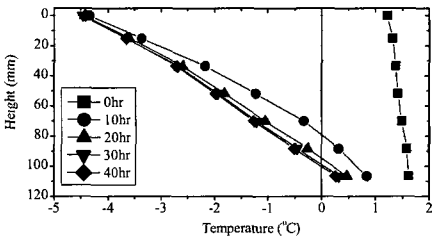

(b) Temperature distributions

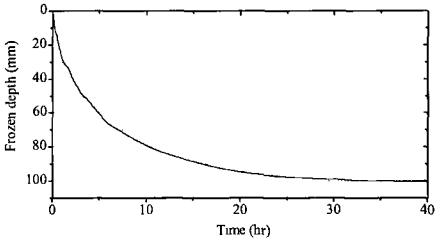

(c) Frozen depth

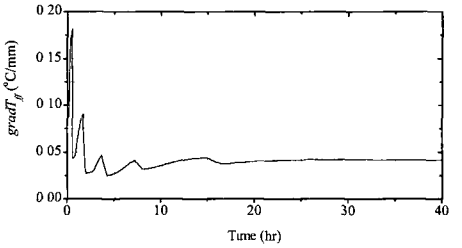

(d) Temperature gradient of frozen fringe

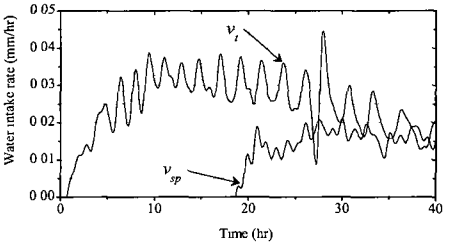

(e) Water intake rates

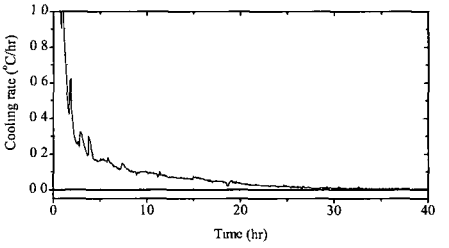

(f) Cooling rate of frozen fringe

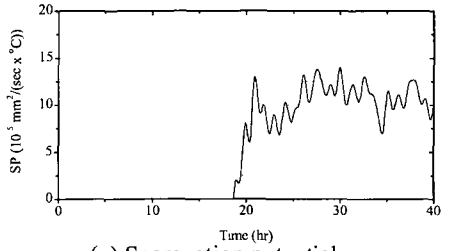

(g) Segregation potential

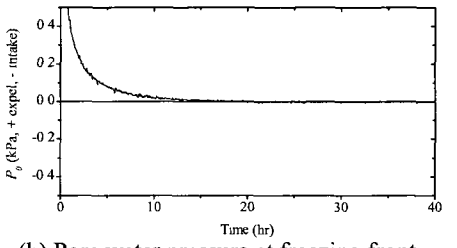

(h) Pore water pressure at freezing front

Figure B.1 Results from step-freezing test, STEP-1.

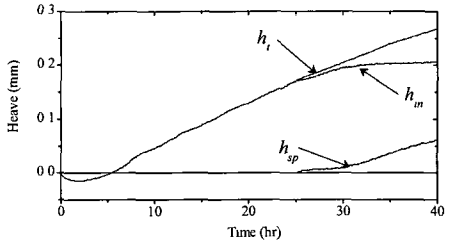

(a) Heave

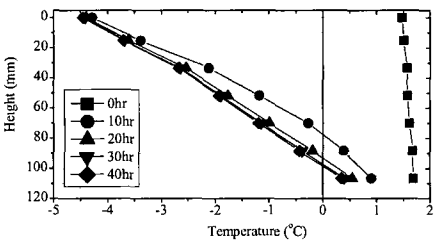

(b) Temperature distributions

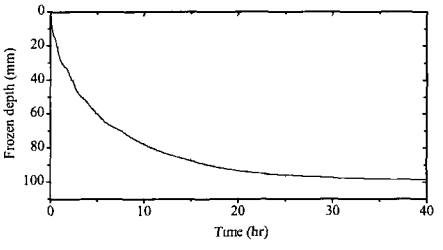

(c) Frozen depth

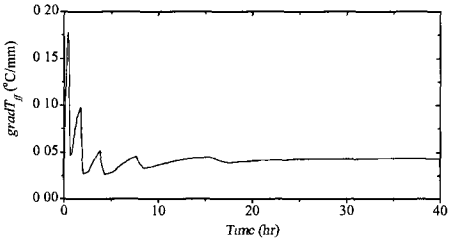

(d) Temperature gradient of frozen fringe

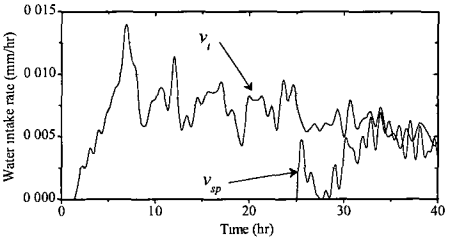

(e) Water intake rates

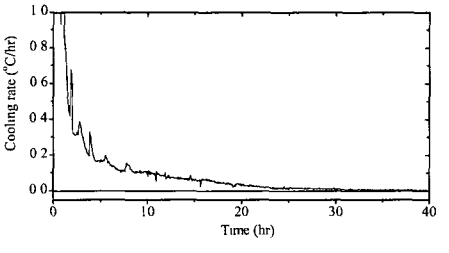

(f) Cooling rate of frozen fringe

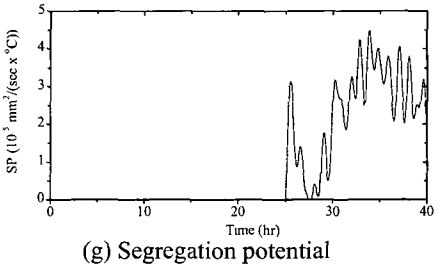

(g) Segregation potential

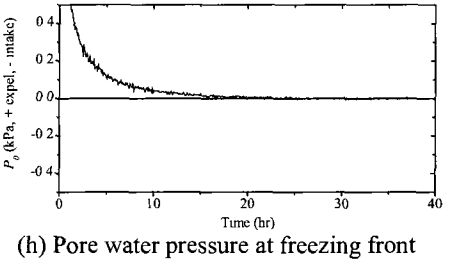

(h) Pore water pressure at freezing front

Figure B.2 Results from step-freezing test, STEP-2.

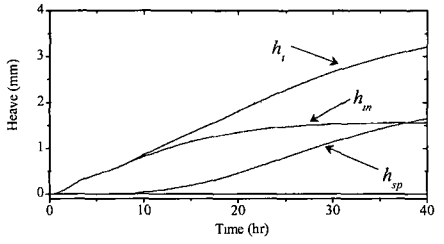

(a) Heave

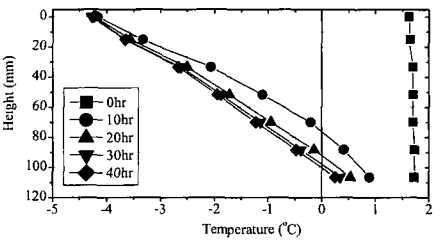

(b) Temperature distributions

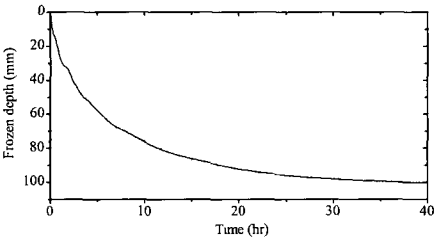

(c) Frozen depth

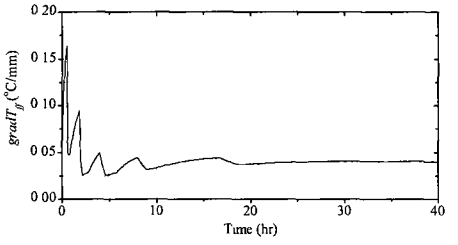

(d) Temperature gradient of frozen fringe

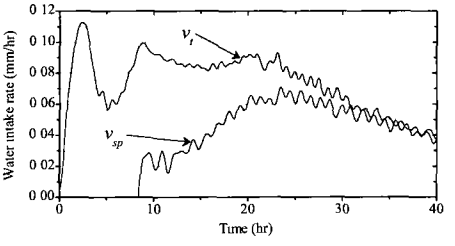

(e) Water intake rates

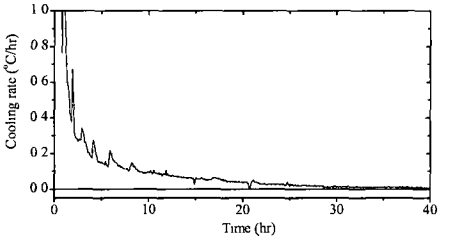

(f) Cooling rate of frozen fringe

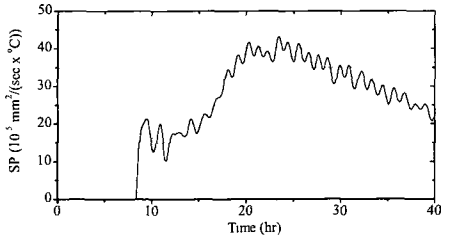

(g) Segregation potential

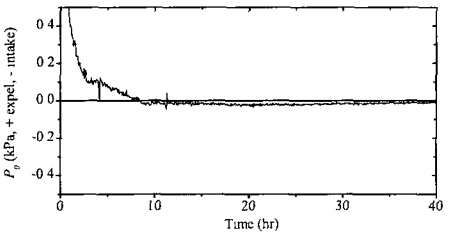

(h) Pore water pressure at freezing front

Figure B.3 Results from step-freezing test, STEP-3.

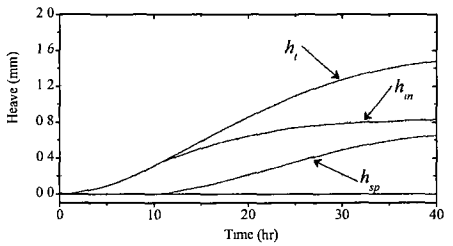

(a) Heave

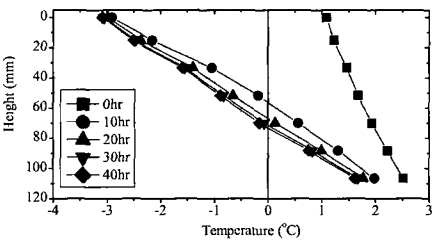

(b) Temperature distributions

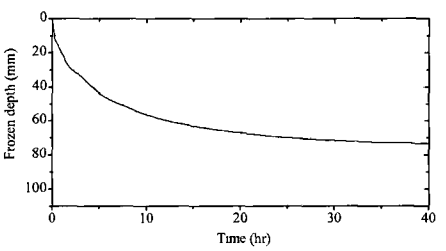

(c) Frozen depth

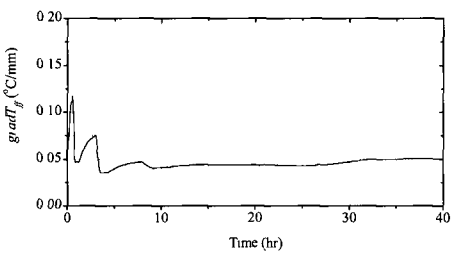

(d) Temperature gradient of frozen fringe

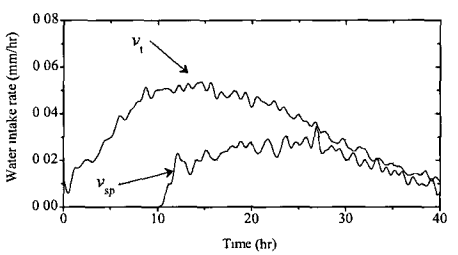

(e) Water intake rates

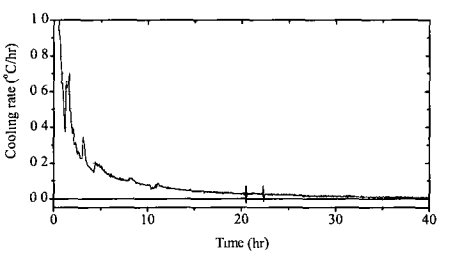

(f) Cooling rate of frozen fringe

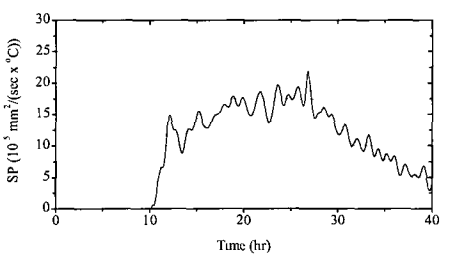

(g) Segregation potential

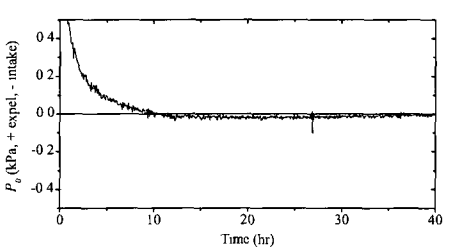

(h) Pore water pressure at freezing front

Figure B.4 Results from step-freezing test, STEP-4.

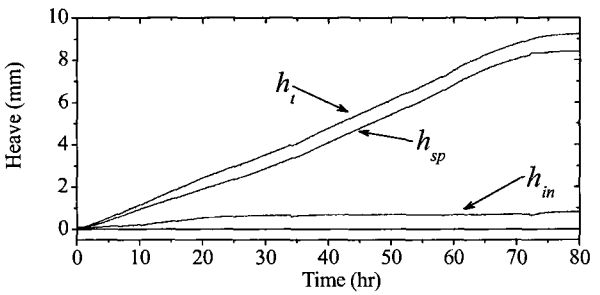

(a) Heave

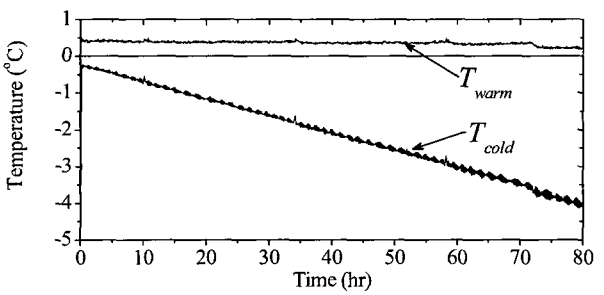

(b) Pedestal temperatures

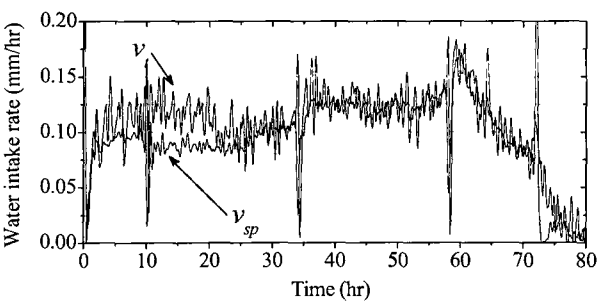

(c) Water intake rates

Figure B.5 Results from JGST-freezing test, JGST-1.

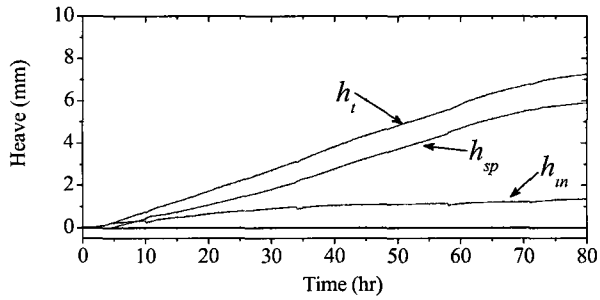

(a) Heave

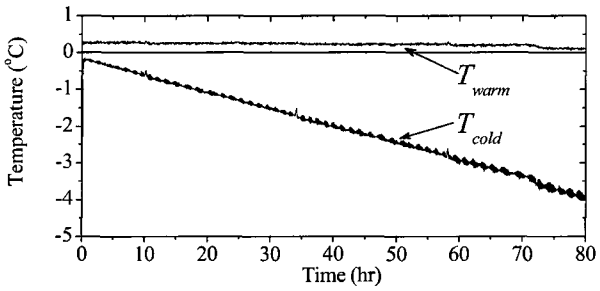

(b) Pedestal temperatures

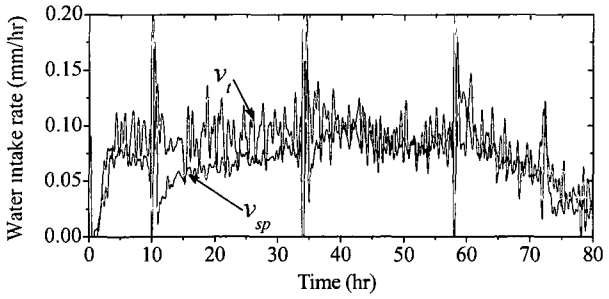

(c) Water intake rates

Figure B.6 Results from JGST-freezing test, JGST-2.

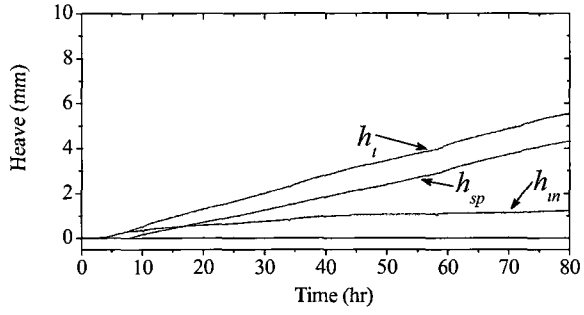

(a) Heave

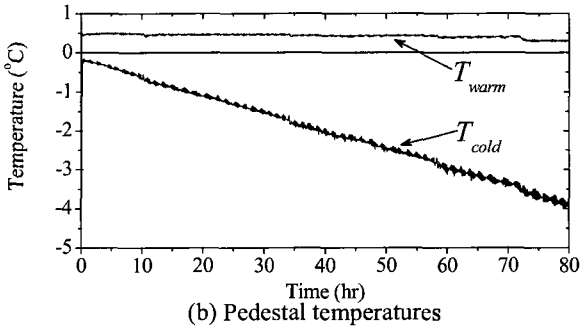

(b) Pedestal temperatures

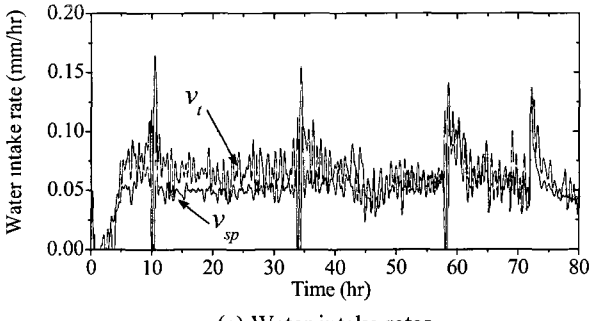

(c) Water intake rates

Figure B.7 Results from JGST-freezing test, JGST-3.

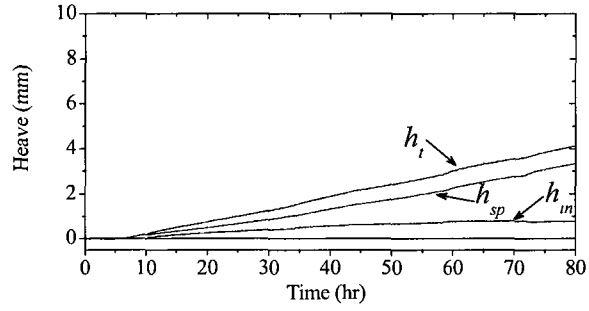

(a) Heave

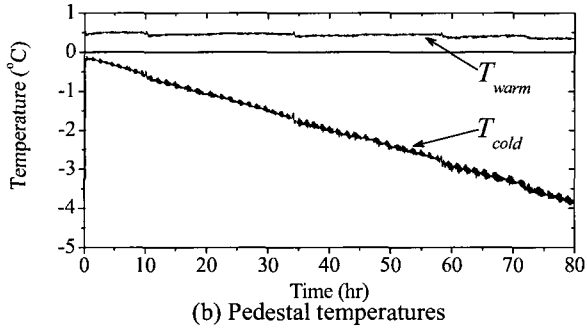

(b) Pedestal temperatures

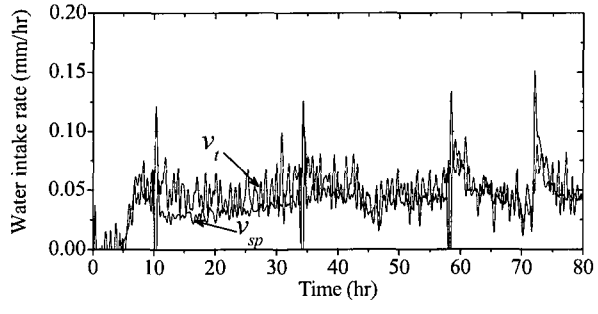

(c) Water intake rates

Figure B.8 Results from JGST-freezing test, JGST-4.

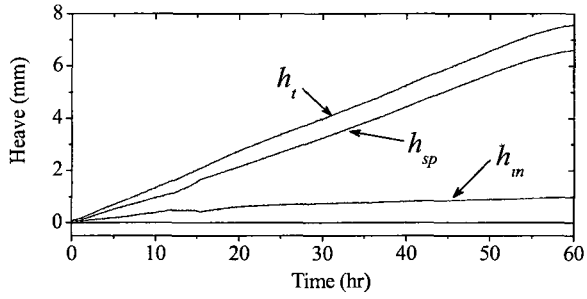

(a) Heave

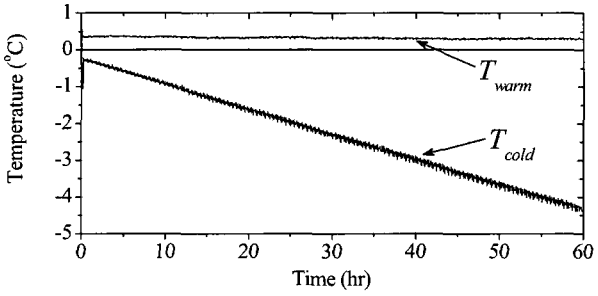

(b) Pedestal temperatures

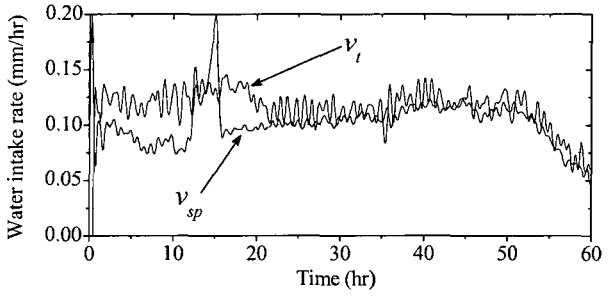

(c) Water intake rates

Figure B.9 Results from JGST-freezing test, JGST-5.

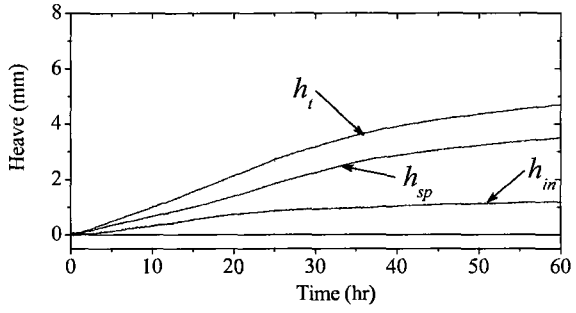

(a) Heave

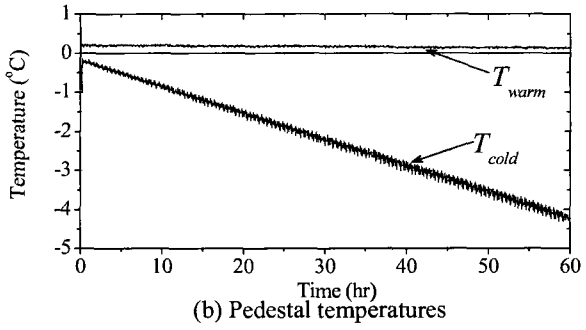

(b) Pedestal temperatures

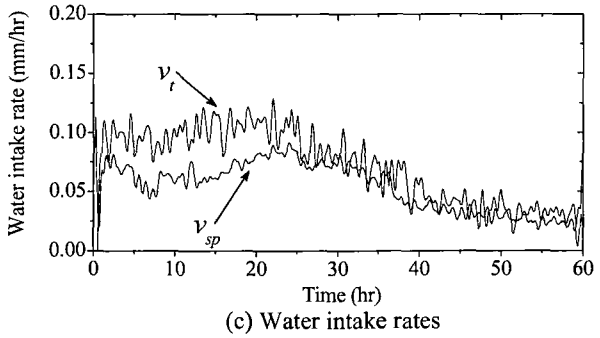

(c) Water intake rates

Figure B.10 Results from JGST-freezing test, JGST-6.

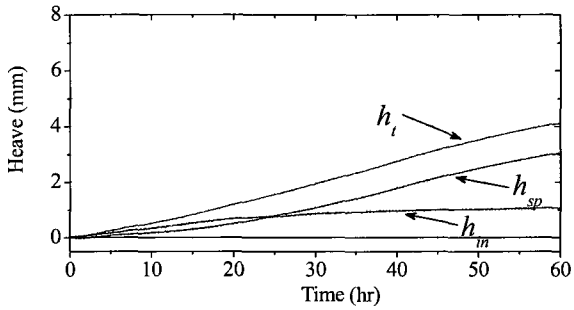

(a) Heave

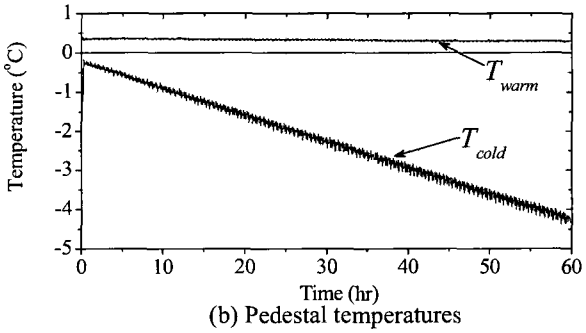

(b) Pedestal temperatures

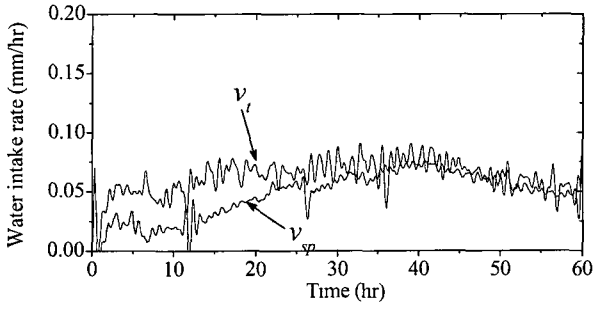

(c) Water intake rates

Figure B.11 Results from JGST-freezing test, JGST-7.

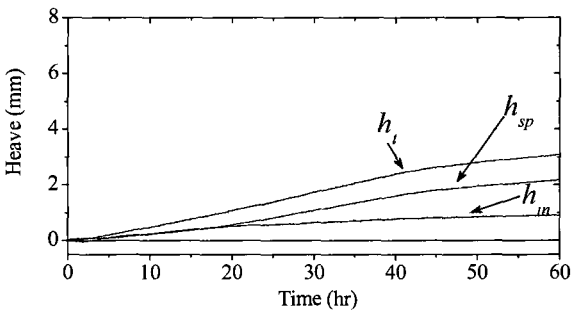

(a) Heave

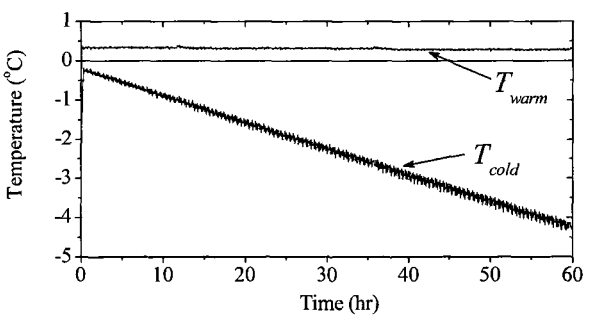

(b) Pedestal temperatures

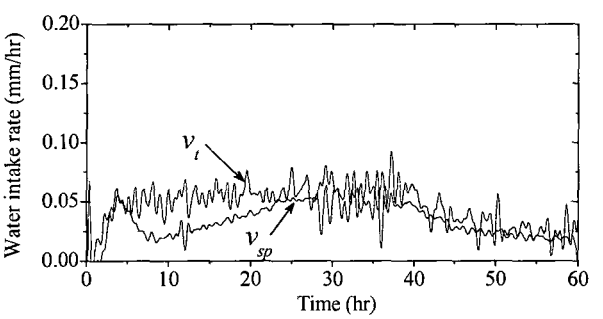

(c) Water intake rates

Figure B.12 Results from JGST-freezing test, JGST-8.

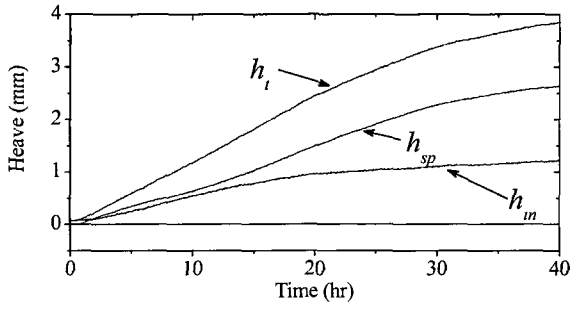

(a) Heave

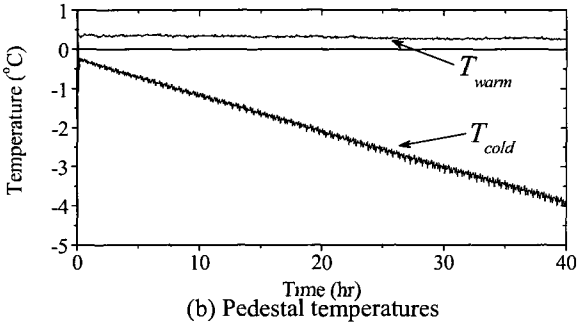

(b) Pedestal temperatures

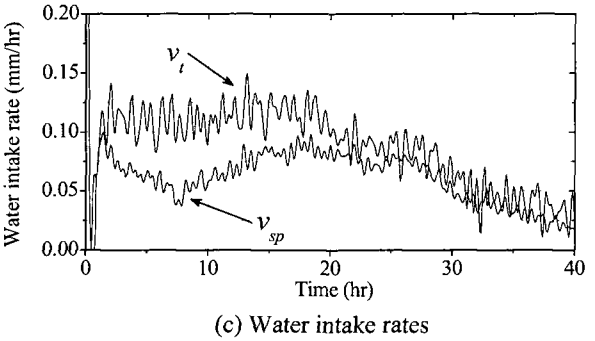

(c) Water intake rates

Figure B.13 Results from JGST-freezing test, JGST-9.

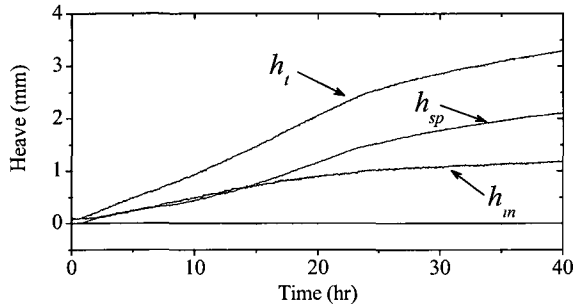

(a) Heave

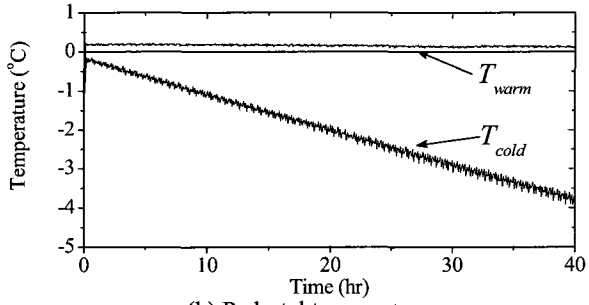

(b) Pedestal temperatures

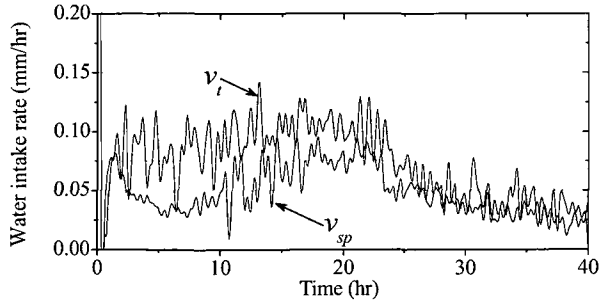

(c) Water intake rates

Figure B.14 Results from JGST-freezing test, JGST-10.

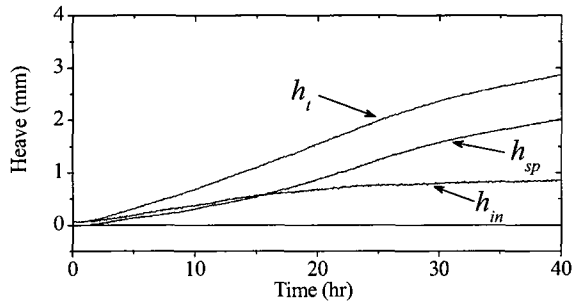

(a) Heave

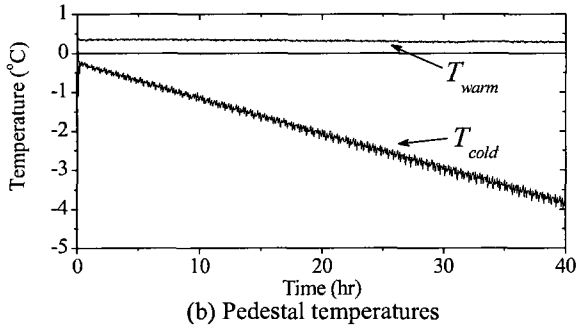

(b) Pedestal temperatures

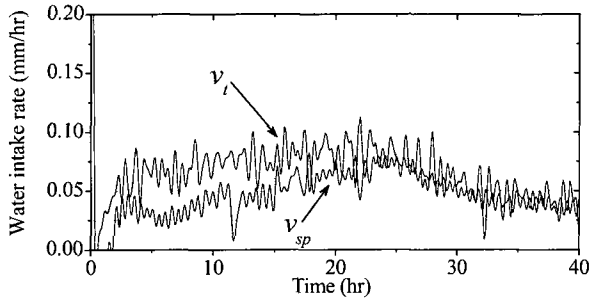

(c) Water intake rates

Figure B.15 Results from JGST-freezing test, JGST-11.

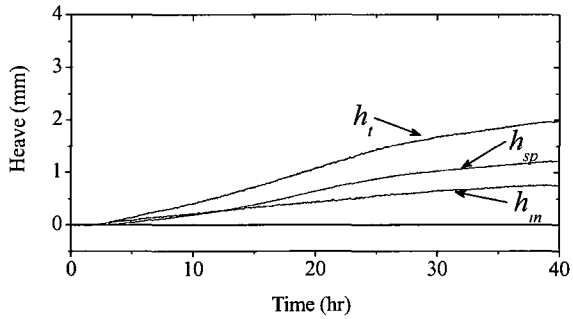

(a) Heave

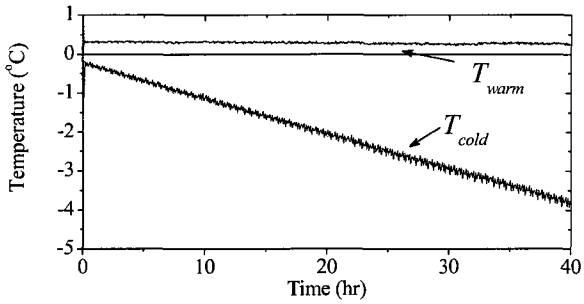

(b) Pedestal temperatures

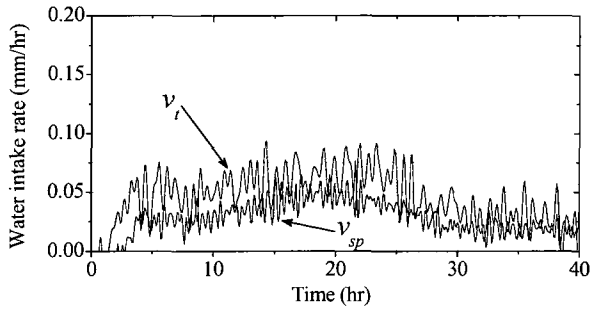

(c) Water intake rates

Figure B.16 Results from JGST-freezing test, JGST-12.

APPENDIX C: User defined function for SP porosity growth function

APPENDIX C.1 User defined function in one dimension

```
C**********************************************************************
C USER SUBROUTINES FOR ONE-DIMENSIONALSP POROSITY GROWTH FUNCTION
C
C WRITTEN BY KIM, KOUI, 2008
C**********************************************************************
C
C**********************************************************************
C
C SDVINI  ABAQUS WILL CALL THIS ROUTINE TO DEFINE
C THE INITIAL SOLUTION DEPENDENT STATE VARIABLE FLELDS
C AT PARTICULAR MATERIAL POINTS
C USED WITH THE *INITIAL CONDITIONS, TYPE=SOLUTION, USER OPTION IN INPUT FILE
C
C**********************************************************************
C
      SUBROUTINE SDVINI(STATEV,COORDS,NSTATV,NCRDS,NOEL,NPT,LAYER,KSPT)
C
      INCLUDE 'ABA_PARAM INC'
C
C     THE NUMBER OF STATE VARIABLES (NSTATV) IS DEFINED USING *DEPVAR OPTSON
C     IN THE INPUT FILE
      DIMENSION STATEV(NSTATV),COORDS(NCRDS)
C
C     THE VALUES OF N_0 AND W_0 MUST MATCH WITH THE DENSITY OF SOIL
C     SKELTON SO THAT THE INITIAL ICE CONTENT IS ZERO
C     INITIAL VALUE FOR POROSITY  N_0
      STATEV(13) = 0 471584454D0
C     INITIAL VALUE FOR UNFROZEN WATER CONTENT  W_0
      STATEV(15) = 0 325D0
C     INITIAL VALUE FOR VOLUMETRIC ICE CONTENT
      STATEV(17) = 0 D0
C
      RETURN
      END
C
C
C**********************************************************************
C
C USDFLD  TO OBTAIN THE TEMPERATURE
C THIS SUBROUTINE IS CALLED AT ALL MATERIAL CALCULATION POINTS OF ELEMENTS
C FOR WHICH THE MATERIAL DEFINITION INCLUDES THE *USER DEFINED FIELD OPTION
C USED WITH
C *INITIAL CONDITIONS, TYPE=FIELD
C
C**********************************************************************
C
      SUBROUTINE USDFLD(FIELD,STATEV,PNEWDT,DIRECT,T,CELENT,TIME,DTIME,
     $ CMNAME,ORNAME,NFIELD,NSTATV,NOEL,NPT,LAYER,KSPT,KSTEP,KINC,
     $ NDI,NSHR,COORD,JMAC,JMTYP,MATLAYO,LACCFLG)
C
      INCLUDE 'ABA_PARAM INC'
C
      CHARACTER*80 CMNAME,ORNAME
      CHARACTER*3  FLGRAY(62)
      DIMENSION FIELD(NFIELD),STATEV(NSTATV),DIRECT(3,3),T(3,3),TIME(2),
     $ COORD(*),JMAC(*),JMTYP(*)
      DIMENSION ARRAY(62),JARRAY(62)
C
C GET APPARENT SPECIFIC HEAT FROM PREVIOUS INCREMENT
      CALL GETVRM('SDV',ARRAY,JARRAY,FLGRAY,JRCD,
     $    JMAC, JMTYP, MATLAYO, LACCFLG)
      FIELD(1) = ARRAY(27)
```

```
C
C   CHARACTERISTIC ELEMENT LENGTH
    STATEV(33) = CELENT
C
C GET HEAT FLUX FROM PREVIOUS INCREMENT
    CALL GETVRM('HFL',ARRAY,JARRAY,FLGRAY,JRCD,
   $   JMAC, JMTYP, MATLAYO, LACCFLG)
C   HEAT FLUX IN 1-DIRECTION (X)
    STATEV(38) = ARRAY(2)
C   HEAT FULX IN 2-DIRECTION (Y)
    STATEV(39) = ARRAY(1)
C
    RETURN
    END
C
C
C*************************************************************************C
C UEXPAN: TO DEFINE INCREMENTAL THERMAL STRAINS.
C THIS SUBROUTINE IS CALLED AT ALL INTEGRATION POINTS OF ELEMENTS
C FOR WHICH THE MATERIAL OR GASKET BEHAVIOR DEFINITION CONTAINS THE *EXPANSION,
C USER OPTION
C
C*************************************************************************
C
    SUBROUTINE UEXPAN(EXPAN,DEXPANDT,TEMP,TIME,DTIME,PREDEF,DPRED,
   $   STATEV,CMNAME,NSTATV,NOEL)
C
    INCLUDE 'ABA_PARAM.INC'
C
    CHARACTER*80 CMNAME
C
    DIMENSION EXPAN(*),DEXPANDT(*),TEMP(2),TIME(2),PREDEF(*),
   $   DPRED(*),STATEV(NSTATV)
C
C
C-----------------------------------------------
C   TEMPERATURE
C-----------------------------------------------
C   TEMPERATURE AT THE END OF THE INCREMENT (ALSO CALLED CURRENT TEMPERATURE)
    ETEMP = TEMP(1)
C   TEMPERATURE INCREMENT
    DTEMP = TEMP(2)
C   TEMPERATURE AT THE BEGINNING OF THE INCREMENT
    STEMP = TEMP(1) - TEMP(2)
C   SAVE THE TEMPERATURES AS SDVS
    STATEV(1) = STEMP
    STATEV(2) = ETEMP
    STATEV(3) = DTEMP
C CALCULATE THE RATE OF COOLING (C/HR)
    DTDT = -1.D0 * DTEMP / DTIME * 3600D0
C
C=================================================================================
C-----------------------------------------------
C   PARAMETERS FOR TEMPERATURE
C-----------------------------------------------
    ASPWTEMP = -0.15D0
    ASPCTEMP = -0.35D0
C
C-----------------------------------------------
C   PARAMETERS FOR SP POROSITY RATE FUNCTION
C-----------------------------------------------
    PMAXSP = 18.D-11

    TMSP = 0.03D0
    T0SP = 0.025D0
```

```
      CRC = 0 075D0
      CRSP = 0 015D0

C
C CALCULATE SP VALUE (M2/(SEC*C))
      IF (DTDT  GT  CRC) THEN
        PSP0 = 0 D0
      ELSE IF (DTDT  LT  CRSP) THEN
        PSP0 = 0 D0
      ELSE
        PSP0 = PMAXSP * ((DTDT + T0SP) / (TMSP + T0SP))**2 D0
     $      * EXP(1 D0 - ((DTDT + T0SP) / (TMSP + T0SP))**2 D0)
      END IF
C
C     CHARACTERISTIC ELEMENT LENGTH
      PINIEL = 1 0D-3
      PEL = STATEV(33)**2 D0 / PINIEL
C
C     MAXIMUM POROSITY
      PM = 0 7D0
C     POISSON'S RATION
      PSN = 0 3D0
C
C     PARAMETER IN POROSITY GROWTH TENSOR TO DETERMINE ISOTROPIC OR ORTHOTROPIC
C     GROWTH
C     IN THE DIRECTION OF HEAT FLOW  SI IS BETWEEN 1/3 (ISOTROPIC) AND 1 0
C     (UNIDERECTIONAL GROWTH IN THE DIRECTION OF HEAT FLOW)
      SI = 1 D0
C
C=======================================================================
C
C-----------------------------------------------------------------------
C     FIND THE ANGLE BETWEEN THE X-AXIS AND THE LINE OF THE HEAT FLOW DIRECTION
C-----------------------------------------------------------------------
C
      IF (ABS(STATEV(19))  LE  1 0E-7) THEN
        THETA = 3 14159265358D0 / 2 0D0
      ELSE
        THETA = ATAN(STATEV(20) / STATEV(19))
      END IF
      DIRM = COS(THETA)
      DIRN = SIN(THETA)
C
      STATEV(30) = THETA * 180D0 / 3 14159265358D0
      STATEV(31) = DIRM
      STATEV(32) = DIRN
C
C-----------------------------------------------------------------------
C     CALCULATE THE IN-SITU VOLUMETRIC STRAIN  DE_IN
C-----------------------------------------------------------------------
C CALCULATE FREEZING RATE DEPENDANCE FOR IN-SITU
      PMAXIN = 0 8D0

      Y01 = 0 2D0
      TMIN1 = 0 08D0
      T0IN1 = 0 0D0

      Y02 = 0 08D0
      TMIN2 = 0 075D0
      T0IN2 = TMIN2 - TMIN1

      CRIN = 0 4D0
C
      IF (DTDT  LE  0 D0) THEN
        PIN0 =0 D0
      ELSE
```

```
      IF (DTDT  GT  CRIN) THEN
       PIN0 = 0 D0
      ELSE IF (DTDT  LT  TMIN1) THEN
       PIN0 = Y01 + (PMAXIN - Y01) * ((DTDT - T0IN1) / TMIN1)**2 D0
     $      * EXP(1 D0 - ((DTDT - T0IN1) / TMIN1)**2 D0)
      ELSE
       PIN0 = Y02 + (PMAXIN - Y02) * ((DTDT - T0IN2) / TMIN2)**2 D0
     $      * EXP(1 D0 - ((DTDT - T0IN2) / TMIN2)**2 D0)
      END IF
     END IF
C
     DEIN = -0 09D0 * PIN0 * STATEV(22)
     $    * STATEV(16)/(STATEV(15)-STATEV(16))
C
C-----------------------------------------------------------------------
C    CALCULATE THE SP VOLUMETRIC STRAIN  DE_SP
C-----------------------------------------------------------------------
C CALCULATE THE MAXZRNUM SPACIAL TEMPERATURE GRADIENT (C/M)
     DTDL = SQRT (STATEV(19)**2 D0+ STATEV(20)**2 D0)
C
C CALCULATE THE FRACTION OF COOLING RATE
     IF (DTEMP  GE  0 D0) THEN
      PFDT = 0 D0
     ELSE
      PFDT = 1 D0
     END IF
C
C CALCULATE THE FRACTION OF FROZEN FRINGE
C    CASE1
     IF ((STEMP  GT  ASPWTEMP)  AND  (ETEMP  LT  ASPWTEMP)) THEN
      PFFF = 1 D0
C    CASE2
     ELSE IF ((STEMP  LE  ASPWTEMP)  AND  (ETEMP  GE  ASPCTEMP)) THEN
      PFFF = 1 D0
C    CASE3
     ELSE IF ((STEMP  GT  ASPCTEMP)  AND  (ETEMP  LT  ASPCTEMP)) THEN
      PFFF = 1 D0
C    CASE4
     ELSE
      PFFF = 0 D0
     END IF
C
C CALCULATE THE FRACTION OF ELEMENT NUMBER
     IF (DTDL  EQ  0 D0) THEN
      PFEL = 0 D0
     ELSE
      PFEL = ((ASPWTEMP - ASPCTEMP) / DTDL) / PEL
     END IF
C
C CALCULATE THE SP POROSITY FUNCTION
     IF (PFEL  EQ  0 D0) THEN
      PSP = 0 D0
     ELSE
      PSP = PSP0 / (PEL * PFEL)
     END IF
C
C CALCULATE THE SP VOLUMETRIC STRAIN  DE_SP
     IF (STATEV(13)  GE  PM) THEN
       DESP = 0 D0
     ELSE
       DESP = PFDT * PFFF
     $      * 1 09D0 * PSP
     $      * DTDL
     END IF
C
C-----------------------------------------------------------------------
```

```
C    CALCULATE THE TOTAL VOLUMETRIC STRAIN  DE_TOTAL
C-------------------------------------------------------------------------------
C
     DE = DEIN
    $  + DESP* DTIME
C
C GET GRADTSP (C/CM)
     IF (PFFF   EQ  0 D0) THEN
       VGRADTSP=0 D0
     ELSE
       VGRADTSP=DTDL/100 D0
     END IF
C
C GET EFFECTIVE ELEMENT SIZE (Permafrost Subcommittee)
     IF (PFFF   EQ  0 D0) THEN
       VEEL=0 D0
     ELSE
       VEEL=PFEL * PEL * 1000 D0
     END IF
C
C GET DE_SP (1/HR)
     IF (PFFF   EQ  0 D0) THEN
       VDESP=0 D0
     ELSE
      IF (DTDT  LE  CRL) THEN
        VDESP = 0 D0
      ELSE
        VDESP = PFDT * PFFF
    $        * 1 09D0 * PSP
    $        * DTDL * 3600 D0
      END IF
     END IF
C
C GET DTDT FOR SP (C/HR)
     IF (PFFF   EQ  0 D0) THEN
       VDTSP = 0 D0
     ELSE
             VDTSP = DTDT
     END IF
C
C GET PSP0 (M2/(SEC*C))
     IF (PFFF   EQ  0 D0) THEN
       VPSP0 = 0 D0
     ELSE
             VPSP0 = PFFF * PSP0
     END IF
C
C
     STATEV(4) = DE
     STATEV(40) = DEIN
     STATEV(41) = DESP
     STATEV(42) = DTDT
     STATEV(43) = DTDL
     STATEV(44) = PRE
     STATEV(45) = PSP0
     STATEV(46) = PSP
     STATEV(47) = PFDT
     STATEV(48) = PFFF
     STATEV(49) = PEL
     STATEV(50) = PFEL
     STATEV(51) = PFFR
     STATEV(52) = PIN0
     STATEV(53) = VGRADTSP
     STATEV(54) = VEEL
     STATEV(55) = VDESP
     STATEV(56) = VDTSP
```

```
      STATEV(57) = VPSP0
C     STATEV(58) =
C     STATEV(59) =
C     STATEV(60) =

C
      EXPAN(1) = ((DIRM**2 D0) * (SI+0 5D0*PSN*(1 D0-SI))
     $       + (DIRN**2 D0)* 0 5D0 * (1 D0+PSN) * (1 D0-SI)) * DE
      EXPAN(2) = ((DIRN**2 D0) * (SI+0 5*PSN*(1 D0-SI))
     $       + (DIRM**2 D0)* 0 5D0 * (1 D0+PSN) * (1 D0-SI)) * DE
      EXPAN(3) = DIRM * DIRN * (3 D0 * SI -1 D0) * DE
C
      STATEV(5) = EXPAN(1)
      STATEV(6) = EXPAN(2)
      STATEV(7) = EXPAN(3)
C     STATEV(8) =
C     STATEV(9) =
C
      RETURN
      END
C
C
C*************************************************************************
C
C HETVAL  TO OBTAIN THE TEMPERATURE
C THIS SUBROUTINE IS CALLED AT ALL MATERIAL CALCULATION POINTS OF ELEMENTS
C FOR WHICH THE MATERIAL DEFINITION INCLUDES THE *HEAT GENERATION OPTION
C
C*************************************************************************
C
      SUBROUTINE HETVAL(CMNAME,TEMP,TIME,DTIME,STATEV,FLUX,
     1 PREDEF,DPRED)
C
      INCLUDE 'ABA_PARAM INC'
C
      CHARACTER*80 CMNAME
C
      DIMENSION TEMP(2),STATEV(*),PREDEF(*),TIME(2),FLUX(2),
     1 DPRED(*)
C
C=======================================================================
C-----------------------------------------------
C     PARAMETERS FOR TEMPERATURE
C-----------------------------------------------
      ALIQTEMP = 0 0D0
      AINTEMP = -0 1D0
C
C-----------------------------------------------
C     PARAMETERS FOR UNFROZEN WATER CONTENT CURVE
C-----------------------------------------------
C     INITIAL WATER CONTENT, RESIDUAL WATER CONTENT
      WBAR = 0 325D0
      WSTAR= 0 0325D0
      AF = 2 925D0
C
C-----------------------------------------------
C     SOIL PROPERTY CONSTANTS
C-----------------------------------------------
C     DENSITIES OF SOIL SKELETON, WATER, AND ICE
      DENSKEL = 2746 D0
      DENWATER = 1000 D0
      DENICE = 1000 D0 / 1 09D0
C     MASS SPECIFIC HEAT CAPACITIES OF SOIL SKELETON, WATER AND ICE
      SHTSKEL = 800 D0
      SHTWATER = 4200 D0
      SHTICE = 2090 D0
```

```
C    LATENT HEAT OF FUSION OF WATER
     WLATENT = 333700 D0
C
C-----------------------------------------------------
C    PARAMETERS FOR THERMAL CONDUCTIVITY
C-----------------------------------------------------
     PROINI = 0 471584454D0
     DENSOINI = DENSKEL * PROINI
C    SATURATION
     SR=1 0D0
C    QUARTZS
     PQ=0 1D0
C
C=====================================================================
C
C-----------------------------------------------
C    TEMPERATURE DEFINITION
C-----------------------------------------------
C    TEMPERATURE AT THE START OF THE INCREMENT (ALSO CALLED CURRENT
C    TEMPERATURE)
     STATEV(10) = TEMP(1)
C    TEMPERATURE AT THE END OF THE INCREMENT
     STATEV(11) = TEMP(1) + TEMP(2)
C    TEMPERATURE INCREMENT
     STATEV(12) = TEMP(2)
C
C-----------------------------------------------------
C    UPDATE POROSITY
C-----------------------------------------------------
C CALCULATE THE POROSITY INCREMENT
     STATEV(14) = (1 D0 - STATEV(13)) * STATEV(4) / (1 D0 + STATEV(4))
C CALCULATE THE POROSITY AT THE END OF THIS INCREMENT
     STATEV(13) = STATEV(13) + STATEV(14)
C
C-----------------------------------------------------
C    UPDATE GRAVIMETRIC UNFROZEN WATER CONTENT
C-----------------------------------------------------
C GET THE UNFROZEN WATER CONTENT AT THE START OF THE INCREMENT
     WATT = STATEV(15)
C CALCULATE THE WATER CONTENT AT THE END OF THE INCREMENT
           IF (STATEV(2)  GE  ALIQTEMP) THEN
        STATEV(15) = WBAR
      ELSE IF (STATEV(2)  LE  AINTEMP) THEN
        STATEV(15) = WSTAR
      ELSE
        STATEV(15) = WBAR + AF * STATEV(2)
      END IF
C CALCULATE THE UNFROZEN WATER CONTENT INCREMENT
     STATEV(16) = STATEV(15) - WATT
C
C-----------------------------------------------------
C    CALCULATE VOLUMETRIC ICE CONTENT
C-----------------------------------------------------
C GET THE ICE CONTENT AT THE BEGINNING OF THE INCREMENT
     VIATT = STATEV(17)
C CALCULATE THE ICE CONTENT AT THE END OF THE INCREMENT
     STATEV(17) = STATEV(13) - (DENSKEL / DENWATER)
    $          * STATEV(15) * (1 D0 - STATEV(13))
C
           IF (STATEV(17)  LT  0 D0) THEN
       STATEV(17) = 0 0D0
           END IF
C CALCULATE THE INCREMENT
     STATEV(18) = STATEV(17) - VIATT
C
C-----------------------------------------------------
```

```
C    UPDATE VOLUMETRIC FRACTIONS
C-----------------------------------------------------------
C CALCULATE VOLUMETRIC FRACTION OF SKEIETON, WATER AND ICE
C    POROSITY AT THE BEGINNING OF THE INCREMENT
     PROBEGIN = STATEV(13) - STATEV(14)
C    VOLUMETRIC FRACTION OF ICE AT THE BEGINNING OF THE INCREMENT
     VICEBEGIN = STATEV(17) - STATEV(18)
C    VOLUMETRIC FRACTION OF SKELETON, WATER, AND ICE
     VSKEL = 1 D0 - PROBEGIN
     VWATER = PROBEGIN - VICEBEGIN
     VICE = VICEBEGIN
C
C-------------------------------------------------------------------
C    CALCULATE FROZEN SOIL PROPETIES
C-------------------------------------------------------------------
C    DRY FROZEN SOIL DENSITY
     DENSOIL = VSKEL * DENSKEL
C    CALCULATE DENSITY OF POROSITY
     DENPRO = VWATER / PROBEGIN * DENWATER
    $      + VICE /PROBEGIN * DENICE
C    CALCULATE THE GRAVIMETRIC WATER CONTENT
     TGWATER =PROBEGIN / (1 D0 - PROBEGIN) * DENPRO / DENSKEL
C
C-------------------------------------------------------------------
C    CALCULATE SPECIFIC HEAT CAPACITY AND APPARENT HEAT CAPACITY
C-------------------------------------------------------------------
C CALCULATE SPECIFIC HEAT CAPACITY
     SPECHT=(VSKEL*DENSKEL*SHTSKEL)+(VWATER*DENWATER*SHTWATER)
    $     +(VICE*DENICE*SHTICE)
C CALCULATE APPARENT HEAT CAPACITY
     IF (STATEV(3)  GE  0 D0) THEN
      ASPECHT = 0 D0
     ELSE
      ASPECHT = ABS(WLATENT * DENICE * STATEV(18) / STATEV(3))
     END IF
C CALCULATE TOTAL HEAT CAPACITY
     TSPECHT = SPECHT + ASPECHT
C
C-------------------------------------------------------------------
C    CALCULATE THERMAL CONDICTIVITY BY JOHANSEN'S METHOD
C-------------------------------------------------------------------
C CALCULATE THE CONSTANT VOLMETRIC WATER CONTENT
C AT THE START OF THE INCREMENT
     CVWATER = (DENSKEL / DENWATER) * WATT * (1 D0 - PROINI)
C
      CONDDRY=(0 137D0*DENSOINI+64 7D0)/(2 7D3-0 947D0*DENSOINI)
      CONDSKEL=7 7D0**PQ*2 D0**(1 D0-PQ)
C    THAWED CONDITION
     IF (STATEV(1)  GE  0 D0) THEN
      CONDE=LOG10(SR)+1 D0
      CONDSAT=(0 57D0**PROINI)*(CONDSKEL**(1 D0-PROINI))
      COND=(CONDSAT-CONDDRY)*CONDE+CONDDRY
C    FROZEN CONDITION
     ELSE
      CONDE=SR
      CONDSAT=2 2D0**PROINI*CONDSKEL**(1 D0-PROINI)*0 269D0**CVWATER
      COND=(CONDSAT-CONDDRY)*CONDE+CONDDRY
     ENDIF
C
C-----------------------------------------------------
C    CALCULATE THE TEMPERATURE GRADIENT
C-----------------------------------------------------
C    SPACIAL GRADIENT OF TEMPERATURE IN L-DIRECTION (X)
      STATEV(19) = STATEV(38) / COND
C    SPACIAL GRADIENT OF TEMPERATURE IN 2-DIRECTION (Y)
      STATEV(20) = STATEV(39) / COND
```

```
C
      STATEV(21) = VSKEL
      STATEV(22) = VWATER
      STATEV(23) = VICE
      STATEV(24) = COND
      STATEV(25) = SPECHT
      STATEV(26) = ASPECHT
      STATEV(27) = TSPECHT
      STATEV(28) = DENSOIL
      STATEV(29) = TGWATER
C
C-----------------------------------------------------------
C     INPUT FLUX(1)
C-----------------------------------------------------------
      FLUX(1) = 0.D0
C
      RETURN
      END
```

APPENDIX C.2 User defined function in two dimensions

```
C**********************************************************************
C USER SUBROUTINES FOR TWO-DIMENSIONALSP POROSITY GROWTH FUNCTION
C
C WRITTEN BY KIM, KOUI, 2009
C**********************************************************************
C
C**********************************************************************
C
C SDVINI: ABAQUS WILL CALL THIS ROUTINE TO DEFINE
C THE INITIAL SOLUTION-DEPENDENT STATE VARIABLE FLELDS
C AT PARTICULAR MATERIAL POINTS
C USED WITH THE *INITIAL CONDITIONS, TYPE=SOLUTION, USER OPTION IN INPUT FILE
C
C**********************************************************************
C
      SUBROUTINE SDVINI(STATEV,COORDS,NSTATV,NCRDS,NOEL,NPT,LAYER,KSPT)
C
      INCLUDE 'ABA_PARAM.INC'
C
C     THE NUMBER OF STATE VARIABLES (NSTATV) IS DEFINED USING *DEPVAR OPTSON
C     IN THE INPUT FILE
      DIMENSION STATEV(NSTATV),COORDS(NCRDS)
C
C     THE VALUES OF N_0 AND W_0 MUST MATCH WITH THE DENSITY OF SOIL
C     SKELTON SO THAT THE INITIAL ICE CONTENT IS ZERO
C     INITIAL VALUE FOR POROSITY: N_0
      STATEV(13) = 0.523446435D0
C
C     INITIAL VALUE FOR UNFROZEN WATER CONTENT: W_0
      STATEV(15) = 0.4D0
C
C     INITIAL VALUE FOR VOLUMETRIC ICE CONTENT
      STATEV(17) = 0.D0
C
C     INITIAL VALUE FOR DRY SOIL DENSITY (KG/M^3)
      STATEV(28) = 1308.616088D0
C
C     INITIAL TOTAL WATER CONTENT
      STATEV(29) = 0.4D0
C
C
      RETURN
      END
C
C
C**********************************************************************
C
C USDFLD: TO OBTAIN THE TEMPERATURE
C THIS SUBROUTINE IS CALLED AT ALL MATERIAL CALCULATION POINTS OF ELEMENTS
C FOR WHICH THE MATERIAL DEFINITION INCLUDES THE *USER DEFINED FIELD OPTION
C USED WITH
C *INITIAL CONDITIONS, TYPE=FIELD
C
C**********************************************************************
C
      SUBROUTINE USDFLD(FIELD,STATEV,PNEWDT,DIRECT,T,CELENT,TIME,DTIME,
     $ CMNAME,ORNAME,NFIELD,NSTATV,NOEL,NPT,LAYER,KSPT,KSTEP,KINC,
     $ NDI,NSHR,COORD,JMAC,JMTYP,MATLAYO,LACCFLG)
C
      INCLUDE 'ABA_PARAM.INC'
C
      CHARACTER*80 CMNAME,ORNAME
```

```
      CHARACTER*3 FLGRAY(80)
      DIMENSION FIELD(NFIELD),STATEV(NSTATV),DIRECT(3,3),T(3,3),TIME(2),
     $ COORD(*),JMAC(*),JMTYP(*)
      DIMENSION ARRAY(80),JARRAY(80)
C
C GET APPARENT SPECIFIC HEAT FROM PREVIOUS INCREMENT
      CALL GETVRM('TEMP',ARRAY,JARRAY,FLGRAY,JRCD,
     $    JMAC, JMTYP, MATLAYO, LACCFLG)
      STATEV(57) = ARRAY(1)
C
C GET APPARENT SPECIFIC HEAT FROM PREVIOUS INCREMENT
      CALL GETVRM('SDV',ARRAY,JARRAY,FLGRAY,JRCD,
     $    JMAC, JMTYP, MATLAYO, LACCFLG)
      FIELD(1) = ARRAY(27)
C
C GET HEAT FLUX FROM PREVIOUS INCREMENT
      CALL GETVRM('HFL',ARRAY,JARRAY,FLGRAY,JRCD,
     $    JMAC, JMTYP, MATLAYO, LACCFLG)
C     HEAT FLUX IN 1-DIRECTION (X)
      STATEV(30) = ARRAY(2)
C     HEAT FULX IN 2-DIRECTION (Y)
      STATEV(31) = ARRAY(3)
C     STATEV(32) = ARRAY(4)
C
C     CHARACTERISTIC ELEMENT LENGTH
      STATEV(33) = CELENT
C
C GET MISES STRESS FROM PREVIOUS INCREMENT
      CALL GETVRM('SINV',ARRAY,JARRAY,FLGRAY,JRCD,
     $    JMAC, JMTYP, MATLAYO, LACCFLG)
C     MISES
      STATEV(34) = ARRAY(1)
C
C GET COORDINATE (M)
      STATEV(35) = COORD(1)
      STATEV(36) = COORD(2)
C     STATEV(37) = COORD(3)
C
C-----------------------------------------------
C     PARAMETERS FOR PFFF
C-----------------------------------------------
C     TOTAL TIME AT THE BEGINNING OF THE CURRENT INCREMENT
      TTIME = TIME(2)
C
C DETERMINE ASPWLTEMP
      ASPWLTEMP1 =  0 D0
      ASPWLTEMP2 =  0 D0
      ASPWLTEMP3 =  0 D0
      ASPWLTEMP4 =  0 D0
      ASPWLTEMP5 =  0 D0
C
C DETERMINE ASPS
      ASPS1 = 4 D0
      ASPS2 = 4 D0
      ASPS3 = 4 D0
      ASPS4 = 4 D0
      ASPS5 = 4 D0
C
      ATTIME1 = 11028960
      ATTIME2 = 26295840
      ATTIME3 = 42564960
      ATTIME4 = 74100960
      ATTIME5 = 91756800
C
      IF (TTIME  LE  ATTIME1) THEN
       ASPWLTEMP = ASPWLTEMP1
```

```
      ASPS = ASPS1
     ELSE IF (TTIME  LE  ATTIME2) THEN
      ASPWLTEMP = ASPWLTEMP2
      ASPS = ASPS2
     ELSE IF (TTIME  LE  ATTIME3) THEN
      ASPWLTEMP = ASPWLTEMP3
      ASPS = ASPS3
     ELSE IF (TTIME  LE  ATTIME4) THEN
      ASPWLTEMP = ASPWLTEMP4
      ASPS = ASPS4
     ELSE
      ASPWLTEMP = ASPWLTEMP5
      ASPS = ASPS5
     END IF
C
     STATEV(4) = TTIME
     STATEV(5) = ASPWLTEMP
     STATEV(6) = ASPS
C
C-------------------------------------------------
C    PARAMETERS FOR WATER TABLE
C-------------------------------------------------
C    ELEVATION OF GROUND SURFACE (M)
     AEGS = 1 D0
C    ELEVATION OF SOIL BOUDARY (M)
     AEBS = -857 D-03
C
C    CALCULATE GROUND WATER TABLE (M)
     AWT01 = 0 D0
     AWT02 = 12787200 D0
     AWT03 = 24796800 D0
     AWT04 = 29808000 D0
     AWT05 = 42508800 D0
     AWT06 = 54086400 D0
     AWT07 = 61344000 D0
     AWT08 = 75859200 D0
     AWT09 = 87868800 D0
     AWT10 = 95212800 D0
     AWT11 = 107308800 D0
     AWT12 = 117158400 D0
C
     AWY01 = -2 2D0
     AWY02 = -2 2D0
     AWY03 = 0 5D0
     AWY04 = -1 7D0
     AWY05 = -1 7D0
     AWY06 = 0 D0
     AWY07 = -2 2D0
     AWY08 = -2 2D0
     AWY09 = 0 5D0
     AWY10 = -1 7D0
     AWY11 = -1 7D0
     AWY12 = 0 5D0
C
     AWCT01S = 12787200 D0
     AWCT01E = 17625600 D0
     AWCT02S = 42508800 D0
     AWCT02E = 48470400 D0
     AWCT03S = 75859200 D0
     AWCT03E = 80697600 D0
     AWCT04S = 109728000 D0
     AWCT04E = 113356800 D0
C
     AWCY01 = 0 D0
     AWCY02 = 0 5D0
     AWCY03 = 0 D0
```

```
      AWCY04 = 0.D0
C
      IF (TTIME .LE. AWT02) THEN
       AWY1 = AWY01
       AWY2 = AWY02
       TTIME1 = AWT01
       TTIME2 = AWT02
      ELSE IF (TTIME .LE. AWT03) THEN
       AWY1 = AWY02
       AWY2 = AWY03
       TTIME1 = AWT02
       TTIME2 = AWT03
      ELSE IF (TTIME .LE. AWT04) THEN
       AWY1 = AWY03
       AWY2 = AWY04
       TTIME1 = AWT03
       TTIME2 = AWT04
      ELSE IF (TTIME .LE. AWT05) THEN
       AWY1 = AWY04
       AWY2 = AWY05
       TTIME1 = AWT04
       TTIME2 = AWT05
      ELSE IF (TTIME .LE. AWT06) THEN
       AWY1 = AWY05
       AWY2 = AWY06
       TTIME1 = AWT05
       TTIME2 = AWT06
      ELSE IF (TTIME .LE. AWT07) THEN
       AWY1 = AWY06
       AWY2 = AWY07
       TTIME1 = AWT06
       TTIME2 = AWT07
      ELSE IF (TTIME .LE. AWT08) THEN
       AWY1 = AWY07
       AWY2 = AWY08
       TTIME1 = AWT07
       TTIME2 = AWT08
      ELSE IF (TTIME .LE. AWT09) THEN
       AWY1 = AWY08
       AWY2 = AWY09
       TTIME1 = AWT08
       TTIME2 = AWT09
      ELSE IF (TTIME .LE. AWT10) THEN
       AWY1 = AWY09
       AWY2 = AWY10
       TTIME1 = AWT09
       TTIME2 = AWT10
      ELSE IF (TTIME .LE. AWT11) THEN
       AWY1 = AWY10
       AWY2 = AWY11
       TTIME1 = AWT10
       TTIME2 = AWT11
      ELSE IF (TTIME .LE. AWT12) THEN
       AWY1 = AWY11
       AWY2 = AWY12
       TTIME1 = AWT11
       TTIME2 = AWT12
      ELSE
       AWY1 = AWY11
       AWY2 = AWY11
       TTIME1 = AWT11
       TTIME2 = AWT12
      END IF
C
C     CALCULATE GROUND WATER TABLE (M)
      WTY = AWY1 + (AWY2 - AWY1) / (TTIME2 - TTIME1)
```

```
     $   * (TTIME - TTIME1)
C
C    MODIFY WITH CONFINED EFFECT
     IF ((TTIME  GE  AWCT01S)  AND
     $   (TTIME  LE  AWCT01E)) THEN
       WTY = AWCY01
     ELSE IF ((TTIME  GE  AWCT02S)  AND
     $       (TTIME  LE  AWCT02E)) THEN
       WTY = AWCY02
     ELSE IF ((TTIME  GE  AWCT03S)  AND
     $       (TTIME  LE  AWCT03E)) THEN
       WTY = AWCY03
     ELSE IF ((TTIME  GE  AWCT04S)  AND
     $       (TTIME  LE  AWCT04E)) THEN
       WTY = AWCY04
     ELSE
       WTY = WTY
     END IF
C
C    CALCULATE BULK SOIL DENSITY OF SR(KG/M^3)
     DENSBULK = STATEV(28) * (1 D0 + STATEV(29))
C    BULK SOIL DESNSITY OF USR(KG/M^3)
     DENSBULKUSR = 1716 904308D0
C
C    OVERBURDEN PRESSURE (IN UNIT OF PASCAL)
     IF (STATEV(36)  GE  AEGS) THEN
       PRE = 0 D0
     ELSE IF (WTY  GE  AEBS) THEN
       IF (STATEV(36)  GE  WTY) THEN
         PRE = 9 80665D0 * (DENSBULKUSR*(AEGS - STATEV(36)))
       ELSE IF (STATEV(36)  GE  AEBS) THEN
         PRE = 9 80665D0 * (DENSBULKUSR*(AEGS - WTY)
     $       + (DENSBULKUSR - 1000 D0)*(WTY - STATEV(36)))
       ELSE
         IF (STATEV(57)  LE  STATEV(5)) THEN
           PRE = 9 80665D0 * (DENSBULKUSR*(AEGS - WTY)
     $         + (DENSBULKUSR - 1000 D0)*(WTY - AEBS)
     $         + (DENSBULK -1000 D0)*(AEBS - STATEV(36)))
         ELSE
           PRE = 9 80665D0 * (DENSBULKUSR*(AEGS - WTY)
     $         + DENSBULKUSR*(WTY - AEBS)
     $         + STATEV(28)*(AEBS - STATEV(36)))
         END IF
       END IF
     ELSE
       IF (STATEV(36)  GE  AEBS) THEN
         PRE = 9 80665D0 * (DENSBULKUSR*(AEGS - STATEV(36)))
       ELSE IF (STATEV(36)  GE  WTY) THEN
         PRE = 9 80665D0 * (DENSBULKUSR*(AEGS - AEBS)
     $       + DENSBULK*(AEBS - STATEV(36)))
       ELSE
         IF (STATEV(57)  LE  STATEV(5)) THEN
           PRE = 9 80665D0 * (DENSBULKUSR*(AEGS - AEBS)
     $         + DENSBULK*(AEBS - WTY)
     $         + (DENSBULK - 1000 D0)*(WTY - STATEV(36)))
         ELSE
           PRE = 9 80665D0 * (DENSBULKUSR*(AEGS - AEBS)
     $         + DENSBULK*(AEBS - WTY)
     $         + STATEV(28)*(WTY - STATEV(36)))
         END IF
       END IF
     END IF
C
     STATEV(38) = WTY
     STATEV(39) = DENSBULK
     STATEV(40) = PRE
```

```
C
C   CALCULATE THE AVERAGE TOTAL STRESS
    STATEV(46) = STATEV(34) + STATEV(40)
C
    RETURN
    END
C
C
C*************************************************************************C
C UEXPAN: TO DEFINE INCREMENTAL THERMAL STRAINS.
C THIS SUBROUTINE IS CALLED AT ALL INTEGRATION POINTS OF ELEMENTS
C FOR WHICH THE MATERIAL OR GASKET BEHAVIOR DEFINITION CONTAINS THE *EXPANSION,
C USER OPTION
C
C*************************************************************************
C
    SUBROUTINE UEXPAN(EXPAN,DEXPANDT,TEMP,TIME,DTIME,PREDEF,DPRED,
   $    STATEV,CMNAME,NSTATV,NOEL)
C
    INCLUDE 'ABA_PARAM.INC'
C
    CHARACTER*80 CMNAME
C
    DIMENSION EXPAN(*),DEXPANDT(*),TEMP(2),TIME(2),PREDEF(*),
   $    DPRED(*),STATEV(NSTATV)
C
C---------------------------------------------
C   TEMPERATURE AND TIME
C---------------------------------------------
C   TEMPERATURE AT THE END OF THE INCREMENT (ALSO CALLED CURRENT TEMPERATURE)
    ETEMP = TEMP(1)
C   TEMPERATURE INCREMENT
    DTEMP = TEMP(2)
C   TEMPERATURE AT THE BEGINNING OF THE INCREMENT
    STEMP = TEMP(1) - TEMP(2)
C
C   SAVE THE TEMPERATURES AS SDVS
    STATEV(1) = STEMP
    STATEV(2) = ETEMP
    STATEV(3) = DTEMP
C
    PI = 3.14159265358D0
C CALCULATE THE RATE OF COOLING (C/HR)
    DTDT = -1.D0 * DTEMP / DTIME * 3600D0
C
C=============================================================================
C---------------------------------------------
C   PARAMETERS FOR TEMPERATURE
C---------------------------------------------
    ASPWTEMP = -0.15D0
    ASPCTEMP = -0.35D0
C
C---------------------------------------------
C   PARAMETERS FOR SP POROSITY RATE FUNCTION
C---------------------------------------------
C   SP0 VALUE (M2/(SEC*C))
    PSP0 = 262.4D-11
C   B VALUE (PA^-1)
    PB = 0.02596D-3
C
C   CHARACTERISTIC ELEMENT LENGTH
    AREA = STATEV(33) * STATEV(33)
    PEL = STATEV(33)
    PINIEL = AREA / PEL
C
C   MAXIMUM POROSITY
```

```
      PM = 0 7D0
C     POISSON'S RATION
      PSN = 0 3D0
C
C     PARAMETER IN POROSITY GROWTH TENSOR TO DETERMINE ISOTROPIC OR ORTHOTROPIC
C     GROWTH
C     IN THE DIRECTION OF HEAT FLOW  SI IS BETWEEN 1/3 (ISOTROPIC) AND 1 0
C     (UNIDERECTIONAL GROWTH IN THE DIRECTION OF HEAT FLOW)
      SI = 0 9D0
C
C=====================================================================
C
C---------------------------------------------------------------------
C     FIND THE ANGLE BETWEEN THE X-AXIS AND THE LINE OF THE HEAT FLOW DIRECTION
C---------------------------------------------------------------------
C
      IF (ABS(STATEV(19)) LE 1 0E-7) THEN
       THETA = PI / 2 0D0
      ELSE
       THETA = ATAN(STATEV(20) / STATEV(19))
      END IF
      DIRM = COS(THETA)
      DIRN = SIN(THETA)
C
      STATEV(58) = THETA * 180D0 / PI
      STATEV(59) = DIRM
      STATEV(60) = DIRN
C
C---------------------------------------------------------------------
C     CALCULATE THE IN-SITU VOLUMETRIC STRAIN  DE_IN
C---------------------------------------------------------------------
      DEIN = -0 09D0 * STATEV(23)
     $    * STATEV(16)/(STATEV(15)-STATEV(16))
C
C---------------------------------------------------------------------
C     CALCULATE THE SP VOLUMETRIC STRAIN  DE_SP
C---------------------------------------------------------------------
C CALCULATE THE MAXZRNUM SPACIAL TEMPERATURE GRADIENT (C/M)
      DTDL = SQRT (STATEV(19)**2 D0+ STATEV(20)**2 D0)
C CALCULATE THE FLAG OF WATER TABLE
      IF (THETA EQ PI / 2 0D0) THEN
       PELSP = PINIEL
      ELSE
            PELSP = ABS(PINIEL / COS(PI / 2 0D0 - ABS(THETA)))
      END IF
C
C CALCULATE THE FLAG OF BOTTOM OF SP
      IF (STATEV(36) GE -6 0D0) THEN
       PFB = 1 D0
      ELSE
            PFB = 0 D0
      END IF
C
C CALCULATE THE FLAG OF SIDE OF SP
      IF (STATEV(35) LE STATEV(6)) THEN
       PFS = 1 D0
      ELSE
            PFS = 0 D0
      END IF
C
C CALCULATE THE FLAG OF FREEZING
      IF (DTEMP GE 0 D0) THEN
       PFDT = 0 D0
      ELSE
       PFDT = 1 D0
      END IF
```

```
C
C CALCULATE THE FLAG OF WATER TABLE
    IF (STATEV(36)  GE  STATEV(38)) THEN
      PFWT = 0 D0
    ELSE
          PFWT = 1 D0
    END IF
C
C CALCULATE THE FLAG OF SP FREEZIG ZONE
    IF ((STATEV(2)  LE  STATEV(5))  AND
   $   (STATEV(2)  GE  ASPCTEMP)) THEN
      PFFF = 1 0D0
    ELSE
      PFFF = 0 D0
    END IF
C
C CALCULATE THE FLAG OF SP POROSITY FUNCTION
    PFDESP = PFB * PFS * PFDT* PFWT * PFFF
C
    IF (PFDESP  LE  0 D0) THEN
      PFDESP = 0 D0
    ELSE
      PFDESP = 1 D0
    END IF
C
C CALCULATE THE FRACTION OF ELEMENT NUMBER
    IF (DTDL  EQ  0 D0) THEN
      PFEL = 0 D0
    ELSE
      PFEL = ((ASPWTEMP - ASPCTEMP) / DTDL) / PEL
    END IF
C
C CALCULATE THE SP POROSITY FUNCTION
    IF (PFEL  EQ  0 D0) THEN
      PSP = 0 D0
    ELSE IF (PFEL  GE  1 D0) THEN
      PSP = PSP0 /  (AREA* PFEL) * PELSP
   $     * EXP(-1 D0 * PB * STATEV(46))
    ELSE
      PSP = PSP0 / AREA * PELSP
   $     * EXP(-1 D0 * PB * STATEV(46))
    END IF
C
C CALCULATE THE SP VOLUMETRIC STRAIN  DE_SP
    IF (STATEV(13)  GE  PM) THEN
      DESP = 0 D0
    ELSE
      DESP = PFDESP
   $      * 1 09D0 * PSP * DTDL * DTIME
    END IF
C
C-------------------------------------------------------------------------
C    CALCULATE THE TOTAL VOLUMETRIC STRAIN  DE_TOTAL
C-------------------------------------------------------------------------
      DE = DEIN
   $    + DESP
C
C GET GRADTSP (C/CM)
    IF (PFFF   EQ  0 D0) THEN
      VGRADTSP=0 D0
    ELSE
      VGRADTSP= PFFF * DTDL
    END IF
C
C GET SE (Permafrost Subcommittee)
    IF (PFFF   EQ  0 D0) THEN
```

```
      VSE=0.D0
    ELSE
      VSE = PFFF * STATEV(34)
    END IF
C
C
    STATEV(41) = DE
    STATEV(42) = DEIN
    STATEV(43) = DESP
    STATEV(44) = DTDT
    STATEV(45) = DTDL
C     STATEV(46) = SKK
    STATEV(47) = PSP
    STATEV(48) = PELSP
    STATEV(49) = PFB
    STATEV(50) = PFS
    STATEV(51) = PFWT
    STATEV(52) = PFFF
    STATEV(53) = PFDESP
    STATEV(54) = PFEL
C
    STATEV(55) = VGRADTSP
    STATEV(56) = VSE
C
    EXPAN(1) = ((DIRM**2.D0) * (SI+0.5D0*PSN*(1.D0-SI))
   $       + (DIRN**2.D0)* 0.5D0 * (1.D0+PSN) * (1.D0-SI)) * DE
    EXPAN(2) = ((DIRN**2.D0) * (SI+0.5D0*PSN*(1.D0-SI))
   $       + (DIRM**2.D0)* 0.5D0 * (1.D0+PSN) * (1.D0-SI)) * DE
    EXPAN(3) = 0.D0
    EXPAN(4) = DIRM * DIRN * 0.5D0 * (3.D0 * SI -1.D0) * DE
    EXPAN(5) = 0.D0
    EXPAN(6) = 0.D0
C
    STATEV(7) = EXPAN(1)
    STATEV(8) = EXPAN(2)
C     STATEV(9) = EXPAN(3)
    STATEV(10) = EXPAN(4)
C     STATEV(11) = EXPAN(5)
C     STATEV(12) = EXPAN(6)
C
    RETURN
    END
C
C
C*************************************************************************
C
C HETVAL: TO OBTAIN THE TEMPERATURE
C THIS SUBROUTINE IS CALLED AT ALL MATERIAL CALCULATION POINTS OF ELEMENTS
C FOR WHICH THE MATERIAL DEFINITION INCLUDES THE *HEAT GENERATION OPTION
C
C*************************************************************************
C
    SUBROUTINE HETVAL(CMNAME,TEMP,TIME,DTIME,STATEV,FLUX,
   1 PREDEF,DPRED)
C
    INCLUDE 'ABA_PARAM.INC'
C
    CHARACTER*80 CMNAME
C
    DIMENSION TEMP(2),STATEV(*),PREDEF(*),TIME(2),FLUX(2),
   1 DPRED(*)
C
C=======================================================================
C-----------------------------------------------------
C    PARAMETERS FOR TEMPERATURE
C-----------------------------------------------------
```

```
      ALIQTEMP = 0 0D0
      AINTEMP = -0 1D0
C
C-----------------------------------------------------
C     PARAMETERS FOR UNFROZEN WATER CONTENT CURVE
C-----------------------------------------------------
C     INITIAL WATER CONTENT, RESIDUAL WATER CONTENT
      WBAR = 0 4D0
      WSTAR= 0 07D0
      AF = (WBAR - WSTAR) / (ALIQTEMP - AINTEMP)
C
C-----------------------------------------------------
C     SOIL PROPERTY CONSTANTS
C-----------------------------------------------------
C     DENSITIES OF SOIL SKELETON, WATER, AND ICE
      DENSKEL = 2746 D0
      DENWATER = 1000 D0
      DENICE = 1000 D0 / 1 09D0
C     MASS SPECIFIC HEAT CAPACITIES OF SOIL SKELETON, WATER AND ICE
      SHTSKEL = 800 D0
      SHTWATER = 4200 D0
      SHTICE = 2090 D0
C     LATENT HEAT OF FUSION OF WATER
      WLATENT = 333700 D0
C
C-----------------------------------------------------
C     PARAMETERS FOR THERMAL CONDUCTIVITY
C-----------------------------------------------------
      PROINI = 0 523446435D0
      DENSOINI = DENSKEL * (1 D0 - PROINI)
C     SATURATION
      SR=1 0D0
C     QUARTZS
      PQ=0 6D0
C=====================================================================
C
C-----------------------------------------------------
C     UPDATE POROSITY
C-----------------------------------------------------
C CALCULATE THE POROSITY INCREMENT
      STATEV(14) = (1 D0 - STATEV(13))
     $          * STATEV(41) / (1 D0 + STATEV(41))
C CALCULATE THE POROSITY AT THE END OF THIS INCREMENT
      STATEV(13) = STATEV(13) + STATEV(14)
C
C-----------------------------------------------------
C     UPDATE GRAVIMETRIC UNFROZEN WATER CONTENT
C-----------------------------------------------------
C GET THE UNFROZEN WATER CONTENT AT THE START OF THE INCREMENT
      WATT = STATEV(15)
C CALCULATE THE WATER CONTENT AT THE END OF THE INCREMENT
            IF (STATEV(2)  GE  ALIQTEMP) THEN
        STATEV(15) = WBAR
      ELSE IF (STATEV(2)  LE  AINTEMP) THEN
        STATEV(15) = WSTAR
      ELSE
         STATEV(15) = WBAR + AF * STATEV(2)
      END IF
C CALCULATE THE UNFROZEN WATER CONTENT INCREMENT
      STATEV(16) = STATEV(15) - WATT
C
C-----------------------------------------------------
C     CALCULATE VOLUMETRIC ICE CONTENT
C-----------------------------------------------------
C GET THE ICE CONTENT AT THE BEGINNING OF THE INCREMENT
      VIATT = STATEV(17)
```

```
C CALCULATE THE ICE CONTENT AT THE END OF THE INCREMENT
      STATEV(17) = STATEV(13) - (DENSKEL / DENWATER)
     $           * STATEV(15) * (1.D0 - STATEV(13))
C
            IF (STATEV(17) .LT. 0 D0) THEN
         STATEV(17) = 0.0D0
            END IF
C CALCULATE THE INCREMENT
      STATEV(18) = STATEV(17) - VIATT
C
C-------------------------------------------------------
C    UPDATE VOLUMETRIC FRACTIONS
C-------------------------------------------------------
C CALCULATE VOLUMETRIC FRACTION OF SKEIETON, WATER AND ICE
C    POROSITY AT THE BEGINNING OF THE INCREMENT
      PROBEGIN = STATEV(13) - STATEV(14)
C    VOLUMETRIC FRACTION OF ICE AT THE BEGINNING OF THE INCREMENT
      VICEBEGIN = STATEV(17) - STATEV(18)
C    VOLUMETRIC FRACTION OF SKELETON, WATER, AND ICE
      VSKEL = 1.D0 - PROBEGIN
      VWATER = PROBEGIN - VICEBEGIN
      VICE = VICEBEGIN
C
C-------------------------------------------------------------------------
C    CALCULATE FROZEN SOIL PROPETIES
C-------------------------------------------------------------------------
C    DRY FROZEN SOIL DENSITY
      DENSOIL = VSKEL * DENSKEL
C    CALCULATE DENSITY OF POROSITY
      DENPRO = VWATER / PROBEGIN * DENWATER
     $      + VICE /PROBEGIN * DENICE
C    CALCULATE THE GRAVIMETRIC WATER CONTENT.
      TGWATER =PROBEGIN / (1.D0 - PROBEGIN) * DENPRO / DENSKEL
C
C-------------------------------------------------------------------------
C    CALCULATE SPECIFIC HEAT CAPACITY AND APPARENT HEAT CAPACITY
C-------------------------------------------------------------------------
C CALCULATE SPECIFIC HEAT CAPACITY
      SPECHT=(VSKEL*DENSKEL*SHTSKEL)+(VWATER*DENWATER*SHTWATER)
     $     +(VICE*DENICE*SHTICE)
C CALCULATE APPARENT HEAT CAPACITY
      IF (STATEV(3) .GE. 0 D0) THEN
       ASPECHT = 0.D0
      ELSE
       ASPECHT = ABS(WLATENT * DENICE * STATEV(18) / STATEV(3))
      END IF
C CALCULATE TOTAL HEAT CAPACITY
      TSPECHT = SPECHT + ASPECHT
C
C-------------------------------------------------------------------------
C    CALCULATE THERMAL CONDICTIVITY BY JOHANSEN'S METHOD
C-------------------------------------------------------------------------
C CALCULATE THE CONSTANT VOLMETRIC WATER CONTENT
C AT THE START OF THE INCREMENT
      CVWATER = (DENSKEL / DENWATER) * WATT * (1.D0 - PROINI)
C
       CONDDRY=(0.137D0*DENSOINI+64 7D0)/(2.7D3-0.947D0*DENSOINI)
       CONDSKEL=7.7D0**PQ*2.D0**(1.D0-PQ)
C    THAWED CONDITION
      IF (STATEV(2)  GE  0.D0) THEN
       CONDE=LOG10(SR)+1 D0
       CONDSAT=(0.57D0**PROINI)*(CONDSKEL**(1 D0-PROINI))
       COND=(CONDSAT-CONDDRY)*CONDE+CONDDRY
C    FROZEN CONDITION
      ELSE
       CONDE=SR
```

```
      CONDSAT=2.2D0**PROINI*CONDSKEL**(1.D0-PROINI)*0.269D0**CVWATER
      COND=(CONDSAT-CONDDRY)*CONDE+CONDDRY
    ENDIF
C
C-----------------------------------------------------
C    CALCULATE THE TEMPERATURE GRADIENT
C-----------------------------------------------------
C    SPACIAL GRADIENT OF TEMPERATURE IN 1-DIRECTION (X)
    STATEV(19) = STATEV(30) / COND
C    SPACIAL GRADIENT OF TEMPERATURE IN 2-DIRECTION (Y)
    STATEV(20) = STATEV(31) / COND
C    SPACIAL GRADIENT OF TEMPERATURE IN 3-DIRECTION (Z)
C     STATEV(21) = STATEV(32) / COND
C
    STATEV(22) = VSKEL
    STATEV(23) = VWATER
    STATEV(24) = VICE
    STATEV(25) = COND
    STATEV(26) = SPECHT
    STATEV(27) = TSPECHT
    STATEV(28) = DENSOIL
    STATEV(29) = TGWATER
C
C-----------------------------------------------------
C    INPUT FLUX(1)
C-----------------------------------------------------
    FLUX(1) = 0.D0
C
    RETURN
    END
```

APPENDIX C.3 User defined function in three dimensions

```
C**********************************************************************
C USER SUBROUTINES FOR THREE-DIMENSIONALSP POROSITY GROWTH FUNCTION
C
C WRITTEN BY KIM, KOUI, 2009
C**********************************************************************
C
C**********************************************************************
C
C SDVINI: ABAQUS WILL CALL THIS ROUTINE TO DEFINE
C THE INITIAL SOLUTION-DEPENDENT STATE VARIABLE FLELDS
C AT PARTICULAR MATERIAL POINTS
C USED WITH THE *INITIAL CONDITIONS, TYPE=SOLUTION, USER OPTION IN INPUT FILE
C
C**********************************************************************
C
      SUBROUTINE SDVINI(STATEV,COORDS,NSTATV,NCRDS,NOEL,NPT,LAYER,KSPT)
C
      INCLUDE 'ABA_PARAM.INC'
C
C     THE NUMBER OF STATE VARIABLES (NSTATV) IS DEFINED USING *DEPVAR OPTSON
C     IN THE INPUT FILE
      DIMENSION STATEV(NSTATV),COORDS(NCRDS)
C
C     THE VALUES OF N_0 AND W_0 MUST MATCH WITH THE DENSITY OF SOIL
C     SKELTON SO THAT THE INITIAL ICE CONTENT IS ZERO
C     INITIAL VALUE FOR POROSITY. N_0
      STATEV(13) = 0.523446435D0
C
C     INITIAL VALUE FOR UNFROZEN WATER CONTENT: W_0
      STATEV(15) = 0.4D0
C
C     INITIAL VALUE FOR VOLUMETRIC ICE CONTENT
      STATEV(17) = 0.D0
C
C     INITIAL VALUE FOR DRY SOIL DENSITY (KG/M^3)
      STATEV(28) = 1308 616088D0
C
C     INITIAL TOTAL WATER CONTENT
      STATEV(29) = 0.4D0
C
C
      RETURN
      END
C
C**********************************************************************
C
C USDFLD· TO OBTAIN THE TEMPERATURE
C THIS SUBROUTINE IS CALLED AT ALL MATERIAL CALCULATION POINTS OF ELEMENTS
C FOR WHICH THE MATERIAL DEFINITION INCLUDES THE *USER DEFINED FIELD OPTION
C USED WITH
C *INITIAL CONDITIONS, TYPE=FIELD
C
C**********************************************************************
C
      SUBROUTINE USDFLD(FIELD,STATEV,PNEWDT,DIRECT,T,CELENT,TIME,DTIME,
     $ CMNAME,ORNAME,NFIELD,NSTATV,NOEL,NPT,LAYER,KSPT,KSTEP,KINC,
     $ NDI,NSHR,COORD,JMAC,JMTYP,MATLAYO,LACCFLG)
C
      INCLUDE 'ABA_PARAM INC'
C
      CHARACTER*80 CMNAME,ORNAME
      CHARACTER*3  FLGRAY(80)
```

APPENDIX C.3 User defined function in three dimensions

```
C**********************************************************************
C USER SUBROUTINES FOR THREE-DIMENSIONALSP POROSITY GROWTH FUNCTION
C
C WRITTEN BY KIM, KOUI, 2009
C**********************************************************************
C
C**********************************************************************
C
C SDVINI  ABAQUS WILL CALL THIS ROUTINE TO DEFINE
C THE INITIAL SOLUTION-DEPENDENT STATE VARIABLE FLELDS
C AT PARTICULAR MATERIAL POINTS
C USED WITH THE *INITIAL CONDITIONS, TYPE=SOLUTION, USER OPTION IN INPUT FILE
C
C**********************************************************************
C
      SUBROUTINE SDVINI(STATEV,COORDS,NSTATV,NCRDS,NOEL,NPT,LAYER,KSPT)
C
      INCLUDE 'ABA_PARAM INC'
C
C     THE NUMBER OF STATE VARIABLES (NSTATV) IS DEFINED USING *DEPVAR OPTSON
C     IN THE INPUT FILE
      DIMENSION STATEV(NSTATV),COORDS(NCRDS)
C
C     THE VALUES OF N_0 AND W_0 MUST MATCH WITH THE DENSITY OF SOIL
C     SKELTON SO THAT THE INITIAL ICE CONTENT IS ZERO
C     INITIAL VALUE FOR POROSITY  N_0
      STATEV(13) = 0 523446435D0
C
C     INITIAL VALUE FOR UNFROZEN WATER CONTENT  W_0
      STATEV(15) = 0 4D0
C
C     INITIAL VALUE FOR VOLUMETRIC ICE CONTENT
      STATEV(17) = 0 D0
C
C     INITIAL VALUE FOR DRY SOIL DENSITY (KG/M^3)
      STATEV(28) = 1308 616088D0
C
C     INITIAL TOTAL WATER CONTENT
      STATEV(29) = 0 4D0
C
C
      RETURN
      END
C
C**********************************************************************
C
C USDFLD  TO OBTAIN THE TEMPERATURE
C THIS SUBROUTINE IS CALLED AT ALL MATERIAL CALCULATION POINTS OF ELEMENTS
C FOR WHICH THE MATERIAL DEFINITION INCLUDES THE *USER DEFINED FIELD OPTION
C USED WITH
C *INITIAL CONDITIONS, TYPE=FIELD
C
C**********************************************************************
C
      SUBROUTINE USDFLD(FIELD,STATEV,PNEWDT,DIRECT,T,CELENT,TIME,DTIME,
     $ CMNAME,ORNAME,NFIELD,NSTATV,NOEL,NPT,LAYER,KSPT,KSTEP,KINC,
     $ NDI,NSHR,COORD,JMAC,JMTYP,MATLAYO,LACCFLG)
C
      INCLUDE 'ABA_PARAM INC'
C
      CHARACTER*80 CMNAME,ORNAME
      CHARACTER*3  FLGRAY(80)
```

```
      DIMENSION FIELD(NFIELD),STATEV(NSTATV),DIRECT(3,3),T(3,3),TIME(2),
     $ COORD(*),JMAC(*),JMTYP(*)
      DIMENSION ARRAY(80),JARRAY(80)
C
C GET APPARENT SPECIFIC HEAT FROM PREVIOUS INCREMENT
      CALL GETVRM('TEMP',ARRAY,JARRAY,FLGRAY,JRCD,
     $    JMAC, JMTYP, MATLAYO, LACCFLG)
      STATEV(54) = ARRAY(1)
C
C GET APPARENT SPECIFIC HEAT FROM PREVIOUS INCREMENT
      CALL GETVRM('SDV',ARRAY,JARRAY,FLGRAY,JRCD,
     $    JMAC, JMTYP, MATLAYO, LACCFLG)
      FIELD(1) = ARRAY(27)
C
C GET HEAT FLUX FROM PREVIOUS INCREMENT
      CALL GETVRM('HFL',ARRAY,JARRAY,FLGRAY,JRCD,
     $    JMAC, JMTYP, MATLAYO, LACCFLG)
C     HEAT FLUX IN 1-DIRECTION (X)
      STATEV(30) = ARRAY(2)
C     HEAT FLUX IN 2-DIRECTION (Y)
      STATEV(31) = ARRAY(3)
C     HEAT FLUX IN 3-DIRECTION (Z)
      STATEV(32) = ARRAY(4)
C
C     CHARACTERISTIC ELEMENT LENGTH
      STATEV(33) = CELENT
C
C GET MISES STRESS FROM PREVIOUS INCREMENT
      CALL GETVRM('SINV',ARRAY,JARRAY,FLGRAY,JRCD,
     $    JMAC, JMTYP, MATLAYO, LACCFLG)
C     MISES
      STATEV(34) = ARRAY(1)
C
C GET COORDINATE (M)
      STATEV(35) = COORD(1)
      STATEV(36) = COORD(2)
      STATEV(37) = COORD(3)
C
C-------------------------------------------------
C     PARAMETERS FOR PFFF
C-------------------------------------------------
C     TOTAL TIME AT THE BEGINNING OF THE CURRENT INCREMENT
      TTIME = TIME(2)
C
C DETERMINE ASPWLTEMP:
      ASPWLTEMP1 =  0.5D0
      ASPWLTEMP2 =  0.2D0
      ASPWLTEMP3 =  0.1D0
      ASPWLTEMP4 =  0.05D0
      ASPWLTEMP5 =  -0.01D0
C
C DETERMINE ASPS:
      ASPS1 = 2.D0
      ASPS2 = 2.5D0
      ASPS3 = 3.D0
      ASPS4 = 4.D0
      ASPS5 = 4.D0
C
      ATTIME1 = 11028960
      ATTIME2 = 26295840
      ATTIME3 = 42564960
      ATTIME4 = 74100960
      ATTIME5 = 91756800
C
      IF (TTIME .LE. ATTIME1) THEN
       ASPWLTEMP = ASPWLTEMP1
```

```
      ASPS = ASPS1
     ELSE IF (TTIME .LE. ATTIME2) THEN
      ASPWLTEMP = ASPWLTEMP2
      ASPS = ASPS2
     ELSE IF (TTIME .LE. ATTIME3) THEN
      ASPWLTEMP = ASPWLTEMP3
      ASPS = ASPS3
     ELSE IF (TTIME .LE. ATTIME4) THEN
      ASPWLTEMP = ASPWLTEMP4
      ASPS = ASPS4
     ELSE
      ASPWLTEMP = ASPWLTEMP5
      ASPS = ASPS5
     END IF
C
     STATEV(4) = TTIME
     STATEV(5) = ASPWLTEMP
     STATEV(6) = ASPS
C
C-------------------------------------------
C    PARAMETERS FOR WATER TABLE
C-------------------------------------------
C    ELEVATION OF GROUND SURFACE (M)
     AEGS = 1.D0
C    ELEVATION OF SOIL BOUDARY (M)
     AEBS = -857 D-03
C
     AWT01 = 0.D0
     AWT02 = 12787200.D0
     AWT03 = 24796800.D0
     AWT04 = 29808000.D0
     AWT05 = 42508800.D0
     AWT06 = 54086400.D0
     AWT07 = 61344000.D0
     AWT08 = 75859200.D0
     AWT09 = 87868800.D0
     AWT10 = 95212800.D0
     AWT11 = 107308800.D0
     AWT12 = 117158400.D0
C
     AWY01 = -1.7D0
     AWY02 = -1.7D0
     AWY03 = 0.5D0
     AWY04 = -1.7D0
     AWY05 = -1.7D0
     AWY06 = 0 D0
     AWY07 = -2.2D0
     AWY08 = -2.2D0
     AWY09 = 0 5D0
     AWY10 = -1 7D0
     AWY11 = -1.7D0
     AWY12 = 0.5D0
C
     AWCT01S = 12787200.D0
     AWCT01E = 17625600 D0
     AWCT02S = 42508800.D0
     AWCT02E = 48470400.D0
     AWCT03S = 75859200 D0
     AWCT03E = 80697600 D0
     AWCT04S = 109728000 D0
     AWCT04E = 113356800 D0
C
     AWCY01 = 0.D0
     AWCY02 = 0 5D0
     AWCY03 = 0.D0
     AWCY04 = 0.D0
```

```
C
      IF (TTIME .LE. AWT02) THEN
       AWY1 = AWY01
       AWY2 = AWY02
       TTIME1 = AWT01
       TTIME2 = AWT02
      ELSE IF (TTIME .LE  AWT03) THEN
       AWY1 = AWY02
       AWY2 = AWY03
       TTIME1 = AWT02
       TTIME2 = AWT03
      ELSE IF (TTIME .LE. AWT04) THEN
       AWY1 = AWY03
       AWY2 = AWY04
       TTIME1 = AWT03
       TTIME2 = AWT04
      ELSE IF (TTIME .LE. AWT05) THEN
       AWY1 = AWY04
       AWY2 = AWY05
       TTIME1 = AWT04
       TTIME2 = AWT05
      ELSE IF (TTIME .LE. AWT06) THEN
       AWY1 = AWY05
       AWY2 = AWY06
       TTIME1 = AWT05
       TTIME2 = AWT06
      ELSE IF (TTIME .LE  AWT07) THEN
       AWY1 = AWY06
       AWY2 = AWY07
       TTIME1 = AWT06
       TTIME2 = AWT07
      ELSE IF (TTIME .LE  AWT08) THEN
       AWY1 = AWY07
       AWY2 = AWY08
       TTIME1 = AWT07
       TTIME2 = AWT08
      ELSE IF (TTIME .LE. AWT09) THEN
       AWY1 = AWY08
       AWY2 = AWY09
       TTIME1 = AWT08
       TTIME2 = AWT09
      ELSE IF (TTIME .LE. AWT10) THEN
       AWY1 = AWY09
       AWY2 = AWY10
       TTIME1 = AWT09
       TTIME2 = AWT10
      ELSE IF (TTIME  LE. AWT11) THEN
       AWY1 = AWY10
       AWY2 = AWY11
       TTIME1 = AWT10
       TTIME2 = AWT11
      ELSE IF (TTIME  LE  AWT12) THEN
       AWY1 = AWY11
       AWY2 = AWY12
       TTIME1 = AWT11
       TTIME2 = AWT12
      ELSE
       AWY1 = AWY11
       AWY2 = AWY11
       TTIME1 = AWT11
       TTIME2 = AWT12
      END IF
C
C     CALCULATE GROUND WATER TABLE (M)
      WTY = AWY1 + (AWY2 - AWY1) / (TTIME2 - TTIME1)
     $   * (TTIME - TTIME1)
```

```
C
C   MODIFY WITH CONFINED EFFECT
    IF ((TTIME .GE. AWCT01S) .AND.
   $   (TTIME .LE. AWCT01E)) THEN
     WTY = AWCY01
    ELSE IF ((TTIME .GE. AWCT02S) .AND.
   $        (TTIME .LE. AWCT02E)) THEN
     WTY = AWCY02
    ELSE IF ((TTIME .GE. AWCT03S) .AND.
   $        (TTIME .LE. AWCT03E)) THEN
     WTY = AWCY03
    ELSE IF ((TTIME .GE. AWCT04S) .AND.
   $        (TTIME .LE. AWCT04E)) THEN
     WTY = AWCY04
    ELSE
     WTY = WTY
    END IF
C
C   CALCULATE BULK SOIL DENSITY (KG/M^3)
    DENSBULK = STATEV(28) * (1.D0 + STATEV(29))
C   BULK SOIL DESNSITY OF USR(KG/M^3)
    DENSBULKUSR = 1716.904308D0
C
C   OVERBURDEN PRESSURE (IN UNIT OF PASCAL)
    IF (STATEV(36) .GE. AEGS) THEN
     PRE = 0.D0
    ELSE IF (WTY .GE. AEBS) THEN
     IF (STATEV(36) .GE. WTY) THEN
      PRE = 9.80665D0 * (DENSBULKUSR*(AEGS - STATEV(36)))
     ELSE IF (STATEV(36) .GE. AEBS) THEN
      PRE = 9.80665D0 * (DENSBULKUSR*(AEGS - WTY)
   $      + (DENSBULKUSR - 1000.D0)*(WTY - STATEV(36)))
     ELSE
      IF (STATEV(54) .LE. STATEV(5)) THEN
       PRE = 9.80665D0 * (DENSBULKUSR*(AEGS - WTY)
   $        + (DENSBULKUSR - 1000.D0)*(WTY - AEBS)
   $        + (DENSBULK -1000.D0)*(AEBS - STATEV(36)))
      ELSE
       PRE = 9.80665D0 * (DENSBULKUSR*(AEGS - WTY)
   $        + DENSBULKUSR*(WTY - AEBS)
   $        + STATEV(28)*(AEBS - STATEV(36)))
      END IF
     END IF
    ELSE
     IF (STATEV(36) .GE. AEBS) THEN
      PRE = 9.80665D0 * (DENSBULKUSR*(AEGS - STATEV(36)))
     ELSE IF (STATEV(36) .GE. WTY) THEN
      PRE = 9.80665D0 * (DENSBULKUSR*(AEGS - AEBS)
   $      + DENSBULK*(AEBS - STATEV(36)))
     ELSE
      IF (STATEV(54) .LE. STATEV(5)) THEN
       PRE = 9.80665D0 * (DENSBULKUSR*(AEGS - AEBS)
   $        + DENSBULK*(AEBS - WTY)
   $        + (DENSBULK - 1000.D0)*(WTY - STATEV(36)))
      ELSE
       PRE = 9.80665D0 * (DENSBULKUSR*(AEGS - AEBS)
   $        + DENSBULK*(AEBS - WTY)
   $        + STATEV(28)*(WTY - STATEV(36)))
      END IF
     END IF
    END IF
C
    STATEV(38) = WTY
    STATEV(39) = DENSBULK
    STATEV(40) = PRE
C
```

```
C    CALCULATE THE AVERAGE TOTAL STRESS
     STATEV(46) = STATEV(34) + STATEV(40)
C
     RETURN
     END
C
C
C*************************************************************************C
C UEXPAN  TO DEFINE INCREMENTAL THERMAL STRAINS
C THIS SUBROUTINE IS CALLED AT ALL INTEGRATION POINTS OF ELEMENTS
C FOR WHICH THE MATERIAL OR GASKET BEHAVIOR DEFINITION CONTAINS THE *EXPANSION,
C USER OPTION
C
C*************************************************************************
C
     SUBROUTINE UEXPAN(EXPAN,DEXPANDT,TEMP,TIME,DTIME,PREDEF,DPRED,
    $    STATEV,CMNAME,NSTATV,NOEL)
C
     INCLUDE 'ABA_PARAM INC'
C
     CHARACTER*80 CMNAME
C
     DIMENSION EXPAN(*),DEXPANDT(*),TEMP(2),TIME(2),PREDEF(*),
    $    DPRED(*),STATEV(NSTATV)
C
C-----------------------------------------------
C    TEMPERATURE AND TIME
C-----------------------------------------------
C    TEMPERATURE AT THE END OF THE INCREMENT (ALSO CALLED CURRENT TEMPERATURE)
     ETEMP = TEMP(1)
C    TEMPERATURE INCREMENT
     DTEMP = TEMP(2)
C    TEMPERATURE AT THE BEGINNING OF THE INCREMENT
     STEMP = TEMP(1) - TEMP(2)
C    TEMPERATURE AT THE END OF THE INCREMENT (ALSO CALLED CURRENT TEMPERATURE)
     TTIME = TIME(2)
C
C    SAVE THE TEMPERATURES AS SDVS
     STATEV(1) = STEMP
     STATEV(2) = ETEMP
     STATEV(3) = DTEMP
C
     PI = 3 14159265358D0
C CALCULATE THE RATE OF COOLING (C/HR)
     DTDT = -1 D0 * DTEMP / DTIME * 3600D0
C
C=============================================================================
C-----------------------------------------------
C    PARAMETERS FOR TEMPERATURE
C-----------------------------------------------
     ASPWTEMP = -0 15D0
     ASPCTEMP = -0 35D0
C
C-----------------------------------------------
C    PARAMETERS FOR SP POROSITY RATE FUNCTION
C-----------------------------------------------
C    SP0 VALUE (M2/(SEC*C))
     PSP0 = 262 4D-11
C    B VALUE (PA^-1)
     PB = 0 02596D-3
C
C    CHARACTERISTIC ELEMENT LENGTH
     EVOL = STATEV(33) * STATEV(33) * STATEV(33)
     PEW = 1 25D0
     PEL = SQRT (EVOL / PEW)
     PAREAINI = PEL * PEW
```

```
C
C   MAXIMUM POROSITY
    PM = 0.7D0
C   POISSON'S RATION
    PSN = 0.3D0
C
C   CALCULATE THE AVERAGE TOTAL STRESS
    SKK = STATEV(34) + STATEV(40)
C
C   PARAMETER IN POROSITY GROWTH TENSOR TO DETERMINE ISOTROPIC OR ORTHOTROPIC
C   GROWTH
C   IN THE DIRECTION OF HEAT FLOW. SI IS BETWEEN 1/3 (ISOTROPIC) AND 1.0
C   (UNIDERECTIONAL GROWTH IN THE DIRECTION OF HEAT FLOW)
    SI = 0.9D0
C
C=======================================================================
C CALCULATE THE MAXZRNUM SPACIAL TEMPERATURE GRADIENT (C/M):
    DTDL = SQRT (STATEV(19)**2.D0+ STATEV(20)**2.D0
   $                + STATEV(21)**2.D0)
C
C FIND THE ANGLE BETWEEN THE X-AXIS AND THE LINE OF THE HEAT FLOW DIRECTION
    IF (ABS(STATEV(19)) .LE. 1.0E-7) THEN
     PHI = PI / 2.0D0
    ELSE
     PHI = ATAN(STATEV(20) / STATEV(19))
    END IF
C
C FIND THE ANGLE BETWEEN THE Z-AXI AND THE LINE OF THE HEAT FLOW DIRECTION
    IF (SQRT (STATEV(19)**2.D0+ STATEV(20)**2.D0) .LE. 1.0E-7) THEN
     PSI = PI / 2.0D0
    ELSE
     PSI = PI / 2.0D0 - ATAN(STATEV(21)
   $     / SQRT (STATEV(19)**2.D0+ STATEV(20)**2.D0))
    END IF
C
    DIRMPH = COS(PHI)
    DIRNPH = SIN(PHI)
C
    DIRMPS = COS(PSI)
    DIRNPS = SIN(PSI)
C
    STATEV(55) = PHI * 180.D0 / PI
    STATEV(56) = PSI * 180.D0 / PI
    STATEV(57) = DIRMPH
    STATEV(58) = DIRNPH
    STATEV(59) = DIRMPS
    STATEV(60) = DIRNPS
C
C-----------------------------------------------------------------------
C   CALCULATE THE IN-SITU VOLUMETRIC STRAIN: DE_IN
C-----------------------------------------------------------------------
    DEIN = -0.09D0 * STATEV(23)
   $    * STATEV(16)/(STATEV(15)-STATEV(16))
C
C-----------------------------------------------------------------------
C   CALCULATE THE SP VOLUMETRIC STRAIN: DE_SP
C-----------------------------------------------------------------------
C CALCULATE THE AREA:
C    IF (PSI .EQ. PI / 2.0D0) THEN
C      PAREAPSI = PAREAINI
C    ELSE
C           PAREAPSI = ABS(PAREAINI / COS(PI / 2.0D0 - ABS(PSI)))
C    END IF
C
    IF (PHI .EQ. PI / 2.0D0) THEN
     PAREASP = PAREAINI
```

```
      ELSE
            PAREASP = ABS(PAREAINI / COS(PI / 2.0D0 - ABS(PHI)))
      END IF
C
C CALCULATE THE FLAG OF BOTTOM OF SP:
      IF (STATEV(36) .GE. -6.0D0) THEN
       PFB = 1.D0
      ELSE
            PFB = 0.D0
      END IF
C
C CALCULATE THE FLAG OF SIDE OF SP:
      IF (STATEV(35) .LE. STATEV(6)) THEN
       PFS = 1.D0
      ELSE
            PFS = 0.D0
      END IF
C
C CALCULATE THE FLAG OF FREEZING:
      IF (DTEMP .GE. 0.D0) THEN
       PFDT = 0.D0
      ELSE
       PFDT = 1.D0
      END IF
C
C CALCULATE THE FLAG OF WATER TABLE:
      IF (STATEV(36) .GE. STATEV(38)) THEN
       PFWT = 0.D0
      ELSE
            PFWT = 1.D0
      END IF
C
C CALCULATE THE FLAG OF SP FREEZIG ZONE:
      IF (STATEV(32) .GE. 30.D0) THEN
       IF ((STATEV(2) .LE. STATEV(5)) .AND.
     $    (STATEV(2) .GE. ASPCTEMP)) THEN
         PFFF = 1.0D0
       ELSE
         PFFF = 0.D0
       END IF
      ELSE
       IF ((STATEV(2) .LE. 0.D0) .AND.
     $    (STATEV(2) .GE. ASPCTEMP)) THEN
         PFFF = 1.0D0
       ELSE
         PFFF = 0.D0
       END IF
      END IF
C
C CALCULATE THE FLAG OF SP POROSITY FUNCTION
      PFDESP = PFB * PFS * PFDT * PFWT * PFFF
C
      IF (PFDESP .LE. 0.D0) THEN
       PFDESP = 0.D0
      ELSE
       PFDESP = 1.D0
      END IF
C
C CALCULATE THE FRACTION OF ELEMENT NUMBER
      IF (DTDL .EQ. 0.D0) THEN
       PFEL = 0.D0
      ELSE
       PFEL = ((ASPWTEMP - ASPCTEMP) / DTDL) / PEL
      END IF
C
C CALCULATE THE SP POROSITY FUNCTION
```

```
      IF (PFEL .EQ. 0.D0) THEN
        PSP = 0.D0
      ELSE IF (PFEL .GE. 1.D0) THEN
        PSP = PSP0 / (EVOL* PFEL) * PAREASP
     $     * EXP(-1.D0 * PB * STATEV(46))
      ELSE
        PSP = PSP0 / EVOL * PAREASP
     $     * EXP(-1.D0 * PB * STATEV(46))
      END IF
C
C CALCULATE THE SP VOLUMETRIC STRAIN: DE_SP
      IF (STATEV(13) .GE. PM) THEN
        DESP = 0.D0
      ELSE
        DESP = PFDESP
     $     * 1.09D0 * PSP * DTDL * DTIME
      END IF
C
C-----------------------------------------------------------------------
C     CALCULATE THE TOTAL VOLUMETRIC STRAIN: DE_TOTAL
C-----------------------------------------------------------------------
        DE = DEIN + DESP
C
C GET GRADTSP (C/CM)
      IF (PFFF . EQ. 0.D0) THEN
        VGRADTSP=0.D0
      ELSE
        VGRADTSP= PFFF * DTDL
      END IF
C
C GET SE (Permafrost Subcommittee)
      IF (PFFF . EQ. 0.D0) THEN
        VSE=0.D0
      ELSE
        VSE = PFFF * STATEV(34)
      END IF
C
C GET LSP (Permafrost Subcommittee)
      IF (PFFF . EQ. 0.D0) THEN
        VPFEL=0.D0
      ELSE
        VPFEL=PFFF * PFEL
      END IF
C
      STATEV(41) = DE
      STATEV(42) = DEIN
      STATEV(43) = DESP
      STATEV(44) = DTDT
      STATEV(45) = DTDL
C     STATEV(46) = SKK
      STATEV(47) = PFEL
      STATEV(48) = PAREASP
      STATEV(49) = PFFF
      STATEV(50) = PFDESP
C
      STATEV(51) = VGRADTSP
      STATEV(52) = VSE
      STATEV(53) = VPFEL
C
      EXPAN(1) = DE * (SI * DIRNPS**2.D0 * DIRMPH**2.D0
     $       + 0.5D0 * (1.D0-SI) * DIRNPH**2.D0
     $       + 0.5D0 * (1.D0-SI) * DIRMPS**2.D0 * DIRMPH**2.0D0)
      EXPAN(2) = DE * (SI * DIRNPS**2.D0 * DIRNPH**2.D0
     $       + 0.5D0 * (1.D0-SI) * DIRMPH**2.D0
     $       + 0.5D0 * (1.D0-SI) * DIRMPS**2.D0 * DIRNPH**2.0D0)
      EXPAN(3) = DE * (SI * DIRMPS**2.D0
```

```
     $       + 0.5D0 * (1.D0-SI) * DIRNPS**2.D0)
      EXPAN(4) = DE * (SI * DIRNPS**2.D0 * DIRMPH* DIRNPH
     $       - 0.5D0 * (1.D0-SI) * DIRMPH * DIRNPH
     $       + 0.5D0 * (1.D0-SI) * DIRMPS**2.D0 * DIRMPH * DIRNPH)
      EXPAN(5) = DE * (SI * DIRMPS * DIRNPS * DIRMPH
     $       - 0.5D0 * (1.D0-SI) * DIRMPS * DIRNPS * DIRMPH)
      EXPAN(6) = DE * (SI * DIRMPS * DIRNPS * DIRNPH
     $       - 0.5D0 * (1.D0-SI) * DIRMPS * DIRNPS * DIRNPH)
C
      STATEV(7) = EXPAN(1)
      STATEV(8) = EXPAN(2)
      STATEV(9) = EXPAN(3)
      STATEV(10) = EXPAN(4)
      STATEV(11) = EXPAN(5)
      STATEV(12) = EXPAN(6)
C
      RETURN
      END
C
C
C**********************************************************************************
C
C HETVAL: TO OBTAIN THE TEMPERATURE
C THIS SUBROUTINE IS CALLED AT ALL MATERIAL CALCULATION POINTS OF ELEMENTS
C FOR WHICH THE MATERIAL DEFINITION INCLUDES THE *HEAT GENERATION OPTION
C
C**********************************************************************************
C
      SUBROUTINE HETVAL(CMNAME,TEMP,TIME,DTIME,STATEV,FLUX,
     1 PREDEF,DPRED)
C
      INCLUDE 'ABA_PARAM.INC'
C
      CHARACTER*80 CMNAME
C
      DIMENSION TEMP(2),STATEV(*),PREDEF(*),TIME(2),FLUX(2),
     1 DPRED(*)
C
C==================================================================================
C----------------------------------------------------
C   PARAMETERS FOR TEMPERATURE
C----------------------------------------------------
      ALIQTEMP = 0.0D0
      AINTEMP = -0.1D0
C
C----------------------------------------------------
C   PARAMETERS FOR UNFROZEN WATER CONTENT CURVE
C----------------------------------------------------
C   INITIAL WATER CONTENT, RESIDUAL WATER CONTENT
      WBAR = 0.4D0
      WSTAR= 0.07D0
      AF = (WBAR - WSTAR) / (ALIQTEMP - AINTEMP)
C
C----------------------------------------------------
C   SOIL PROPERTY CONSTANTS
C----------------------------------------------------
C   DENSITIES OF SOIL SKELETON, WATER, AND ICE
      DENSKEL = 2746.D0
      DENWATER = 1000.D0
      DENICE = 1000.D0 / 1.09D0
C   MASS SPECIFIC HEAT CAPACITIES OF SOIL SKELETON, WATER AND ICE
      SHTSKEL = 800.D0
      SHTWATER = 4200.D0
      SHTICE = 2090.D0
C   LATENT HEAT OF FUSION OF WATER
      WLATENT = 333700.D0
```

```
C
C-----------------------------------------------------
C   PARAMETERS FOR THERMAL CONDUCTIVITY
C-----------------------------------------------------
    PROINI = 0.523446435D0
    DENSOINI = DENSKEL * (1.D0 - PROINI)
C   SATURATION
    SR=1.0D0
C   QUARTZS
    PQ=0.6D0
C=====================================================================
C
C-----------------------------------------------------
C   UPDATE POROSITY
C-----------------------------------------------------
C CALCULATE THE POROSITY INCREMENT
    STATEV(14) = (1.D0 - STATEV(13))
   $        * STATEV(41) / (1.D0 + STATEV(41))
C CALCULATE THE POROSITY AT THE END OF THIS INCREMENT
    STATEV(13) = STATEV(13) + STATEV(14)
C
C-----------------------------------------------------
C   UPDATE GRAVIMETRIC UNFROZEN WATER CONTENT
C-----------------------------------------------------
C GET THE UNFROZEN WATER CONTENT AT THE START OF THE INCREMENT
    WATT = STATEV(15)
C CALCULATE THE WATER CONTENT AT THE END OF THE INCREMENT
            IF (STATEV(2) .GE. ALIQTEMP) THEN
       STATEV(15) = WBAR
      ELSE IF (STATEV(2) .LE. AINTEMP) THEN
       STATEV(15) = WSTAR
      ELSE
        STATEV(15) = WBAR + AF * STATEV(2)
      END IF
C CALCULATE THE UNFROZEN WATER CONTENT INCREMENT
    STATEV(16) = STATEV(15) - WATT
C
C-----------------------------------------------------
C   CALCULATE VOLUMETRIC ICE CONTENT
C-----------------------------------------------------
C GET THE ICE CONTENT AT THE BEGINNING OF THE INCREMENT
    VIATT = STATEV(17)
C CALCULATE THE ICE CONTENT AT THE END OF THE INCREMENT
    STATEV(17) = STATEV(13) - (DENSKEL / DENWATER)
   $          * STATEV(15) * (1 D0 - STATEV(13))
C
            IF (STATEV(17) .LT. 0.D0) THEN
       STATEV(17) = 0.0D0
            END IF
C CALCULATE THE INCREMENT
    STATEV(18) = STATEV(17) - VIATT
C
C-----------------------------------------------------
C   UPDATE VOLUMETRIC FRACTIONS
C-----------------------------------------------------
C CALCULATE VOLUMETRIC FRACTION OF SKEIETON, WATER AND ICE
C   POROSITY AT THE BEGINNING OF THE INCREMENT
    PROBEGIN = STATEV(13) - STATEV(14)
C   VOLUMETRIC FRACTION OF ICE AT THE BEGINNING OF THE INCREMENT
    VICEBEGIN = STATEV(17) - STATEV(18)
C   VOLUMETRIC FRACTION OF SKELETON, WATER, AND ICE
    VSKEL = 1.D0 - PROBEGIN
    VWATER = PROBEGIN - VICEBEGIN
    VICE = VICEBEGIN
C
C-----------------------------------------------------------------
```

```
C    CALCULATE FROZEN SOIL PROPETIES
C-----------------------------------------------------------------------
C    DRY FROZEN SOIL DENSITY
     DENSOIL = VSKEL * DENSKEL
C    CALCULATE DENSITY OF POROSITY:
     DENPRO = VWATER / PROBEGIN * DENWATER
    $      + VICE /PROBEGIN * DENICE
C    CALCULATE THE GRAVIMETRIC WATER CONTENT·
     TGWATER =PROBEGIN / (1.D0 - PROBEGIN) * DENPRO / DENSKEL
C
C-----------------------------------------------------------------------
C    CALCULATE SPECIFIC HEAT CAPACITY AND APPARENT HEAT CAPACITY
C-----------------------------------------------------------------------
C CALCULATE SPECIFIC HEAT CAPACITY
     SPECHT=(VSKEL*DENSKEL*SHTSKEL)+(VWATER*DENWATER*SHTWATER)
    $     +(VICE*DENICE*SHTICE)
C CALCULATE APPARENT HEAT CAPACITY
     IF (STATEV(3) .GE. 0 D0) THEN
      ASPECHT = 0.D0
     ELSE
      ASPECHT = ABS(WLATENT * DENICE * STATEV(18) / STATEV(3))
     END IF
C CALCULATE TOTAL HEAT CAPACITY
     TSPECHT = SPECHT + ASPECHT
C
C-----------------------------------------------------------------------
C    CALCULATE THERMAL CONDICTIVITY BY JOHANSEN'S METHOD
C-----------------------------------------------------------------------
C CALCULATE THE CONSTANT VOLMETRIC WATER CONTENT
C AT THE START OF THE INCREMENT
     CVWATER = (DENSKEL / DENWATER) * WATT * (1.D0 - PROINI)
C
      CONDDRY=(0.137D0*DENSOINI+64.7D0)/(2.7D3-0.947D0*DENSOINI)
      CONDSKEL=7.7D0**PQ*2.D0**(1.D0-PQ)
C    THAWED CONDITION
     IF (STATEV(2) .GE. 0.D0) THEN
      CONDE=LOG10(SR)+I D0
      CONDSAT=(0.57D0**PROINI)*(CONDSKEL**(1.D0-PROINI))
      COND=(CONDSAT-CONDDRY)*CONDE+CONDDRY
C    FROZEN CONDITION
     ELSE
      CONDE=SR
      CONDSAT=2 2D0**PROINI*CONDSKEL**(1.D0-PROINI)*0.269D0**CVWATER
      COND=(CONDSAT-CONDDRY)*CONDE+CONDDRY
     ENDIF
C
C-----------------------------------------------------------
C    CALCULATE THE TEMPERATURE GRADIENT
C-----------------------------------------------------------
C    SPACIAL GRADIENT OF TEMPERATURE IN 1-DIRECTION (X)
     STATEV(19) = STATEV(30) / COND
C    SPACIAL GRADIENT OF TEMPERATURE IN 2-DIRECTION (Y)
     STATEV(20) = STATEV(31) / COND
C    SPACIAL GRADIENT OF TEMPERATURE IN 3-DIRECTION (Z)
     STATEV(21) = STATEV(32) / COND
C
     STATEV(22) = VSKEL
     STATEV(23) = VWATER
     STATEV(24) = VICE
     STATEV(25) = COND
     STATEV(26) = SPECHT
     STATEV(27) = TSPECHT
     STATEV(28) = DENSOIL
     STATEV(29) = TGWATER
C
C-----------------------------------------------------------
```

```
C    INPUT FLUX(1)
C-----------------------------------------------------
     FLUX(1) = 0 D0
C
     RETURN
     END
```